Abstract

Title of Dissertation: THE DEVELOPMENT AND IMPLEMENTATION OF NUMERICAL TOOLS FOR INVESTIGATION INTO THE GRANULAR DYNAMICS OF SOLID SOLAR SYSTEM BODIES

Stephen Ross Schwartz, Doctor of Philosophy, 2013

Dissertation directed by: Professor Derek Charles Richardson
Department of Astronomy

The work advanced in this thesis joins together the disciplines of planetary science and granular physics. Grain dynamics have played a prominent role in the evolution of our Solar System from planetesimal formation billions of years ago to the surface processes that take place today on terrestrial planets, moons, and small bodies. Recent spacecraft images of small Solar System bodies provide strong evidence that the majority of these bodies are covered in regolith. This regolith ranges in size from the fine powder found on the Moon to large rocks and boulders, like the 27 m Yoshinodai boulder on the small asteroid Itokawa. Accordingly, the processes that take place on the solid bodies of the Solar System vary widely based upon the material properties of the regolith and the gravitational environments on their surfaces. An understanding of granular dynamics is also critical for the design and operations of landers, sampling devices and rovers to be included in space missions.

Part of my research is concerned with the development of numerical tools that have the ability to provide explanations for the types of processes that our spacecraft have observed. Granular processes on Earth are incredibly complex and varied, and constitute an enormous field of study on their own, with input taken from across the broad disciplines of engineering and the physical sciences. In microgravity, additional forces, which on Earth are relevant only to micron-size particles or smaller, are expected to become important for material up to the size of large rocks, adding further complexity.

The numerical tools developed in this work allow for the simulation of grains using an adaptation of the Soft-Sphere Discrete Element Method (SSDEM) along with implementations of cohesive forces between particles into an existing parallel gravity tree code.

THE DEVELOPMENT AND IMPLEMENTATION OF NUMERICAL TOOLS FOR INVESTIGATION INTO THE GRANULAR DYNAMICS OF SOLID SOLAR SYSTEM BODIES

by

Stephen Ross Schwartz

Dissertation submitted to the Faculty of the Graduate School of the
University of Maryland at College Park in partial fulfillment
of the requirements for the degree of
Doctor of Philosophy
2013

Advisory Committee:

Professor Derek Charles Richardson, chair
Doctor Patrick Michel, co-chair
Professor Michael F. A'Hearn
Professor Olivier S. Barnouin
Doctor Andrew F. Cheng
Professor Douglas P. Hamilton
Professor M. Coleman Miller
Professor Alan L. Sussman

Preface

The code developments included in this work are based upon a numerical gravity solver, `pkdgrav`, first developed for cosmological modeling at the University of Washington (Stadel 2001). The code was adapted to treat hard-sphere collisions for planetesimal modeling by Richardson et al. (2000). The main technical features of the code include a hierarchical tree algorithm for reducing the computational cost of interparticle force calculations and a complete parallel implementation for balancing work across an arbitrary number of processors. The soft-sphere collisional routines and deformable bonding (cohesive force) routines are new to this work. Portions of Chapters 2 and 3 appeared in modified form in the journals *Granular Matter* (Schwartz et al. 2012c) and *Icarus* (Schwartz et al. 2013), respectively. A write-up of the study outlined in Chapter 4 is being drafted for submission to *Icarus*. Overviews of the work and/or methodology from Chapter 2 were the subject of oral presentations at the 2011 European Planetary Science Congress/Division for Planetary Sciences of the American Astronomical Society (EPSC-DPS) Joint Meeting, held October 2–7 in Nantes, France (Schwartz et al. 2011; Walsh et al. 2011); at the 2010 DPS held October 3–8 in Pasadena, California (Richardson et al. 2010); at the 2012 Lunar and Planetary Science Conference (LPSC), held March 19–23 in The Woodlands, Texas (Richardson et al. 2012b); and at the 2012 DPS held October 14–19 in Reno, Nevada (Michel et al. 2012a; Richardson et al. 2012a). Various portions of the work and/or methodology from Chapter 3 were presented at the 2008 DPS held October 10–15 in Ithaca, New York (Richardson et al. 2008); the 2009 DPS held October 4–9 in Fajardo, Puerto Rico (Schwartz et al. 2009; Walsh et al. 2009); the 2009 American Astronomical Society's Division on Dynamical Astronomy (DDA) held May 2–5 in Virginia Beach, Virginia (Richardson et al. 2009b); the 2011 EPSC-DPS Joint Meeting (Michel et al. 2011); the 2012 LPSC (Michel et al. 2012b). The work discussed in Chapter 4 was presented at the 2012 DPS (Schwartz et al. 2012a), the 2012 Asteroids, Comets, Meteors (ACM) conference held May 16–20 in Niigata, Japan (Schwartz et al. 2012b), and the 2012 EPSC (Michel et al. 2012c) held September 23–28 in Madrid, Spain.

I dedicate this thesis to my grandfather, J. Leonard Konigsberg, and also to my grandmother, Ann Konigsberg, my grandmother, Rose Schwartz, and my grandfather, Max Schwartz.

Acknowledgements

Many more thanks are deserved than will be given. First and foremost though, Derek has been about the best advisor that a student could ask for. Besides sending me to conferences and workshops around the world, he always took the time to speak with me about any issue, no matter how minor, and welcomed any question or comment I may have had. He's also just really fun to be around. I would also like to thank him for introducing me to Patrick. Patrick has been about the best advisor that a student could ask for. I appreciate all the kindness and patience in his efforts to make me feel comfortable while I was in France, and in his and Derek's efforts to make me comfortable in a professional capacity as well. I am appreciative of my unique fortune to have had the advisor duo of Derek and Patrick, and likely will even more so in retrospect. I would also like to thank my advisory committee at Maryland—best a student could ask for—Mike A'Hearn, Doug Hamilton, and Cole Miller, for providing outside perspectives, advice, and support. Many thanks are owed to the rest of the faculty and staff, and to my fellow graduates. The special ones know they're special and get a secret thanks...so do family and friends on the outside for sanity and good times.

The material in this thesis is based on work supported by the National Aeronautics and Space Administration under Grant No. NNX08AM39G issued through the Office of Space Science, and by the National Science Foundation under Grant Nos. AST0524875 and AST1009579. Part of the work was performed in France, supported by the Chateaubriand 2011 fellowship from the Embassy of France in the United States. Some material was also performed as part of the International Team collaboration number 202 sponsored by the International Space Science Institute (ISSI) in Bern, Switzerland. Simulations were performed on the `yorp` cluster administered by the Center for Theory and Computation of the Department of Astronomy at the University of Maryland in College Park, the `deepthought` cluster administered by the Office of Information Technology at the University of Maryland in College Park, and on the computer cluster `SIGAMM` at the Côte d'Azur Observatory in Nice (France).

Contents

List of Tables

List of Figures

Chapter 1

Introduction

Besides being of relevance to a variety of applications in industry, the study of granular materials and their dynamics is of great importance in the field of planetary science. Much of the work contained in this thesis concerns the development of numerical tools designed to explore the granular dynamics that take place on small Solar System bodies, typically with a mind toward replicating them in simulation. In order to place this work in a larger context, I first briefly review the state of knowledge of solid body surfaces in the Solar System while touching upon past and future spacecraft missions to these bodies, then I present an overview of the types of granular processes that we have witnessed in the Solar System, as well as on Earth and in the laboratory. Next, I discuss the science of granular dynamics, including the utilities and shortcomings of addressing granular media as a fluid. And finally, I give a brief account of the development of numerical approaches to granular physics research, and how these can be applied to the study of granular processes in the Solar System.

1.1 The surfaces of the solid bodies of our Solar System

Government funded space agencies around the world, using radar and direct imaging by unmanned craft, have uncovered a great deal in regard to the diversity between the surfaces of small Solar System bodies (SSSBs). Most solid celestial bodies' surfaces are not bare rock, but are instead covered in granular material. For example, many scientists had once assumed that every small asteroid was a simple monolith—one large, bare rock (Housen et al. 1979). For the most part, their reasoning was that any ejecta resulting from an impact onto these bodies would inevitably escape due to the extremely low gravitational pull that these small asteroids exhibit (Housen & Holsapple 2011).

However, since entering the age where we have begun to take direct images of SSSBs by spacecraft, the prevailing theories about these small bodies have changed. What we see from these images is that granular material is ubiquitous in our Solar System, and seems to cover the majority of solid bodies, even small asteroids well under 1 km across. This granular material can take the form of very fine regolith as we see on the Moon (Figs. 1.1–1.2), or it can take the form of pebbles or gravel, as on the 320-meter size near-Earth asteroid Itokawa (Fig. 1.9).

From asteroids and comets to moons and planets, a given body's collisional history and chemical makeup determine its overall size and surface properties, including, if solid, its grain size, porosity, cohesive strength, and thermal properties. Our direct knowledge of these properties of Solar System bodies has grown enormously and continues to expand due to Earth-based radar imaging, but also due in very large part to the increasing number of flybys and in-situ spacecraft missions performed over the past two decades.

Credit: *NASA*

Figure 1.1: Lunar footprint, Neil Armstrong, commander of the Apollo 11 mission, July 1969.

To date (mid-2013), spacecraft have been sent to 12 asteroids and 5 comets, showing evidence for granular material on each of these bodies.[1] In addition, the Cassini mission to Saturn, which entered orbit around the planet in 2004, has provided stunning evidence of granular flow on many of the moons of Saturn (e.g., Fig. 1.19). Below, I provide a brief discussion on the types of surface environments that our

[1]Two of these asteroids, (243) Ida and (951) Dactyl, are a binary system. This number of 12 asteroids and 5 comets does not include the distant Cassini and New Horizons flybys of asteroids (2685) Masursky and (132524) APL, respectively. This number also does not include: Comet (21P/)GiacobiniZinner, the target of the International Cometary Explorer (ICE) spacecraft (not equipped with a camera), which passed through its plasma tail at a distance of about 7800 km from the comet's nucleus (Stelzried et al. 1986); Comet (26P/)GriggSkjellerup, visited by the Giotto probe within a distance of 200 km, but without taking pictures (Grensemann & Schwehm 1993); nor Comet C/2006 P1 (Comet McNaught), whose ion tail was crossed by the Ulysses spacecraft (Neugebauer et al. 2007), gathering significant data about the comet, including some of its chemical properties, but again without taking pictures.

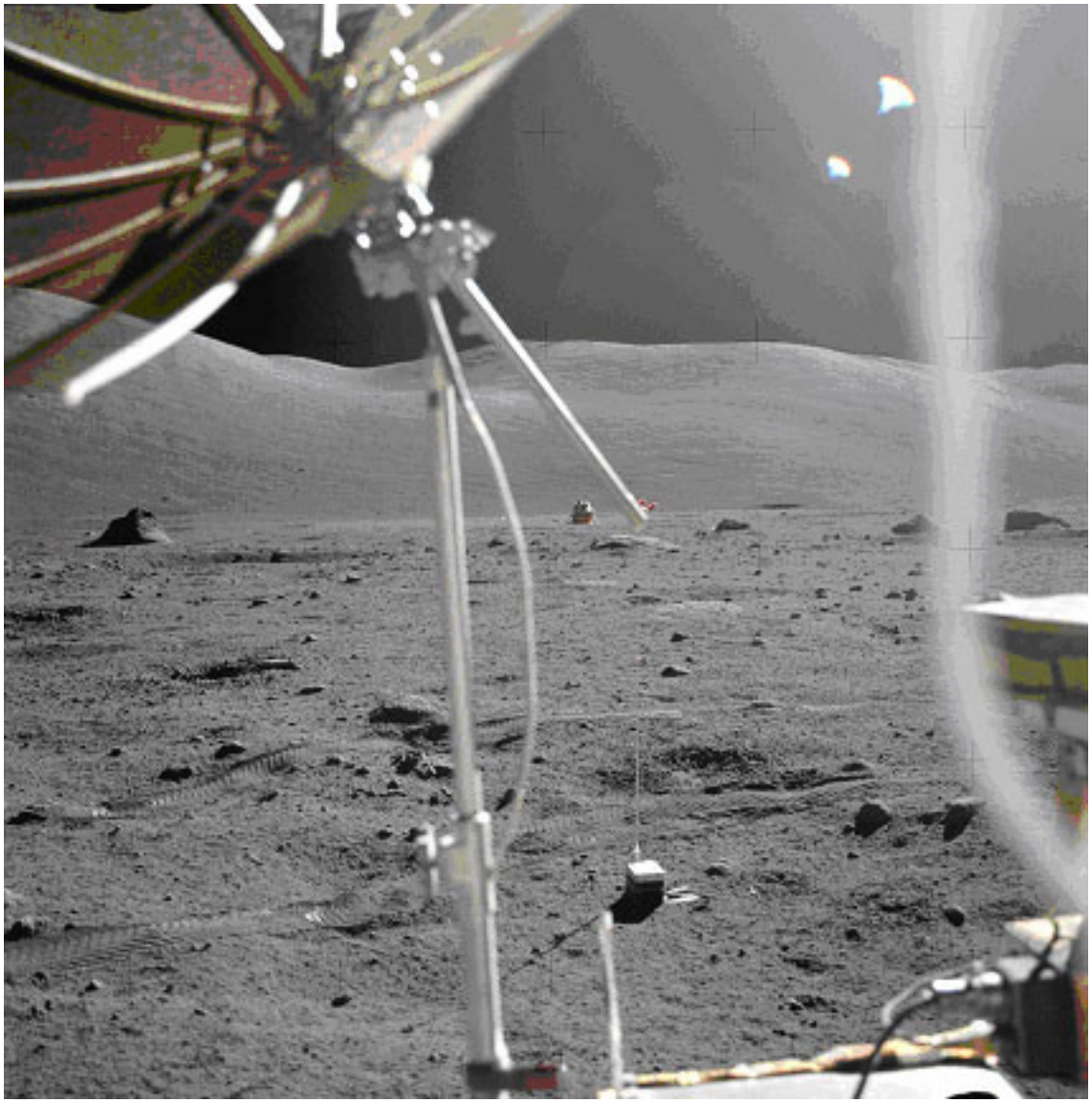

Credit: *NASA*

Figure 1.2: One of eight explosive packages (white-capped box near the bottom of the image) deployed by the Apollo 17 astronauts to provide data for the lunar seismic profiling experiment, which measured the thickness of regolith in the Taurus-Littrow Valley (Crawford 2012). The tracks left by the Lunar Roving Vehicle (pictured in the foreground) give a sense of the powdery nature typical of lunar regolith.

spacecraft have witnessed.

1.1.1 Spacecraft missions to solid celestial bodies

Space mission images of SSSBs have shown a great diversity of shapes, sizes, and morphologies (Fig. 1.3). Both observational and numerical work suggest that a large fraction of SSSBs, possibly down to a few hundreds of meters in size, consist of rubble piles, whose strength is dominated by self-gravity (e.g., Benz & Asphaug 1999). However, these small gravitational aggregates[2] may also exhibit some cohesion. The smaller members of the SSSB population are likely dominated by cohesion, since these bodies typically spin too fast to be able to retain their shape if gravity alone were the only source of strength (Holsapple 2007; also, additional discussion of cohesion in gravitational aggregates can be found in Section 1.1.2.3). The following is a summary of results related to the structures and surfaces of many of the bodies that have thus far been visited: (253) Mathilde and (433) Eros, by Near-Earth Asteroid Rendezvous – Shoemaker; (243) Ida, Dactyl, and (951) Gaspra, by Galileo; (2867) Šteins and (21) Lutetia, by Rosetta; (25143) Itokawa, by Hayabusa; (4179) Toutatis, by Chang'E 2; (4) Vesta, by Dawn; Comet 9P/Tempel (Tempel 1) and Comet 103/P Hartley 2, by Deep Impact; and also included in this summary are the Martian satellites, Phobos and Deimos.

[2]A "gravitational aggregate" is a body constituted of many "loose" components held together predominantly by gravity, although weak cohesive forces between components may also be present. Most planetary scientists use the term "rubble pile," however some geologists object to this use of this term, since "rubble" implies a certain typical component size. Consequently, "gravitational aggregate" was suggested instead by Richardson et al. (2002); in that work, a "rubble pile" is a special case of gravitational aggregate consisting of a jumbled collection of rocks. The term "gravitational aggregate" however, has not been universally adopted.

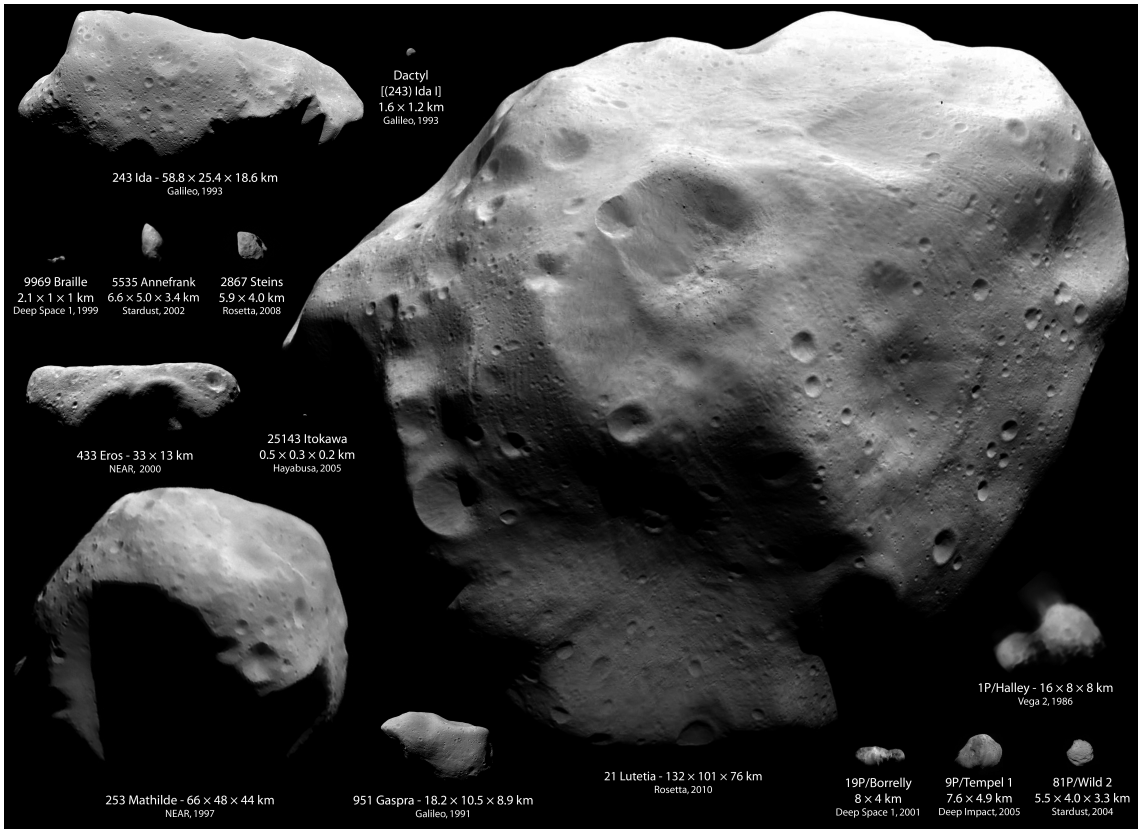

Credit: *NASA*

Figure 1.3: Images of asteroids and comets visited by spacecraft, shown to relative size. This composite does not include the asteroids Vesta (Dawn, Section 1.1.1.7), Toutatis (Chang'E 2, Section 1.1.1.6), Masursky (Cassini), nor APL (New Horizons). It also does not include the comets Hartley 2 (Deep Impact spacecraft, Section 1.1.1.8), GiacobiniZinner (ICE), GriggSkjellerup (Giotto), nor C/2006 P1 (Ulysses).

1.1.1.1 (253) Mathilde

The bulk densities that have been measured for some SSSBs suggest that their internal structure contains some degree of porosity, as they have systematically smaller bulk densities than their meteoritic analogues (Consolmagno et al. 2008). For instance, the National Aeronautics and Space Administration's (NASA) Near-Earth Asteroid Rendezvous – Shoemaker (NEAR Shoemaker) spacecraft performed a flyby of the asteroid (253) Mathilde in 1997, which allowed the determination of the bulk density of this dark (albedo of about 4%, Veverka et al. 1997; Britt

& Consolmagno 2000) C-type asteroid (Yeomans et al. 1997).[3] Mathilde is about 50 km across and has a bulk density of about 1.35 g cm^{-3}, which suggests a porosity fraction up to 40–50% when compared to the bulk density of carbonaceous chondrites (Cheng 2004). What this porosity implies about the asteroid's interior makeup is a matter of some debate. If up to 50% of the interior volume consists of empty space, most of the body might consist of fluffy, poorly packed, powdery material, or, instead, it could imply the existence of macroscopic voids between boulders. The scales of the void-spaces could also range between these two extremes. If the porosity is of a microscopic or mesoscopic scale, this would favor a compaction-type of cratering (Housen & Holsapple 2003). However, there are structural features, such as polygonal craters and a 20-km-long scarp (Cheng 2004), which indicate that Mathilde has some degree of cohesion. Whatever the nature of the porosity, its high value indicates that Mathilde likely does not transmit impact shock in an efficient manner, which could help to preserve the surface's structural features to a high degree (Veverka et al. 1999).

Although NEAR Shoemaker was only able to see slightly over half of Mathilde's surface, the homogeneity in surface color, in spite of its deep craters, indicates a correspondingly large degree of homogeneity in its interior (Clark et al. 1999). Unlike other SSSBs, or, especially, the Moon, whose fresh craters uncover material typically of vastly different coloring than the surrounding surface (e.g., Fig. 1.18),

[3]C-type asteroids, which are the most common (about 75% of known asteroids), are carbonaceous, and are believed to consist of clay and silicate rocks. This is based upon the analysis of carbonaceous meteorites assumed as their analogs, and on remote spectral observations. They are characterized by their low albedo and tend to exist relatively far from the Sun, showing less alteration due to the effects of heat. Because of this fact, and since there is often an observed absorption feature near 3 microns in their spectra, it is believed that many C-type asteroids hold a significant amount of water (Gaffey et al. 1989).

Mathilde could be a relatively pristine sample of the early solar system.

1.1.1.2 (433) Eros

After making its flyby of Mathilde, NEAR Shoemaker visited (433) Eros—the second-largest near-Earth asteroid behind (1036) Ganymed (Fieber-Beyer et al. 2007)—and made a series of observations of the asteroid, reporting back to Earth with by far the most detailed data and dazzling images of any small body in the Solar System up to that point, before eventually landing on its surface, making Eros the first asteroid subjected to in-situ observation. Eros has a 3:1:1 axis ratio and measures about 35 km on its longest axis (Zuber et al. 2000). NEAR Shoemaker touched down in the so-called "saddle" region of the asteroid, and survived for at least 16 days on its surface (Worth 2001). Eros, an S-type asteroid,[4] has a relatively high density (~ 2.67 g cm^{-3}) in comparison to other asteroids (Yeomans et al. 2000). As we can see by its shape model (Fig. 1.4), the slope of the surface with respect to the direction of effective gravity varies considerably over the surface of the asteroid, with slopes ranging from 0 degrees (flat) to ~ 40 degrees. For terrestrial slopes composed of mixtures of grains of various sizes, the angle of repose is typically between 34 degrees and 37 degrees (Strahler 1971). Therefore, despite these regions of considerable inclination on Eros, all could be consistent with surfaces of loose granular material. It is believed that the regolith on Eros consists of a fine dust with an estimated depth between 10 m and 100 m (Veverka et al. 2000). Eros has a paucity of small craters (on the order of meter-sized) when compared to extrapolations from the number of larger craters (Michel et al. 2009, based upon scaling laws of Bottke et al. 2005; O'Brien et al. 2006; and from what we would expect in light of what

[4]S-type asteroids consist mainly of iron and magnesium silicates, and get their name because they appear to be of a "stony" composition (Chapman et al. 1975; Bus & Binzel 2002a).

is observed on the Moon, Veverka et al. 2001). Richardson et al. (2004), as well as Michel et al. (2009), conclude that Eros is likely small enough that seismic shaking, sufficient to erase meter-sized craters by allowing regolith to shift and resettle, could account for the observed small crater deficit.

1.1.1.3 (243) Ida and Dactyl, (951) Gaspra

The Galileo mission, launched in October 1989, was the first to take pictures of small bodies during flyby. Before observing the fragments of Comet Shoemaker-Levy 9 (SL9) crash into Jupiter (the first confirmed collision of two Solar System bodies to be observed beyond Earth), the spacecraft visited (951) Gaspra and (243) Ida, discovering Ida's satellite, Dactyl. SSSB binary systems are a valuable way of estimating bulk densities (Richardson & Walsh 2006).

If we assume the objects are made of comparable material and have similar internal structure, so that we can assume their bulk densities are about the same, and if P and a can be measured, along with the body shapes (e.g., from radar imagery), then from Newton's form of Kepler's third law, estimates of the component masses can be made. For the vast majority of binary SSSBs however, the shapes are poorly known; in those cases only the total mass of the system can be determined, which approximates to the mass of the primary if the secondary is demonstrably small. One benefit of inserting spacecraft into orbits around these bodies comes from the fact that this constructs an "SSSB–spacecraft" binary whose parameters can be constrained with great precision.

Ida has a mean radius of about 16 km, and is believed to be covered in about 100 m of regolith (Chapman 1996; Geissler et al. 1996). Greeley et al. (1994) reports evidence of recent downslope regolith movement on Ida. Its satellite, Dactyl, covered in craters, measures about 1.4 km across, but is otherwise poorly characterized due

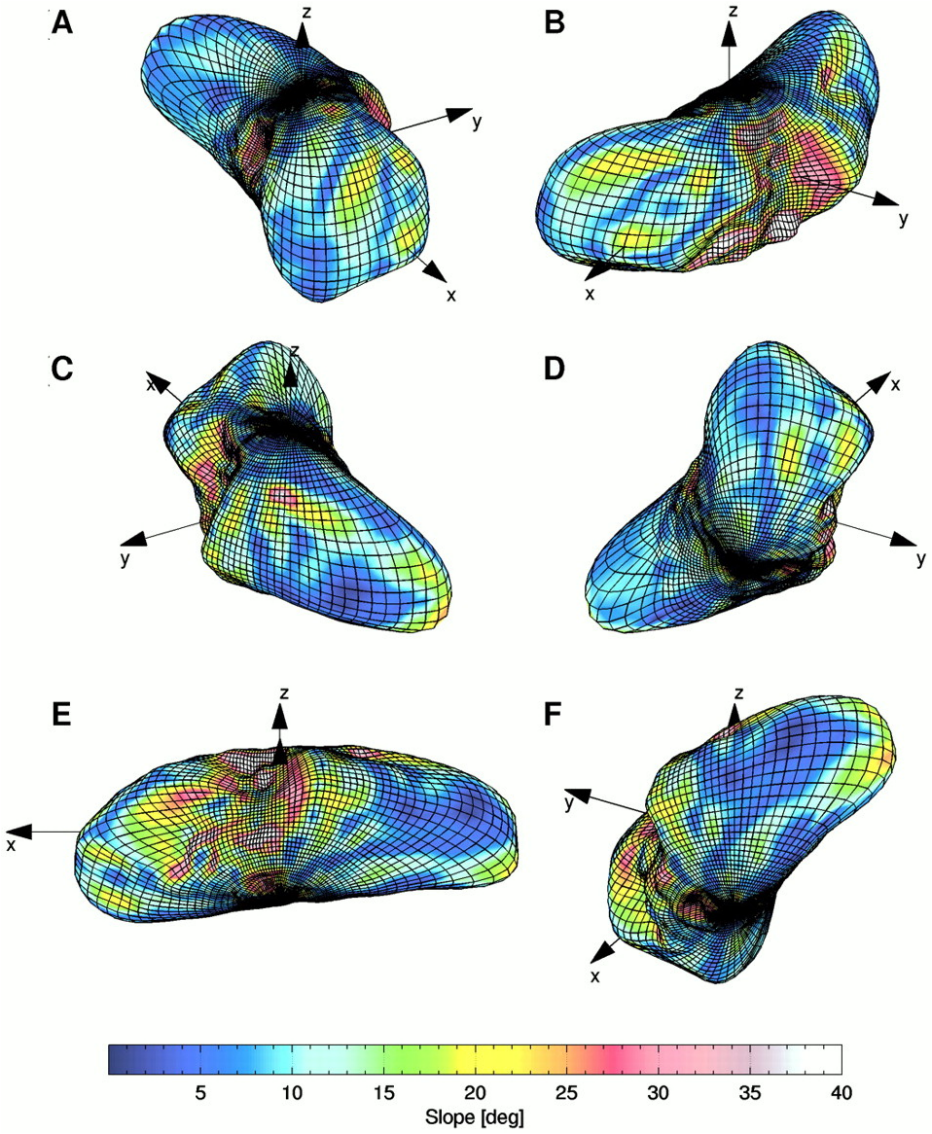

Credit: *Zuber et al. (2000)*

Figure 1.4: Six perspective views of a three-dimensional shape model of (433) Eros from the NEAR Shoemaker Laser Rangefinder (NLR) plotted to spherical harmonic degree and order 24. The mesh represents the scaled shape, and the surface facets are color-coded according to the surface slope with respect to a constant-density gravity field derived from the shape model (gravity was calculated from the shape model assuming homogeneous density; also centrifugal accelerations due to the asteroid's rotation were taken into account). The asteroid is viewed at the following (elevation, azimuth) pairs: (A) 30N, 60E; (B) 30N, 120E; (C) 30N, 0E; (D) 30S, 60E; (E) 30S, 300E; and (F) 30S, 0E. (Figure caption adapted from Zuber et al. 2000.)

Credit: *NASA / JPL*

Figure 1.5: Left: (243) Ida color mosaic, enhanced with infrared data, taken by the Galileo spacecraft during its visit to the medium-sized asteroid.

to its small size and the scarce number of images obtained of it. Fig. 1.5 shows a 30-frame mosaic image of the Ida–Dactyl system on the left side, and a zoom-in on one of these frames, which contains the most detailed image obtained of Dactyl, on the right.

Gaspra has a mean radius of about 6 km, and features surface grooves up to a few hundred meters wide, 2.5 km long, and several tens of meters deep. These grooves may have been created by impacts that shattered the bedrock beneath a layer of fine granular material. Veverka et al. (1994) argues that these features, which "appear to reflect structural grain, including ridges, grooves, and flat surfaces, suggest that Gaspra is a single coherent body and not a binary or a rubble pile." In the more than two decades of space missions to SSSBs since Galileo, we have gathered increasing direct evidence (e.g., Itokawa, Section 1.1.1.6) for the prevalence of rubble-pile asteroids. Although we have learned a great deal from the Galileo mission, the internal makeup of Gaspra remains far from certain.

1.1.1.4 "Top"-shaped asteroid (2867) Šteins

Visited by the Rosetta spacecraft in 2008, (2867) Šteins is an E-type asteroid[5] (Fornasier et al. 2006) with a mean diameter of 5.3 km (Keller et al. 2010) and the shape of a cut diamond or of a spinning top (Fig. 1.6). Keller et al. (2009), Jutzi et al. (2010), Schröder et al. (2010), and Besse et al. (2012), among others, argue that its top-like shape could have been caused by the Yarkovsky–O'Keefe–Radzievskii–Paddack (YORP) effect. A term coined by Rubincam (2000), YORP can change the spin state of solid bodies that are sufficiently small and close to the Sun (see Section 1.1.2.3). A gradual increase in the spin rate of a gravitational aggregate can cause material from the body's poles to migrate toward its equator; the resulting shape (Walsh et al. 2008, 2012) is consistent with the images that were taken of Šteins, as well as radar-derived shapes of a number of other SSSBs, including the primary of the 1999 KW4 binary system. Although its current spin period (Lamy et al. 2008 give a precise spin period of 6.04679 ± 0.00002 hrs) is too long to cause such reshaping now (Keller et al. 2010), its spin period may have been shorter in the past. Had the YORP effect shortened the spin period to 3 hrs, the effective gravitational potential on the surface of Šteins would make slopes of 30–45 degrees at intermediate latitudes, a range sufficient to trigger downslope motion towards the equator from both hemispheres (Jorda et al. 2012). Changes in the asteroid's overall shape caused by this motion on the surface may have eventually changed the direction of the YORP torque, causing Šteins to spin down to its current rate.

[5]Taxonomies attempting to classify E-type asteroids are varied (Tholen 1984; Bus 1999; Bus & Binzel 2002b,c), but all tend to include those with high albedos. Clark et al. (2004) posited at the time that less than 6% of the surveyed near-Earth asteroids might be E-type asteroids and less than 3% of the classified main belt asteroids are E-types, and, further, that the E-type asteroid class contains at least three distinct lithologies.

By applying standard inversion procedures (e.g., Kaasalainen et al. 2001) to future light curve observations of the asteroid, Šteins' period could be assessed over time to determine $\dot{P}$, the rate of change of its period, which could constrain formation scenarios and possibly provide additional direct evidence for the YORP effect.

1.1.1.5 (21) Lutetia

Visited by the Rosetta spacecraft on July 10, 2010 (flyby), asteroid (21) Lutetia (Fig. 1.7) has one of the highest densities (3.4 ± 0.3 g cm^{-3}) of any asteroid measured thus far (Pätzold et al. 2011). Its axes measure about 121 x 101 x 75 km across, and it resides in the main belt. Its complex geology indicates a very old surface. If a modest macroporosity of 12% were assumed, this would imply that the bulk density of its material constituents would exceed that of stony meteorites. Pätzold et al. (2011) suggest that its high density indicates a bulk composition enriched in high-atomic-number elements like iron, unless Lutetia has anomalously low porosity compared with other asteroids in its size range. This may also be evidence for a partial differentiation of the asteroid body, resulting in a metallic core overlain by a primitive chondritic crust (Weiss et al. 2012).

Lutetia shows an extensive and uniform fine regolith cover. Images show older craters in the Baetica region (Fig. 1.7B,C) partially buried in ejecta, and from this it is estimated that the ejecta blanket in that region may be up to 600 m thick (Sierks et al. 2011). Surface slopes are below the angle of repose for loose regolith almost everywhere, but large features reveal underlying structure. Thick layers of regolith in the north-pole region appear to flow downslope in major landslides (Fig. 1.7B). The linear features seen on the surface (Fig. 1.7C,D) are similar in appearance to those on the martian moon Phobos (Fig. 1.16), which are commonly interpreted as resulting from a large impact (Thomas et al. 1979). Sierks et al. (2011) conclude

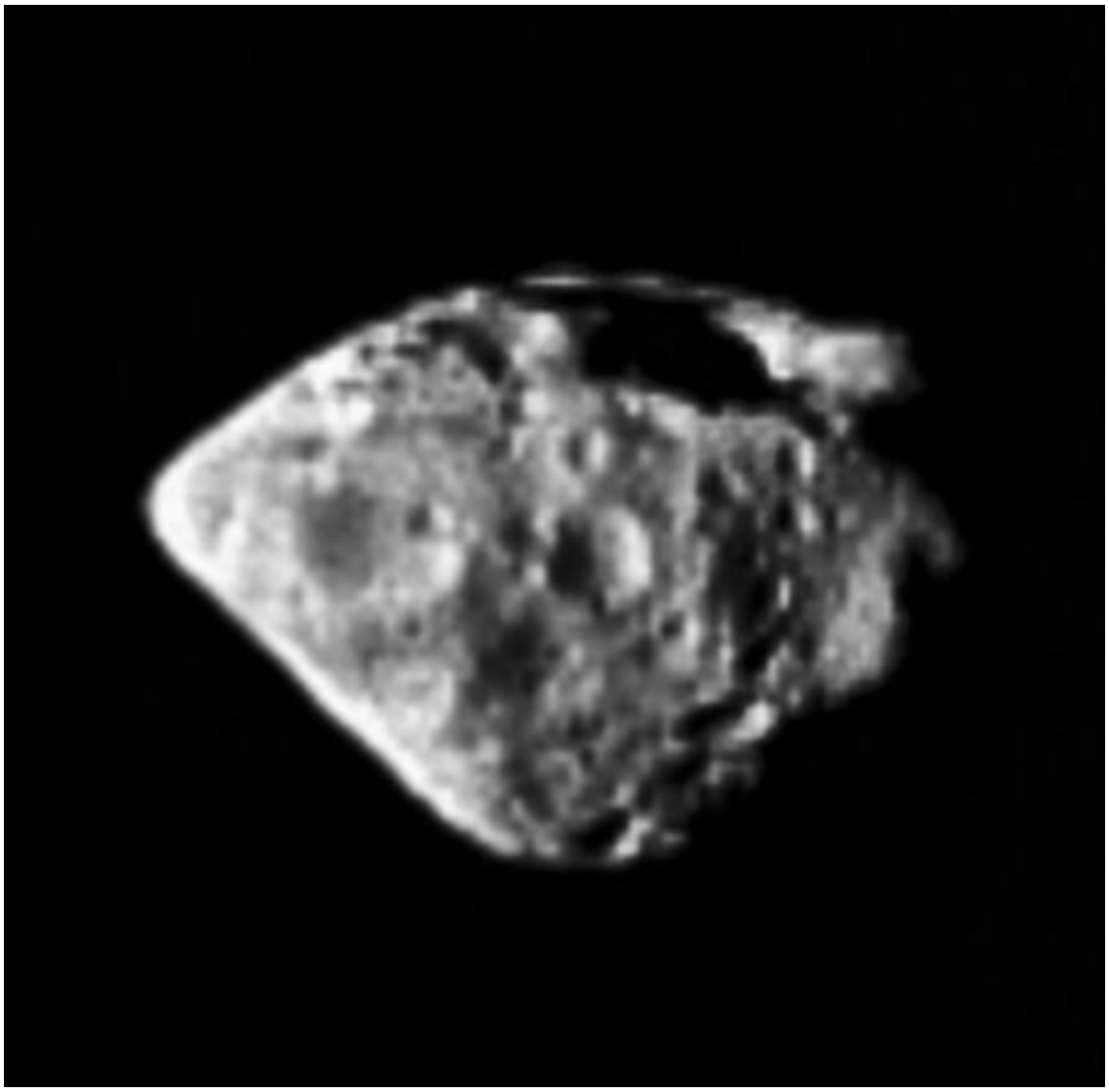

Credit: *Rosetta Team, European Space Agency (ESA)*

Figure 1.6: The Rosetta spacecraft passed by asteroid 2867 Šteins in 2008 (it would later visit (21) Lutetia; see Section 1.1.1.5). Notable is the diamond shape of the asteroid, offering indirect evidence of the YORP mechanism and its importance in the evolution of small, SSSBs. Burchell & Leliwa-Kopystynski (2010) count about 40 craters on Šteins, including a massive crater on its south pole (north points down in this image) that measures 2.1 km across and 300 m deep. The impact that created this crater is evidence for, and likely contributed to, its apparent rubble-pile nature (Jutzi et al. 2010; Keller et al. 2010; Marchi et al. 2010).

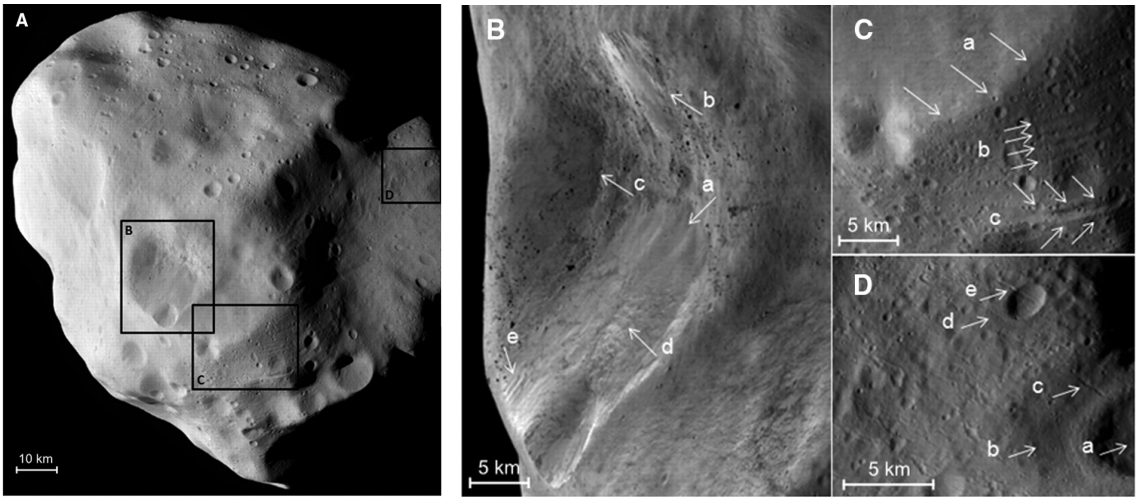

Credit: *Rosetta Team, ESA / Sierks et al. (2011)*

Figure 1.7: (**A**) Rosetta spacecraft image of Lutetia at close approach (just beyond 3,000 km). (**B**) The central 21 km-diameter crater cluster in the Baetica region. Arrows *a*, *b*, and *c* point to landslides. Landslides *a* and *b* appear to have buried the boulders that are otherwise pervasive within the crater. Landslide *b* may have exposed a rocky outcrop of underlying structure. Opposite *e*, another potential outcrop is seen. The material at point *d* has a mottled appearance. (**C**) The boundary between Baetica (young terrain associated with the central crater cluster) and Noricum (old terrain) is extremely well defined in some places, as indicated by the arrow *a*. Arrows *b* and *c* highlight curvilinear features. (**D**) Arrows *c*, *d*, and *e* point to further curvilinear features, which cut the crater and its rim. Feature *c* cuts through the debris apron *b* of the crater *a*. This implies that these linear features are younger than the craters or that they result from an impact into an area with existing large-scale cracks and subsequent regolith movement. (Figure caption adapted from Sierks et al. 2011.)

that Lutetia, unlike, e.g., Itokawa (Section 1.1.1.6), does not show evidence of being a rubble pile, but rather that it has likely survived for the age of the Solar System with its primordial structure intact.

1.1.1.6 Small asteroids (25143) Itokawa & (4179) Toutatis

Near-Earth asteroid (25143) Itokawa is the quintessential rubble-pile asteroid, covered in rocks of varying shapes and size, from fine-grained regolith to boulders tens of meters across. Perhaps the reaccumulation of shattered material following the disruption of a larger body (e.g., as modeled by Michel & Richardson 2013), its bulk density is below 2 g cm^{-3} (Abe et al. 2006; Fujiwara et al. 2006), implying the existence of void space in its interior. The longest axis of Itokawa is about twice that of its other two axes and measures about 500 m across. Its appearance suggests that it is made up of two primary components: a "body" and a "head." Some remark that its shape resembles that of a river otter, or of an unshelled peanut (see Fig. 1.8). The Japan Aerospace Exploration Agency (JAXA) space mission Hayabusa visited Itokawa in 2005, provided incredibly detailed images (Saito et al. 2006), and returned to Earth in 2010 with some sample grains from the tiny asteroid (Yano et al. 2006). As on Eros, the lack of small craters observed on Itokawa suggest that the surface is "young," getting refreshed periodically, erasing these small craters. This lends credence to the idea that periodic seismic shaking takes place on the asteroid, perhaps due to impacts. Images such as those in Fig. 1.9, among many others taken by Hayabusa during its visit to Itokawa, show that the rocks on the surface are oriented horizontally, typically resting on their largest faces in such a way as to minimize the altitudes of their centers of gravity and thus minimizing their potential energy (rocks are not precariously positioned atop one another or on an edge close to toppling over).

Although impacts seem like the most plausible mechanism for the periodic resurfacing that appears to take place on Itokawa (Fujiwara et al. 2006), Chapman (2010) argued that tidal forces can contort a loosely bound rubble pile (Richardson et al. 1998), changing its shape, sometimes pulling it apart, just as SL9 was disrupted

in 1992 by Jupiter's tidal forces. Also, Binzel et al. (2010) claim that tidal stress, strong enough to disturb and expose unweathered surface grains, is the most likely dominant short-term asteroid resurfacing process. Scheeres et al. (2007) argue the possibility that the YORP effect could also be enough to explain the reconfigurations that seem to take place on the surface (see Section 1.1.2.3).

Global shaking, explained in any of these fashions, is more easily achieved for the smaller (and less dense) Itokawa than it is for Eros, which also shows evidence of resurfacing (Section 1.1.1.2). Furthermore, if we look at the size distribution of grains, rocks, and boulders on Itokawa, we see a strong correlation between grain/rock size and the gravitational potential at the surface (Fujiwara et al. 2006). Tancredi et al. (in prep.), using the Barnouin & Kahn (2012) data set, overlaid a grey-scale image of Itokawa with a corresponding color-coded map of the potential across the surface (Fig. 1.8). We can see from these images that the larger boulders are concentrated in the regions of higher potential (the reddish regions), and the smaller rocks are located in regions of lower potential (the blueish regions). We also find intermediate-size rocks and boulders in the regions of intermediate potential (the cyan and yellow regions). This shows that smaller grains are able to find their way down between larger grains to places of lower potential energy. So we see a minimization of potential energy both on the local scale by the orientation of individual rocks, and on the global scale by the correlation between rock size and gravitational potential. This, along with the lack of small craters on its surface, makes a strong case for the occurrence of seismic shaking on the surface of Itokawa. Boulders on the surface have the ability to absorb some or all of the incident energy delivered to Itokawa by small impactors, a process known as armoring (Michel et al. 2009); this could further account for the diminished number of craters.

The near-Earth asteroid (4179) Toutatis is near the 3:1 orbital mean-motion

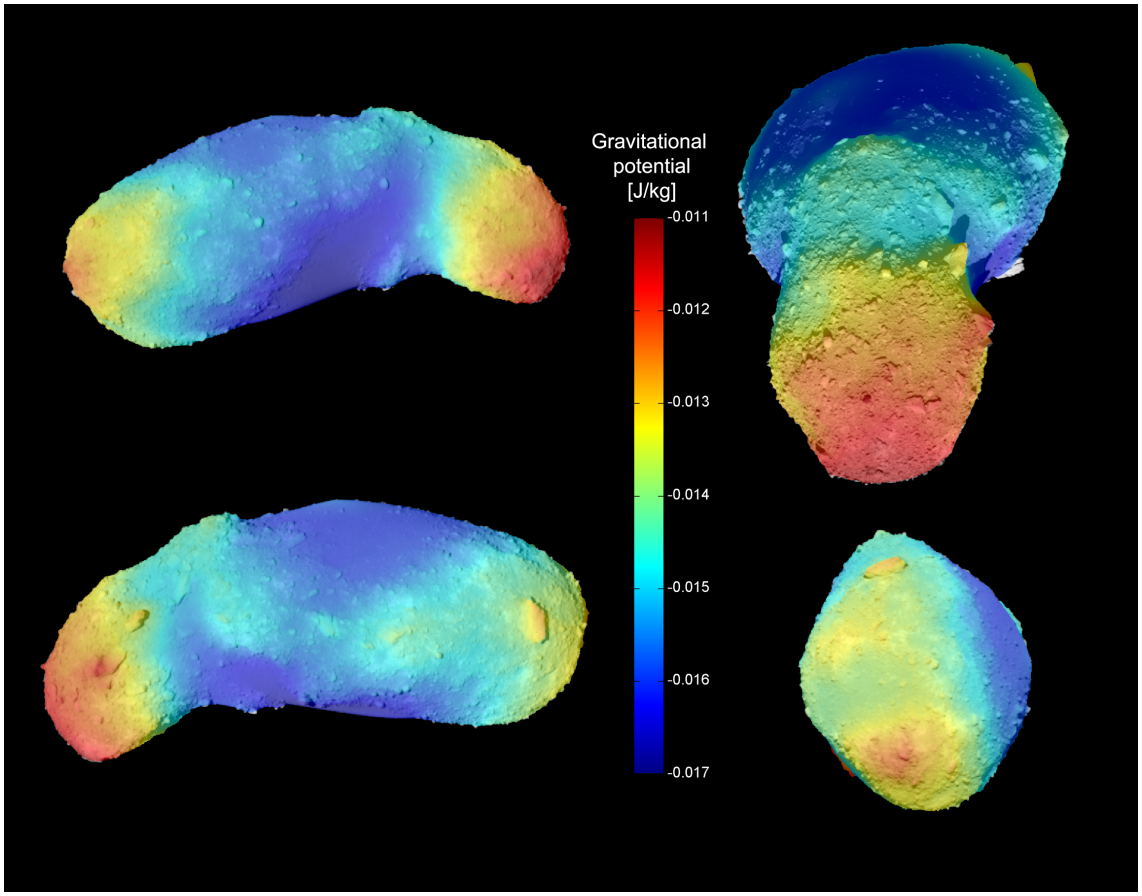

Credit: *Gonzalo Tancredi, Instituto de Física, Montevideo, Uruguay*

Figure 1.8: Grey-scale images of (25143) Itokawa overlaid with color-coded plots of the total potential given by the Barnouin & Kahn (2012) data set. The potential ranges from a minimum in the smooth "neck" region between the "head" and "body" known as the Muses Sea, to a maximum on the asteroid's "head." Boulders of sizes in the range tenths to tens of meters can be observed on the surface. There is a correlation between the size of the boulders and the potential: large boulders are concentrated in the regions of higher potential (the head and the bottom correspond with the reddish areas), and smaller boulders are located in regions of lower potential (the neck corresponds with the bluish area). Furthermore, the highlands on the body with medium- and large-size boulders have intermediate values of the potential (whitish areas). (Figure caption adapted from Gonzalo Tancredi, personal communication, 2013.)

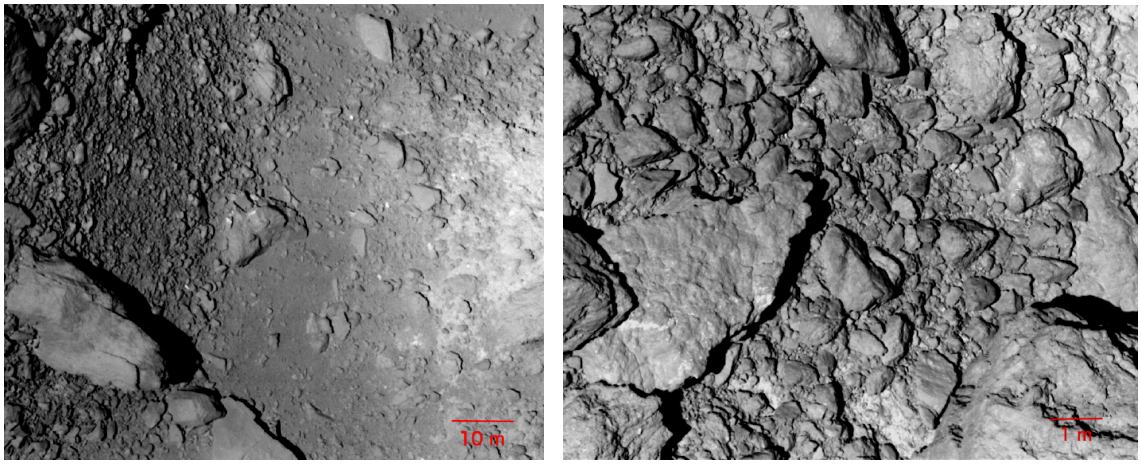

Credit: *Univ. Tokyo / JAXA*

Figure 1.9: Two photos of (25143) Itokawa taken by the Japanese spacecraft Hayabusa during its visit to the small asteroid. Note the scale bars in the lower right-hand corner in each image.

resonance with Jupiter and near the 1:4 orbital mean-motion resonance with the Earth. Unlike most well-known bodies of the solar system, Toutatis does not rotate around its principal axis. Due to its close approaches to the terrestrial planets, it is difficult to project the asteroid's precise trajectory beyond many such encounters. Its minimum orbit intersection distance, the distance between the closest points of the osculating orbits of itself and the Earth, is less than 0.5 au, which is why it is classified as a potentially hazardous object (Gehrels et al. 1994).[6]

An object of Toutatis' size and proximity to the Sun should inevitably be subject to YORP effects over its lifetime. However, at the present era, the direction of the induced torque on Toutatis changes chaotically along with the orientation of its spin axis, which does not allow the Sun to continue seeing the exact same faces of the asteroid. The YORP effect occurs due to the fact that the net torque over a single rotation is, although very small, for the most part constant from one to the next,

[6]An Astronomical Unit (au) is defined as the semi-major axis of the Earth's orbit around the Sun, equal to 149,597,870,700 ± 3 m (Pitjeva & Standish 2009; Luzum et al. 2011).

allowing the effect to accumulate over many, nearly identical, rotations. Thus the effect does not apply in the same way to tumblers. Bottke (2007), however, argue that YORP may have played a dominant role in determining Toutatis' current spin-state. They propose that the asteroid was once a principal-axis rotator of moderate spin, but was spun down by YORP to such an extent that it lost most of its angular momentum, and only then did it adopt its current tumbling motion. So it is still a matter of debate as to whether Toutatis has been a tumbler since its formation due to some happenstance of its violent collisional history, leaving it with very little angular momentum up to the present day, or if it was once a principal-axis rotator, but was spun down by YORP.

Toutatis has a surface composition that is thought to be similar to that of (433) Eros (Reddy et al. 2012). Using data from the Goldstone Radar Observatory (located in California's Mojave Desert) acquired during Toutatis' close approach in 1996, and based upon shape models from 1992 radar observations (Hudson & Ostro 1995), Ostro et al. (1999) reports that a fine regolith layer covers a large part of the surface of Toutatis. Even after the Chang'E 2 spacecraft mission, we still cannot be sure how deep this layer of regolith is.

In December 2012, after visiting the Moon and the L2 Lagrangian point of the Sun-Earth system,[7] the Chinese spacecraft Chang'E 2, named after the Chinese moon goddess, flew by Toutatis, coming within just 3.2 km of the surface (Fig. 1.10). These visual images, in addition to the radar images from Earth-based observatories,

[7]On the line that passes through the Sun and the Earth, the L2 Lagrange point lies on the opposite side of the Earth as the Sun at such a point where the combined gravity of both bodies exerts a force equal to the centripetal force necessary to keep a point mass in circular orbit around the Sun. Significantly shielded (but not completely) by the Earth from the Sun, and thus conducive for the placement of scientific instruments, a spacecraft at L2 would orbit the Sun with the same orbital period of the Earth (one year) and always see the Earth's night-side.

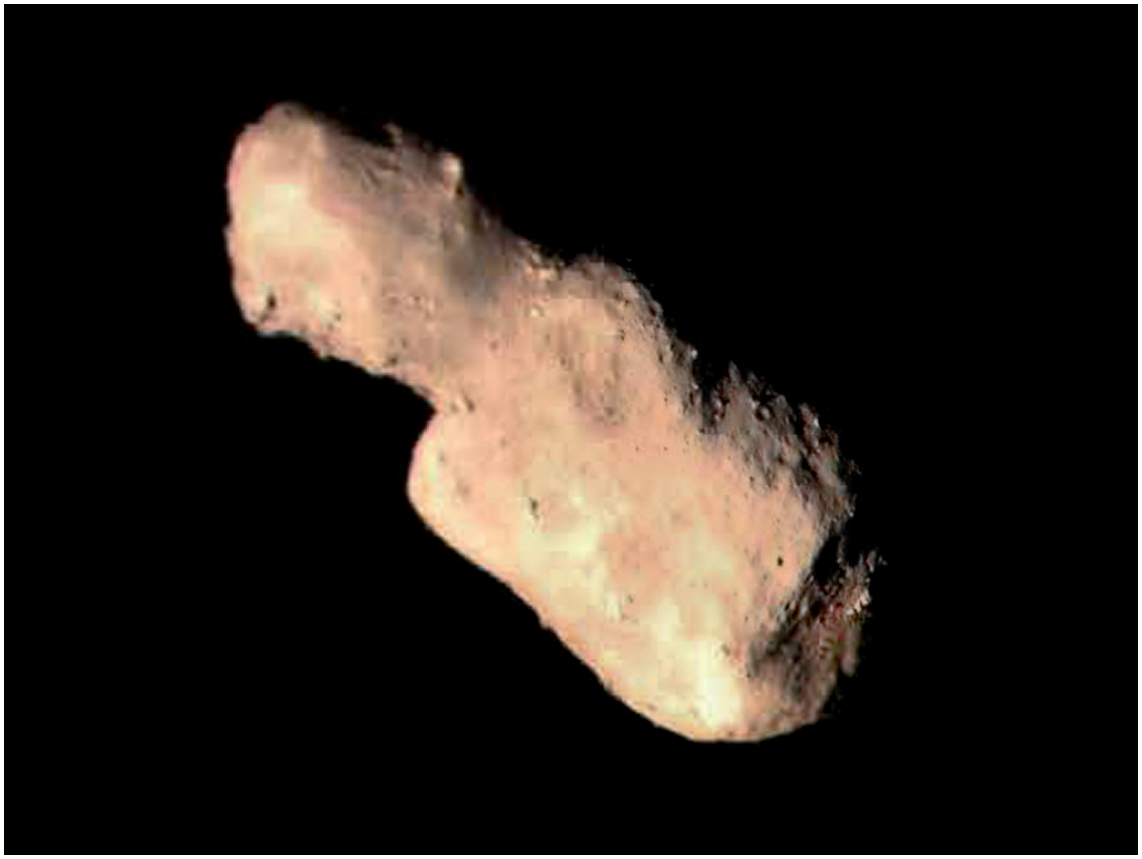

Credit: *Chinese Academy of Sciences / Daniel Macháček*

Figure 1.10: A mosaic of four (4179) Toutatis photos taken just seconds apart by the Chinese spacecraft Chang'E 2 as it receded from the asteroid after flyby.

show that Toutatis has much in common with Itokawa: they show mineralogical similarities and similar surface regolith properties. The asteroids' physical shapes are reminiscent of each other, suggesting a larger component and a smaller component, with fine regolith covering the neck that bridges the two components. Although Toutatis is significantly larger than Itokawa, both are relatively small asteroids. They both seem to be gravitational aggregates of rocks, boulders, and grains.

1.1.1.7 (4) Vesta

Asteroid (4) Vesta is the second-largest asteroid by mass, after (1) Ceres,[8] comprising about 9% of the total mass of the asteroid belt (Pitjeva 2005). Considering the age of the Solar System and typical timescales for solid bodies of the inner Solar System to obtain a balance between gravity and internal pressure (Anderson & Anderson 2010), Vesta's mass puts it near hydrostatic equilibrium, which explains its roughly spherical shape. There remain arguments both for and against reclassifying Vesta as a dwarf planet (and upgrading it from its current classification as an SSSB). The strongest argument against its reclassification is its deviation from a fluid equilibrium shape. Due in part to the the impacts near Vesta's southern pole that created the Rheasilvia and Veneneia craters (Fig. 1.11), it is considerably less spherical than bodies currently classified as dwarf planets (Asphaug 1997).[9] Arguments for its reclassification include the fact that it has a differentiated interior with an iron core (Russell et al. 2012) and other planet-like geological features. Buczkowski et al. (2012), for instance, argue that many structural features on the surface of Vesta should be classified as "graben," depressed blocks of land bordered by parallel faults. They postulate that an impact into a differentiated body such as Vesta could result in graben, while grooves and fractures would form on undifferentiated asteroids. Further, they posit that the existence of graben is a particularly planetary attribute—a geological delineation that could help distinguish planets from SSSBs. Regardless of its status, it is clear that Vesta is somewhere near the boundary

[8]Asteroid (2) Pallas seems to have a larger volume than Vesta, but has only about 80% of its density (Schmidt et al. 2008; Russell et al. 2012).

[9]Starting with a spherical model of Vesta, impact simulations representing those that created the two craters were performed, reproducing well the general morphology of Vesta today, which deviates form a perfect sphere (Jutzi et al. 2013).

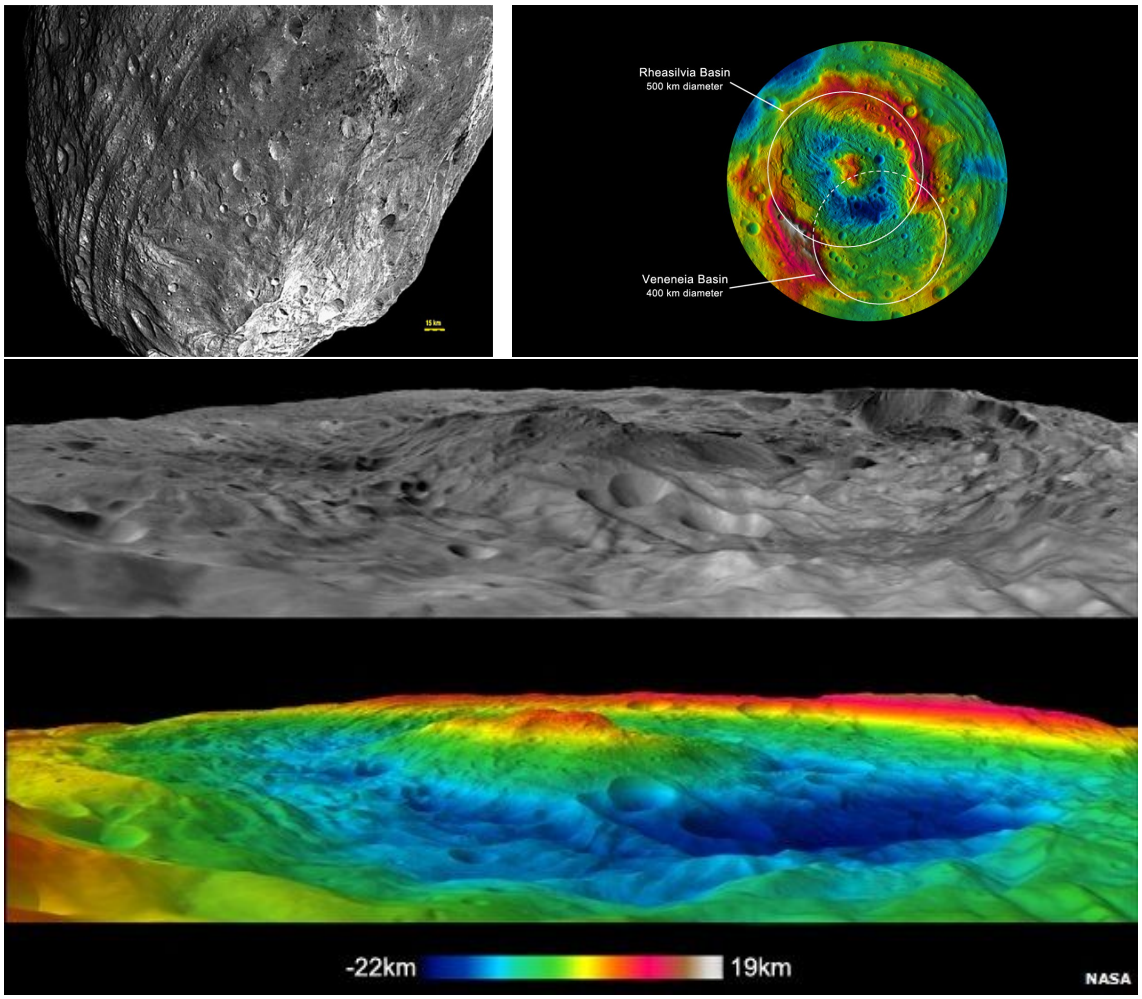

Credit: *NASA / JPL-Caltech / UCLA / MPS / DLR / IDA / PSI*

Figure 1.11: Top-left: Photo of (4) Vesta showing the deformation thought to be caused by impacts near its southern pole. These are thought to include two large basins at the impact sites as well as the lateral features near the equator (Buczkowski et al. 2012). Top-right: Computer-generated topographic map showing the two impact basins: Rheasilvia, the largest (about 500 km across); and the older Venenia (about 400 km across). Bottom: Relief maps of a computer-generated perspective of Vesta's southern pole and its Rhea Silvia basin.

between these two classifications.

NASA's Dawn spacecraft arrived at Vesta on July 16, 2011, and spent 141 days in the Low-Altitude Mapping Orbit (LAMO), during which the Framing Camera 2 (FC2) obtained 10251 images (Carsenty et al. 2013). The surface of Vesta reveals a

diverse geological structure that includes numerous impact craters of varying size,[10] preserved ejecta blankets, lava flows, large impact basins, and an enormous trough system around the equator. An ample number of steep slopes indicate that the surface regolith rests atop bedrock (Cheng et al. 2002; Jaumann et al. 2012).

The pitted terrain observed on Vesta has not been observed on other airless bodies (Denevi et al. 2012b), but shares similarities with terrain observed in association with numerous craters on Mars (e.g., McEwen et al. 2007; Tornabene et al. 2012; Boyce et al. 2012). Pits observed in conjunction with Martian craters are thought to form through degassing of volatile-bearing material heated by the impact. If the pitted terrain on Vesta has a similar formation scenario, this would signify relatively large volatile components within these portions of the surface. Water-rich carbonaceous chondrites, and/or other material, perhaps exogenic, originating from bodies beyond the inner Solar System, may be the source of volatiles (De Sanctis et al. 2012). Among others, Denevi et al. (2012a,b) claim that the pits at the center of Marcia crater denote the presence of water or other volatiles on Vesta. Similar features have been observed in four other craters in the asteroid's northern hemisphere (Yingst et al. 2012). Impactor materials on Vesta preserved locally in high abundance point to the conclusion that impactor composition has played an important role in shaping Vesta's geology.

A unique surface feature exhibited by Vesta is an elongated concentration of small craters located in the so-called Pinaria quadrangle, referred to as "The Swarm"

[10]Craters on Vesta show a size frequency distribution (SFD) for small projectile sizes (down to 10 m diameter) consistent with current predictions of collisional and dynamical models (Bottke & Chapman 2006; Bottke et al. 2006). If the SFD has not changed over the last several billions of years, this implies that the absolute number of small asteroids in the main belt has remained in a steady state over this period (Marchi et al. 2013). This would be an intriguing finding, and would immediately lead to questions about how the small-body population gets replenished.

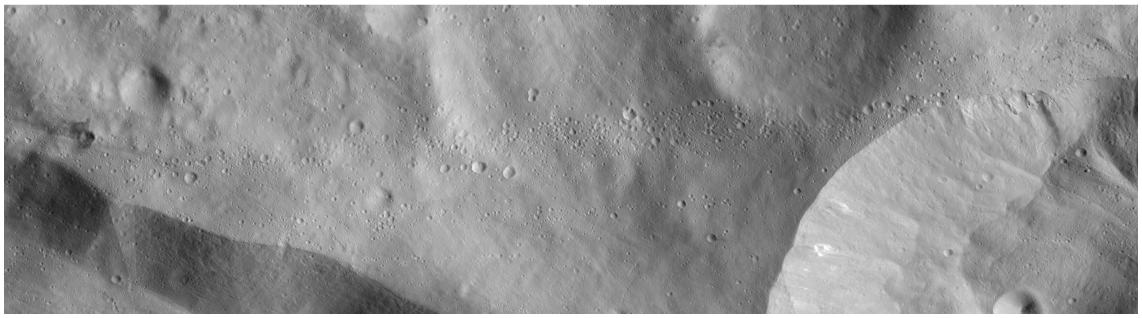

Credit: *Carsenty et al. (2013)*

Figure 1.12: Image mosaic of "The Swarm" phenomenon of (4) Vesta, a concentration of small craters that extend around much of the body's equator.

(Fig. 1.12). It is not a collection of single chains, and the crater density decreases as a function of the distance away from the central symmetry axis along the chain. Carsenty et al. (2013) suggest collapse pits, secondaries from an unknown primary crater, impact of a small, fragmented rubble-pile satellite, and impact of fragments of an ancient disk as possible formation scenarios of this intriguing feature. Combinations of these scenarios are also possible. For example, impact fragments from in-spiraling debris could heat up, and perhaps be the source of, volatiles, which outgas at the impact sites, leading to this feature, which presents an intriguing puzzle. At the moment, neither dynamical explanations involving interaction with past bodies nor geological explanations such as a much more expansive presence of volatiles on Vesta can be ruled out as causes.

1.1.1.8 Comets 9P/Tempel (Tempel 1) 103P/Hartley (Hartley 2)

The two comets best imaged by spacecraft were those visited by NASA's Deep Impact probe as part of the Extrasolar Planet Observation and Deep Impact Extended Investigation (EPOXI): 9P/Tempel (Tempel 1) in 2005, and 103P/Hartley (Hartley 2) in 2011. Tempel 1 was revisited by the Stardust probe, after it had performed a flyby of 81P/Wild (Wild 2), as part of the STARDUST New Exploration

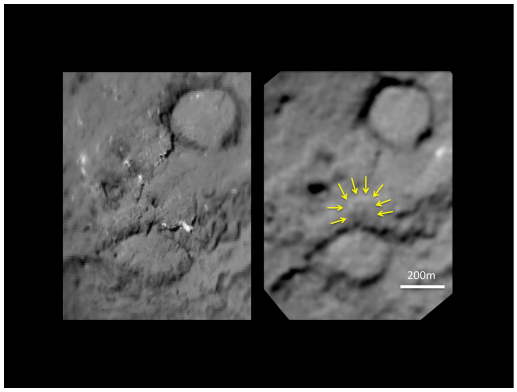

Credit: *NASA / JPL-Caltech / University of Maryland / Cornell*

Figure 1.13: Before-and-after comparison of the part of Comet Tempel 1 that was hit by the impactor from NASA's Deep Impact spacecraft. Left: A mosaic made from images obtained by Deep Impact in July of 2005. Right: Image taken by the Stardust-NExT mission in February of 2011. Arrows in this image identify the rim of the impact crater, estimated to be 150 m in diameter. A brighter mound in the center of the crater, likely ejecta from the impact, can also be seen.

of Tempel 1 (Stardust-NExT) mission.

Discovered by Wilhelm Tempel in 1867, Comet 9P/Tempel (Tempel 1) measures about 6 km in diameter, orbits the Sun at a distance of 4.739 au at aphelion and 1.509 au at perihelion, and was the first target of NASA's Deep Impact probe, which deliberately launched a projectile and struck the comet to analyze the chemical makeup of its near-surface layers (initial analysis detailed in A'Hearn et al. 2005). The crater made by the impact was seen, one full orbit later, by the Stardust probe, as part of the Stardust-NExT mission (Fig. 1.13). Granular processes taking place on the surface happen in conjunction with outgassing—the erosion seen in Fig. 1.14 is not driven primarily by ordinary granular processes, but rather by the sublimation and evaporation of volatile substances.

In 1986, Malcolm Hartley discovered 103P/Hartley (Hartley 2), a small comet whose perihelion is just 5.87 au from the Sun, and whose aphelion is 1.05 au from the Sun, close to the Earth's orbit at 1 au. Its diameter is estimated to be 1.2–1.6 km and its density estimated to be 2.3–3.0 g cm^{-3} (Belton et al. 2013; Thomas

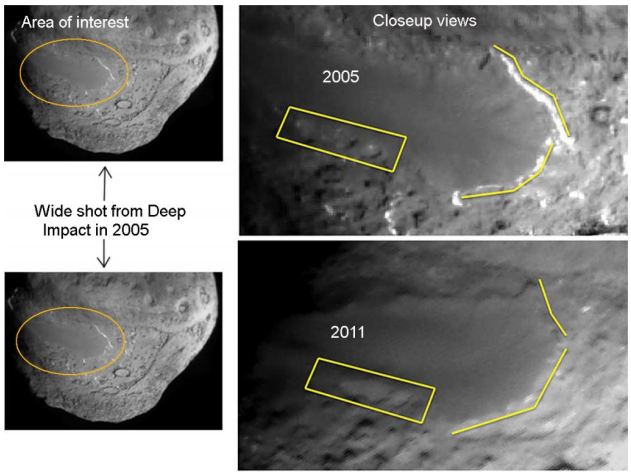

Credit: *NASA / JPL-Caltech / University of Maryland / Cornell*

Figure 1.14: Changes in the surface of Comet Tempel 1 between July of 2005 (top-right) and February of 2011 (bottom-right). The smooth terrain is at a higher elevation than the more textured surface around it. Cliffs on the comet, illustrated with yellow lines to the right, seem to have have eroded ~ 30 m to the left in this view, and the boxes show depressions that have merged together.

et al. 2013).[11] The shape of Hartley 2 (Fig. 1.15) is reminiscent of Itokawa (Section 1.1.1.6), and despite the influence that gases have on the comet, which distinguishes it from an asteroid, gradations of surface roughness to smoothness seem to be tightly correlated with increasing potential, as is seen on Itokawa Fig. 1.8. This lends credence to the idea that this manner of grain distribution might be applied with more generality to small bodies, including comets as well as asteroids, although the resurfacing processes may differ significantly between the two.

[11] A'Hearn & DIXI Team (2012) provide an overview of the composition of Hartley 2 and its unique outgassing mechanism, as obtained by the Deep Impact probe. The composition includes H_2O ice in regions of rough topography, and in what is believed to be the morning hemisphere. The outgassing mechanism has gaseous CO_2 as the primary driver of activity, rather than gaseous H_2O.

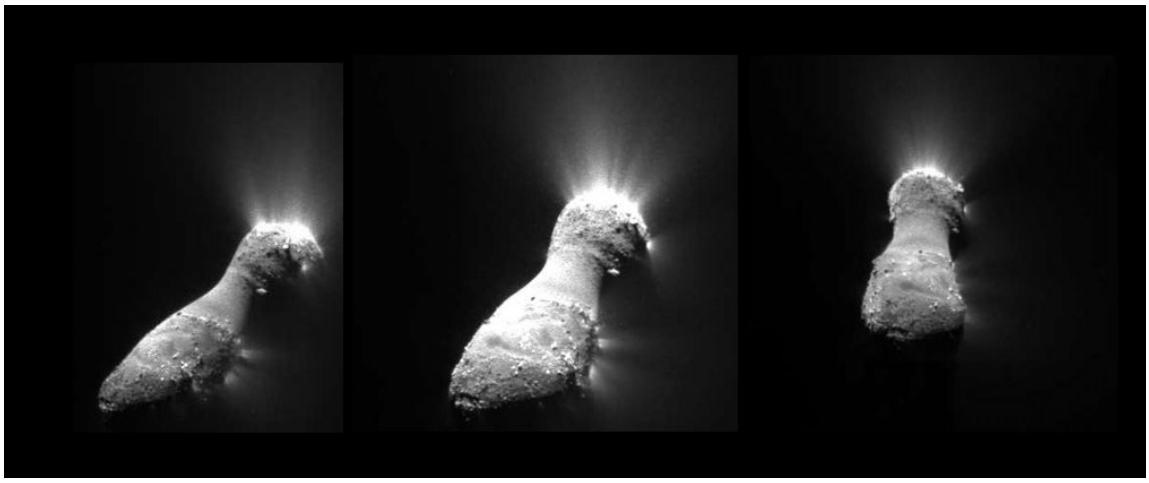

Credit: *NASA / JPL-Caltech / University of Maryland*

Figure 1.15: Three photos of Comet Hartley 2 imaged by NASA's Deep Impact spacecraft, as part of the EPOXI mission, as the spacecraft came within 700 km of the comet during flyby on November 4, 2010.

1.1.1.9 Martian satellites Phobos and Deimos

Phobos has a mean diameter of about 22 km and a bulk density of 1.876 g cm^{-3} (Zellner & Capen 1974; Andert et al. 2010), and exhibits a very tight orbit around Mars (within areosynchronous orbit[12]), at a distance of 9,377 km from Mars' center of mass, or about 6,000 km from the surface (Fig. 1.16). It appears, from spectroscopic images, that its composition is similar to low-albedo D-type asteroids (Lewis 2004).[13] Phobos has been visited by the spacecraft Mariner 9 in 1971, Viking 1 in

[12]An areosynchronous orbit of a satellite is an orbit that completes one revolution around Mars in the same amount of time that Mars completes a single rotation. Thus, a satellite in an areosynchronous, circular orbit around the equator with an angular momentum vector oriented in the same direction as the rotation vector of Mars would keep overhead of the same spot on the Martian surface; this is called an areostationary orbit, a special class of areosynchronous orbit. The analogous terms for synchronous orbits around the Earth are geosynchronous and geostationary orbits.

[13]Like the C-types, D-type asteroids have low albedos, are reddish, and typically show few strong absorption features. Because of these characteristics, they are believed to contain significant

1977, The Mars Global Surveyor in 1997 and 2003, Mars Express three times from 2004 until 2010, and by the Mars Reconnaissance Orbiter (MRO), in orbit around Mars since 2006. Recent images indicate that Phobos is covered with a layer of fine-grained regolith of considerable depth, to perhaps hundreds of meters (Zelenyi et al. 2010; Lorenz et al. 2012).

Deimos has a mean diameter of about 13 km and a bulk density of 1.471 g cm^{-3} (Thomas et al. 1996), and orbits at a distance of 23,460 km from Mars' center of mass (Jacobson 2010). It is similar spectroscopically to Phobos, and shares its low albedo, but is noticeably smoother than Phobos due to a more extensive filling of its craters with regolith (Fig. 1.17). The regolith itself is highly porous and has a radar-estimated density of 1.1 g cm^{-3} (Busch et al. 2007). Both Martian satellites are believed by many to be captured asteroids (e.g., Barlow 2008).[14]

1.1.2 Granular processes

The surface properties of SSSBs that we have visited have been discussed above; this includes evidence for the occurrence of specific granular processes. Landslides, global resurfacing, effects from YORP spin-up, as well as other processes, are reviewed below.

---

amounts of organic compounds (Gradie & Veverka 1980). The so-called "Nice Model" predicts that D-type asteroids may have been formed in the Kuiper belt ((Morbidelli et al. 2005); McKinnon (2008)).

[14]For a further discussion, see Burns (1992).

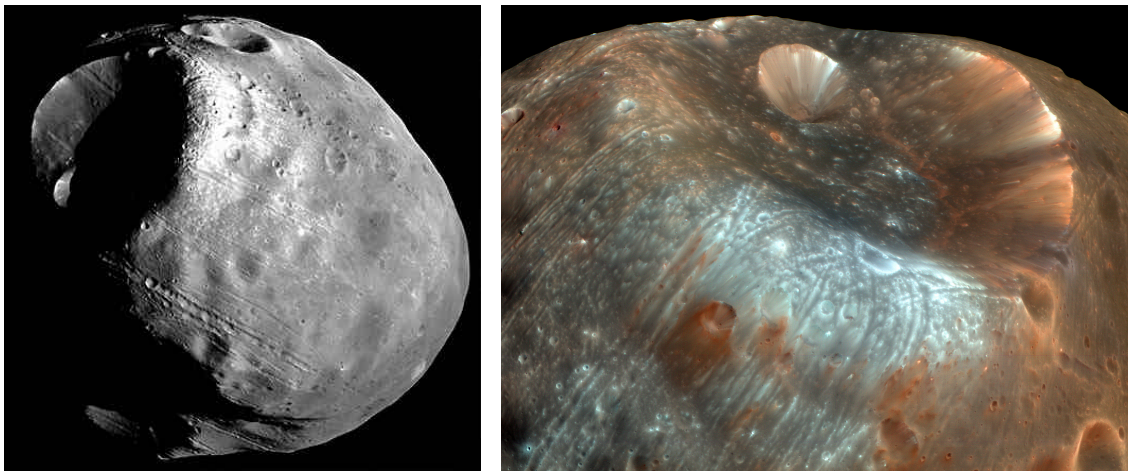

Credit: *NASA / JPL-Caltech / University of Arizona*

Figure 1.16: Left: A mosaic of three separate images of Martian satellite Phobos, taken by Viking 1 on October 19, 1978. Right: Phobos' Stickney crater. False color image taken by MRO on March 23, 2008.

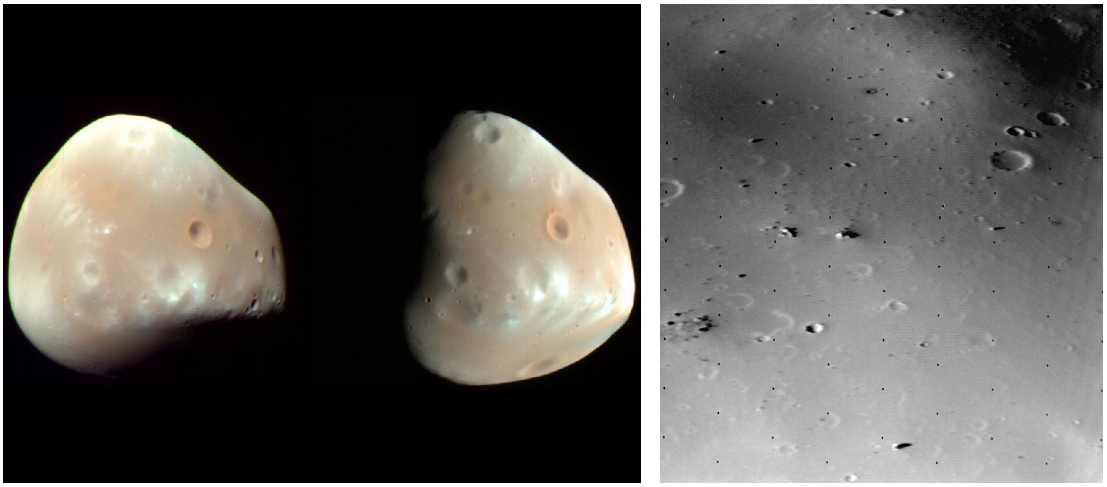

Credit: *NASA / JPL-Caltech / University of Arizona*

Figure 1.17: Left: A color-enhanced composite image of Martian satellite Deimos; images obtained by MRO on February 21, 2009. Right: Surface of Deimos, imaged by the Viking 2 spacecraft on October 5, 1977.

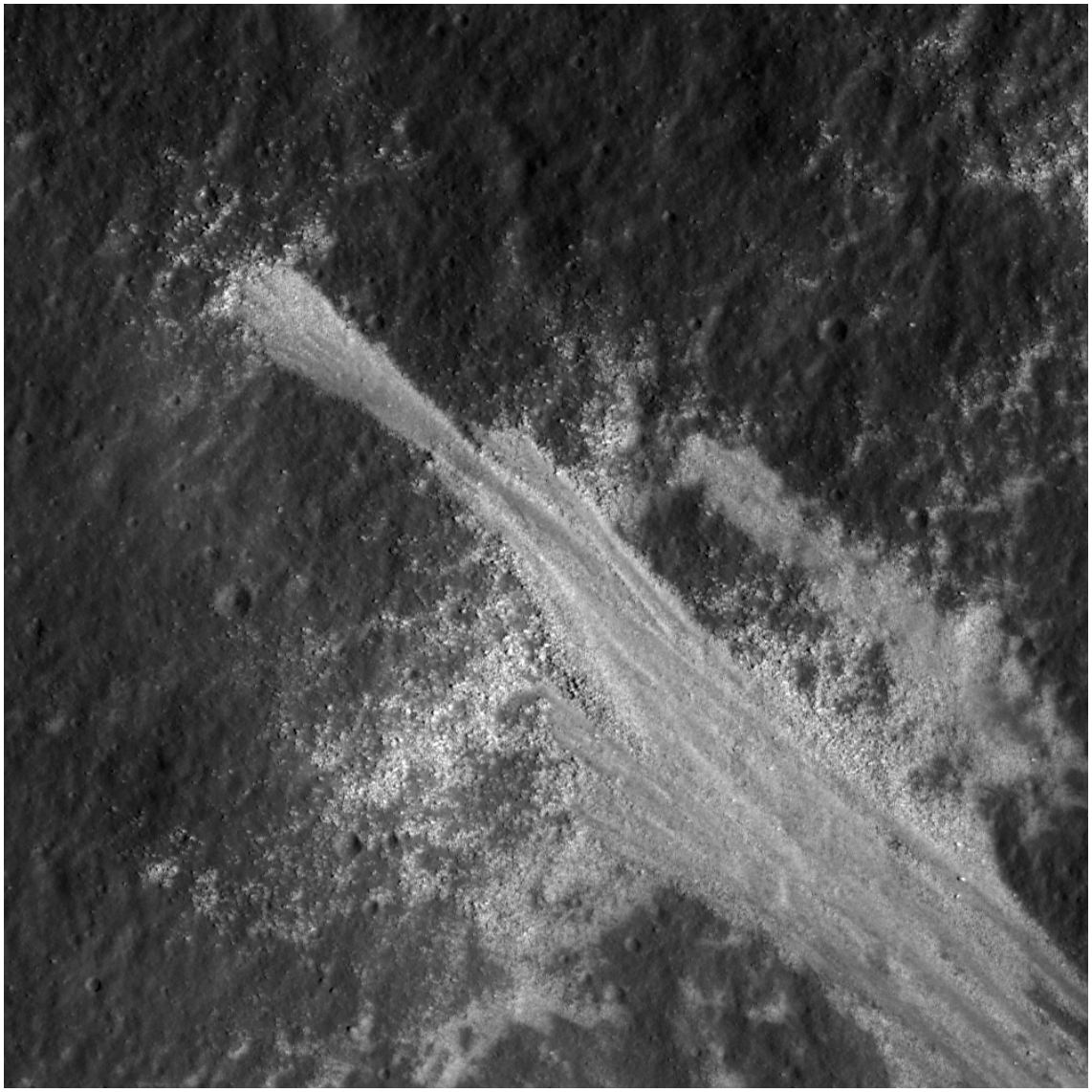

Credit: *NASA / GSFC / Arizona State University*

Figure 1.18: The stream of bright material shows a flow of rocks and boulders down the slope of the inner wall of lunar crater Riccioli CA. Images were taken by the Lunar Reconnaissance Orbiter. The slope direction is from the lower-right corner to the upper-left corner.

1.1.2.1 Landslides

Landslides occur in the Solar System in a large range of gravitational environments: on our Moon, Saturnian satellite Helene, Vesta, and Lutetia.

Riccioli CA is a lunar satellite crater, 14 km from the center of Riccioli lunar

crater. Fig. 1.18 shows bright, loose, granular material flowing toward the floor of the crater. The end of the flow (upper-left corner of the image) resembles the wet sediments at the end of an alluvial fan, though this is dry, granular flow, making this a colluvial fan.[15] Fig. 1.19 shows strong evidence of landslide activity covering much of Saturnian satellite Helene's surface. Some of the most striking evidence for landslides on SSSBs can be found on Lutetia (see a discussion in Section 1.1.1.5). Images like Fig. 1.20, showing the rim of Vesta's Marcia crater, an example of the high-quality data that we obtain from modern-day spacecraft, help us analyze the qualities of erosion and crater degradation including the timescales on which they occur. They also provide ways of measuring typical angles of repose of the regolith on Vesta and other small bodies, which is helpful in conducting numerical simulations of granular processes on these bodies.

1.1.2.2 Resurfacing

It has been found that the granular material on SSSBs can flow under various conditions, such as global shaking due to small impacts on low-gravity bodies that cause the propagation of seismic waves (e.g., Richardson et al. 2005b). From the very strong evidence of global resurfacing in the context of Itokawa in Section 1.1.1.6, which includes mention of the striking correlation between the grain sizes on the surface and the effective potential at that particular point (Fig. 1.8), there remains little doubt that global resurfacing is taking place.

However, even if the outcome is apparent, the specific mechanisms are still not

[15]In discussing water flows on the Earth, Bull (1977) defines an alluvial fan as "a deposit whose surface forms a segment of a cone that radiates downslope from the point where the stream leaves the source area." What we see in this image could be described as a colluvial fan, as colluvium sediment such as this does not require a flow of liquid.

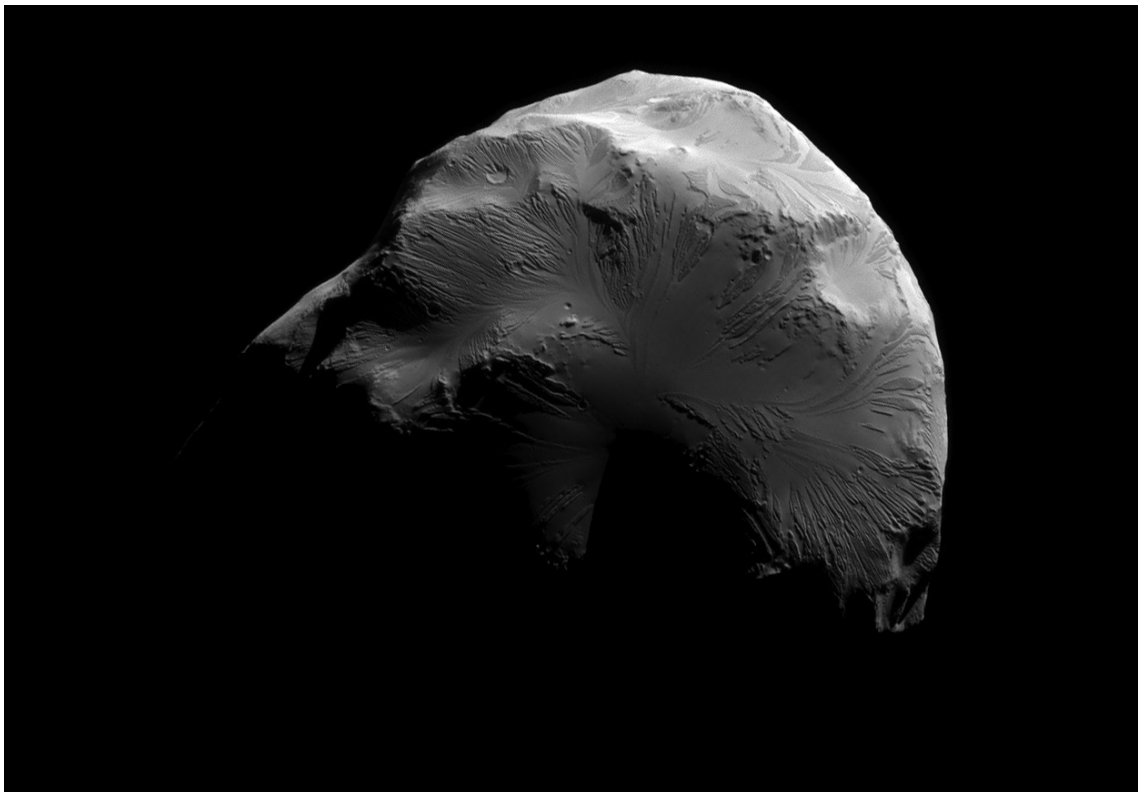

Credit: *NASA / JPL / Space Science Institute*

Figure 1.19: Cassini spacecraft image of Saturn's moon Helene taken on June 18, 2011. Inferred from density measurements and spectral signatures, Helene (33 km across) is comprised of large quantities of water-ice, like most moons of Saturn. Lit terrain seen here is on the leading hemisphere. This view is from a distance of approximately 7,000 kilometers and is very suggestive of granular flow in the form of global landslides.

well understood. Ejecta from impacts onto some of the smallest of SSSBs like Itokawa, if not liberated from the asteroid, have the ability to settle nearly anywhere on the surface. This could explain the resurfacing that we see, but the effects from changes in surface gravity suffered due to encounters with other bodies (tides) could also play a role.

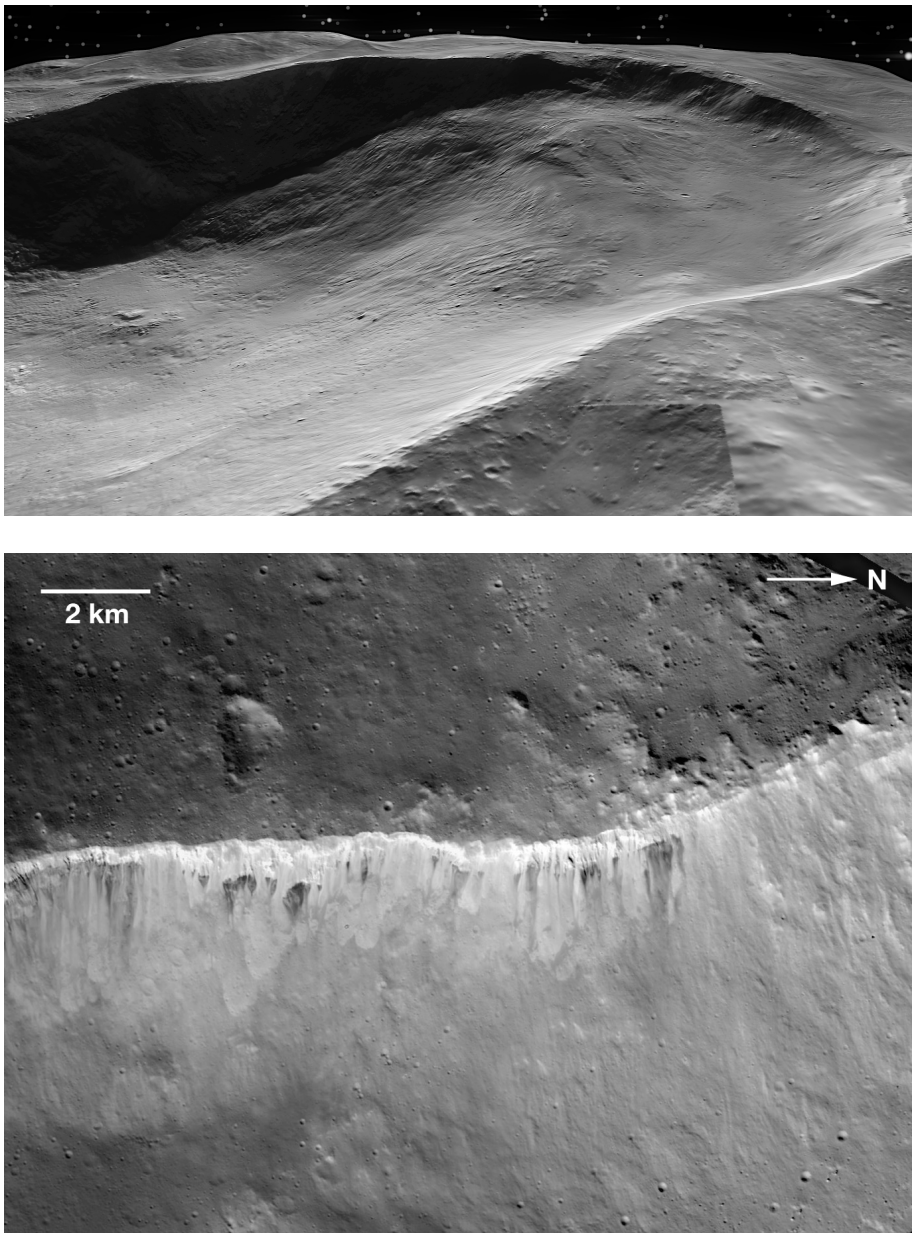

Credit: *NASA / JPL-Caltech / UCLA / MPS / DLR / IDA / LPI / ASU*

Figure 1.20: Top: Composite image of Marcia crater located near Vesta's equator. Bottom: Image mosaic of the rim of Marcia crater. Measuring 58 km across and estimated to be only about 70 million years old (Marchi et al. 2012), this crater does not have the typical bowl shape due to the movements of granular material in and around the crater. The angle of repose, governed by the ability to resist shearing, can lead to insight about the material properties of Vesta's regolith.

1.1.2.3 The YORP effect

Asteroids larger than $\sim$ 50 km in diameter have spin rates that follow a single Maxwellian distribution, while smaller asteroids have a more dispersed distribution, with both slow and fast spinning populations (Harris & Pravec 2006). A mechanism that explains these data must account for the size-dependent effect. Further, most observed near-Earth asteroid binaries include primaries rotating just near rotational break-up (Pravec & Harris 2000; Pravec et al. 2005). The fact that the SSSB binary population is not limited to near-Earth asteroids, but also includes a similar fraction of small main belt asteroids also rotating very close to their break-up limits, suggests that a binary formation mechanism not related to close tidal encounters with the terrestrial planets must exist (Pravec & Harris 2006, 2007).

The prevalence of extreme spin rates among near-Earth asteroids and small bodies of the main belt provides evidence for a mechanism of spin-up that applies broadly to small bodies, like what could be provided by the so-called YORP effect.

The YORP effect is a high-order solar thermal effect; it is the result of the fact that these bodies have net surface asymmetries (e.g., small craters, rocks, irregular shaping). Sunlight bouncing off, or reradiating, from particular surface irregularities on the face that the asteroid is showing to the Sun produces a small net torque at any given moment in time. Integrating the net torque that is produced for each of the different faces that the Sun sees over a full rotation of the body gives the net torque over the entire period of the asteroid. The angular momentum gained or lost by the asteroid over a single period is tiny, but for the most part constant, and accumulates until something disrupts this process. If the body is small enough, and close enough to the Sun, it can gain sufficient angular momentum to radically alter its spin-state.

The YORP effect is extremely sensitive: Statler (2009) argues that expected

errors will be of order 100% if observations constrain the surface to a spherical harmonic order $l \leq 10$, and for errors under 10%, the surface must be constrained to at least $l = 20$. Furthermore, a single boulder comparable to Yoshinodai on Itokawa ($\sim$ 27 m), moved by as little as twice its own diameter, can alter the magnitude of the torque by factors of several, and change the sign of the spin component at all obliquities.

The components of the vector that describes the net force on the body (due to reflection and re-emission of sunlight) directed along the body center gives rise to a lower-order process known as the Yarkovsky effect (Hartmann et al. 1997), which drives a radial drift that is determined by properties such as: the absorption, emission, and reflectivity of the surface at the Sun's electromagnetic frequencies; the surface area exposed to the sunlight; and the distance of the body from the Sun. Although this force increases with size since the surface area goes as the square of the radius, the inertia of the body also increases with size since the mass goes as the cube of the radius. Therefore, although the force is greater on larger bodies, the acceleration is smaller. For these reasons, the Yarkovsky effect is not relevant for large bodies (or bodies far from the Sun). Ample evidence exists that the Yarkovsky effect influences the orbital dynamics of asteroids less than $\sim$ 20 km in diameter (Nesvorný & Bottke 2004; Mueller 2007).

Besides indirect evidence of its role in the orbital evolution of asteroids over long time intervals (Morbidelli & Vokrouhlický 2003), the Yarkovsky effect has been observed directly by measuring changes in orbital parameters that are better explained by Yarkovsky drift than by any other known mechanism (Chesley et al. 2003; Farnocchia et al. 2013). More recently, Lowry et al. (2007); Taylor et al. (2007) observed the spin rate of asteroid (54509) 2000 PH5 (since named YORP) increasing at the rate of 0.0002 ± 0.00002 deg day^2, which between 2001 and 2005

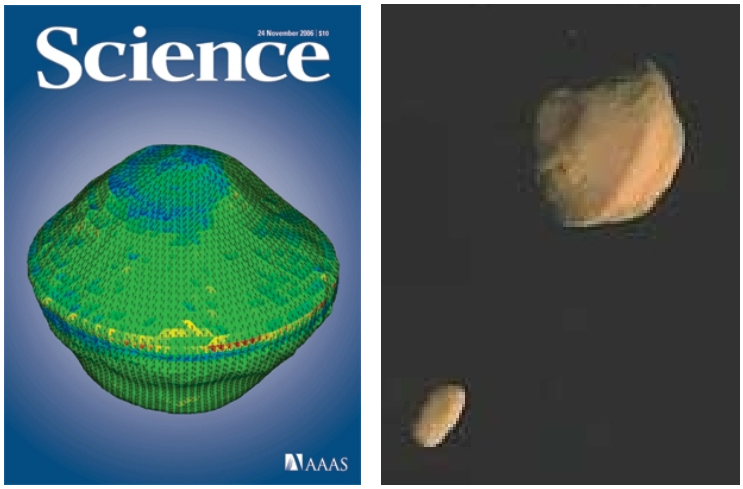

Credit: *"Science" / JPL / University of Michigan*

Figure 1.21: Left: Arecibo radar image of (66391) 1999 KW_4 reconstructed by Ostro et al. (2006) as appeared on the cover of *Science*, 24 November 2006, color-coded to show the slope of the surface with respect to the the tangent of the gravitational force vector, from 0 degrees and flat (blue) to 75 degrees (red). Right: Radar-derived image of the (66391) 1999 KW_4 binary.

caused the asteroid to rotate about 250 degrees further than its spin rate in 2001 would have predicted, providing direct evidence for the YORP effect. Kaasalainen et al. (2007) reported a change in the rotation rate of the 1.5 km diameter asteroid (1862) Apollo of one extra rotation cycle in 40 years, which is also best explained by the YORP mechanism. Other (indirect) evidence exists through the clustering of the directions of rotation axes in asteroid families (Vokrouhlický & Čapek 2002).

Observed with the Arecibo radar dish in 2001, and considered the best characterized asteroid binary, (66391) 1999 KW_4 is the archetypal model of a YORP binary system, pictured in Fig. 1.21. The detailed shape model was constructed by Ostro et al. (2006), and the dynamical model by Scheeres et al. (2006), who also constructed a color-coded relief map over 1999 KW_4 Alpha, the primary, showing the magnitude of the local surface acceleration of a point particle at every location on the asteroid (Fig. 1.22).

We can imagine that the fixed points for a particle at the two poles of a body

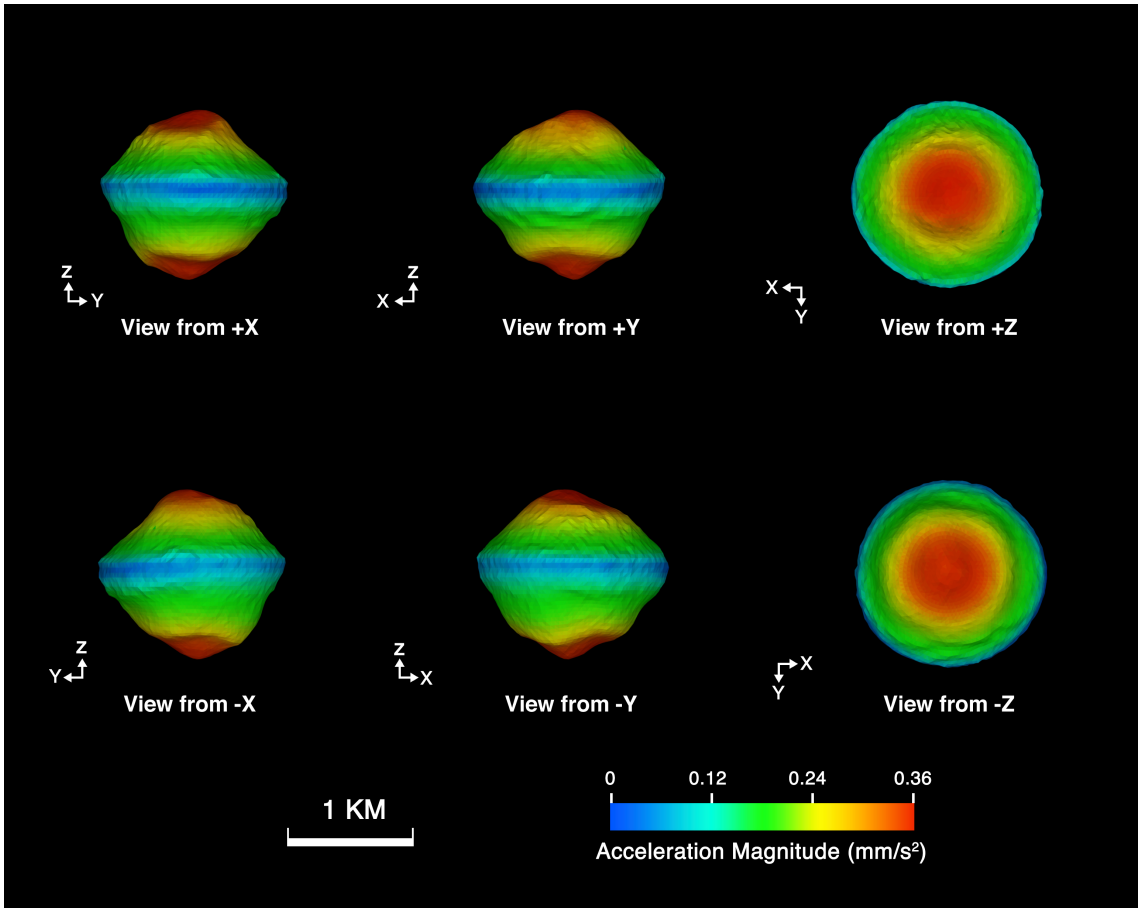

Credit: *JPL / University of Michigan*

Figure 1.22: Six views of the shape model asteroid 1999 KW_4, color-coded by the surface accelerations of a point particle; note that loose particles on the equator are effectively unbound.

like 1999 KW_4 Alpha become more and more unstable as the body's spin increases, causing material to cascade down toward the equator from higher latitudes. This material, once at the equator, can then become unbound leading to mass loss. Walsh et al. (2008, 2012) using a numerical model (Richardson et al. 2000) to compute a potential fate for the ejecta, and make a case that the ejecta could coalesce into a satellite. Scheeres (2007) and Jacobson & Scheeres (2012) postulate that binaries could form due to direct asteroid fission (the gradual spin-up of a body could cause a hunk of it to split off, forming a binary asteroid system). Both interpretations rely on YORP as a mechanism for the gain in angular momentum.

About 15% of near-Earth asteroids and small Main Belt asteroids are estimated to be binaries (e.g., Bottke & Melosh 1996; Pravec & Harris 2007). The prevalence of binaries favors YORP as a ubiquitous formation mechanism capable of explaining the types of binaries that are observed: KW_4–type (there are also at least two triple-systems containing a top-shape primary, 1994 CC and 2001 SN_263; see Brozovic et al. 2010, Fang et al. 2011), asteroids with bifurcated mass distributions (contact-binaries), and the apparent population of "split" binary pairs (Pravec et al. 2010 that suggest that certain asteroid pairs with similar orbital elements may have once belonged to the same small parent body, which had fissioned due to the YORP effect). It has been suggested by, e.g., Ćuk (2007), and modeled by Ćuk & Nesvorǹy (2010), that binaries should also be destroyed by the binary YORP effect (BYORP), which would increase or decrease the secondary's orbit, depending on the satellite's overall shape, surface features, and material properties. This could be causing a decrease in the number of observed binary SSSBs. A steady state between binary production due to YORP and binary destruction due to BYORP would need to explain the estimated 15% of small asteroids that are binaries. If BYORP destabilizes binary SSSBs, pushing the orbit of the secondary away from the primary while YORP is still active on the primary, this process may help explain the existence of triple-systems 1994 CC and 2001 SN_263. If the secondary's orbit is decreased, this could be seen in the number of contact binaries observed. The BYORP mechanism, however, remains poorly understood and insufficiently modeled to draw conclusions about its role with respect to these phenomena.

In addition to the outcomes of future numerical modeling (Section 5.2.9), much could be learned from a spacecraft visit to a body shedding material due to YORP spin-up. One might expect to see rocks and grains of various sizes suspended around the body at low latitudes. Fine regolith would be unlikely to survive long out of

contact with the body due to effects of solar radiation, but could be replenished with additional shedding of material or by the grinding of hovering rocks.

1.1.2.4 Other granular processes

Granular processes in the Solar System are not limited to the surfaces of bodies. The growth of dust grains into meter-sized boulders in the early Solar System is a poorly understood granular dynamics problem (Stark & Kuchner 2009). Accretion by way of low-speed collisions of grains with sufficient cohesion to adhere seems to be required. Also, Saturn's rings are comprised mostly of water frost and only a small amount of rocky material (Miner et al. 2007; Dougherty et al. 2009). Laboratory experiments and numerical simulations suggest that interpenetration of thin, frost-coated surface layers on Saturn's A ring particles may lead to weak cohesive bonding at the low impact speeds characteristic of the rings (Hatzes et al. 1991; Perrine et al. 2011; Perrine & Richardson 2012). Tremaine (2003) suggests that radial banded structures in Saturn's B ring (Fig. 1.23) may consist of large-scale transiently bonded particles that orbit Saturn effectively as a solid. These banded structures have also been attributed to viscous overstability in the dense rings (Spitale & Porco 2010).

1.1.2.5 Understanding the effects of grains in the Solar System

The qualities of a specific surface effect such as a landslide (Section 1.1.2.1), formation of a granular pond, or global events like seismic shaking (Sections 1.1.1.6 and 1.1.2.2) and large-scale migration and reshaping (Section 1.1.2.3), are determined by the gravitational environment and the properties of the granular materials that are involved. Clues pertaining to the properties of these materials are contained in images from spacecraft sent to Solar System bodies, which we continue to accumulate. Modern computing, combined with carefully chosen Earth-based laboratory data,

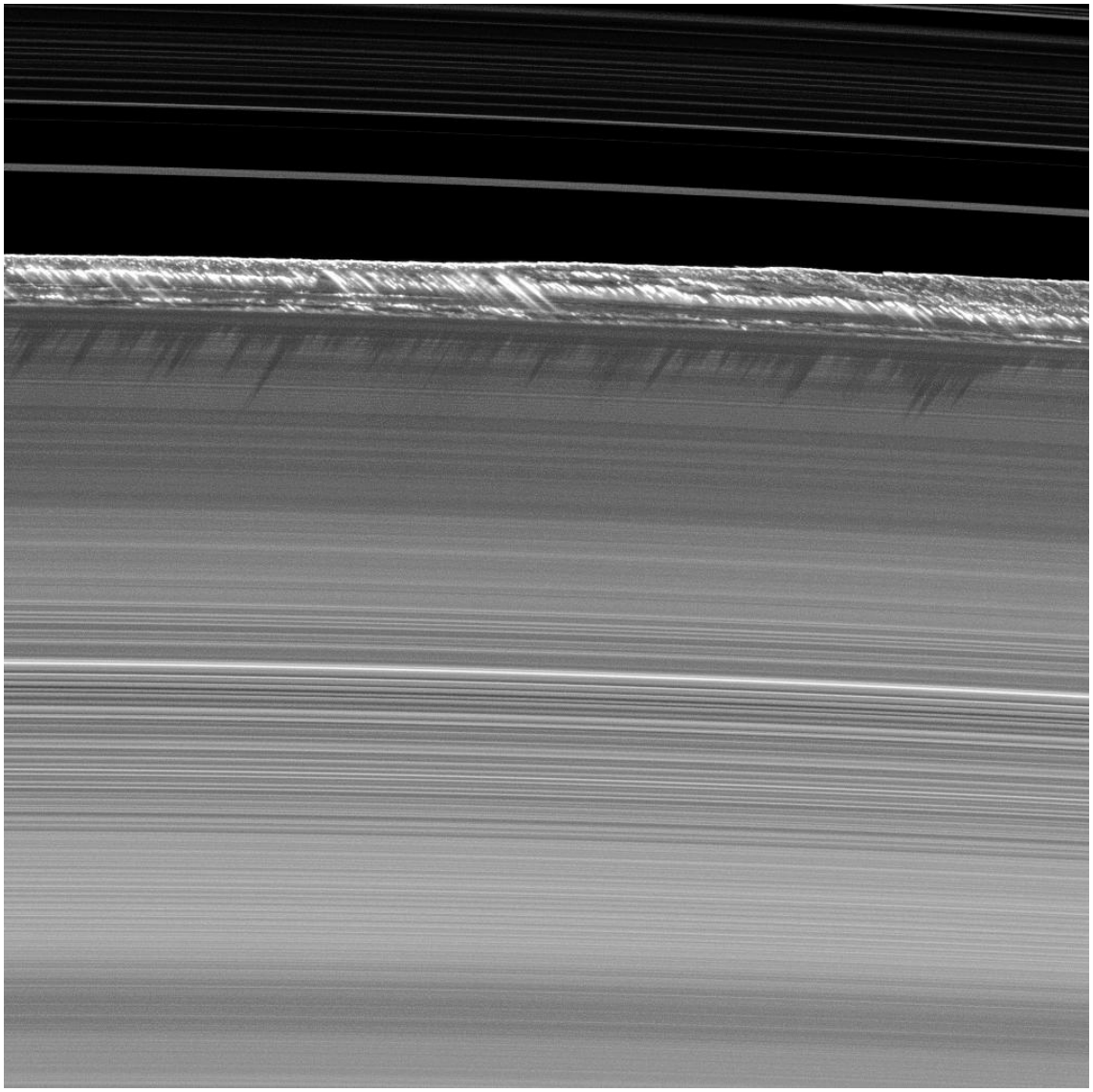

Credit: *NASA / JPL / SSI*

Figure 1.23: Vertical structures, among the tallest seen in Saturn's main rings, rise abruptly from the edge of the B ring to cast long shadows in this image taken by NASA's Cassini spacecraft two weeks before the planet's August 2009 equinox. A 1,200 km-long section arcs along the outer edge of the B ring and reaches heights as high as 2.5 km above the plane of the rings (vertical thicknesses of the A, B, and C rings are typically about 10 m). The vertical excursions may be caused by perturbations from moonlets $\sim$1 km in size.

allows for the development of new numerical tools to aid in our understanding of these phenomena. Such tools are developed in this thesis work. By matching well-tuned numerical simulations to resemble what we see in these images, we uncover the properties of different types of granular media that exist in our Solar System.

1.1.3 Upcoming visits to solid Solar System bodies

Having a sense of the types of surface environments found on these bodies puts the task of numerical investigation into context. Moreover, there are missions to unexplored SSSBs that are still ongoing, as well as some that are in various stages of development. The numerical tools developed in this work will aid in the interpretation of these data and images and add to our understanding of the dynamical processes of SSSB granular material. These tools are also being used to assist in the development of sampling strategies for some of the upcoming missions discussed below.

1.1.3.1 Future work for Dawn and Rosetta

The Rosetta mission will attempt to land on Comet 67P/ChuryumovGerasimenko in November 2014 and accompany it around the Sun through perihelion (August 13, 2015), offering an exciting glimpse into its outgassing and other surface processes as it progresses through its orbit.

The Dawn mission, after having departed from Vesta on September 5, 2012, will arrive at (1) Ceres in February 2015. In the asteroid belt, it is the most massive object, making up about a third of the entire mass (Carry et al. 2008). Ceres is an oblate spheroid having an equatorial radius of about 480 km, a polar radius of just over 450 km, and a mean density of about 2.15 g cm^{-3} (Thomas et al. 2005). It may have a differentiated interior, and is confirmed to have a shape that is in

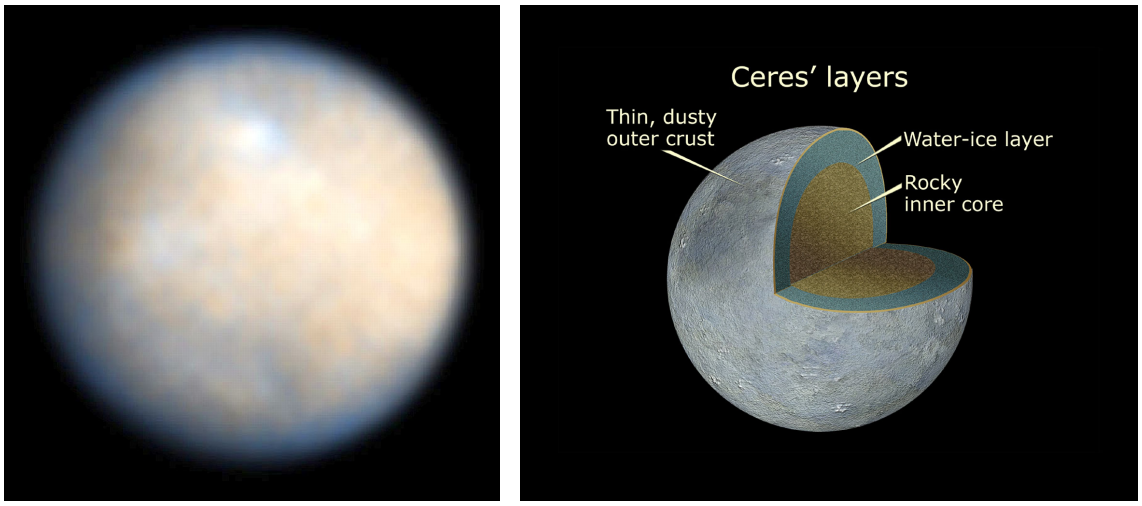

Credit: *NASA / ESA / SwRI / Cornell / UMD / STScI*

Figure 1.24: Left: Hubble image of (1) Ceres, taken January 24, 2004. Right: One model of Ceres' interior.

hydrostatic equilibrium, justifying its classification as a dwarf planet (Ksanfomality 2007). Dawn will investigate Ceres' apparent lack of large-scale topography (Carry et al. 2010; Rivkin & Volquardsen 2010). Bland et al. (2013) argue that if Ceres has a near-surface ice layer tens of kilometers thick (see Fig. 1.24), radiogenic heating would be sufficient to completely relax impact craters $\geq$4 km in diameter in the equatorial region over short timescales of 10^6–10^9 years and craters at mid-latitudes over 10^8–10^9 years. Moderate-sized craters in the cold polar regions should remain largely preserved and even large craters ($\sim$ 12 km) in those regions should retain large depths.

While Bland et al. (2013) expect a near-surface ice layer with smooth topography at the equator, and crater counts that increase with latitude, consensus will likely not be reached before Dawn's visit. For example, Zolotov (2009) takes Ceres to have a dark, non-icy surface with signs of hydrated minerals, and further points out that a rocky crust would be gravitationally unstable, and would be overturned by any thick water mantle beneath it. Therefore, Ceres could be largely undifferentiated,

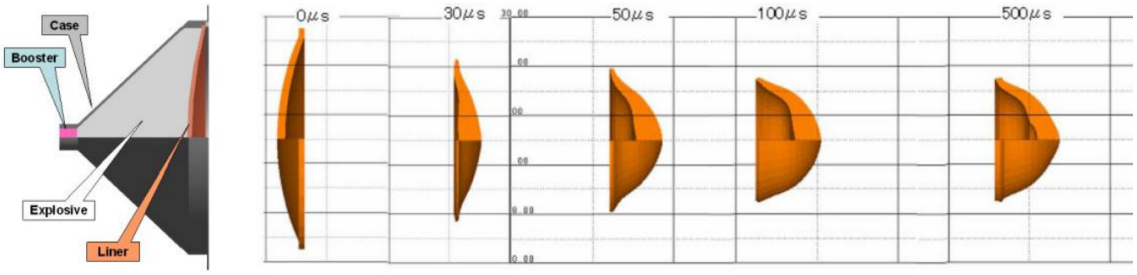

Credit: *Arakawa et al. (2013)*

Figure 1.25: Time evolution of the copper liner projectile after explosion of the SCI aboard Hayabusa2.

and its low density explained by macro-porosity. However, as is the case with much of Ceres' interior, the evidence for a rocky crustal exterior is not conclusive. Dawn's visit should answer questions about Ceres' interior and shed light on the types of processes that occur on its surface.

1.1.3.2 Hayabusa2

In January 2012, the Hayabusa2 mission received approval from the Japanese government to visit and retrieve samples from asteroid (162173) 1999 JU3, a primitive (C-type) asteroid, with a proposed launch in July of 2014. 1999 JU3 has an effective diameter of 870 m and a retrograde rotation of 7.63 hrs (Müller et al. 2010).

The spacecraft borrows heavily from the design of the original Hayabusa Section 1.1.1.6, but features several upgrades, including to its four ion engines and to its antenna (Yoshikawa et al. 2012). Hayabusa2 will also make several sampling attempts, two similar in strategy to those that Hayabusa made at Itokawa, plus a third using a different strategy. The first two involve touchdowns, whereupon a 5 g tantalum projectile will be fired into the surface at 300 m s^{-1} (Tachibana et al. 2013). The debris from the impact will be collected. The target sites will be in regions identified to be especially rich in hydrated minerals and organic molecules. Preliminary tests related to this mechanism form the basis of the work addressed in Chapter 4.

The third sampling attempt planned for Hayabusa2 involves a small copper impactor attached to an explosive—this was not aboard the Hayabusa mission to Itokawa (Arakawa et al. 2013). The explosive device, called the Small Carry-on Impactor (SCI), will be released from Hayabusa2 at an estimated altitude of 500 m above the surface of 1999 JU3. After 40 minutes, giving the spacecraft time to "hide" behind the asteroid (and to release a camera on the way to safety that can witness the impact), the SCI is detonated. Slamming into the asteroid at about 2 km s^{-1}, the impactor, originally disk-shaped with a radius of 15 cm, is expected to deform as a result of the explosion into something like a hollow semi-spherical shape with a radius of $\sim$ 10 cm by the time of impact (Fig. 1.25). The impact is to occur within a 200 m radius of its target point on the surface, form a crater, and excavate fresh, unweathered material from beneath the surface. Hayabusa2 will keep its distance from the surface of the asteroid for over 2 weeks to avoid damage from debris created by the impact, then attempt to make a soft landing at or near the impact site. This third sampling acquisition procedure will collect excavated material from the newly formed crater.

Besides having three containers aboard instead of two, one for each sampling operation, Hayabusa2's container sealing method is also improved over the one that Hayabusa used: Hayabusa2 will use an aluminum metal seal, instead of the double viton O-rings used on Hayabusa, in order to avoid the terrestrial air contamination suffered by the Hayabusa container (Okazaki et al. 2011).

On Hayabusa's visit to asteroid Itokawa, the sampling projectile did not fire, limiting the sample collection to very tiny grains. The design of Hayabusa2's sampler horn includes an upturned tip, like the teeth of a comb, which is intended to lift pebbles up during the touchdown procedures. These samples will be put into their respective containers by the deceleration of the spacecraft. This configuration will

act as a backup to the primary sampling procedures during each of the three operations. Depending on the texture of the rocks on 1999 JU3, Hayabusa2 should pick up between a gram and several grams of samples, significantly less than amounts expected to be returned by OSIRIS-REx (Section 1.1.3.3).

1.1.3.3 OSIRIS-REx

Selected in 2011, NASA's third New Frontiers mission, OSIRIS-REx, will rendezvous in 2018 with a primitive near-Earth asteroid, (101955) Bennu (formerly 1999 RQ36). Bennu is an Apollo (Earth-crossing) asteroid with an estimated mean radius of 247 m (Nolan et al. 2007; Chesley et al. 2012). After being inserted into orbit around the body and conducting measurements for up to 505 days, which includes the creation of a global surface map, a Touch-And-Go-Sample Acquisition Mechanism (TAGSAM) will be deployed to collect material from the asteroid's surface (Berry et al. 2013).

The TAGSAM is designed to approach Bennu's surface at a gentle 10 cm s^{-1}, touch the surface within 25 m of the selected target location, and then spend 5 seconds collecting samples before returning the sample to the spacecraft (Lauretta 2012).

Once contact with the surface has been made, molecular nitrogen gas, N_2(g), is to be injected into the regolith, blasting material into the collection device. This strategy relies upon a certain degree of implantation into the surface prior to the N_2(g) injection. An onboard camera will document the sampling process once per second. To ensure that the appropriate penetration into the surface is achieved, the mechanism requires thorough modeling; multiple teams are currently conducting this research both in experiment and simulation by considering the "compliance" of the surface as the sampler head is implanted. One such team uses the code

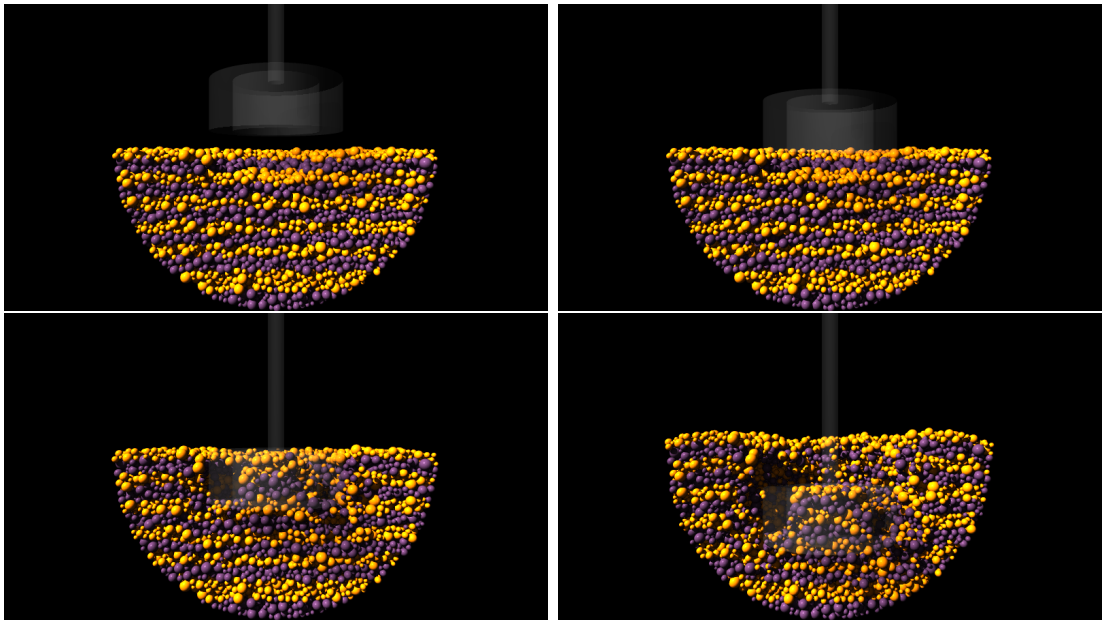

Credit: *Ronald Ballouz, UMD*

Figure 1.26: Sequence of images showing the computed positions of simulated asteroid grains and the sampler-head from an OSIRIS-REx TAGSAM study, in advance of the spacecraft's rendezvous with (101955) Bennu in 2018. The snapshots are shown at 0.00 seconds (top-left), 0.50 seconds (top-right), 1.50 seconds (bottom-left), and 2.50 seconds (bottom-right). Contact with the surface is made at about 0.55 seconds. The TAGSAM is rendered highly translucent so that particles inside can be seen. (Note that these images do not reflect the actual dimensions of the TAGSAM.)

developments presented in this thesis, primarily from Chapters 2 and 4, to simulate the TAGSAM (Fig. 1.26).

The science team expects OSIRIS-REx to return home in 2023 with at least 60 g of pristine sample material from the asteroid. Analysis of the sample will help us to better understand, and answer long-held questions about, the formation of the Solar System and shed light on the origin of volatiles and complex organic molecules on Earth. Assumptions about the surface (Fig. 1.27) rely heavily on the data that have been collected during prior missions to SSSBs (Section 1.1.1).

Credit: *NASA / GSFC / University of Arizona*

Figure 1.27: Simulated image of asteroid (101955) Bennu, derived from radar readings and estimates of the topography.

1.1.3.4 MarcoPolo-R

MarcoPolo-R is a sample-return mission to a primitive near-Earth asteroid proposed to the European Space Agency (ESA). In February 2011, it, along with 3 other mission designs, were selected from among 47 proposals into the Assessment Study Phase (ASP) to compete to be the third M-class mission of the agency's Cosmic Vision 2 program, with a targeted launch date of 2024 (MarcoPolo-R would expect

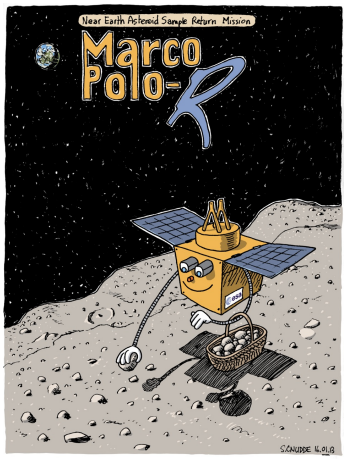

Credit: *Sylvain Cnudde, 2013*

Figure 1.28: The cover a cartoon promoting MarcoPolo-R, created for public outreach.

to launch in 2022–2024).

The baseline target of MarcoPolo-R is the primitive asteroid (341843) 2008 EV5, with binary asteroid (175706) 1996 FG3 as the backup target. Since direct investigation of both the regolith and fresh interior fragments is not possible by means other than sample return, having multiple samples from unique SSSBs is important (it will supplement what is to be collected by OSIRIS-REx and Hayabusa2).

Two sampling mechanisms for use aboard MarcoPolo-R are currently under assessment by the European companies AVS and Selex Galileo. The science requirements for the sampling device dictate that it must have the capability to acquire a minimum mass of $\sim$ 100 g, consisting of cm-sized fragments, and a large amount of small particles (Barucci et al. 2013).

1.1.3.5 Manned spacewalk mission simulations

For the development of its Capability Driven Framework (Leonard 2011), NASA is identifying the exploration systems required for human exploration of near-Earth asteroids, which would include stays in the proximity of the asteroid of between 14 and 56 days (Abercromby et al. 2013; Chappell et al. 2013). One class of manned

mission under consideration by NASA would involve a primary spacecraft, which would remain between 500 m and 2 km away from the asteroid for the duration of the mission. Exploration and sampling of the asteroid's surface would be conducted by astronauts leaving this spacecraft on brief expeditions (Abercromby et al. 2013b) in extravehicular activity (EVA) suits (spacesuits) equipped with jetpacks, or multi-day expeditions in a small pressurized spacecraft, the Multi-Mission Space Exploration Vehicle (MMSEV).

NASA's Research and Technology Studies (RATS) 2012 virtual reality simulation focused on the development of these techniques, including the evaluation of different combinations of vehicles, crew members, tools, and equipment that could be used to perform exploration tasks on the surface of a near-Earth asteroid (Abercromby et al. 2013, Fig. 1.29). The virtual reality exploration of the asteroid Itokawa was based upon the high-resolution images obtained by the Hayabusa mission (Section 1.1.1.6). This study built upon the work performed during NASA's Desert Research and Technology Studies (Desert RATS) 2011 field test, which consisted of simulations designed to evaluate SEV and extravehicular operations and interactions in the micro-gravity environments found on the surface of near-Earth asteroids (Abercromby et al. 2013a).

NASA's RATS 2012 test subjects conducted simulated spacewalks, making use of head-mounted displays and instrumented gloves. During test conditions in which the MMSEV was anchored to the asteroid, one test subject would perform EVA tasks (during simulated spacewalk) in virtual reality, using a simulated jetpack, while a second performed anchored EVA tasks using simulated microgravity. "This test did not attempt to evaluate specific NEA anchoring technologies due to the immaturity of those technologies and the inability to meaningfully test them within the existing software simulation" (Abercromby et al. 2013). Much work still needs to

be put toward the investigation of the anchoring systems and sampling mechanisms. Although the primary purposes for missions like Hayabusa2 (Section 1.1.3.2; also see Chapter 4), OSIRIS-REx (Section 1.1.3.3), and MarcoPolo-R (Section 1.1.3.4) are for planetary science, these unmanned missions will go a long way toward understanding the surface environments that astronauts and more advanced landers of the future will encounter on the surfaces of these small bodies. The research and numerical tools contained in this thesis have direct applications toward the investigation of anchoring systems and sampling mechanisms in the micro-gravity, regolith-coated environments of near-Earth asteroids (see Chapter 4).

RATS are not the only manned asteroid mission simulations that NASA conducts. NASA Extreme Environment Mission Operations (NEEMO) is an underwater spaceflight analog that allows a mission-like operational environment and uses buoyancy effects and added weight to simulate different gravity levels. The 13-day NEEMO 16 mission was performed at the Aquarius undersea research habitat (Fig. 1.29, Chappell et al. 2013). The test subjects performed tasks including rock chip sampling, core sampling, soil sampling, and large instrument deployment, making use of the insights from previous near-Earth asteroid spacewalk analog tests (Reagan et al. 2012).

The Asteroid Retrieval and Utilization (ARU) mission, alternatively named the Asteroid Retrieval Mission (ARM), and popularly known as the "Asteroid Initiative," is a potential future space mission proposed by NASA, which has garnered much press recently (Klotz 2013). Still in the early stages of planning and development, ARU is a mission to bring a small near-Earth asteroid of roughly 7 to 10 meters diameter into high Earth orbit or lunar vicinity (Prado 2013), where it could be further analyzed both by unmanned craft and by a future manned mission, possibly making use of the Orion Multi-Purpose Crew Vehicle (Loff & Lind 2013). The

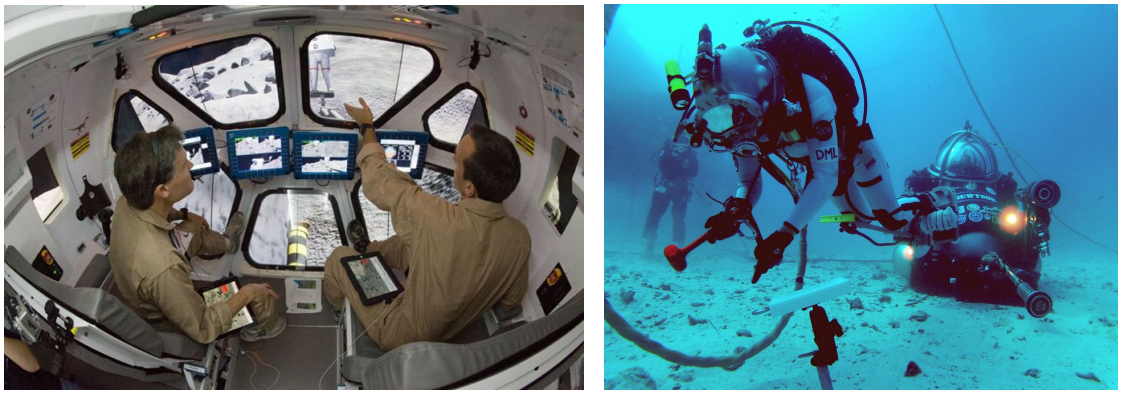

Credit: *NASA / ESA / Herve Stevenin*

Figure 1.29: Left: Two NASA Research and Technology Studies (RATS) 2012 test subjects inside the Gen 2A MMSEV while another performs a virtual reality spacewalk. Video walls displaying the NEA simulation can be seen through the windows. Right: NASA astronaut Dottie Metcalf-Lindenburger tests different ways to anchor to the surface of an asteroid on a simulated spacewalk on the ocean floor during the NEEMO 16 mission.

Obama White House had included $105 million to the NASA 2014 budget for the first year of its funding. However, in addition to the understandable engineering hurdles, the likelihood of the 113^{th} U.S. Congress funding even preliminary stages of this endeavor put the mission in doubt (Leone 2013). Nonetheless, there seems to be a push from the major space agencies and other government agencies for the continued development of capabilities to explore SSSBs.

1.2 Granular media research

Research into granular materials is pursued in a wide variety of scientific disciplines, including condensed-matter and solid-state physics (e.g., Chen 2008; Wang & Zhu 2008), soft-matter physics, geology (e.g., Ingale 2008; Moore & Iverson 2002), powder technology (e.g., Cowin 1974; Campbell 2006), agronomy (e.g., Sayre & Clark 1938; Lebron & Robinson 2003), and more recently the fields of planetary science and extraterrestrial geology (e.g., Sánchez & Scheeres 2011; Murdoch et al. 2012;

Schwartz et al. 2012c; Tancredi et al. 2012). The number of disciplines to which granular materials research applies highlights the importance of the field, however these disciplines can be poorly connected, having the consequence that developments in the field of granular materials can occur in isolation. These scientific communities remain largely segregated, in part because journals are often unknown or difficult to access between disciplines. Modest but important strides have been made to help bridge these gaps between communities by holding conferences where scientists with diverse research interests in this area can share developments and ideas (e.g., O'Hern 2013; Soto 2012).

1.2.1 Granular media on Earth

Granular materials research is increasingly relevant to the field of planetary science. Although good examples of extraterrestrial granular dynamics have been observed only very recently, here on Earth we have been witness throughout human history to the granular material processes that continue to shape our planet. Processes like landslides, erosion, and dune formation have forged the geology on the surface and continue to refresh it. The underlying morphology of the near-surface layers have been determined by plate tectonics. From a geological perspective, an understanding of granular media has lent insight into the ways that life on this planet has evolved, and it of course holds contemporary economic significance as well.

From the perspective of industry, granular processes are important to understand. Roughly half of all products in the chemical industry, for example (detergents, etc.), and at least 75% of the raw materials are in the form of granular solids (Nedderman 2005). Detailed working knowledge is required of granular materials involved in the agricultural industry for the harvesting, storing, transporting, and refining of grains, sugar, and other produce. The same applies to the construction

industry in regard to sand, gravel, asphalt, cement, and concrete. Civil engineers in earthquake-prone regions must consider the effects of seismic oscillations on their projects, while some consider using "granular dampers" tuned to the building's natural oscillation frequency to mitigate stresses (Nayfeh et al. 2002; Varanasi & Nayfeh 2003; Pestana & Salvati 2006). With the increasing exploration and utilization of tar-sands and fracking extraction methodologies in the energy industry comes new problems in collection and processing, and in the clean-up efforts from recent spills, which can differ greatly from classic oil spills due to the solid components of the bitumen (tar-sands oil) (Souraki et al. 2012). The pharmaceutical industry is one of many industries that require delicate programmed automation for the combination and packaging of many different types of granular compounds.

1.2.2 The complex state of granular material

Granular matter is of course in the solid phase, but it can take on fluid-like properties on macroscopic scales. For example, consider sand poured into a container, taking on the shape of the container in the manner of a liquid. Also, if the kinetic energy of the grains becomes large, then sustained contacts become infrequent and the material can take on gas-like properties; e.g., consider sparse granular material in a closed container being vigorously shaken—this material would occupy the volume of the container in a similar manner as would a gas. However, in both cases, there are important differences between these "granular fluids" and actual fluids: save for the effects of surface tension, liquids will minimize their gravitational potential energy before coming to rest, whereas grains will heap; and very much unlike an ideal gas, so-called "granular gases" will tend to cluster due to the energy dissipation that occurs during collisions (van der Weele et al. 2001). These two factors—granular matter's resistance to shear, and its inelastic collisions—are what give rise to much

of the complexities that warrant the entire field of study.

At first glance, the physics of granular material may seem simple and straightforward. Fundamentally, in regard to the example just given of liquid-like behavior, there is no qualitative difference, other than scaling, between this and meter-sized, irregularly shaped boulders filling an enormous container (perhaps on the order of kilometers). Indeed for grains on Earth that are larger than hundreds of microns, where van der Waals forces and phenomena like capillary action and the motions of molecules in the air (with or without a net wind) become relevant, this is an apt comparison (see Section 1.2.2.4 for a description of the forces of relevance to small grains). When grain sizes are large enough, granular dynamics is simply the study of the macroscopic effects that arise as a consequence of solid-body mechanics applied to many mutually interacting solid bodies. However, when we observe these macroscopic effects on Earth, we see incredibly varied, interesting, complex phenomena such as size-sorting in rock avalanches (e.g., Iverson & Vallance 2001), dune formation across different areas of the globe (Fig. 1.30 [top-left]), and sand-sheets and -ripples (Fig. 1.30 [top-right]).[16]

Sand-ripples are formed by wind and range in size; they can be tiny, with wavelengths (distance between adjacent crests) of a few centimeters, or large, with wavelengths of nearly 1 km (Harms 1969). Ripples are formed in materials ranging in grain size from silt to pebbles, and they can exhibit size-sorting: interiors can consist of thinly stacked layers, each layer made up of a particular grain size. The coarsest grains usually accumulate on crests, in contrast to avalanches and dunes, which typically have larger grains deposited away from their peaks (Goudie 2008 gives an historical accounting of how wind erosion has shaped desert landscapes on Earth).

[16]Many of these features also appear on Mars (Fig. 1.30, bottom).

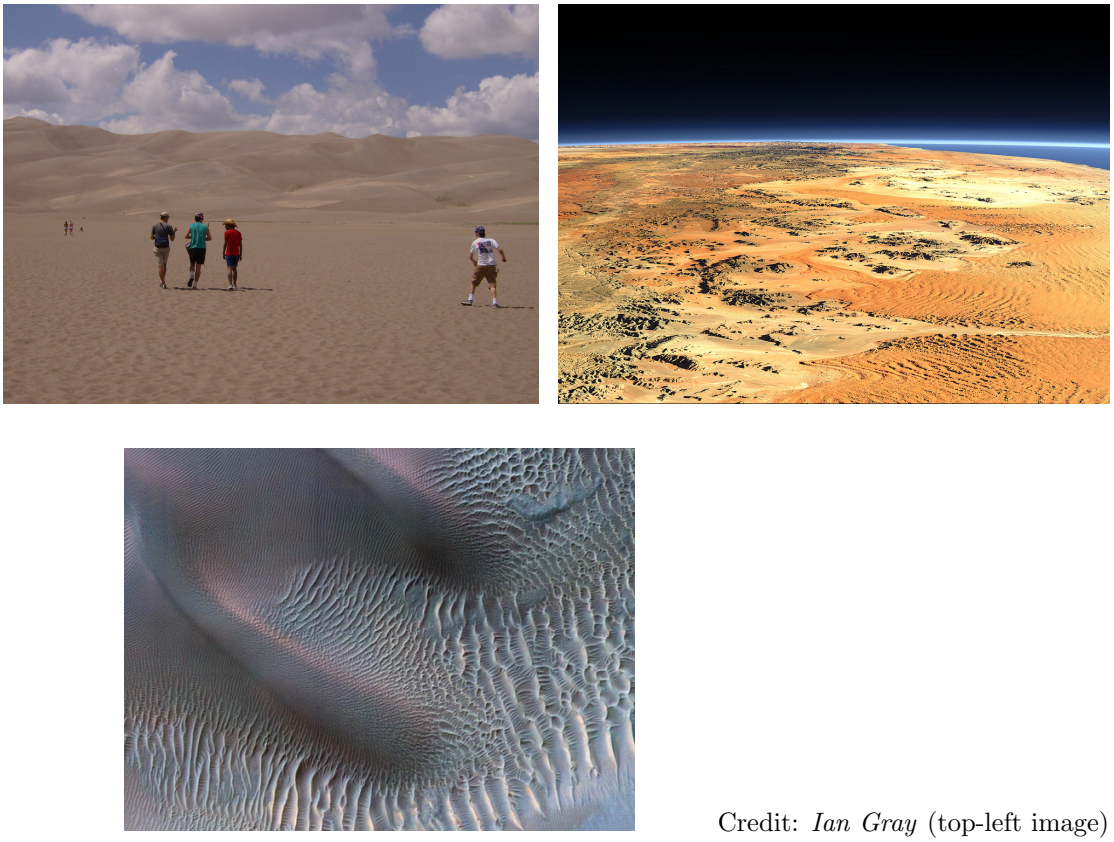

Credit: *Ian Gray* (top-left image)
Christoph Hormann 2006, "Views of the Earth" (top-right image)
NASA / University of Arizona (bottom image)

Figure 1.30: Top-left: The Great Sand Dunes National Park and Preserve in Colorado. Strong prevailing southwesterly winds carry tiny grains, originally from Lake Alamosa and the San Juan Mountains, across the plains ∼100 km before the winds die down at the Sangre de Cristo mountains (Madole et al. 2008). Occasional storm winds from the other direction help the grains to grow vertically. Although smaller dunes can move around at a rate of meters per week, the regularity of the wind patterns over time has built up dunes covering more than 80 km^2, reaching as tall as 250 m. The process is estimated to have begun about $4x10^5$ yr ago. Top-right: The Namib Desert in southern Africa. With an annual water precipitation of only 2 mm in some parts, and endured arid conditions for about $7x10^7$ yr, the Namib is the oldest desert in the world. It has striking granular features like sand-sheets near the coast, and a dune region 32 km wide with dunes 300 m tall. Bottom: Dunes and ripples in a variety of shapes, sizes, and orientations in the Noachis Terra region of southern Mars. This enhanced-color MRO image shows the distribution of these features, themselves determined by changes in wind direction and strength, which aids in the study of ongoing Martian geologic processes.

1.2.2.1 Laboratory experiments in granular media

Laboratory experiments constructed to research the complex nature of grain motions are extensive. Just a few representative examples of some of these studies are given below; they include characterizations of granular vortices, granular force networks, the failure of energy equipartition, granular crystallization, grain motion dependence on an ensemble's packing and flow history, and the qualities of flows in microgravity.

Vortex patterns have been observed experimentally in vertically vibrated granular rods (Blair et al. 2003). Above a critical packing fraction, moving ordered clusters of nearly vertical rods spontaneously form and coexist with horizontal rods. Over time, rods orient vertically and form large vortices.

Very different from molecules, stresses are spread very unevenly through granular media, typically along lines of force, which branch off and join together at different points. Only a small fraction of grains may be supporting most of the pressure at a given moment in time. Many will feel almost no pressure from surrounding grains (Fig. 1.31). This is the case even in a collection of monodisperse grains (Fig. 1.31 [right]; see also Section 2.3.4 for the results of a study on hopper discharge contained in this work).

Losert et al. (1999) observed the breakdown of energy equipartition in polydisperse "granular gases" (experiment discussed in Section 1.2.2.3). Berardi et al. (2010) find through experiment that dense ensembles of chrome spheres spontaneously assemble into regions of local crystalline order in a quasi-two-dimensional driven system (Fig. 1.32). They also find highly cooperative, string-like, motion in the boundary regions of the ordered groups. The addition of small particles to the granular gas allows the scale of this collective motion to be controlled. The number of these "granular strings" is found to increase with the concentration of small particles (presumably, there is a concentration that maximizes the appearance of

strings, although this is not addressed in their work).

Using a Taylor-Couette shear cell, Toiya et al. (2004) find that the prior direction of shearing flow affects strongly how a granular shear flow initiates. If the shear direction is reversed, the material goes through a transient period during which the shear force is small due to dilatency effects, and the shear band is wide while the material compacts.

Murdoch et al. (2013) conducted experiments using a shear cell of Taylor-Couette-type under the conditions of parabolic fight micro-gravity to show that gravity plays an important role in the dynamics of sheared, dense granular flow. They find that radial flows are strongly affected by the presence of a gravitational field: the flows become larger in magnitude as gravity increases, and disappear altogether in micro-gravity. They propose that gravity determines the extent of the particles' frictional interactions with each other and with the walls of the cell, which in turn incite the convective secondary flow. Without a gradient in friction, or with low friction, the secondary flow is halted.

1.2.2.2 Shear strength

The heaping that occurs in granular material is due to its resistance to shearing, which is the most essential property of grains that distinguishes them from a fluid. The shapes of the grains physically impede their neighbors from flowing around them to a lower energy state. The macroscopic effect is a pile of granular material with an angle of repose that is characteristic of that material. The angle of repose depends not only on the bulk shapes of the grains, but on the other material properties that dictate the frictional forces to which they are subject. A stack of perfectly smooth, frictionless cannonballs can be stable simply because of their rigid shapes (so long as the bottom plane is fixed). Friction is not required to maintain a nonzero angle

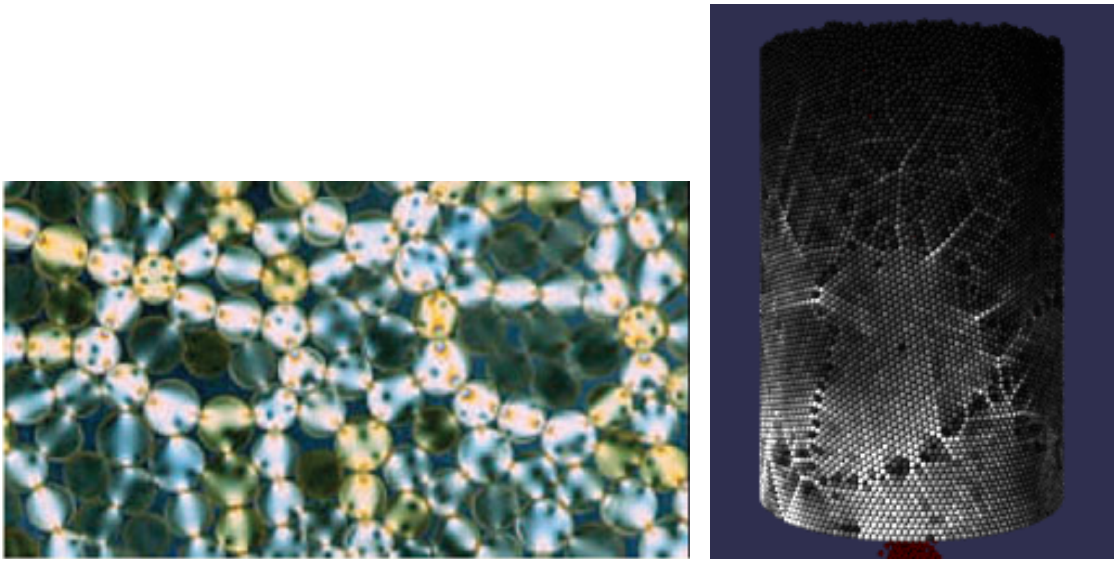

Credit (left image): *Van Hecke (2005)*

Figure 1.31: Left: A force network, typical of granular media, revealed in a layer of laboratory-manufactured photoelastic disks. The bright disks are experiencing the largest forces, and appear to align in "force-chains." Right: A snapshot from one of my simulations (cf. Chapter 2), showing a container of 50 cm radius, filled with monodisperse grains of 1 cm radius discharging through an opening at the bottom, 10 cm in radius. The lighter-colored particles are those feeling the most stress (red particles barely visible at the bottom feel no net force as they are in free fall). Mature force networks along the sides of the container form a few seconds after flow is initiated and continue to evolve during discharge. The monodispersity in grain size allows for large regions of efficient packing to develop. Stresses are communicated between these regions through strong force chains. This snapshot shows the force networks at the sides of the container 11.25 seconds after the onset of discharge in Earth-normal gravity.

of repose, however friction can increase this angle (Zhou et al. 2002; Richardson et al. 2012a). It is essentially from this fact—that material at the grain-scale shows resistance to deformation under confining pressure—that our ability to walk on sand arises.

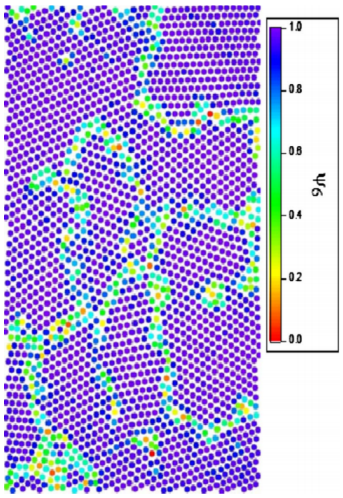

Credit: *Berardi et al. (2010)*

Figure 1.32: Based off of particle positions measured during a granular experiment, then entered into a computer for visualization, this rendered image illustrates how grains of equal sizes tend to order themselves into crystalline structures. Chrome spheres of 3 mm and 2 mm (97% and 3% by number, respectively) are densely packed into a quasi-two-dimensional circular container 3.1 mm in height and 146 mm in radius. The system is oriented horizontally and shaken vertically at 125 Hz with peak acceleration equal to 4.5 times Earth's gravity. This produces a hot granular gas, which, initially mixed, segregates itself into heterogeneous configurations to achieve better packing. Particles in this rectangular region of the experiment are colored according to a dimensionless measure of their hexagonal-close-pack (HCP) crystallization, Ψ_6, which ranges from 0.0 (least ordered, red particles) to 1.0 (most ordered, purple particles). (See Reis et al. 2006 for an explanation of how this measure of order is determined.) Granular "strings" (a line of grains in cooperative motion) are sometimes observed along grain-boundary regions.

1.2.2.3 Granular temperature and granular gases

A "granular temperature" can be defined in multiple ways, but essentially it is a measure of the average of energy fluctuations exhibited by a collection of grains. An example of one such definition, for a collection of N grains of average velocity $\bar{\mathbf{v}}$ and average spin $\bar{\boldsymbol{\omega}}$, with each grain having a mass m_i, velocity $\mathbf{v}_i$, moment of inertia I_i, and spin $\boldsymbol{\omega}_i$, the granular temperature is

$$T_g = \frac{1}{2nk_B} \sum_{i=1}^{n} \left(m_i \left| \mathbf{v}_i \right|^2 + I_i \left| \boldsymbol{\omega}_i \right|^2 \right). \tag{1.1}$$

This quantity does not include, but is analogous to, the thermodynamic temperature (Walton & Braun 1986). It bears repeating that granular dynamics is the study of the macroscopic phenomena that arise from solid-body dynamics of many bodies, and, as such, it can be appropriate to define and make use of quantities that are analogous to established physical quantities of a different scale.[17]

The use of this concept is ubiquitous in the literature after first appearing in Ogawa (1978). As a typical example, which emphasizes the differences between a molecular gas and a granular gas, Losert et al. (1999) performed an experimental study of the velocity statistics in excited granular media using a partial layer of inelastic, colliding beads driven by a vertically oscillating boundary that provided accelerations of 3–8 times Earth's gravity over multiple experiments. They defined the granular temperature as the mean square particle speed (rotations were likely relatively low and difficult to measure), and found that it varied with particle density, and exhibited a maximum at intermediate densities. This implies that there exists some critical density where confined grains, externally driven, are "hottest." Also, the more massive particles were found to have greater kinetic energy. This last finding highlights an important quality of granular dynamics, namely the inelastic nature of intergranular collisions. If it were a molecular gas, and a "real" temperature, this would violate the laws of thermodynamics.

Along these lines, the so-called "Maxwell's Demon" thought experiment, described in 1871 by James Clerk Maxwell, consists of a demon capable of separating slow-moving molecules from fast molecules in a gas, in order to create a hot compartment and a "cold" one. This would of course violate the second law of

[17]Strictly speaking, thermodynamic temperature is a macroscopic quantity as well, but it arises directly from energies on the microscopic scale, whereas granular temperature arises from average energies of collections of bulk solids (grains), which are not on the microscopic scale.

thermodynamics, but as van der Weele et al. (2001) show, a granular gas, driven at the correct frequency, can do just this (however, there is no violation because the system is not closed if it is being driven).

1.2.2.4 Van der Waals forces

Intermolecular forces between grains of modest size are typically governed by gravity and the contact forces (an electrostatic force). However, when the grain sizes are sufficiently small, short-range intermolecular forces become more relevant. This is because the van der Waals forces scale with grain size in a different manner than the gravitational force does (see below). In a uniform gravitational field, the force of gravity felt by a grain (its weight, W) will scale as its radius, s, as $W \propto s^3$.

A useful representation of the strength of a non-gravitational force used in granular dynamics is the so-called "bond number," which gives the ratio of the considered non-gravitational force to the gravitational force felt by the grain. Taking the non-gravitational force to be of the form $F = Cs^n$ (Scheeres et al. 2010):

$$B \equiv \frac{F}{W}, \tag{1.2}$$

$$= \frac{3C}{4\pi\rho a_g} s^{n-3}, \tag{1.3}$$

where C is a constant with units of [mass][length$^{(1-n)}$][time$^{(-2)}$], n gives the dependence on s of the non-gravitational force under consideration, W is the weight of the grain, ρ is the density of the grain, s is its radius, and a_g is the acceleration due to gravity.

The van der Waals force is a general and somewhat loosely defined term used to account for attractive intermolecular forces, excluding ionic and covalent forces. There is some equivocation in regard to which forces are considered to be part of the van der Waals set. The prototypical van der Waals force is known as the London dispersion force, described next.

The electric field around an atom or molecule exhibits small-scale fluctuations in time and space (London 1936). Therefore, noble gases and nonpolar molecules will show spherical asymmetry in their charge distributions at a given instant in time. If this, say, helium atom shows a slightly more negative charge to a second helium atom than this second atom is showing to the first, then a temporary dipole can be induced in this second atom, which will reflect back at the first with an opposite charge. This is called the London dispersion force, and is the reason why helium can enter the liquid state; it is an instantaneous dipole-induced dipole force. Other forces that are commonly fit under the heading of the van der Waals type include (permanent) dipole-induced dipole and dipole-dipole forces, both of which are stronger than London dispersion forces, typically by about an order of magnitude, or more, in the case of permanent dipoles. Hydrogen bonding is a specific type of dipole-dipole force, often omitted from the van der Waals grouping. Hydrogen is not an especially electronegative atom, and so it tends to be attracted to exposed valance electron pairs of electronegative atoms like fluorine, chlorine, and oxygen. Hydrogen bonding is important to the cellular function of life on Earth due to cells' complex organic compounds with their extensive and varied hydrogenation (a large molecule can even bend around and exhibit hydrogen bonding with itself, effecting different physiologic properties), but it can also be important to the dynamics of small grains.

The van der Waals attraction between two spherical particles of equal radius, s, is (Hamaker 1937):

$$F = \frac{A_h}{12X^2}s, \tag{1.4}$$

where A_h is the Hamaker constant (typically of order 10^{-20}–10^{-19} J), and X is the separation between the particles' surfaces. So these van der Waals-type forces increase linearly with grain radius (assuming the effective separation remains con-

stant), which, for example, explains why the boiling point of neon is higher than that of helium. But recall that the weight of a grain scales as the cube of its radius. This means that as grain size decreases, both the net van der Waals force and the gravitational force decrease, but the gravitational force drops off much faster. Putting this into Eq. (1.3), it is clear that as the size of the grain decreases, the van der Waals force will become increasingly relevant and eventually dominate over the gravitational force. For typical values on Earth, these forces need to be considered when grain sizes are hundreds of microns or less, and become dominant for grains of size ~ 10 microns or less (Castellanos 2005) when bond numbers begin to exceed unity. However, using appropriate values in Eqs. (1.3) and (1.4) van der Waals forces should be considered for rocks up to meters in size in micro-gravity.

1.2.2.5 Homogenization theory for use in analyzing granular dynamics

Granular physicists attempt to classify the macro-behavior of granular materials in terms of micro-quantities. To this end, continuum theories have been developed that attempt to treat granular media not as discrete grains, but effectively as continuous solids. Continuum mechanical properties like Poisson's ratio and the bulk, Young's, and shear moduli are derived from assuming homogeneity in solids on the smallest of scales. In numerical modeling of granular material (Section 1.2.3), these properties are essential to continuum modeling of entire granular systems (Section 1.2.3.1), and for the modeling of individual grains in discrete soft-sphere methods (Section 1.2.3.5), such as the one developed in the present work (Section 2.1).

There is ambiguity in the literature regarding the delineation between continuum theories and homogenization theories. Here, a "continuum theory," or, later, when computation is discussed, a "continuum numerical approach" when applied to granular media should be taken in the broadest sense: the treatment of granular ma-

terial as a continuous solid, as contrasted with discretized theories and approaches. Homogenization is a process that translates unwieldy physical properties into useful empirical quantities. Average-field theories of linear continuum mechanics are attempts at homogenization. Classical fluid mechanics is a continuum theory, and is sometimes, but not always associated with the term homogenization.

John Hunter at the University of California, Davis campus describes homogenization theory in the following way: *"Homogenization theory is concerned with the derivation of equations for averages of solutions of equations with rapidly varying coefficients. This problem arises in obtaining macroscopic, or 'homogenized' or 'effective', equations for systems with a fine microscopic structure. Our goal is to represent a complex, rapidly-varying medium by a slowly-varying medium in which the fine-scale structure is averaged out in an appropriate way."*

Homogenization theory considers a volume of material and asks for certain quantities (e.g., quantities that describe the manner of the stress that the material is feeling and quantities that describe how it reacts those stresses). None of the complexities of the material are relevant to the theory, except in so far as they may influence the quantities of the specific homogenization technique. The volume under consideration is essentially a "black box." That is, we ignore the actual material inside and concern ourselves only with specific quantities that come out, i.e., its effective macroscopic behavior.

This relates to the way that granular dynamics has been described in this discussion (Section 1.2.2). One doesn't need to know the detailed history of each individual grain of sand; one wants to know the overall effects. This is a powerful approach in that it greatly simplifies intractable problems that may otherwise involve an overwhelming number "of equations with rapidly varying coefficients." But with each homogenization technique, one must always be careful to consider what

assumptions are being made and what important factors may be being overlooked.

1.2.2.6 Granular dynamics treated as fluid dynamics

Haff (1983) made an attempt to address a problem in granular dynamics by adapting fluid dynamical equations to represent a granular medium. By treating individual grains as volumes of fluid, various Couette-type problems were solved analytically. The standard continuity and momentum equations (conservation of mass and conservation of momentum, respectively) were used along with the energy equation, which is necessary to account for the inelastic collisions in granular material.[18] Simple kinetic models were invoked for deriving expressions for the "coefficients" of viscosity, thermal diffusivity, and energy absorption due to collisions. The coefficients varied as functions of the local state of the medium, dependent upon the local granular temperature (Eq. (1.1)) and the density. In order to solve these equations analytically, the resulting equations needed to be linearized, which is only applicable in dense media where the spacing between grains is small in comparison to the grain sizes (otherwise the linear approximation doesn't hold). The fluid model of this granular medium created by Haff (1983) had many limitations, but it was one of the first complete attempts to address a problem in granular dynamics as one of fluid mechanics.

With the aid of computers, much more sophisticated adaptations of fluid dynamics have since been developed to "correct" for the discrete nature inherent in granular dynamics. To the extent that the relevant macroscopic effects arising from the interactions between irregularly shaped grains, including the contacts and void

[18]Recall the implicit analogy of the granular gas given at the beginning of this section, which emphasizes the importance of inelastic collisions as one of the two salient differences, along with shear strength (Section 1.2.2.2), between granular dynamics and fluid dynamics.

spaces between them, can be codified into these continuum theories, they can have great predictive power. In the realm of numerical computation, many of these theories have been applied to integrate a granular system forward along time derivatives that depend upon the time-varying state of the system. The results of a continuum code will only be as good as its ability to account/correct for the discontinuities that arise as a result of the discrete nature of granular media (e.g., energy drain and jamming effects).

1.2.3 Numerical research into granular materials

With advances in computer hardware and software, numerical modeling has become increasingly useful for the study of granular systems. In fact, numerical approaches have been crucial to our understanding of, for example, scaling laws.[19] Different approaches exist to perform modeling of granular materials; for a comprehensive review, see Mehta (2007).

A useful way to understand the different types of numerical approaches is to first divide them into the broad categories of continuum and discrete. Just as laboratory experiments and numerical simulations have their relative advantages and disadvantages, in the realm of numerical simulation, continuum approaches and discrete approaches have their advantages and disadvantages. In general, discrete approaches attempt to treat material as individual particles, perhaps with large particles as proxies for groupings of smaller particles. Continuum approaches average the physics of nearby particles, and use smooth transitions to account for variance. Much has been and will be learned by using both methodologies, each having their

[19] "Scaling laws" address how various parameters—such as crater diameter or depth in an impact experiment—scale quantitatively with others. In extreme physical regimes where experiments cannot be easily conducted, numerical simulations can be used to try to examine these dependencies.

strengths in different physical regimes.

For the most part, I have been taking the discrete approach in my numerical work to investigate aspects of granular material in the Solar System. Although, in order to help put this methodology into perspective, I will briefly explain some of the basic principles behind continuum approaches in Sections 1.2.3.1 and 1.2.3.2.[20] In Sections 1.2.3.3–1.2.3.5, I will discuss the treatments of granular materials that use discrete methodologies. Next, in Section 1.2.3.6, I will compare the continuum and discrete treatments of granular materials. For many numerical applications of granular dynamics, cohesion must be addressed as well; this will be discussed in Section 1.2.3.7. Finally, in Section 1.2.3.8, I consider numerical applications to planetary science where collisions, and forces other than just gravity, must be taken into account.

1.2.3.1 The continuum approach to numerical simulation

An alternative to treating all particles separately (the discrete approach) is to average the physics across many particles and thereby treat the material as a continuum. The starting point to the continuum approach is to divide a parameter space or dimensional space into regions and to follow the relevant conservation laws. At minimum, these should include mass conservation (for each region, the mass that leaves must be equal to the mass that enters), momentum conservation (Newton's second law, that the change of momentum on material in a region must equal the net impulse—force applied over a given period of time—on material in the region), and the conservation of energy together with the first law of thermodynamics (en-

[20]The differences between the discrete and continuum approaches are emphasized here in order to help highlight some of the numerical subtleties. There are codes, however, that use these numerical approaches in conjunction, such as Grof et al. (2009), Wachs (2009), and Han & Cundall (2012).

ergy may change forms, but the sum of all forms of energy must remain constant, including gravitational and chemical potential energy, kinetic/heat energy, etc.). These regions may be described in Eulerian terms, where a volume in space is held constant, with material passing in and out of this volume, or in Lagrangian terms, where a region is described by the material itself as it moves around in space (e.g., see Springel & Hernquist 2002 for a fully conservative derivation of a Lagrangian treatment in a smoothed-particle hydrodynamics (SPH) code). The numerical viscosity problems that stem from continuum codes (see a discussion below in Section 1.2.3.2) are somewhat easier to mitigate in Eulerian approaches (Springel 2010), whereas the principle advantage to the Lagrangian approach is that the resolution of the system adjusts automatically to the movement of the material. Sophisticated codes that use hybrids of Eulerian and Lagrangian descriptions, together with complex physical laws and computational parameters, have been developed (see Monaghan 1988 for an early historical perspective).

In the modeling of granular media, the continuum approach usually treats the material as a deformable solid and models it with some chosen finite-element (e.g., Crosta et al. 2009) or mesh-free (Lagrangian) method suited for the particular situation at hand (e.g., Elaskar et al. 2000). Depending on the system, the continuum approach may treat the material as a fluid and use computational fluid dynamics. However, grains have sharp discontinuities that pose many challenges when taking a continuum approach, and thus the homogenization of granular-scale physics is not necessarily appropriate for capturing the discrete nature of the particles and the forces between them (and the forces between them and their wall-boundaries, e.g., Wada et al. 2006). If the goal of a given simulation is related to capturing the discrete nature of individual particles or if this nature has important effects on the outcome, then the effects of such homogenization must be examined thoroughly.

Haff (1983), in his article describing his efforts to treat granular media as a fluid analytically (Section 1.2.2.6), considers many of the potential hazards and payoffs of using fluid dynamics from his analytical approach. These same considerations that arise analytically (i.e., the sharp boundary conditions on grain surfaces, including the complex frictional forces at play on these surfaces), also arise numerically.

1.2.3.2 Numerical viscosity

Numerical viscosity has been a known problem for continuum models since von Neumann & Richtmyer (1950). The effect of numerical viscosity comes from the use of a homogenizing assumption in the elements or control volumes underlying the approximation scheme. To illustrate: in a given timestep, when momentum is exchanged between neighboring elements through convection, the resulting contributions to a given element in the simulation are added to the previous value to arrive at a new value of average momentum over that element. This homogenization introduces a smoothing effect. (Essentially, it is the averaging together of these momentum contributions that accounts for the homogenizing process as related to velocity). When another timestep is taken, this new value is then passed on to the next element in the direction of motion. The accumulation over many iterations of this smoothing operation contributes to a "diffusion" of momentum in the direction of flow. Although diffusion can be the desired behavior, it is a numerical effect dependent upon the choice of computational grid resolution and timestep (Powers 2004). In addition, numerical viscosity makes it hard to follow shock fronts without an explicit shock-capturing scheme (which are more easily implemented in Eulerian approaches, giving them an advantage over, e.g., SPH when shocks are important).

There have been significant advances in continuum coding approaches that mitigate some of the problems of numerical viscosity. Recent attempts at combining

fluid mechanical approaches with continuum mechanics (fluid flow with yield criteria) have had recent success in simulating split-bottom cells, such as Couette shear cells (Henann & Kamrin 2013). The approach relies upon an assumption that the dependence of the shear stress divided by the confining pressure (analogous to friction coefficients that depend on the normal force in basic dynamics) is a function of the so-called inertial number, I, where

$$I = 4\,|\dot{\boldsymbol{\epsilon}}|\,\sqrt{s^2}\rho/\,|\mathbf{F}_N|\,, \tag{1.5}$$

and where $\dot{\boldsymbol{\epsilon}}$ is the strain-rate, s and ρ are the radius and density of the grain, respectively, and $\mathbf{F}_N$ is the normal force. This can be rearranged to give the strain rate as a function of the shear stress and normal force, along with material constants. Staron et al. (2013) used this relation in simulations of 2-dimensional hopper discharge, giving satisfactory results (this work is touched upon again in Section 1.2.3.6).

1.2.3.3 The discrete approach to numerical simulation

The discrete-element method (DEM) is a general term applied to the class of discrete approaches to the numerical simulation of particle motion, where particles typically represent actual grains (or collections of grains), unlike the continuum approach that uses averages to homogenize the material. In the standard implementation, particles are approximated as having perfect spherical geometry (more complex geometries are also possible). DEM computes the motion of large numbers of individual (spherical) particles. It is relatively computationally intensive, which tends to limit either the length of a simulation or the number of particles in the simulation. DEM numerical codes are typically carried out by way of hard-sphere (HSDEM) or soft-sphere (SSDEM) particle dynamics.

1.2.3.4 The hard-sphere discrete-element method (HSDEM)

The numerical approach to solving the equations of motion in HSDEM is to discretize the simulation in time, with variables progressing in small steps (timesteps) by forward advancing along derivatives. Collisions are predicted in advance in HSDEM by analyzing particle motion and checking for potential contacts that will occur within the current timestep. Spheres are not allowed to penetrate each other (overlaps are not allowed). HSDEM codes carry out collisions between spheres by treating collisions as instantaneously occurring at a single point of contact that lies on the particles' surfaces. Thus this methodology treats motions and mutual interactions of non-deformable, indestructible (hard) spheres. The assumption of hard spheres allows collisions to be carried out analytically, with post-collision velocities and rotations given by, e.g., Richardson (1994).

The collision handling does not drive the timestep. Since collisions are predicted in advance and then treated as instantaneous, the external dynamics (e.g., gravity) dictates the step size. Although the timestep may also be limited by concerns over missing a collision, having collisions predicted in advance allows HSDEM codes the advantage of accommodating large time steps, which in turn dramatically increases the speed of a simulation. Increased speed allows for the use of more particles and for the simulations to be integrated out further in time. In dense regimes, however, the speed of the integration is typically limited by collisional bottlenecks owing to the fact that collisions must be computed one at a time. This is because HSDEM generally does not support simultaneous collisions, which limits the efficiency of parallel processing.

Collision prediction can also prove to be computationally difficult in HSDEM, especially in the common case of collisions between particles and boundary surfaces (walls) with complex geometries and/or motions. This problem is exacerbated when

trying to incorporate particles with shapes that deviate from spheres (this would also require the use of Euler's rigid-body equations; see, e.g., Richardson 1995). Another drawback of treating collisions between particles as instantaneous, is that this discounts the fact that during the finite amount of time that it takes for two real particles to collide, they are in contact exchanging energy and momentum. In sufficiently dense regimes, a third particle may intrude on this collision by making contact with either particle or with both particles, changing the outcome. Since multiple contact effects are not taken into account in HSDEM, where collisions are separate and instantaneous, its use is therefore more appropriate in dilute regimes, where collisions almost exclusively involve only two particles. However, even in 2-body collisions, HSDEM can make errors. Consider the unit normal vector $\hat{\mathbf{n}}$, which gives the direction from a particle's center-of-mass to its colliding neighbor particle's center-of-mass. This vector can rotate significantly during realistic, finite, oblique collisions—an effect not taken into account in standard hard-sphere approaches, altering the outcome of the collision (Müller & Pöschel 2012). Attempts have been made to use HSDEM with added analytical corrections to account for rotations of the 2-body system while particles are colliding (Müller & Pöschel 2013), and to account for finite collision times (by "pausing" collisions). These are most effective in regimes when (third-) particle intruders can be safely ignored.

Despite its drawbacks, HSDEM can be the appropriate choice in certain dilute/ballistic regimes (cf. Richardson et al. 2011), where it is advantageous over continuum models for its speed and accuracy, and over SSDEM for its speed given its ability to handle large timesteps. For the simulation of dense environments, however, including many granular regimes in which grain deformation, multicontact physics, and the complexity of frictional forces during contact cannot be neglected, SSDEM is the better choice.

1.2.3.5 The soft-sphere discrete element method (SSDEM)

SSDEM is commonly used in the study of granular materials,[21] and has often been applied to industrial problems (e.g., Tsuji et al. 1992; Cleary & Sawley 2002; Kosinski & Hoffmann 2009). SSDEM treats particles as deformable spheres, allowing overlaps between particles to act as proxies for actual deformation. Particles are taken to be in contact if and only if their surfaces are touching or mutually penetrating. The greater the extent of this penetration, the more repulsive force is generated. The majority of codes either assume a linear force dependence or a Hertzian dependence on penetration depth ($F \propto x$ or $F \propto x^{3/2}$, where x is the penetration in units of length). Once a contact is established, particles are subject to frictional forces often making use of material parameters based on continuum mechanical theory; these forces will vary depending on the specific SSDEM code (see Radjaï & Dubois 2011 for a comprehensive overview on the different classes of SSDEM codes and common variations). Collisions typically require dozens of timesteps to resolve, thus timesteps in SSDEM can often be smaller than those used in identical HSDEM simulations by factors of 10^2.

Although SSDEM has the advantages of accuracy, versatility, and not requiring collisions to be predicted in advance, it comes at the expense of much smaller integration timesteps, which can limit the integration timescale. On the other hand, because it can be implemented into a code that is fully and efficiently parallelized, as was accomplished in the present work, presently it is possible to follow the evolution of millions of particles over a fairly large range of conditions, which is not possible with HSDEM. Further description, along with the specific implementation used in

[21] SSDEM is also used in other disciplines of physics under the name of Molecular Dynamics (MD), computing the motions of atoms and particles. In fact, this application and nomenclature predates SSDEM for use in a granular physical context (Alder & Wainwright 1959).

this work is found in Chapter 2.

As a direct comparison of the two collisional methodologies, simulations of low-speed rubble pile collisions were performed using both SSDEM and HSDEM in the same numerical code (Richardson et al. 2012b). In the tests, self-gravitating rubble piles (without friction or cohesive forces) were collided together at low speed. The results from the two collisional routines were generally similar. SSDEM often, but not in all cases, showed a somewhat higher final ellipticity of the largest collisional remnant, suggesting a higher shear strength that may arise from its more careful treatment of contact forces and finite collisional times.

1.2.3.6 DEM vs. continuum approaches

Continuum codes in general are inherently conducive to parallelization, especially fixed-grid continuum codes. Several DEM codes also take advantage of parallel processing capabilities to scale up the number of particles or length of the simulation (e.g., Richardson et al. 2000; Cleary & Sawley 2002; Kacianauskas et al. 2010; Schwartz et al. 2012c). HSDEM codes that have to compute collisions one at a time face more challenges in this regard, whereas SSDEM codes, like continuum codes, can accommodate true parallelization.

A study was performed by Richardson et al. (2005a) using HSDEM to compare the results of rubble pile equilibrium shapes in simulation to continuum theory. Due to the non-zero angle of repose exhibited by granular material, which is the case even when the grains are cohesionless and support no tangential friction (see Section 1.2.2.2), "perfect" rubble piles (no cohesion) can maintain non-spherical shapes without bulk spin, unlike a fluid. Rubble piles can also spin faster than a perfect fluid before shedding mass. Investigated were the shape and spin limits of self-gravitating rubble piles that consist of identical HSDEM particles and no sliding friction, and

this entirely discrete approach was found to be consistent with the theory for the more general continuum rubble-pile model as analyzed by Holsapple (2004). Rubble piles that reassembled following a catastrophic disruption reconfigured themselves to lie within stability limits predicted by the continuum theory. In the Holsapple model, the Mohr–Coulomb (MC) prescription was used to describe pressure-dependent yield to obtain rubble pile stability limits; later, the same analysis was performed using the Drucker–Prager (DP) relation giving very similar results (Holsapple & Michel 2006). As an additional follow-up to these continuum studies, a comprehensive analysis was performed that extended the continuum theory for (cohesionless) rubble piles to give an upper bound on actual load limits of bodies with cohesion (Holsapple & Michel 2008). To compare with these results, preliminary work was performed that included gravitational aggregates with and without cohesion using a portion of the numerical tools described in Chapter 3 (Richardson et al. 2008). This work expanded upon the discrete numerical work of Richardson et al. (2005a). More recently, SSDEM has been used to analyze equilibrium shapes of rubble piles without the use of cohesion, also finding agreement with the Holsapple analyses (Sánchez & Scheeres 2012).

Jiang et al. (2013) conducted two identical simplified braced excavation[22] simulations in granular ground, one using SSDEM, and the other using the Finite Difference Method (FDM), a continuum code that uses MC and DP models, to check their applicability. The results indicated that the DEM simulation was capable of reproducing the main responses of a "granular ground" during excavation. Two types of

[22]In practice, a braced excavation involves isolating a specific underground region for excavation by placing boundaries that extend from the surface to some specified depth. These boundaries, or diaphragm walls, are braced at the top by horizontal struts while material in the region is removed. The bracings are placed to protect nearby buildings and underground pipelines adjacent to deep excavation sites. It is crucial to estimate the deflection of the diaphragm wall and the extent of surface settlement in braced excavation in advance as a way of risk management.

stress paths in front of and behind the wall were observed, and obvious principal stress rotations of soils were recognized. Compared with DEM results, MC and DP models can generally be used to predict excavation responses qualitatively but they under-estimate the ground deformation and internal forces on the wall. This is due to the inability of the two continuum models to capture the mechanical behavior of granular material under complicated stress conditions in braced excavation. Based on these observations and comparisons, the authors offered features to be considered for future MC and DP continuum models, including stress-path dependency and shear dilatancy.[23] These issues can be addressed in continuum coding, but must be added explicitly to MC and DP models for granular material.

The Staron et al. (2013) study mentioned in Section 1.2.3.2 included a qualitative comparison between continuum and discrete numerical approaches. The continuum approach consisted of a Navier-Stokes solver that used the stress dependence on inertial number, I, given in Eq. (1.5), to model viscous behavior. The discrete method used was a Contact Dynamics algorithm, a type of hard-sphere approach (Radjaï & Richefeu 2009). Discharges of granular hopper silos were simulated in 2 dimensions from the early stages of the discharge until complete release of the material. Both cases recovered the so-called "Beverloo correlation" (see Section 2.3.2) and were able to reproduce the correct qualitative behavior with good agreement in regions of rapid flow. However, slow, staggered creep was not entirely captured by the continuum model.

In general, SSDEM approaches are inherently well suited to capturing the discrete nature of granular systems, and tend to rely upon fewer free parameters to reproduce the correct behavior of many granular systems. Also, typically continuum codes have a difficult time conserving angular momentum due to the effects

[23] A shear-dilatant material is one in which viscosity increases with the rate of shear strain.

of numerical viscosity. This can particularly be a problem in certain planetary science applications when considering isolated bodies in space. However, in comparison with the continuum approach, DEM is not well suited to the treatment of supersonic motion, particle fragmentation, or phase-changing material.

1.2.3.7 Cohesion in DEM

The inclusion of cohesion in numerical coding may be adapted to many different granular dynamics applications. For example, it may be used to treat ionic or covalent molecular bonds, the weaker intermolecular bonds, e.g., van der Waals forces (Section 1.2.2.4), or electrostatic forces. A number of codes have been developed in the general field of cohesive granular systems. For instance, Richefeu et al. (2009) used a 3-D DEM approach with spherical particles supplemented by a capillary force law[24] to model the overall cohesion of wet granular materials. Also using a discrete-element approach, Delenne et al. (2009) introduced a local cohesion law that accounts for the transition from capillary to cemented bonding in granular materials partially saturated with an aqueous solution. Radjaï et al. (2010) treated the solid binding matrix filling (fully or partially) the interstitial space in a cohesive granular media by using a Lattice Element Method, which was based on a lattice-type discretization of the particles and material matrix.

Recently, Sánchez & Scheeres (2013) performed a simulation using two spherical, meter-sized particles (boulders) with small ($\sim$ few cm) cohesive particles (regolith) between them, and measured the force necessary to pull the large particles apart.

[24]The capillary force law is a result of hydrogen bonding, a specific type of dipole-dipole interaction (see Section 1.2.2.4). It is referred to by some as a form of van der Waals force; it is effectively a repulsive force stemming from the fact that polar molecules are more attracted to other polar molecules than they are to nonpolar atoms and molecules.

The cohesion conforms to Hamaker's generalized van der Waals force law for interacting spheres, Eq. (1.4). These intermolecular cohesive forces, of regolith especially, may be of importance in low-gravity environments (see Section 1.2.2.4), and could be helpful to explain the rotation rates of some of the smallest SSSBs catalogued by Pravec et al. (2005), and more recently, Statler et al. (2013). It is beyond doubt that many fast rotators spin in excess of their gravitational break-up limits. Some could be monoliths, but, through use of a portion of the numerical tools in the present work (outlined in Section 3.2.1), it has been shown that a small amount of cohesion is sufficient to explain these rotation rates (Richardson et al. 2008, 2009b).

1.2.3.8 Numerical modeling of granular systems in low-gravity environments and in the field of planetary science

Numerical continuum approaches to granular dynamics in the field of planetary science have been in use for many years (e.g., Holsapple 1992). They have since grown significantly in sophistication (some in current use for the modeling of asteroid shapes and the scaling laws for disruption are, e.g., Holsapple 2009; Holsapple & Michel 2008 and Sharma et al. 2009). Discrete numerical approaches have been in use in the field of planetary science since, e.g., Brahic (1975, 1977), who simulated Saturn's rings, and Asphaug & Benz (1994); Richardson et al. (1995), who simulated the breakup of Comet SL9 in SSDEM, and HSDEM, respectively. In light of advances in computer processor speeds, only quite recently have robust versions of SSDEM begun to be applied to the realm of planetary science. SSDEM granular physics codes are now developed or adapted specifically for planetary applications by various groups (e.g., Wada et al. 2006; Sánchez & Scheeres 2011; Schwartz et al. 2012c; Tancredi et al. 2012) using various integration schemes and implementations of the types of friction between grains. Other codes, using a continuum approach,

have also been developed to investigate, for instance, collisions between porous aggregates (Sirono 2004).

Granular material dynamics research in low-gravity environments is not limited to the field of planetary science. For example, in 1998, NASA's sponsorship of the Mechanics of Granular Materials (MGM) experiment aboard the U.S. Space Shuttle investigated the behavior of granular materials under conditions when Earth's confining gravitational pressure is not present (Dooling 1998). This has very practical relevance toward the mitigation of earthquake and tsunami damage, which is due, in large part, to the sudden loss of the ground's shear strength normally provided for by confining pressure. This can have the effect of "fluidizing" granular regions under the surface. Numerical modeling in this area of study can not only save time and money on experiments, but, more importantly, verified techniques can be used to carry out deep exploration into regimes where laboratory experiments, for practical reasons, simply cannot reach.

1.2.4 The work presented in this thesis

Our knowledge of the internal makeup of small bodies is still very poor; the response of small bodies to various kinds of influences—processes such as impacts or shaking—depends on their surface and/or internal properties in a way that is not yet well understood. In turn, such processes can then modify this makeup. Since we do not have precise knowledge of either, it is important to create models that can represent small bodies in order to study how material properties influence the way a body may respond to the different processes it undergoes during its lifetime.

An understanding of the material properties of the grains and the processes that they undergo is important for the interpretation of images taken by spacecraft of the surfaces of planets, satellites, and small bodies. It is also relevant to the

development of efficient sampling designs and anchoring tools for space missions aimed at attaching to, or obtaining a sample from, the surfaces of such bodies (see Sections 1.1.3.2, 1.1.3.3, 1.1.3.4, and Chapter 4). The computational tools in this work are developed in subsequent chapters with the aim of describing these mechanisms and to explore designs for lander sampling devices suitable for these environments.

Before applying the code to the wide range of regimes relevant to planetary science, comparison with well-known results and laboratory experiments is required for validation. First presented, in Chapter 2, is my implementation of SSDEM in PKDGRAV, including all the parameters used and the contact forces that are taken into account (Section 2.1). Then, in Section 2.3, cylindrical hopper simulations performed with this code are compared to well-established experimental correlations in order to check the validity of the numerical approach. In Chapter 3, my inclusion of cohesive forces is presented. This addition incorporates (optional) cohesion into the HSDEM and SSDEM collisional routines (Section 3.2.1). Also developed is the ability to build up, from overlapping spheres, deformable cohesive agglomerates of arbitrary strength and complexity (Section 3.2.2). These tools are then validated by their use in reproducing numerically the morphologies and strengths of laboratory-sintered (fused by heat) impact targets (Section 3.3). The impacts themselves were also simulated, and, were found to match the laboratory results well qualitatively, using visualization tools, and quantitatively, on the basis of fragment size distribution comparisons. In Chapter 4, impact experiments into granular beds related to the sampling mechanism aboard Hayabusa2 were simulated (Section 4.4), and a new approach was developed to account for non-spherical projectiles (Section 4.3). Conclusions and perspectives are presented in Chapter 5 along with discussion of the ongoing and upcoming uses of the numerical tools developed in this work.

Chapter 2

Soft-Sphere Collisional Dynamics

In this chapter, I present my implementation of the soft-sphere discrete-element method (SSDEM) in the parallel gravitational N-body code PKDGRAV. Presented first, in Section 2.1, is a numerical description of the physical interactions between spherical particles using SSDEM, including all the parameters used and the contact forces that are taken into account. In Section 2.2, I explain my technique to compute collisions between soft spheres and specific elemental boundary shapes (walls). Then, in Section 2.3, I compare cylindrical hopper simulations against experiments in order to check the validity of the numerical model. Conclusions and perspectives are presented in Section 2.4. Much of the material for this chapter appeared as Schwartz et al. (2012c).

2.1 Soft-sphere numerical methodology

I have implemented SSDEM in the N-body code PKDGRAV, a parallel gravity code originally designed for collisionless cosmology simulations (Stadel 2001) and adapted for collisional Solar System applications (Richardson et al. 2009a, 2000). The main technical features of the code include a hierarchical tree algorithm for reducing

the computational cost of interparticle force calculations and a complete parallel implementation for balancing work across an arbitrary number of processors.

SSDEM permits realistic modeling of the contact forces between particles in a granular material. The soft-sphere collisional model is carried out by allowing particle surfaces to penetrate each other (Cundall & Strack 1979). When an overlap occurs, the particles are subject to forces that depend on the degree of overlap and the relative velocities and spins of the particles, as well as their material properties. Overlaps are detected each timestep by taking advantage of PKDGRAV's hierarchical tree data structure (Richardson et al. 2000) to generate particle neighbor lists in $\mathcal{O}(N \log N)$ time, where N is the number of particles in the simulation.

A second-order leapfrog integrator is used, in which particle positions and velocities are alternately "drifted" and "kicked" according to

$$\begin{aligned} \dot{\mathbf{r}}_{i,n+\frac{1}{2}} &= \dot{\mathbf{r}}_{i,n} + (h/2)\ddot{\mathbf{r}}_{i,n} && \text{“kick”} \\ \mathbf{r}_{i,n+1} &= \mathbf{r}_{i,n} + h\dot{\mathbf{r}}_{i,n+\frac{1}{2}} && \text{“drift”} \\ \dot{\mathbf{r}}_{i,n+1} &= \dot{\mathbf{r}}_{i,n+\frac{1}{2}} + (h/2)\ddot{\mathbf{r}}_{i,n+1} && \text{“kick”}, \end{aligned} \tag{2.1}$$

where $\mathbf{r}_{i,n}$ is the position of particle i at step n, h is the (constant) timestep that takes the system from step n to step $n+1$, and the derivatives are with respect to time. This integrator has the desirable property that it is symplectic, meaning it exactly solves an approximate Hamiltonian of the system, thereby conserving phase-space volume so that, for example, the energy error remains bounded (for sufficiently small h; see Saha & Tremaine (1992) for details). Symplectic methods are ideal for equations of motion of the form $\ddot{x} = F(x)$, of which the simple harmonic oscillation of a spring is a prime example. For this reason, this approach is well-suited in general to SSDEM.

However, most SSDEM simulations include dissipation, in the form of a damped spring (cf. Section 2.1.3), and/or other types of friction (Sections 2.1.4 and 2.1.5).

Although this would seem to negate the usefulness of the leapfrog, the relative simplicity of the integrator, coupled with the ease with which it can be parallelized, still make it a good choice for SSDEM applications. One complication is that the damping term is usually an explicit function of velocity, which is out of sync with position during the leapfrog integration step. This is addressed in a naïve way by using "predicted" velocities $\dot{\mathbf{r}}_{i,n+1} \approx \dot{\mathbf{r}}_{i,n} + h\ddot{\mathbf{r}}_{i,n}$ and spins $\dot{\boldsymbol{\omega}}_{i,n+1} \approx \dot{\boldsymbol{\omega}}_{i,n} + h\ddot{\boldsymbol{\omega}}_{i,n}$ to solve for $F(x)$. The proper way is to derive the correct Hamiltonian for the modified equations of motion and construct an appropriate leapfrog integration scheme from that (see Quinn et al. (2010) for discussion in the context of the shearing-sheet scenario). However, this level of sophistication is not needed here because very conservative timesteps (small h) are taken and integration errors are generally subsumed in the imposed damping and/or friction anyway.

Since SSDEM forces are computed only once per timestep, and simultaneously for all particles, the approach benefits tremendously from PKDGRAV's parallelization, with wallclock time dropping nearly linearly with the number of cores (the precise scaling prefactor depends on the details of the networking between cores). As a result, simulations of systems comprised of millions of particles, such as those presented in Section 2.3, can be completed in a matter of a few days on single 12-core 3-GHz nodes.

My methodology in carrying out particle-particle collisions with SSDEM is based on the work of Cundall & Strack (1979), although several more features have been added, such as rolling and twisting friction. In this section, I describe the modeling of normal and tangential deformations, along with different types of friction, in particular the rolling and twisting friction that are often neglected in SSDEM codes. I then explain how the coefficient of restitution is treated in the case of particle collisions and how the timestep necessary to perform the computations is chosen.

When computing forces in PKDGRAV as part of the regular integration step, neighbor searches are performed using the tree code. The amount of overlap between neighboring particles is then computed, given by

$$x = s_1 + s_2 - |\boldsymbol{\rho}|, \tag{2.2}$$

where s_1 is the particle radius (particles are spheres), s_2 is the neighbor particle radius, and $\boldsymbol{\rho} = \mathbf{r}_2 - \mathbf{r}_1$ is the relative position between the particle and neighbor centers of mass (COMs), so $|\boldsymbol{\rho}|$ is the scalar distance between the particle COMs. Quantitatively, x represents the extent of particle overlap, but can be interpreted physically as the sum of the particles' deformations along the line that connects their centers due to their mutual contact (see Fig. 2.1a).

2.1.1 Normal deformation

Consider a pair of particles for which x is positive, a repulsive restoring spring force is generated along the normal according to Hooke's law,[1]

$$\mathbf{F}_{N,\text{restoring}} = -k_n x\, \hat{\mathbf{n}}, \tag{2.3}$$

where $\hat{\mathbf{n}} \equiv \boldsymbol{\rho}/|\boldsymbol{\rho}|$ is a unit vector that gives the direction from the particle's center to the neighbor's center and k_n is the constant for the normal spring, which can be adjusted in order to control the amount of interparticle penetration that is allowed in a given simulation. In choosing a value for k_n, it has been the practice to limit x to $\sim$1% of the smallest particle radius in the simulation (Cleary 1998). In order to choose k_n so that it is assured that the maximum values of x are close to this limit, two regimes are considered: one where particle kinetic energy dominates and

[1]Other functional dependencies on x are easily implemented, such as $x^{3/2}$ (Hertzian), etc. A linear dependence is chosen because it is a simple choice that is often used.

determines the interparticle penetration, and another where the confining pressure on low-energy particles in a dense medium is responsible for the maximum interparticle penetration. In the first regime, if the maximum particle speed during the simulation can be predicted, putting that kinetic energy entirely into a single spring with x equal to the desired maximum value $x_{\max}$ gives a recommended value for k_n of

$$k_n \sim m \left(\frac{v_{\max}}{x_{\max}} \right)^2, \tag{2.4}$$

where the mass, m, corresponds to the typical mass of these most energetic particles. For example, if typical particles are 10 g in mass with diameters of 1 cm, and maximum speeds do not tend to exceed about 10 m s^{-1}, a k_n value of $\sim$ few $\times 10^8$ kg s^{-2} is suggested. Note that one does not need to compute an "exact" k_n, just a conservative value; the code monitors each collision and generate a warning if $x_{\max}$ is greatly exceeded.

In the second regime of low-energy particles under confining pressure due to a global potential (e.g., gravity or spin), one simply has to estimate what this pressure might be and then choose a value of k_n such that the maximum opposing SSDEM normal force (Eq. (2.3)) will correspond to the desired maximum penetration, $x_{\max}$. For example, consider a box with an open top of height H filled with low-energy, identical particles of radius s ($s \ll H$) and density ρ under the influence of gravity (here ρ refers to the density of a single particle, as distinguished from the bulk density of the collection). In this case, particles near the bottom would be expected to each exhibit typical repulsive forces of $\sim \phi \rho a_g H s^2$, where a_g is the uniform gravitational acceleration and ϕ is the packing efficiency (so the bulk density is $\phi\rho$). Taking $x_{\max}$ $\sim 0.01s$ and $\phi = 65\%$, and balancing with Eq. (2.3) gives

$$k_n \sim \frac{\phi \rho a_g H s^2}{x_{\max}} \sim 65 \rho a_g H s. \tag{2.5}$$

As an example, if we take $\rho = 4$ g cm^{-3}, $s = 1$ cm, $H = 1$ m, and a_g equal to Earth

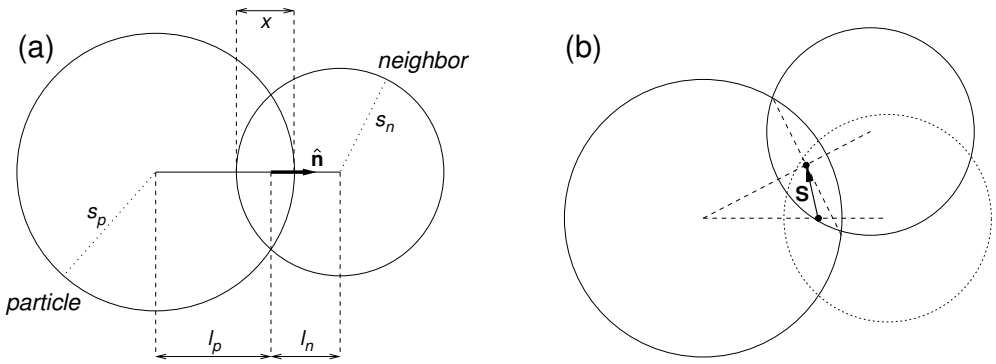

Figure 2.1: A (spherical) particle in overlap with one of its neighbors. (a) Labels show quantities needed to compute the reaction force due to overlap, regardless of duration. Here s_1, l_1, s_2, and l_2 are the radii and moment arms for the particle and its neighbor, respectively. The particle's moment arm is given by the scalar distance from the particle's center to the contact point (likewise for the neighbor's moment arm). The quantity x is the scalar distance between the surfaces of the two particles along the line that connects their centers and $\hat{\mathbf{n}}$ is a unit vector that gives the direction from the contact point to the neighbor's center. (b) Illustration of the quantity needed for the tangential component of the restoring force, which arises from a persistent contact: $\mathbf{S}$ is the tangential component of a vector that points from the equilibrium contact point to the current contact point and is generated by integrating all tangential motion that has occurred over the history of the contact. Note that both x and $\mathbf{S}$ are exaggerated to illustrate the method; x typically does not exceed $0.005(s_2 + s_1)$, and $|\mathbf{S}| \ll s_1, s_2$, so that $\mathbf{S}$ is close to perpendicular to both the initial and current lines that connect the two particles' centers.

gravity, g, we find an optimum value for k_n of a few $\times 10^4$ kg s^{-2}.

Fundamentally, a higher k_n results in smaller overlaps, but a larger repulsive force, so the principal disadvantage of raising k_n is that smaller timesteps are needed to resolve the forces (see Section 2.1.7).

In cases where it is important to match the sound speed of real materials, k_n can also be chosen to control the speed of energy propagation through a medium represented by soft-sphere particles. In densely packed material, this speed should be close to $2s\tau_{\text{overlap}}^{-1}$ for monodisperse particles (for polydisperse particles, replace s with an appropriate mean or typical value for particle radius), where τ_{overlap} is the typical

duration of collisional overlap (see Sections 2.1.6 and 2.1.7 along with Eq. (2.36) for the derivation of τ_{overlap}). In practice, some experimentation will be needed to tune the sound propagation speed. For instance, it might be beneficial to adjust k_n to match the sound speeds of real material for impact events in energy regimes where significant fracturing is not expected, but where nonetheless sound propagation might still be important. However, for many slow-speed granular processes, the computational cost of using a "realistic" value for k_n could be very high (Eq. (2.39) relates the value of k_n to a recommended timestep), especially for certain materials, and may not result in any worthwhile insight. Indeed, once above a certain k_n value, the outcomes can be largely independent of the specific value. In these cases, "softening" the material while increasing the resolution of the simulation might be more cost-effective than ensuring that a specific value of k_n is being used.

2.1.2 Tangential deformation

The restoring force in the tangential direction is given by

$$\mathbf{F}_{T,\text{restoring}} = k_t \mathbf{S}, \tag{2.6}$$

where k_t is the constant for the tangential spring and $\mathbf{S}$ is the tangential displacement from the equilibrium contact point, defined as

$$\mathbf{S} \equiv \int_{\text{overlap}} \mathbf{u}_t(t)\, dt + \mathbf{S}_0, \tag{2.7}$$

where the integral is over the duration of the static overlap (i.e., the interval over which static friction is acting), $\mathbf{u}_t$ is the relative tangential motion at the contact point (see Eq. (2.12)), and $\mathbf{S}_0$ is the tangential extension at the start of a static overlap. $\mathbf{S}_0$ is zero when particles first penetrate, but can be non-zero in the event of slipping (see Section 2.1.4).

Essentially, $\mathbf{S}$ is a vector that gives the tangential component of the deformation, and so its negative points from the current contact point to the point of tangential equilibrium (see Fig. 2.1b). As particles move, not only will the contact point move, but the equilibrium contact point will also change in the reference frame of the system. This motion is accounted for at every step by transforming $\mathbf{S}$ according to the change in $\hat{\mathbf{n}}$ over the previous step. This is done in two stages: a rotation around the $\hat{\mathbf{n}}$ vector, and a rotation around the vector orthogonal to $\hat{\mathbf{n}}$, around which $\hat{\mathbf{n}}$ has rotated over the previous step. This calculation, which is done for every contact in the system at every step, can be computationally expensive, but is important for lasting contacts.

2.1.3 Kinetic friction (damping)

Kinetic friction is implemented by damping the springs in the normal and tangential directions according to the widely used "dashpot" model. We start with the total relative velocity, which is given by

$$\mathbf{u} = \mathbf{v}_2 - \mathbf{v}_1 + l_2(\hat{\mathbf{n}}\times\boldsymbol{\omega}_2) - l_1(\hat{\mathbf{n}}\times\boldsymbol{\omega}_1), \tag{2.8}$$

where $\mathbf{v}_1$ is the COM velocity of the particle, $\mathbf{v}_2$ is the COM velocity of the neighbor particle, $\boldsymbol{\omega}_1$ is the spin of the particle, $\boldsymbol{\omega}_2$ is the spin of the neighbor particle, and l_1 and l_2 are lever arms from the particle centers to the effective point of contact, which is taken to be at the center of the circle that corresponds to the intersection of the particles' spherical surfaces. This point lies on the line segment that connects the particles' centers, at a distance

$$l_1 = \frac{s_1^2 - s_2^2 + |\boldsymbol{\rho}|^2}{2|\boldsymbol{\rho}|} \tag{2.9}$$

from the particle in question. The lever arm for the neighbor particle is simply

$$l_2 = |\boldsymbol{\rho}| - l_1. \tag{2.10}$$

The normal and tangential components of $\mathbf{u}$ are given by

$$\mathbf{u}_n = (\mathbf{u}\cdot\hat{\mathbf{n}})\hat{\mathbf{n}}, \tag{2.11}$$

$$\mathbf{u}_t = \mathbf{u} - \mathbf{u}_n. \tag{2.12}$$

The tangential unit vector $\hat{\mathbf{t}}$ is then given by $\hat{\mathbf{t}} \equiv \mathbf{u}_t/|\mathbf{u}_t|$ (if $\mathbf{u}_t = 0$, $\hat{\mathbf{t}}$ is then set to zero). The normal and tangential components of the damping forces are then given by

$$\mathbf{F}_{n,\text{damping}} = C_n\mathbf{u}_n, \tag{2.13}$$

$$\mathbf{F}_{t,\text{damping}} = C_t\mathbf{u}_t, \tag{2.14}$$

where C_n and C_t are the damping coefficients along $\hat{\mathbf{n}}$ and $\hat{\mathbf{t}}$, respectively. For the Hooke's restitution law, C_n can be related to the familiar normal coefficient of restitution, ε_n, according to

$$C_n = -2\ln\varepsilon_n\sqrt{\frac{k_n\,\mu}{\pi^2 + (\ln\varepsilon_n)^2}} \tag{2.15}$$

(see Section 2.1.6 for the derivation), where μ is the reduced mass of the colliding pair ($\mu \equiv m_1m_2/(m_1+m_2)$, where m_1 and m_2 are the masses of the particle in question and its neighbor, respectively). There is no equivalent simple correspondence between C_t and the tangential coefficient of restitution sometimes used in HSDEM implementations (see Section 2.1.6 for further discussion).

Combining Eqs. (2.3)–(2.6), (2.13), and (2.14), the normal and tangential components of the total SSDEM force are

$$\mathbf{F}_n = -k_nx\hat{\mathbf{n}} + C_n\mathbf{u}_n, \tag{2.16}$$

$$\mathbf{F}_t = k_t\mathbf{S} + C_t\mathbf{u}_t. \tag{2.17}$$

By Newton's 3$^{\text{rd}}$ law, the neighbor particle feels the same total force in the opposite direction.

2.1.4 Static friction

Depending on the coefficient of static friction (μ_s) at the contact point, slippage may occur as a result of tangential stress. For real material, this is governed by the molecular arrangements around the point of contact. The coefficient of static friction in common use is a macroscopic approximation that estimates the total amount of tangential force that can be supported by the contact, with the assumption that this threshold of force scales linearly with the normal force at the contact. In this implementation, if this force is exceeded, depending on the value of a parameter, b, that ranges from zero to unity, $\mathbf{S}$ is reset to $b\mathbf{F}_{t,\max}$, where $\mathbf{F}_{t,\max}$ is this threshold tangential force, given by

$$|\mathbf{F}_{t,\max}| = \mu_s |\mathbf{F}_n|. \tag{2.18}$$

In the event of slipping, this allows us the option to set the tangential strain at the contact point to zero (the default is $b = 0$) or to some fraction ($b > 0$) of its maximum allowed value, $b\mathbf{F}_{t,\max}$. Additionally, if this damping force alone exceeds $\mathbf{F}_{t,\max}$, then $\mathbf{S}$ is reset to zero for any value of b. So using $b = 0$ (default), Eq. (2.17) now becomes

$$\mathbf{F}_t = \min\left\{\mu_s |\mathbf{F}_n| \hat{\mathbf{S}};\ k_t \mathbf{S} + C_t |\mathbf{u}_t| \hat{\mathbf{t}}\right\}, \tag{2.19}$$

where $\hat{\mathbf{S}} \equiv \mathbf{S}/|\mathbf{S}|$. When this tangential force is applied as torques to the particle and its neighbor (opposite sign), with lever arms of l_1 and l_2, respectively, a change in rotation is induced in both particles. The changes in the rotations of both particles are along the same spin vector ($\hat{\mathbf{n}} \times \hat{\mathbf{t}}$) and of the same sign. To compensate for this gain in angular momentum, the COMs of both particles feel a tangential force equal and opposite to the forces at their respective surfaces. This correction, which serves to conserve angular momentum, is often neglected in SSDEM implementations.

2.1.5 Rolling and twisting friction

Rolling friction is often ignored in the modeling of granular materials. Particles are rolling if $|\mathbf{u}|$ is zero despite relative rotational motion of the particles. To account for the transformation of rotational energy of rolling particles into frictional energy (i.e., microscopic vibrations/heat), a coefficient of rolling friction (μ_r) is introduced in the code. When this quantity is non-zero, it decreases the relative velocity at the contact point that is due to rotation ($\mathbf{v}_{\text{rot}}$, defined below) by adding a spin vector that points in the opposite direction of this motion. The induced torque on the particle due to rotational friction is given by

$$\mathbf{M}_{\text{roll}} = \mu_r \left|\mathbf{F}_n\right| l_1 \frac{\mathbf{v}_{\text{rot}} \times \hat{\mathbf{n}}}{|\mathbf{v}_{\text{rot}}|}, \tag{2.20}$$

where $\mathbf{v}_{\text{rot}} \equiv l_1(\boldsymbol{\omega}_1 \times \hat{\mathbf{n}}) - l_2(\boldsymbol{\omega}_2 \times \hat{\mathbf{n}})$.

There has been considerable debate in the materials science community regarding the optimal way to account for rolling friction, including whether or not it should depend on the speed of rotation (Zhou et al. 1999; Zhu & Yu 2006). Here, a simple implementation that depends only on the rolling friction coefficient, the normal force, and the sign of the "rolling axis" (which is given by the cross product of $\hat{\mathbf{n}}$ with $\mathbf{v}_{\text{rot}}$) is chosen.

Twisting friction (dissipation of relative rotation of the particles around $\hat{\mathbf{n}}$, i.e., the normal axis that passes through the contact point and the particles' centers) is another kind of friction that is often neglected in granular material modeling. Similarly to the case of rolling, these relative rotational motions of the particles are coupled to each other and should damp out (the reason being that the contact "point" is in reality more like a contact area, where the components of the particles grind against each other and dissipate energy). To account for this effect, a twisting

frictional term is included, given by

$$\mathbf{M}_{\text{twist}} = \mu_t \left|\mathbf{F}_n\right| r_c \frac{(\boldsymbol{\omega}_2 - \boldsymbol{\omega}_1)\cdot\hat{\mathbf{n}}}{|(\boldsymbol{\omega}_2 - \boldsymbol{\omega}_1)\cdot\hat{\mathbf{n}}|}\hat{\mathbf{n}}. \tag{2.21}$$

Here, r_c is the radius of contact (where the surfaces of two overlapping particles touch form a circle with the contact point at the center—r_c is the radius of this circle).

There are some issues that arise with this treatment of rolling friction and twisting friction as they have been defined thus far. For example, consider two colliding particles with relative rotation at the contact point. For somewhat high-speed collisions, the normal force between particles will be large, making the damping forces given by Eqs. (2.20) and (2.21) accordingly large. In order to have these types of rotational damping take effect only when appropriate, $\mathbf{M}_{\text{roll}}$ and $\mathbf{M}_{\text{twist}}$ can be set to zero initially (by setting μ_r and μ_t to zero). This is done when the duration of the current overlap, t_{overlap}, is less than the characteristic duration of collision, τ_{overlap} (see Sections 2.1.6 and 2.1.7); this means that particles that are actively bouncing do not experience rolling or twisting friction, whereas particles that are in persistent contact experience these frictional forces. It is worthwhile to note that the change in angular momentum of the particle in both the cases of rotational friction and of twisting friction is equal and opposite to the change in angular momentum of the neighbor, so total angular momentum is conserved.

Combining Eqns. (2.16), (2.19), (2.20), (2.21), and the conservation of angular momentum constraint, the total force on the particle COM is given in Eq. (2.22) and the total torque on the particle is given in Eq. (2.23),

$$\mathbf{F}_1 = -k_n x\hat{\mathbf{n}} + C_n\mathbf{u}_n + \min\left\{\mu_s|\mathbf{F}_n|\hat{\mathbf{S}};\ k_t\mathbf{S} + C_t|\mathbf{u}_t|\hat{\mathbf{t}}\right\}. \tag{2.22}$$

$$\mathbf{M}_1 = -l_1\left[\min\left\{\mu_s|\mathbf{F}_n|\hat{\mathbf{S}};\ k_t\mathbf{S} + C_t|\mathbf{u}_t|\hat{\mathbf{t}}\right\}\right]\times\hat{\mathbf{n}} + \mu_r\left|\mathbf{F}_n\right| l_1\frac{\mathbf{v}_{\text{rot}}\times\hat{\mathbf{n}}}{|\mathbf{v}_{\text{rot}}|} + \mu_t\left|\mathbf{F}_n\right| r_c\frac{(\boldsymbol{\omega}_2 - \boldsymbol{\omega}_1)\cdot\hat{\mathbf{n}}}{|(\boldsymbol{\omega}_2 - \boldsymbol{\omega}_1)\cdot\hat{\mathbf{n}}|}\hat{\mathbf{n}}. \tag{2.23}$$

with corresponding expressions for the neighbor particle.

2.1.6 The coefficient of restitution

It is often useful to parameterize particle collisions with a (normal) coefficient of restitution, ε_n. The coefficient of restitution of a material depends not only on the restitution law used (e.g., Hooke's or Hertzian law), but also on the collisional speeds that we wish to consider. In order to derive a value for the normal damping coefficient C_n that corresponds directly to a given ε_n (assuming appropriate timesteps are used—cf. Section 2.1.7), we start with the definition of ε_n,

$$\varepsilon_n = \frac{|\mathbf{u}_n(t)_{\text{final}}|}{|\mathbf{u}_n(t)_{\text{initial}}|}, \tag{2.24}$$

and the solution to the second-order differential equation of motion for a spring attached to two non-fixed masses of reduced mass μ that obeys Hooke's law with simple damping,

$$x(t)\hat{\mathbf{n}} = x_{\max}\left[e^{-\alpha_n t}\cos(\omega_{1,n}t + \phi)\right]\hat{\mathbf{n}}, \tag{2.25}$$

where $x_{\max}$ is the maximum amplitude, or distention, of the spring, and represents the maximum overlap between the two particles, which, physically, could in turn be taken to represent the maximum deviation (deformation) of the particles from perfect spheres; ϕ is the phase angle; $\alpha_n \equiv \frac{C_n}{2\mu}$; and $\omega_{1,n}$ is the damped harmonic frequency of the oscillating system (along $\hat{\mathbf{n}}$), which is given in terms of the undamped harmonic frequency, $\omega_{0,n}$, and α_n by

$$\omega_{1,n}^2 \equiv \omega_{0,n}^2 - \alpha_n^2, \tag{2.26}$$

where $\omega_{0,n}^2 \equiv \frac{k_n}{\mu}$. In order to solve for ε_n in these terms, we need to solve for the relative normal velocity, or at least the ratio of relative normal velocities before and after a given collision. To solve for $\mathbf{u}_n(t)$ in Eq. (2.27), we take the first derivative

of x as given in Eq. (2.25), recalling that x and $x_{\max}$ lie along the normal.

$$\mathbf{u}_n(t) = -x_{\max} e^{-\alpha_n t} \left[\omega_{1,n} \sin(\omega_{1,n} t + \phi) + \alpha_n \cos(\omega_{1,n} t + \phi)\right] \hat{\mathbf{n}}. \tag{2.27}$$

We will take t just prior to the impact to be zero, which corresponds to a point in the phase where $|\mathbf{u}_n(t)|$ is maximum and $x(t)$ is zero, giving ϕ the value of $\pi/2$. The value of t just after the collision is equal to the time that it takes to complete one collision, which is $\frac{\pi}{\omega_{1,n}}$. In solving for ε_n, the cosine terms are zero at both $t = 0$ and $t = \frac{\pi}{\omega_{1,n}}$, the remaining constants cancel, and the sine terms, offset by a half-phase, are equal and opposite, leaving simply

$$\varepsilon_n = \left| e^{\frac{-\alpha_n \pi}{\omega_{1,n}}} \right|. \tag{2.28}$$

Replacing the terms α_n and $\omega_{1,n}$ with C_n, k_n, and μ, then solving for C_n gives Eq. (2.15). This result agrees with the formulation of C_n used in Cleary (1998).

The formulation of C_t based upon a tangential coefficient of restitution, ε_t, is somewhat more complex because it involves two different frequencies, $\omega_{1,n}$ and $\omega_{1,t}$, which can be independent of each other. Therefore, the sine and cosine arguments at $t = 0$ and at $t = \frac{\pi}{\omega_{1,n}}$ will not be separated unconditionally by a half-phase, but instead by $\pi \frac{\omega_{1,t}}{\omega_{1,n}}$. There is also an additional factor to account for the relative tangential acceleration due to both frictionally induced COM motion and the corresponding rotation of the particle. This acceleration is given as

$$\mathbf{a}_t(\mathbf{S}, \mathbf{u}_t, x) = \left(\frac{k_t}{\mu}\mathbf{S} + \frac{C_t}{\mu}\mathbf{u}_t\right) \left\{1 + \frac{5\left[l_1(x)\right]^2}{2s_1^2}\right\}. \tag{2.29}$$

To simplify things greatly, the assumption is made that $x \ll s_1$ (which is appropriate in the hard-sphere limit as l_1 approaches s_1), and thus $\mathbf{a}_t(\mathbf{S}, \mathbf{u}_t, x)$ becomes

$$\mathbf{a}_t(\mathbf{S}, \mathbf{u}_t) = \frac{7}{2}\left(\frac{k_t}{\mu}\mathbf{S} + \frac{C_t}{\mu}\mathbf{u}_t\right) \tag{2.30}$$

$$= \omega_{0,t}^2 \mathbf{S} + 2\alpha_t \mathbf{u}_t, \tag{2.31}$$

where $\omega_{0,t}^2 \equiv \frac{7k_t}{2\mu}$ and $\alpha_t \equiv \frac{7C_t}{4\mu}$. Note that this treatment of $\omega_{0,t}$ and α_t deviates from how I have defined $\omega_{0,n}$ and α_n: although the damped tangential frequency is still likewise defined as $\omega_{1,t}^2 \equiv \omega_{0,t}^2 - \alpha_t^2$, the factor of $\frac{7}{2}$ is absorbed into the definitions of $\omega_{0,t}$ and α_t. The relative tangential velocity as a function of time, t, can now be expressed as

$$\mathbf{u}_t(t) = -S_{\max} e^{-\alpha_t t} \left[\omega_{1,t} \sin(\omega_{1,t} t + \phi) + \alpha_t \cos(\omega_{1,t} t + \phi)\right] \hat{\mathbf{t}}_i. \quad (2.32)$$

$$\mathbf{u}_{t,\text{initial}} \equiv \mathbf{u}_t(0) = -S_{\max} \omega_{1,t} \hat{\mathbf{t}}_i. \quad (2.33)$$

$$\mathbf{u}_{t,\text{final}} \equiv \mathbf{u}_t\left(\frac{\pi}{\omega_{1,n}}\right) = -S_{\max} e^{\frac{-\alpha_t \pi}{\omega_{1,n}}} \left[\omega_{1,t} \cos\left(\pi \frac{\omega_{1,t}}{\omega_{1,n}}\right) - \alpha_t \sin\left(\pi \frac{\omega_{1,t}}{\omega_{1,n}}\right)\right] \hat{\mathbf{t}}_i. \quad (2.34)$$

Thus the coefficient of tangential restitution, ε_t, is given as

$$\varepsilon_t \equiv \frac{\mathbf{u}_{t,\text{final}} \cdot \hat{\mathbf{t}}_i}{\mathbf{u}_{t,\text{initial}} \cdot \hat{\mathbf{t}}_i} = e^{\frac{-\alpha_t \pi}{\omega_{1,n}}} \left[\cos\left(\pi \frac{\omega_{1,t}}{\omega_{1,n}}\right) - \frac{\alpha_t}{\omega_{1,t}} \sin\left(\pi \frac{\omega_{1,t}}{\omega_{1,n}}\right)\right], \quad (2.35)$$

where $S_{\max} \equiv \max(|\mathbf{S}|)$, which represents the amplitude of the oscillation, and $\hat{\mathbf{t}}_i$ is the direction of tangential motion of the neighbor particle at the point of contact at the start of the overlap. Still, t just prior to the impact is equal to zero, and t just after the collision equal to $\frac{\pi}{\omega_{1,n}}$. After some simplification of terms, one arrives at Eqs. (2.33) and (2.34) as expressions for the initial and final tangential velocities, respectively, which, by Eq. (2.24), gives the coefficient of tangential restitution in Eq. (2.35).

Buried within the expressions for α_t and $\omega_{1,t}$ the dependence of C_n on ε_t is found. Some of the behavior of ε_t can be discerned by examining different cases. When $\omega_{1,t} = \omega_{1,n}$, the tangential spring will have completed one half-cycle at the same time that the normal spring will have completed its half-cycle at the end of the collision, thus ε_t will be negative and have a magnitude equal to the exponential term, which represents the decay of the oscillation due to damping. In the case of $\omega_{1,t} \ll \omega_{1,n}$, the collision will have ended before the phase of the tangential oscillation has had time to evolve, and so ε_t will still be positive, and will have a magnitude equal to

the exponential term, which will depend on how the value of α_t compares to $\omega_{1,n}$. So it can be said that for $q\omega_{1,t} = \omega_{1,n}$, where q is a whole number, the value of ε_t will depend only on the exponential term, and when q is even, ε_t will be positive, and when q is odd, ε_t will be negative. At quarter phases ($\frac{q}{2}$), there is an additional term of $\pm\frac{\alpha_t}{\omega_{1,t}}$ when the magnitude of the cosine term is zero and the sine term is at a maximum.

From these examples, one can begin to understand how the quantities C_t, C_n, k_t, k_n, and μ affect ε_t, although a general analytical solution that gives C_t as a function of ε_n and these other quantities is not as simple as finding the appropriate C_n given the desired value of ε_n (see Eq. (2.15)). The appropriate way to a solution that gives C_t as a function of ε_t would be to use an iterative method, keeping in mind that the solution found would still be based on a hard-sphere approximation (cf. Eqs. (2.29) and (2.30)).

2.1.7 Timestep considerations

Correctly resolving the oscillation half-period of an isolated two-particle collision requires, at a very minimum, 10–20 timesteps over the course of the collision, and preferably close to around 50 (Quinn et al. 2010). From Section 2.1.6, and introducing the damping coefficient, $\xi \equiv \frac{\alpha_n}{\omega_{0,n}}$, we have:

$$\tau_{\text{overlap}} = \frac{\pi}{\omega_{1,n}}, \tag{2.36}$$

$$= \frac{\pi}{\omega_{0,n}\sqrt{1-\xi^2}}, \tag{2.37}$$

$$= \pi\sqrt{\frac{\mu}{k_n(1-\xi^2)}}. \tag{2.38}$$

This suggests a good timestep would be

$$h \approx \frac{\pi}{50}\sqrt{\frac{\mu}{k_n(1-\xi^2)}}. \tag{2.39}$$

Provided that the value of k_n has been chosen appropriately with consideration given to the velocities of particles in the simulation (cf. Section 2.1.1), and that an appropriate timestep is chosen with respect to this value of k_n (Eq. (2.39)), fast-moving particles will not be missed, and particle overlaps will be fully resolved.

2.2 Walls

Walls are used in PKDGRAV to provide hard-surface boundary conditions for granular dynamics simulations. Richardson et al. (2011) describe the geometries and collision conditions used in their HSDEM simulations, for which collisions are predicted prior to contact, requiring often complex equations to be solved repeatedly. Here I provide the solutions for the same geometries but using SSDEM, with the principal advantage that overlaps are detected after the fact, and only once per timestep, greatly simplifying the detection algorithms and reducing the computational cost.

Briefly, during the force calculation of the integration step, every particle in an SSDEM simulation is checked to see whether it overlaps with another particle and/or wall. Corresponding SSDEM forces are applied that depend on the degree of overlap and that are directed along a line between the objects, which in turn depends on the overlap geometry. Particle-particle overlaps are simple to detect as they are just sphere intersect tests (cf. Eq. (2.2)). For walls, each supported geometry is handled separately, as detailed in the following.

To reduce the cost of wall-intersect tests, the code first isolates regions of space that the wall does not occupy, progressively confining the wall until the point of closest contact is found. For example, when checking for an intersection with a finite planar wall, like a rectangle or a disk, it is usually of benefit to first consider the intersection with the wall as though it were simply the infinite plane that contains

the finite wall. In this way, particles that are far above or below the plane can be ruled out without performing more computationally expensive wall-intersect checks. The regions were chosen with both simplicity and efficiency in mind (if regions of space where particles are likely to be found can be carved out with relatively few operations, this will save computational time).

Each particle is checked against each wall to see if an overlap exists. If it does, the point of closest contact is found and used to compute the forces on the particle. Restoring and frictional forces are applied to particles in contact with walls just as they are applied to particles in contact with neighbors as outlined in Section 2.1, but using a contact point on the wall surface (the walls have infinite linear and angular inertia and are not deformable). The contact point has a total relative velocity (Eq. (2.8)) given as the difference between the velocity of the wall at the contact point (taking into account its COM motion as well as any spin or oscillatory motion) and the velocity of the particle at the contact point (taking into account both its COM motion and its spin).

The following describes the primary set of boundary primitives, which can be combined in order to confine particles within certain geometries or to replicate specific mechanical devices.

2.2.1 Infinite plane

Starting from Richardson et al. (2011), the parameters for the infinite plane are the origin $\mathbf{O}$ and normal $\hat{\mathbf{N}}$, plus optional velocity $\mathbf{V}$, oscillation amplitude A, oscillation angular frequency Ω, oscillation normal vector $\hat{\mathbf{\Omega}}$ (so the relative vector displacement after time t due to oscillation, measured from the start of the simulation and evaluated at the start of the step, is $A\sin(\Omega t)\hat{\mathbf{\Omega}}$), and spin Σ around the orientation vector $\hat{\mathbf{N}}$. Note that for an infinite plane with $\Sigma = 0$, the origin can be any point

in the plane (the choice is arbitrary).

To simplify the equations in this and subsequent derivations, I define the relative position vector $\boldsymbol{\rho} \equiv \mathbf{r}_1 - \mathbf{O}$ and separate it into perpendicular and parallel components, $\boldsymbol{\rho}_N$ and $\boldsymbol{\rho}_T$, respectively, where $\boldsymbol{\rho}_N \equiv \rho_N \hat{\mathbf{N}}$, $\rho_N \equiv \boldsymbol{\rho} \cdot \hat{\mathbf{N}}$, and $\boldsymbol{\rho}_T \equiv \boldsymbol{\rho} - \boldsymbol{\rho}_N$ (so $\hat{\mathbf{T}} \equiv \boldsymbol{\rho}_T / |\boldsymbol{\rho}_T|$, which is only defined if $|\boldsymbol{\rho}_T| > 0$, and $\rho_T \equiv \boldsymbol{\rho} \cdot \hat{\mathbf{T}}$). Note, in Section 2.1, $\boldsymbol{\rho}$ was defined as the relative position between particle centers. Also note that $\boldsymbol{\rho}_N$ and $\boldsymbol{\rho}_T$ as defined here are *signed* quantities, i.e., vector components.

Similarly defined is the relative velocity as $\boldsymbol{\nu} = \mathbf{v}_1 - \mathbf{V} - A\Omega \cos(\Omega t)\hat{\boldsymbol{\Omega}}$, with corresponding perpendicular and parallel components. If there is an overlap with a particle, then the total relative velocity between the particle and the wall is given as

$$\mathbf{u} = -\boldsymbol{\nu} + \Sigma \hat{\mathbf{N}} \times \boldsymbol{\rho}_T - l_1(\hat{\mathbf{n}} \times \boldsymbol{\omega}_1). \tag{2.40}$$

Also, rolling and twisting frictional terms arising from particle-wall contacts are calculated by following the methodology laid out in Section 2.1.5 and substituting the spin vector of the neighbor particle $\boldsymbol{\omega}_2$ with $\Sigma \hat{\mathbf{N}}$, and l_2 with $\mathbf{Q} \cdot \hat{\mathbf{T}}$, where $\mathbf{Q}$ signifies the contact point between the particle and the wall.

In the specific case of the infinite plane, the overlap condition is simply $|\rho_N| < s$, where s is the radius of the particle. If this condition is met, the contact point is given by $\mathbf{Q} \equiv \mathbf{O} + \boldsymbol{\rho}_T$. As is done in the case of particle-particle contacts, the code resolves the contact as though it were occurring at a single point (in the case of particle-particle contact, the contact point is taken to lie along the line that connects the centers of the two spheres; in the case of particle-wall contact, the contact point is taken to be the point on the boundary primitive closest to the particle center). In reality, contacts occur over areas, or within small volumes on the molecular scale, and give rise to a complex distribution of forces, to which a rough approximation is provided by including an array of frictional forces (cf. Section 2.1).

2.2.2 Disk

For a disk, the code first isolates the test region to the corresponding infinite plane (all parameters in an infinite plane are included in the set of parameters of a disk), but now $\mathbf{O}$ defines the geometric center of the disk, and R_{out} and R_{in} define its outer and inner radii, respectively, where $R_{\text{out}} > R_{\text{in}}$ (i.e., the disk can have a central hole). For any particles that survive the first cut (i.e., those particles that would be in contact with the disk if it were infinite), $|\boldsymbol{\rho}_T|$ is compared against R_{out} and R_{in}. Three cases are considered: (A) $R_{\text{in}} \leq |\rho_T| \leq R_{\text{out}}$; (B) $R_{\text{in}} < R_{\text{out}} < |\rho_T|$; and (C) $|\rho_T| < R_{\text{in}} < R_{\text{out}}$. If case (A) is true, the particle is touching/overlapping the flat portion of the disk. If (B), the particle may be touching/overlapping the outer periphery of the disk; the potential overlap point is $\mathbf{O}+R_{\text{out}}\hat{\mathbf{T}}$, and the overlap condition is $|\boldsymbol{\rho} - R_{\text{out}}\hat{\mathbf{T}}| \leq s$. If (C), the inner edge is the potential overlap point, given by $\mathbf{O} + R_{\text{in}}\hat{\mathbf{T}}$, with overlap condition $|\boldsymbol{\rho} - R_{\text{in}}\hat{\mathbf{T}}| \leq s$.

A special case arises if $R_{\text{in}} > 0$ and $\rho_T = 0$. This is a subcase of (C) where the particle center lies on the disk orientation axis, above, below, or on $\mathbf{O}$. Here the overlap condition is $\rho^2 - R_{\text{in}}^2 \leq s^2$. If the condition is satisfied, then the contact point $\mathbf{Q}$ is set to a "phantom" point at $\mathbf{O} - R_{\text{in}}\boldsymbol{\rho}/|\boldsymbol{\rho}|$. If $|\boldsymbol{\rho}| = 0$, meaning that the particle center is exactly at the origin, no net force is felt from the disk.

2.2.3 Rectangle

For a rectangle, like the disk, the code first considers the region that corresponds to the infinite plane containing the rectangle. The four vertices of the rectangle are defined by three vectors, the origin $\mathbf{O}$, the vector $\boldsymbol{\Upsilon}_1$ that points from $\mathbf{O}$ to an adjacent corner, and the vector $\boldsymbol{\Upsilon}_2$ that points from $\mathbf{O}$ to the other adjacent corner. For simplicity, I require that $\boldsymbol{\Upsilon}_1$ and $\boldsymbol{\Upsilon}_2$ be orthogonal. Thus the four corners of the

rectangle are $\mathbf{O}$, $\mathbf{O}+\boldsymbol{\Upsilon}_1$, $\mathbf{O}+\boldsymbol{\Upsilon}_2$, and $\mathbf{O}+\boldsymbol{\Upsilon}_1+\boldsymbol{\Upsilon}_2$. Note the normal of the rectangle (used to define the infinite plane in which it lies) is just $\hat{\mathbf{N}} = (\boldsymbol{\Upsilon}_1 \times \boldsymbol{\Upsilon}_2)/|\boldsymbol{\Upsilon}_1 \times \boldsymbol{\Upsilon}_2|$. A necessary condition for the particle to be in contact with the rectangle is that the particle be in contact with the infinite plane containing it, i.e., $|\rho_N| < s$ (see above).

If the particle passes the plane-intersect test, the code next needs to find the point on the plane closest to the particle. If that point is closest to a point on the rectangle's face, then the particle is in overlap with the wall. If not, the code must check to see if the particle is in contact with an edge or corner of the wall. To do this, a coordinate system is constructed, defined by unit vectors $\hat{\mathbf{a}} \equiv \boldsymbol{\Upsilon}_1/|\boldsymbol{\Upsilon}_1|$ and $\hat{\mathbf{b}} \equiv \boldsymbol{\Upsilon}_2/|\boldsymbol{\Upsilon}_2|$, with points (0,0), (1,0), (0,1), and (1,1) corresponding to the four corners of the rectangle. Note that all points on the infinite plane in which the rectangle lies can be described by real values (a, b).

In order to check for an overlap of the particle with the rectangle, the coordinate space defined above is divided into nine test regions. This is done by drawing four (infinite) lines: $(0,0)+m\hat{\mathbf{a}}$; $(0,1)+m\hat{\mathbf{a}}$; $(0,0)+m\hat{\mathbf{b}}$; and $(1,0)+m\hat{\mathbf{b}}$. The resulting nine regions are outlined in Table 2.1, and illustrated in Fig. 2.2 (left).

Next, $\boldsymbol{\rho}_T$ can be transformed into this frame, and will be subject to a different overlap test depending on its coordinates (a, b). Case (A) describes a particle that is necessarily in overlap with the face of the rectangle, and $\mathbf{Q} = \mathbf{O} + \boldsymbol{\rho}_T$, or (a, b) in this frame. For the remaining cases, the potential overlap point, i.e., the point (x, y) on the rectangle closest to the particle, is given for each case as: (B) $(0, b)$; (C) $(1, b)$; (D) $(a, 0)$; (E) $(a, 1)$; (F) $(0, 0)$; (G) $(0, 1)$; (H) $(1, 0)$; (I) $(1, 1)$. The overlap condition is $|\boldsymbol{\rho} - x\boldsymbol{\Upsilon}_1 - y\boldsymbol{\Upsilon}_2| \leq s$. If the condition is met, $\mathbf{Q} = \mathbf{O} + x\boldsymbol{\Upsilon}_1 + y\boldsymbol{\Upsilon}_2$.

Face:	(A) $0 \leq a \leq 1$, $0 \leq b \leq 1$			
Edge:	(B) $a < 0$, $0 \leq b \leq 1$	(C) $a > 1$, $0 \leq b \leq 1$	(D) $0 \leq a \leq 1$, $b < 0$	(E) $0 \leq a \leq 1$, $b > 1$
Corner:	(F) $a < 0$, $b < 0$	(G) $a < 0$, $b > 1$	(H) $a > 1$, $b < 0$	(I) $a > 1$, $b > 1$

Table 2.1: Overlap cases for a particle with a rectangle. **top row-** the case where the particle is flush against a face of the rectangle; **middle row-** cases where the particle is closest to an edge of the rectangle; **bottom row-** cases where the particle is closest to a corner.

2.2.4 Triangle

Although not implemented in Richardson et al. (2011), a triangle is an especially versatile primitive that can be tiled atop 3-dimensional models or used to build complex polygonal shapes. The triangle vertices are defined by an origin $\mathbf{O}$, a vector $\boldsymbol{\Upsilon}_1$ that points from $\mathbf{O}$ to another corner, and a vector $\boldsymbol{\Upsilon}_2$ that points from $\mathbf{O}$ to the remaining corner. Thus the three vertices of the triangle are $\mathbf{O}$, $\mathbf{O} + \boldsymbol{\Upsilon}_1$, and $\mathbf{O} + \boldsymbol{\Upsilon}_2$.

The approach for the triangle is similar to that for the rectangle. The code first carves out the region corresponding to the infinite plane that contains the triangle, for which the normal is again the normalized cross product of the vertex vectors $\boldsymbol{\Upsilon}_1$ and $\boldsymbol{\Upsilon}_2$, and the condition to continue consideration of particle-wall overlap is $|\rho_N| < s$. If this condition is satisfied, then, as for the rectangle, a 2-dimensional reference frame is constructed from unit vectors $\hat{\mathbf{a}}$ and $\hat{\mathbf{b}}$ (generally not orthogonal in this case), pointing in the directions of $\boldsymbol{\Upsilon}_1$ and $\boldsymbol{\Upsilon}_2$, respectively, with the corresponding triangle vertices at (0,0), (1,0), and (0,1). Again all points on the infinite plane in which the triangle lies can be described by real values (a, b).

In order to check for an overlap, the space is divided into 7 regions (rather than the 9 regions used for rectangles). This is done by drawing three (infinite) lines: $(0,0) + m\hat{\mathbf{a}}$; $(0,0) + m\hat{\mathbf{b}}$; and $a + b = 1$. The resulting 7 regions are outlined in

Table 2.2, and illustrated in Fig. 2.2 (left). Again, $\boldsymbol{\rho}_T$ can be transformed into this frame, and will be subject to a different overlap test depending on its coordinates (a, b). As before, case (A) is always in overlap, and $\mathbf{Q} = \mathbf{O} + \boldsymbol{\rho}_T$, or (a, b) in this frame.

For the remaining cases, the potential overlap point, i.e., the point (x, y) on the triangle closest to the particle, is given for each case as: (B) $(0, b)$; (C) $(a, 0)$; (D) $(\frac{a-b+1}{2}, \frac{b-a+1}{2})$; (E) $(0, 0)$; (F) $(1, 0)$; (G) $(0, 1)$. The overlap condition is $|\boldsymbol{\rho} - x\boldsymbol{\Upsilon}_1 - y\boldsymbol{\Upsilon}_2| \leq s$. If the condition is met, $\mathbf{Q} = \mathbf{O} + x\boldsymbol{\Upsilon}_1 + y\boldsymbol{\Upsilon}_2$. The resulting seven regions are outlined in Table 2.2.[2]

Face:	(A) $0 \leq \mathbf{a}$, $0 \leq \mathbf{b}$, $\mathbf{a} + \mathbf{b} \leq 1$		
Edge:	(B) $\mathbf{a} < 0$, $0 \leq \mathbf{b} \leq 1$	(C) $\mathbf{b} < 0$, $0 \leq \mathbf{a} \leq 1$	(D) $\mathbf{a} \leq 1 + \mathbf{b}$, $\mathbf{b} \leq 1 + \mathbf{a}$, $\mathbf{a} + \mathbf{b} > 1$
Corner:	(E) $\mathbf{a} < 0$, $\mathbf{b} < 0$	(F) $\mathbf{a} > 1$, $\mathbf{b} < \mathbf{a} - 1$	(G) $\mathbf{b} > 1$, $\mathbf{a} < \mathbf{b} - 1$

Table 2.2: Overlap cases for a particle with a triangle. **top row-** the case where the particle is flush against a face of the triangle; **middle row-** cases where the particle is closest to an edge of the triangle; **bottom row-** cases where the particle is closest to a corner.

2.2.5 Infinite cylinder

The infinite cylinder is an infinitely long, hollow circular shaft defined by taking $\mathbf{O}$ to be any point along the cylinder axis, $\hat{\mathbf{N}}$ as the orientation of the axis, and R as the radius of the cylinder. The overlap test is $\max\{R - s; 0\} \leq \rho_T \leq R + s$. If the condition is met, the contact point $\mathbf{Q} = \mathbf{O} + \boldsymbol{\rho}_N + R\hat{\mathbf{T}}$. If $\rho_T = 0$, which corresponds to the case where the particle is centered exactly on the cylinder axis, no force is felt by the particle, even if $s > R$.

[2] At present, the code has cases D, F, and G collapsed into a single case.

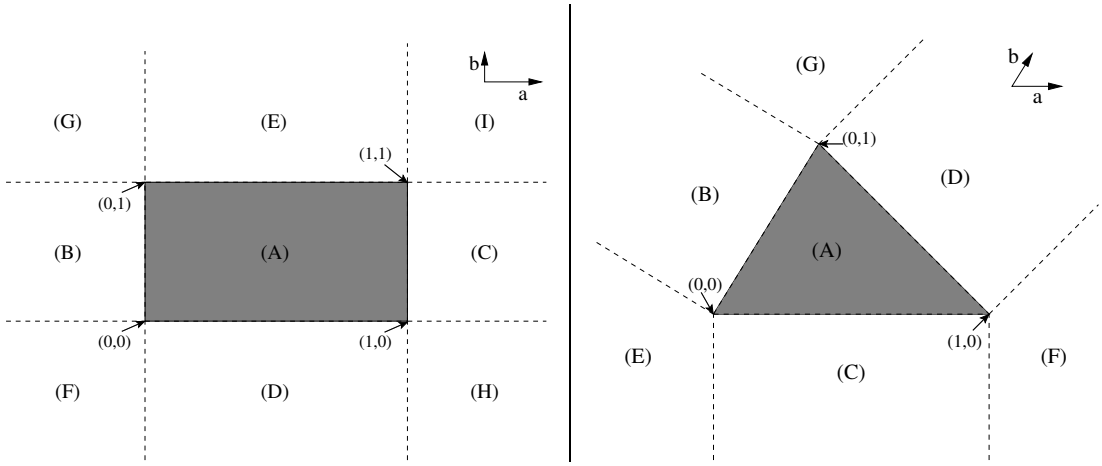

Figure 2.2: Illustrations of regions (A)–(I) for the rectangle primitive (left) and regions (A)–(G) for the triangle primitive (right) from Tables 2.1 and 2.2, respectively. After a particle is determined to intersect with the infinite plane that contains a rectangle, space is divided into the 9 regions shown in the image on the left (or into the 7 regions shown in the image on the right, in the case of the triangle). The region on which the particle's center lies when projected upon the infinite plane determines which point, line, or surface the particle will be tested against for overlap. Shaded regions represent the primitive; dashed lines extend to infinity.

2.2.6 Finite cylinder

The finite cylinder is defined by the same parameters as the infinite cylinder plus the total length along the cylinder axis, L, and the "taper," τ, which gives the ratio of the narrow end of the cylinder to the wide end of the cylinder. Allowed values of τ range from 0 to 1 inclusive, with 0 indicating constant cylinder radius and 1 indicating a closed funnel or cone. In addition, R, $\hat{\mathbf{N}}$, and $\mathbf{O}$ now have more specific meanings: R defines the radius of the wide end, $\hat{\mathbf{N}}$ gives the orientation of the cylinder—pointing along the cylinder axis from the wide end to the narrow end—and $\mathbf{O}$ defines the midpoint along the cylinder axis between the two ends.

For the overlap test, the code first considers a cylindrical region of space aligned along the orientation axis with length $L + 2s$ centered on the origin, with an inner radius of $\max\{R_\tau - s; 0\}$, where $R_\tau \equiv \tau R$, and an outer radius of $R + s$. The entire

finite cylinder, as defined by the parameters $\mathbf{O}$, $\hat{\mathbf{N}}$, R, L, and τ, as well as any particle of radius s that could be in contact with it, is contained within this region of space. If the particle in question has its center outside this region, it cannot be in overlap with the finite cylinder. Otherwise the particle is subject to the following overlap test.

I define $\mathbf{P}_{R_\tau}$ to be the point on the narrow rim of the cylinder that is closest to the particle's center; this is given as $\mathbf{P}_{R_\tau} = R_\tau \hat{\mathbf{T}} + \frac{L}{2}\hat{\mathbf{N}}$. I define $\mathbf{P}_R$ to be the point on the wide rim of the cylinder that is closest to the particle's center; this is given as $\mathbf{P}_R = R\hat{\mathbf{T}} - \frac{L}{2}\hat{\mathbf{N}}$. Next the point on the line segment connecting points $\mathbf{P}_{R_\tau}$ and $\mathbf{P}_R$ that is closest to point $\boldsymbol{\rho}_T$ is found:

$$c'' = \frac{(\mathbf{P}_{R_\tau} - \mathbf{P}_R) \cdot (\boldsymbol{\rho} - \mathbf{P}_R)}{|\mathbf{P}_{R_\tau} - \mathbf{P}_R|^2}, \tag{2.41}$$

$$c' = \max\{0; c''\}, \tag{2.42}$$

$$c = \min\{c'; 1\}, \tag{2.43}$$

$$\mathbf{P}_c = c\mathbf{P}_{R_\tau}, \tag{2.44}$$

where $\mathbf{P}_c$ is the potential contact point (relative to the origin). The overlap condition is $|\mathbf{P}_c - \boldsymbol{\rho}| < s$, where s again is the radius of the particle. If this condition is met, the contact point $\mathbf{Q}$ is taken to be $\mathbf{O} + \mathbf{P}_c$.

As in the case of the disk, there is the special case of $\rho_T = 0$, where the particle is centered on the axis of the cylinder. If there is an overlap in this case, the overlap occurs over a ring that is symmetric around the cylinder axis, and therefore the overlap is radially symmetric. The net force could only point along the axis, so the strategy used here is to create a "phantom" overlap point on the axis that penetrates the particle by the same amount as it is penetrated by the ring. In cylindrical coordinates, the angle is degenerate, and thus the computations can be

done in two dimensions, saving time. After first ruling out the overlap ahead of time if $s < R_\tau$, the code considers whether force should be applied in the positive $\hat{\mathbf{N}}$ direction or the negative $\hat{\mathbf{N}}$ direction. When $\rho_T = 0$ and $\boldsymbol{\rho}\cdot\hat{\mathbf{N}} > L/2$, this corresponds to the first case, where the particle is on the cylinder axis with its center outside of the cylinder on the side of the narrow rim (the centers of both rims, narrow and wide, lie in the same direction from the particle center, but the center of the narrow rim is closer). Here, the overlap condition is $R_\tau^2 + (L/2)^2 < s^2$, with $\mathbf{Q} = \mathbf{O} + \boldsymbol{\rho} - [R_\tau^2 + (L/2)^2]^{1/2}\,\hat{\mathbf{N}}$. Conversely, the force must be applied in the negative $\hat{\mathbf{N}}$ direction when the particle is centered on the cylinder axis and if either τ is nonzero or $\boldsymbol{\rho}\cdot\hat{\mathbf{N}} < -L/2$. Only tapered cylinders ($\tau > 0$) will push out a particle whose center is inside the cylinder and exactly on the axis, so particles inside a non-tapered cylinder are ignored. Strictly speaking, both tapered and non-tapered cylinders should provide frictional stability to particles with radii larger than the cylinders of which they are inside. The code has a way to handle this, but not in the case where the particle is centered exactly on the cylinder axis. This will be a future feature if needed. In the meantime, for the overlap condition in this case, Eqs. (2.41)–(2.44) is used to determine $\mathbf{P}_c$, using corresponding two-dimensional values for $\boldsymbol{\rho}$, $\mathbf{P}_{R_\tau}$, and $\mathbf{P}_R$. If the overlap condition is met, $\mathbf{Q} = \mathbf{O} + \mathbf{P}_c$.

2.3 Comparison to hopper experiments

Experiments of flow from cylindrical hoppers are ideal benchmark tests for numerical simulations, since such flows have been a matter of practical interest for some time (see Nedderman et al. 1982 for background summary). Moreover, empirical relations between mutual parameters involved in these systems have been formulated and rigorously tested, and these provide stringent constraints for the validation of

granular physics codes. Hence Bertrand et al. (2005) suggest the use of the well-explored, fairly simple regime of a particle hopper as a test for collisional codes for which there is much experimental data in the literature. This suggestion is followed as the choice for a validation experiment. Other tests could be considered, but given a particular interest to explore them in more detail in the context of planetary science applications, I elect to leave them for future dedicated studies (see Section 2.4 for some examples).

In this section, I briefly describe the empirical relations that I aim to reproduce, taken primarily from (Nedderman et al. 1982), explain the simulation setup, present the results, and then finally compare these results to the empirically derived, analytical relations.

2.3.1 Using wall primitives to construct the hoppers

Combinations of two of the primitives described above, the disk and the finite cylinder, were used to construct the hoppers. For each hopper of radius R_{hopper}, I used finite cylinders with radius $R = R_\tau = R_{\text{hopper}}$ (no taper) and height H, with a confining bottom disk of radius $R_{\text{out}} = R_{\text{hopper}}$ ($R_{\text{in}} = 0$ at this stage) to simulate the hoppers. In order to fill the hoppers, I attached a large finite cylinder of outer radius R_{funnel} and taper τ such that $R_\tau = \tau R = R_{\text{hopper}}$ to act as a funnel. To commence particle flow, I replaced the disk at the bottom of the hopper with one of identical properties, except that instead of having $R_{\text{in}} = 0$, R_{in} was set to be the desired radius of the aperture.

2.3.2 Empirical findings

Beverloo et al. (1961) found a correlation between the aperture size of a cylindrical hopper and the (mass) flow rate to the 2/5 power:

$$W^{2/5} \propto D + Z, \tag{2.45}$$

where W represents the discharge rate of the hopper in mass per unit time, D is the aperture diameter, and Z is the offset found in the correlation. The 5/2 dependence on the aperture diameter makes intuitive sense as the flux, W, should depend on the product of the aperture area, A, and the velocity normal, v. The area is proportional to D^2, and if one makes the assumption that there exists a height from which the particles begin to free fall above the outlet, and that this height is linearly proportional to D, then one gets an additional dependence of $\sqrt{D}$ from the downward speed of the particles as they exit through the outlet. Through dimensional analysis (Nedderman et al. 1982), the discharge rate also depends linearly on density and should go as the square-root of the acceleration due to gravity.

I will compare the results to the empirical relation

$$W = C\rho\sqrt{a_g}(D - kd)^{5/2}, \tag{2.46}$$

where ρ is the particle density, a_g is the acceleration due to gravity, D is the aperture diameter, and d is the particle diameter (for a monodisperse particle system), while C and k are unitless constants.

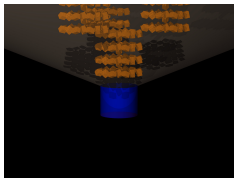

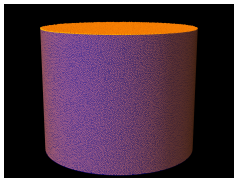

Figure 2.3: Using numerical boundary conditions, hoppers are filled by first suspending randomly oriented rectangular arrays of particles in cubic-close-pack configurations over a funnel that deposits the particles (1 cm radius) into the initially empty hopper (left). After allowing particles to settle, the funnel, along with any excess particles above the hopper rim, are removed, leaving a hopper full of particles (right, zoomed image). This particular example used about 1.5 million particles and a hopper 2.4 m across.

2.3.3 Simulation setup

To construct a hopper of radius R_{hopper}, a cylindrical boundary of that radius and height H sufficiently large relative to the radius (i.e., large enough such that a constant discharge rate should be achieved in most cases) was defined, along with a confining bottom disk also of radius R_{hopper} (see the Appendix for an explanation of the types of boundary primitives that were used and how they are integrated into the code). In order to fill the hopper with particles, a large funnel was placed atop its rim such that the narrow end of the funnel had radius R_{hopper}. I then suspended randomly oriented rectangular arrays of monodisperse particles in cubic-close-pack configuration within the funnel portion of the cylinder (Fig. 2.3a). Next, gravity was turned on to fill the hopper, then removed the funnel and shaved off the particles that were left heaping up over the rim of the cylinder (Fig. 2.3b). I then used these initial conditions and placed circular holes of varying sizes into the centers of the bottom disk to measure properties such as the discharge rate, the velocity distribution, and the distribution of stresses on the particles within the hopper; discharge profiles for various hopper configurations are shown in Fig. 2.4 and are discussed further below. In addition to discharging the hopper with varying aperture sizes, I also discharged

it using an array of densities and material properties (represented by parameters k_n, k_t, ε_n, C_t, μ_s, μ_r, ρ). We also performed some runs varying a_g and R_{hopper}. I allowed every discharge simulation to run until the hopper was nearly empty, which provided the ability to test how discharge rate depends on the height of the particles remaining in the cylinder (there should be no dependence until the hopper is close to empty). In each case, I used 0.8 for the coefficient of restitution of all boundaries (walls), and a static friction coefficient identical to the particle-particle coefficient used in the given simulation.

Simulations provide the benefit of being able to capture directly the instantaneous state of the system throughout, including all of the positions and motions of each particle, and the forces acting on them, and seeing how the state of the system evolves. For example, the ability exists to trace the contact forces and construct a map of the force network, and then see how this evolves in time (cf. Fig. 2.5). A total of 61 hopper discharges were simulated, using an estimated 7.2x10^4 CPU hours, with $\sim$ 3 GHz cores. A range of physical and material parameters were used, and insight was gained on how these parameters affect the rate and quality of the discharge (see Table 2.3). Some of the more important dependencies are discussed below.

2.3.4 Results

For the primary task, the 5/2 dependence of the flow rate on $(D - kd)$ was explored to ensure that the code is able to reproduce this satisfactorily. I also explored the dependence on ρ, a_g, H, the height of the particles in the hopper, R_{hopper}, and the material parameters of the particles. Here, just a few of these relations are described—see Table 2.3 for estimates of the steady-state flow rate for all 61 simulations. Estimates of the steady-state flow rates can be found because the flow

is independent of the height of the particles remaining inside the hopper. It was demonstrated (e.g., by Janssen 1895; Shaxby & Evans 1923) that the walls of the hopper itself bear the majority of the weight of the particles and that the stress near the aperture is largely unaffected by the height of the material in the hopper until it gets below a certain level (e.g., see Fig. 2.4). Rose & Tanaka (1959) argue that the flow rate stays constant even below this level, until the height of the material in the hopper becomes comparable to the size of the aperture, but it was found that this occurs earlier.

Figure 2.6 shows the flow rate as a function of D for different sizes of the hopper drainage aperture. Using least-squares minimization, a function in the form of Eq. (2.46) was fit using the flow rates derived from simulations (Sims.) 7, 27–30, 53, and 59–61, solving for the constants C and k (0.697 ± 0.003 and 2.32 ± 0.07 were found, respectively), with ρ, g, d, and all other material constants held fixed (see Table 2.3 for the values of these parameters). The nine simulations chosen for this fit use hopper radii of 80 cm with aperture radii of 10, 15, 20, 25, and 30 cm and hopper radii of 120 cm with aperture radii of 35, 40, 45, and 50 cm, taking care to ensure that all hoppers were wide enough such that increasing the width further had no effect on flow rate (e.g., in Fig. 2.7, discharge rates through apertures of 10 cm and 15 cm were compared, varying the sizes of the hoppers to find a range of hopper sizes where the flow rates are independent of the hopper size). The slope derived from the simulated flow rates matches well that of the empirical relation so long as the width of the hopper is large enough relative to the size of the hole (the flow rates are too high from narrow hoppers of 20 cm radius, especially for Sim. 42 where the hole size is 15 cm, as can be inferred from Figs. 2.4, 2.6, and 2.7).

The flow rate should be linear with respect to the bulk density of particles ($\phi\rho$, as is defined in Section 2.1.1)—that is, varying the value of $\phi\rho$ should have no effect

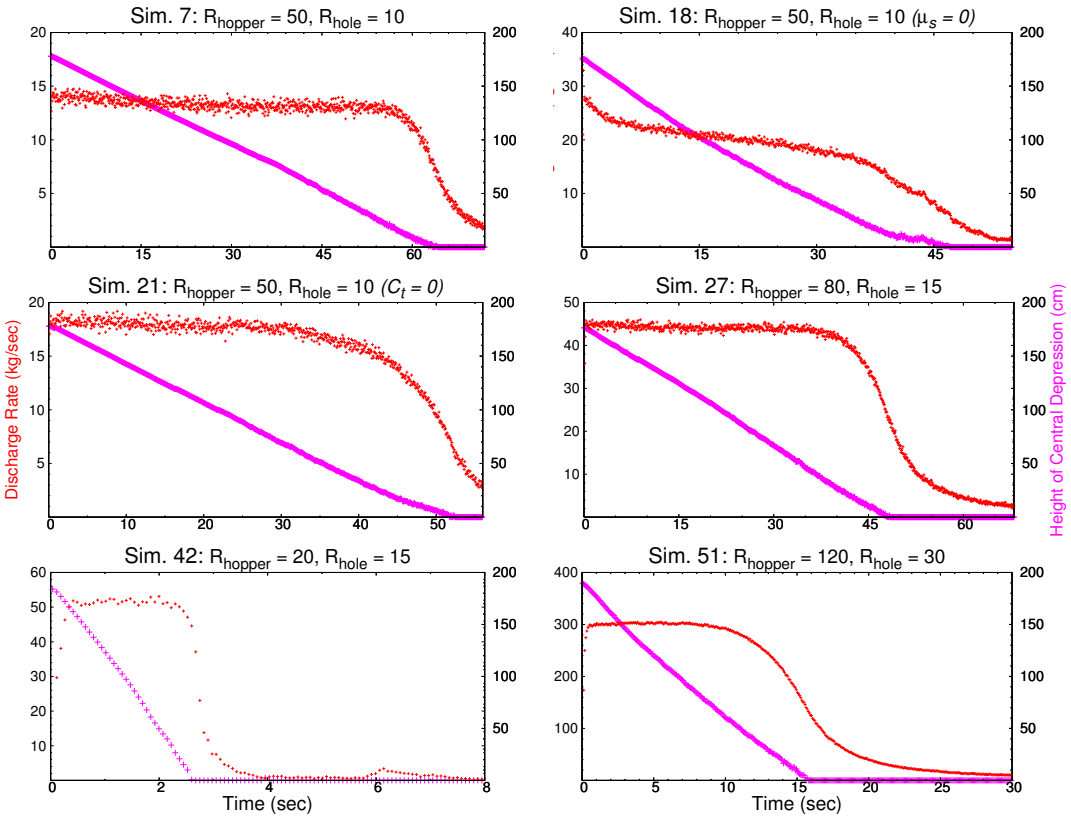

Figure 2.4: Discharge rate in kg s^{-1} (red/small crosses) and height of particles above the center of the hole (magenta/larger crosses) vs. time for six different hopper discharge simulations (see Table 2.3 for a list of parameters for each simulation). Sims. 7 (upper-left), 27 (middle-right), 42 (lower-left), and 51 (lower-right) have the same material parameters and differ only by the widths of the hoppers and the widths of their apertures. The radii of these hoppers are 50 cm, 80 cm, 20 cm, and 120 cm, respectively; their aperture radii are 10 cm, 15 cm, 30 cm, and 15 cm, respectively. Sims. 18 and 21 are identical in both hopper size and aperture size to Sim. 7, but each has a single material parameter that differs: Sim. 18 has $\mu_s = 0$ and Sim. 21 has $C_t = 0$. In both of these two cases, the height of the particles in the hopper was not enough to produce a steady flow rate (although Sim. 21 showed a flow rate that was flatter and more sustained than that of Sim. 18). Sims. 27 and 42 differ only in hopper radius—their aperture radii are identical, which shows that the correlation found in Beverloo et al. (1961) fails as the radius of the aperture approaches the radius of the hopper, as they predict. Note that it takes only a few seconds for essentially all of the particles in Sim. 42 to drain from the hopper.

on the *number* of particles that are discharged over a period of time, as is shown in Fig. 2.8, which relates the particle flow rate to individual particle density (ρ) and to initial bulk density ($\phi\rho$) for equal-sized particles. The number of particles discharged per unit time could also be expected to be independent of individual particle density ρ, however, since the same value is used for the stiffness parameter k_n in all those simulations, the hoppers that are filled with more dense particles have material that is more compacted than those that are filled with less dense particles. This means that the hoppers that are filled with more dense particles will have an increased (mass) flow rate roughly in proportion to the increase in bulk density of the material inside the hopper, which explains what is seen in Fig. 2.8.

Several simulations were carried out with different k_n and k_t. A greater value of k_n should result in a slightly slower discharge rate for a similar reason that greater particle mass density shows a slightly faster discharge rate: the bulk density $\phi\rho$, increases with either a decrease in k_n or an increase in particle density. However, since the material this is used is already quite stiff, using a larger value of k_n does not significantly decrease the degree of overlap and thus has little effect on $\phi\rho$. In fact, comparing the differences in flow rate between Sims. 7 and 55 in Table 2.3, slightly faster flow at higher k_n could be occurring, although the difference is very small and potentially not significant. However, in light of the discussion at the end of Section 2.1.1 about using a "softened" k_n to speed up certain simulations, it will be useful to know the full effects, even subtle ones, that come with using different values of k_n. One might speculate that the higher k_n could be leading to an effective decrease in tangential friction since the time that some particle pairs are in contact is shortened, and that this effect is greater than the opposing effect of having slightly greater packing. In fact, Sims. 7 and 20 have the same 7/2 ratio of k_n/k_t, and may imply a decrease in flow rate at higher stiffness (this ratio is a natural choice: it

comes out of Eq. (2.30) as the stiffness ratio needed to keep normal and tangential oscillation frequencies equal in the hard-sphere limit ignoring the effect of damping on frequency). Increasing k_t alone (Sim. 7 vs. Sim. 19) appears to impede the flow rate. Although these simulations allow us to see some trends, a much more complete study of these parameters would be necessary to draw any firm conclusions.

The flow rate correlates fairly well with the square root of the gravitational acceleration a_g, which agrees with the result given by dimensional analysis. A fit was performed to the equation $W = \beta_1 a_g^{0.5}$ (the dotted/magenta line in Fig. 2.9), solving for β_1, and to $W = \beta_2 a_g^{\gamma}$ (the dashed/blue line), solving for β_2 and γ. The reduced χ^2 is lower by a factor of three when using $\gamma = 0.55$ compared with $\gamma = 0.5$. A higher value of γ was reported (0.6) experimentally by Hofmeister et al. (2009) using a quasi-2D hourglass setup. It could be speculated that net tangential frictional effects may depend on the strength of the gravitational field in real-world experiments, and then reflected in the simulations. This will certainly be an important area to explore in light of the anticipated applications of the code into different gravitational environments.

The influence of static friction μ_s on the flow rate was also investigated. Sims. 7, 18, 43, and 44 were made using a range of values of μ_s from 0 to 0.8 (see Table 2.3). I find that the flow rate decreases with increasing static friction (see Fig. 2.4). This finding, along with the dependence on k_t, seems to contradict the experimental findings made by Beverloo et al. (1961), which indicate that the flow rate is independent of all material properties other than shape. However, this may only be true within the narrow range of static friction values that can be explored easily experimentally. Over the wider range of values that these computer simulations can investigate, I find that the experimental conclusion cannot be generalized, and that some values of the static friction can influence the flow rate. This is an inherent

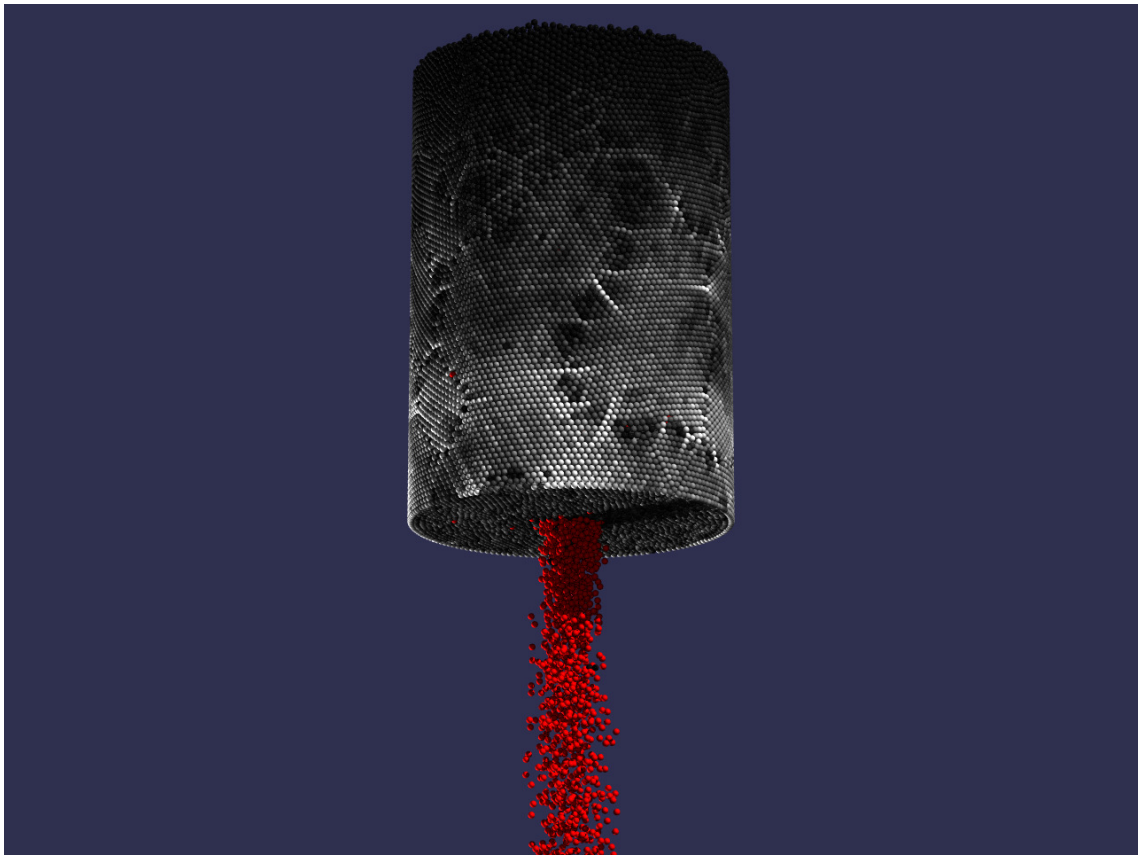

Figure 2.5: Snapshot of Sim. 24 (see Table 2.3 for simulation parameters) showing the network of normal force distribution on particles at the hopper wall after 12.2 seconds of discharge. Particles under maximum stress are shown in white; darker particles feel less stress; red particles (mostly flowing out the bottom) feel no stress.

advantage of computer simulations over real-world experiments: the ability to explore a wide, and sometimes experimentally unreachable, parameter space. I also find that it takes longer (if even possible) to achieve a constant flow rate with μ_s set to zero (see Fig. 2.4). Similarly, setting the tangential damping parameter C_t to zero (Sim. 21 in Fig. 2.4) increases the flow rate and the time needed to achieve a steady flow. Moreover, Sims. 21, 7 and 24 were performed with ϵ_t equal to 0, 0.65, and 0.1, respectively (see Table 2.3). They show that an increase in C_t may weakly inhibit flow, but the parameter significantly affects the packing and distribution of stresses, especially near the silo walls.

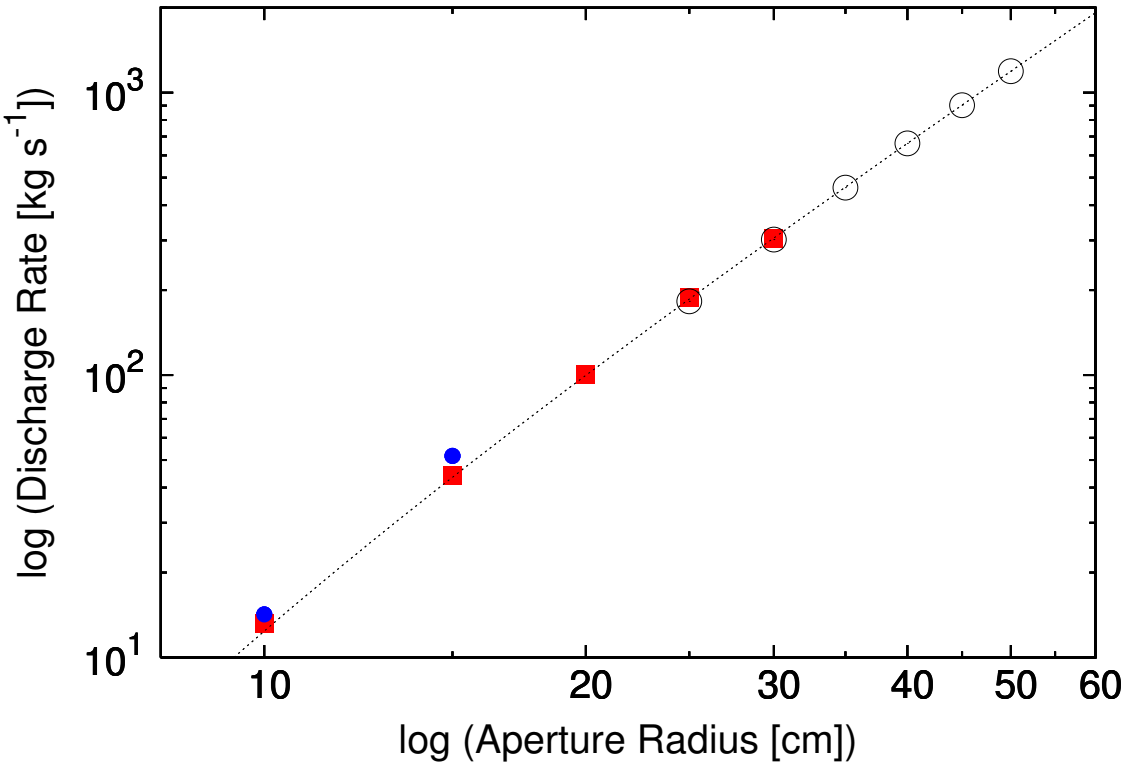

Figure 2.6: Discharge rate as a function of hole size (log-log scale). The filled (red) squares represent simulations from hoppers of radius 80 cm (Sims. 13, 27–30), the open (grey) circles represent simulations from hoppers of radius 120 cm (Sims. 51, 53, 54, 59–61), and the filled (blue) circles represent simulations from hoppers of radius 20 cm (Sims. 1, 42). The dashed line is a least-squares fit for the material constants C and k in the function represented by Eq. (2.46). The rate of flow conforms well to the correlation found by Beverloo et al. (1961), Eq. (2.45). Note the apertures for the 20-cm hoppers (filled/blue circles) are very large relative to the hoppers, resulting in the observed deviation from the empirical model.

The influence of the parameter ε_n was also investigated. Sims. 22, 23, and 7 were performed using ε_n equal to 0.2, 0.5, and 0.8, respectively, with $\epsilon_t = 0.65$ for each. They show that the flow rate has essentially no dependence on ε_n. However, a comparison of Sims. 25 and 24, which were performed with ε_n equal to 0.2 and 0.8, respectively, but with a higher value 0.1 of ϵ_t, shows that there could be a greater influence of ε_n on the flow rate at high values of C_t (low values of ϵ_t), but this inference would need to be investigated further.

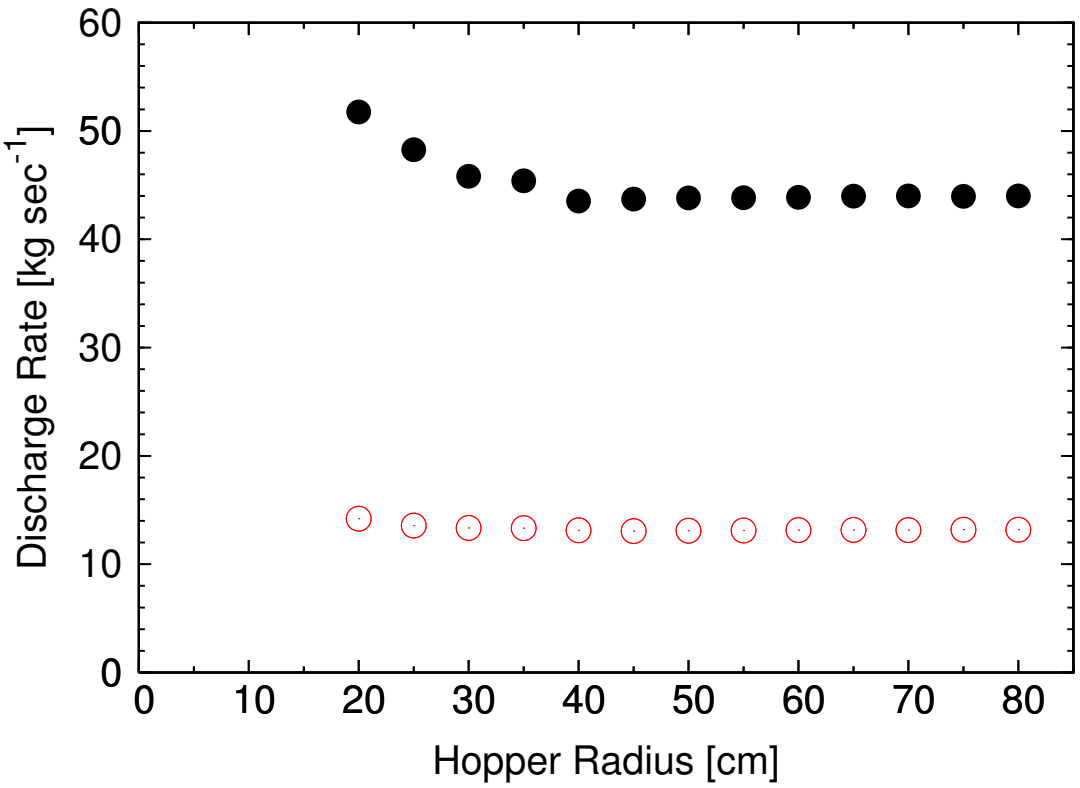

Figure 2.7: Discharge rate as a function of hopper radius. The open (red) circles represent simulations that have aperture radii of 10 cm (Sims. 1–13), and the filled (black) circles represent simulations that have aperture radii of 15 cm (Sims. 27, 31–42). It can be seen that the rate of flow is largely independent of the radius of the hopper provided that it is large enough with respect to the radius of the opening at the bottom of the hopper. Note, however, that estimates of steady-state discharge rates can be less reliable for simulations with hole sizes approaching the sizes of the hopper (see Sim. 42 in Fig. 2.4 for the most extreme case that was simulated).

A simulation (Sim. 26) was also performed using non-zero values of μ_r and μ_t, both set equal to 0.5. It shows a decrease in flow rate, as expected for such a high value of these friction parameters.

Finally, the sensitivity of the results on the timestep was checked. As is shown by comparing the steady-state discharge rates of Sims. 7 and 14–17, no significant change in discharge rate was found when using smaller timesteps, but otherwise identical parameters, indicating that the choice of timestep (3 μs) is a reasonable

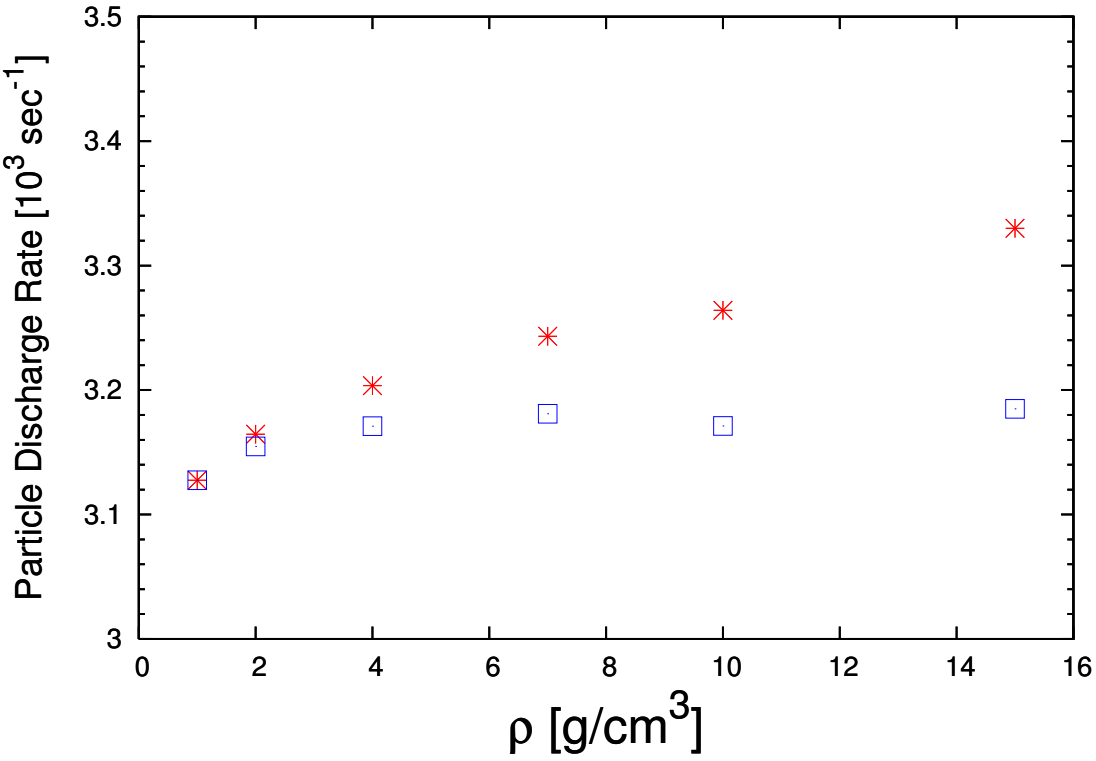

Figure 2.8: Discharge rate (in number) vs. particle density. (Red) asterisks show the discharge rate at different mass densities. (Blue) squares show this discharge rate divided by the initial porosity of the material inside the hopper at that density. Notice that the slope is close to constant if one considers bulk density (blue/squares), in agreement with Beverloo et al. (1961), whereas the rate increases if one considers the density of individual particles (red/asterisks) due to increased compaction at higher densities.

one.

2.4 Conclusions and perspectives on this work

The soft-sphere discrete-element method (SSDEM) has been implemented in the N-body code PKDGRAV. SSDEM allows for the realistic modeling of contact forces between particles in granular material. To account for surface deformation of particles at contact, colliding particles are allowed to overlap, during which time they are subject to forces that work to oppose deformation, and which depend on the relative

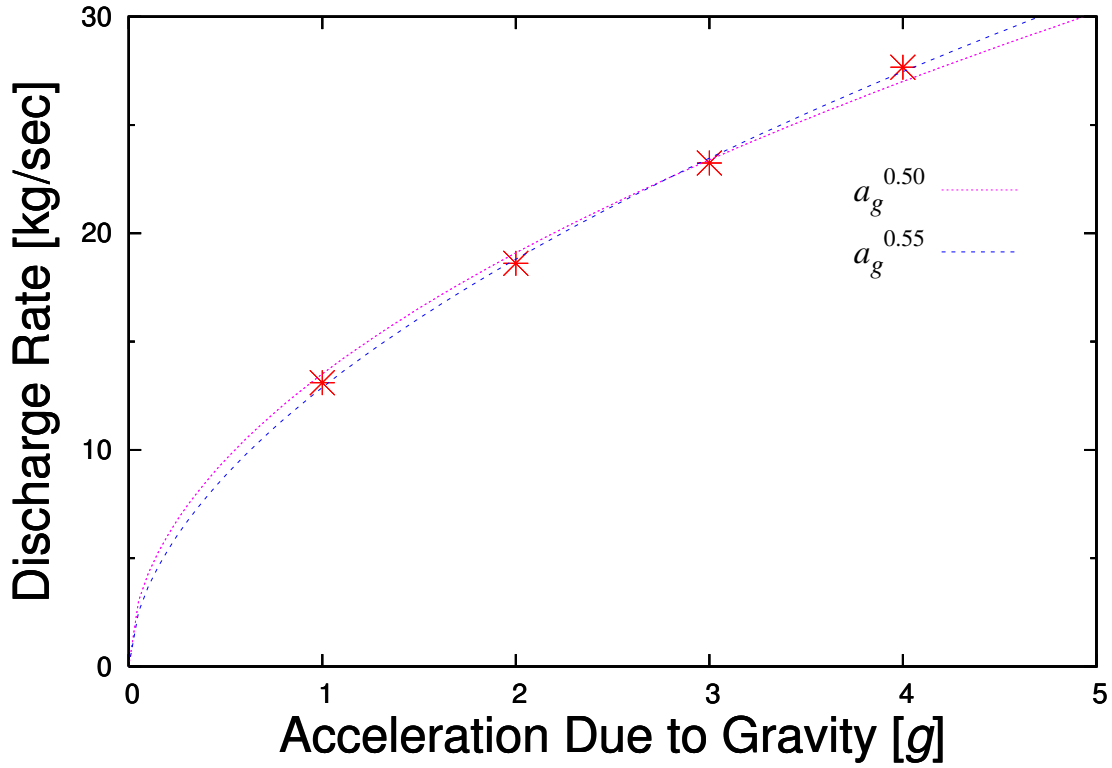

Figure 2.9: Discharge rate as a function of the acceleration due to gravity, a_g. The (red) asterisks are data from the simulations; the (magenta) dotted line gives a $a_g^{0.5}$ dependence; the (blue) dashed line is the best fit to the data, $a_g^{0.55\pm0.02}$, found by minimizing χ^2. Note that the rate found at $4g$ used material with a higher k_n, which may affect the flow rate; however, at these values of k_n, the effect on flow rate is small (see discussion in Section 2.3.4). Data points come from Sims. 7, 53, 57, and 58.

spins and velocities of the particles, their material properties, and the history of the contact. Different frictional forces were taken into account, including rolling and twisting friction, which are often neglected in SSDEM implementations. Moreover, the computation time is optimized thanks to the sophisticated parallelization and tree-code algorithms that are part of the PKDGRAV functionality, which allows all instances of particle overlap to be found in an efficient manner.

I performed a validation test for the numerical code and SSDEM implementation by reproducing successfully the dynamics of granular material flows in cylindrical hopper experiments. A series of empirical relations between mutual parameters in-

volved in these systems have been formulated and rigorously tested by experimental studies, which allows us to test whether this granular physics code gives results that are consistent with those relations. The ability of the numerical code to consider wall boundaries with a wide range of geometries allows us to simulate with great precision the setup of the experiments, in particular the design of the cylindrical hopper. Using the same types of setups that were used in the experiments, it was found that the empirical relations that describe the experimental outcomes can also be used to describe the outcomes of the simulations. Moreover, in simulations, one has the benefit of being able to track the instantaneous state of the system throughout, and seeing how the state evolves, something that cannot, in general, be done experimentally. In particular, the contact forces can be traced, and, from this, a map of the force network can be constructed to see how this network evolves in time. In other words, the dynamics of the system can be investigated in great detail as it evolves, allowing for a better understanding of the dynamical evolution. Furthermore, the sensitivity to those parameters salient to the dynamics of the system can be determined. Sixty-one simulations of hopper discharges were performed, covering a wide range in parameter space. In addition to matching experimental outcomes in most cases, it was found, for instance, that over a range of values of the static friction going from 0 to 0.8, the flow rate increases with decreasing static friction, while such an influence on a much narrower range of values was not identified experimentally, which led to the apparently incorrect conclusion that the flow rate is independent of all material properties other than shape. The influence of other parameters (such as the normal and tangential coefficients of the spring constant used to model the particle's deformation at contact, along with their respective viscous damping terms, and the acceleration due to gravity) on the flow rate was also explored.

Further comparisons to experiments will be performed, such as flows in a tumbler, avalanches, and other phenomena that will test the ability of the code to reproduce the behavior of granular materials in a wide range of contexts. The ultimate goal is to be able to apply the method to planetary science studies (e.g., low-speed impacts on regolith, regolith evolution on solid celestial bodies' surfaces, etc.). Important interpretations of images obtained by spacecraft of planetary and small bodies' surfaces can then be provided, which will aid in the design of devices that will interact with extraterrestrial surfaces (anchors, sample collectors, and so on). Such devices are to be aboard sample-return missions to asteroids (e.g., JAXA's Hayabusa2, to be launched in 2014; OSIRIS-REx, to be launched by NASA in 2016; and MarcoPolo-R, in selection phase at ESA). Also, since the shapes of the grains, as well as the cohesion between them, can have a great influence on their dynamics, one of the next steps will be to account for shape effects and to include cohesive forces in the numerical tool (Chapter 3).

Table 2.3: Complete list of simulation parameters and corresponding steady-state discharge rates that were achieved. Non-default SSDEM parameter values are boldfaced. The last column gives the uniform downward acceleration due to gravity that was used in each simulation, in units of Earth's gravity. (See text for a definition of the other parameters indicated in the table.)

Sim. #	Discharge rate (10^4 g s^{-1})	Hopper radius (cm)	Hole radius (cm)	Particle density (g cm^{-3})	Time-step (10^{-6} s)	k_n (kg s^{-2})	k_t (kg s^{-2})	ε_n	ϵ_t^*	μ_s	μ_r, μ_t	a_g (g)
1	1.421	20	10	1	3	8x10^4	2.29x10^4	0.8	0.65	0.2	0.0	1
2	1.357	25	10	1	3	8x10^4	2.29x10^4	0.8	0.65	0.2	0.0	1
3	1.335	30	10	1	3	8x10^4	2.29x10^4	0.8	0.65	0.2	0.0	1
4	1.333	35	10	1	3	8x10^4	2.29x10^4	0.8	0.65	0.2	0.0	1
5	1.313	40	10	1	3	8x10^4	2.29x10^4	0.8	0.65	0.2	0.0	1
6	1.306	45	10	1	3	8x10^4	2.29x10^4	0.8	0.65	0.2	0.0	1
7	1.310	50	10	1	3	8x10^4	2.29x10^4	0.8	0.65	0.2	0.0	1
8	1.312	55	10	1	3	8x10^4	2.29x10^4	0.8	0.65	0.2	0.0	1
9	1.315	60	10	1	3	8x10^4	2.29x10^4	0.8	0.65	0.2	0.0	1
10	1.316	65	10	1	3	8x10^4	2.29x10^4	0.8	0.65	0.2	0.0	1
11	1.314	70	10	1	3	8x10^4	2.29x10^4	0.8	0.65	0.2	0.0	1
12	1.318	75	10	1	3	8x10^4	2.29x10^4	0.8	0.65	0.2	0.0	1
13	1.319	80	10	1	3	8x10^4	2.29x10^4	0.8	0.65	0.2	0.0	1
14	-[a]	50	10	1	12	8x10^4	2.29x10^4	0.8	0.65	0.2	0.0	1
15	1.304[a]	50	10	1	6	8x10^4	2.29x10^4	0.8	0.65	0.2	0.0	1
16	1.314	50	10	1	1.5	8x10^4	2.29x10^4	0.8	0.65	0.2	0.0	1
17	1.313	50	10	1	0.75	8x10^4	2.29x10^4	0.8	0.65	0.2	0.0	1
18	2.064[a]	50	10	1	3	8x10^4	2.29x10^4	0.8	0.65	**0.0**	0.0	1
19	1.281[a]	50	10	1	3	8x10^4	**8x10^4**	0.8	0.65	0.2	0.0	1
20	1.303	50	10	1	1.5	**3.2x10^5**	**9.14x10^4**	0.8	0.65	0.2	0.0	1
21	1.785[a]	50	10	1	3	8x10^4	2.29x10^4	0.8	**0.0**	0.2	0.0	1
22	1.330[a]	50	10	1	3	8x10^4	2.29x10^4	**0.2**	0.65	0.2	0.0	1
23	1.326	50	10	1	3	8x10^4	2.29x10^4	**0.5**	0.65	0.2	0.0	1
24	1.274	50	10	1	3	8x10^4	2.29x10^4	0.8	**0.1**	0.2	0.0	1
25	1.356	50	10	1	3	8x10^4	2.29x10^4	**0.2**	**0.1**	0.2	0.0	1
26	1.146	50	10	1	3	8x10^4	2.29x10^4	0.8	0.65	0.2	**0.5**	1
27	4.400	80	15	1	3	8x10^4	2.29x10^4	0.8	0.65	0.2	0.0	1
28	10.06	80	20	1	3	8x10^4	2.29x10^4	0.8	0.65	0.2	0.0	1
29	18.86	80	25	1	3	8x10^4	2.29x10^4	0.8	0.65	0.2	0.0	1
30	3.047	80	30	1	3	8x10^4	2.29x10^4	0.8	0.65	0.2	0.0	1
31	4.396	75	15	1	123	8x10^4	2.29x10^4	0.8	0.65	0.2	0.0	1

[*]The quantity ϵ_t used here is not in fact the true tangential coefficient of restitution, ε_t, a quantity

Table 2.4: Hopper simulation parameters . . . . . *(Continued)*

Sim. #	Discharge rate (10^4g s^{-1})	Hopper radius (cm)	Hole radius (cm)	Particle density (g cm^{-3})	Time-step (10^{-6} s)	k_n (kg s^{-2})	k_t (kg s^{-2})	ε_n	ϵ_t	μ_s	μ_r, μ_t	a_g (g)
32	4.400	70	15	1	3	8x10^4	2.29x10^4	0.8	0.65	0.2	0.0	1
33	4.398	65	15	1	3	8x10^4	2.29x10^4	0.8	0.65	0.2	0.0	1
34	4.387	60	15	1	3	8x10^4	2.29x10^4	0.8	0.65	0.2	0.0	1
35	4.385	55	15	1	3	8x10^4	2.29x10^4	0.8	0.65	0.2	0.0	1
36	4.382	50	15	1	3	8x10^4	2.29x10^4	0.8	0.65	0.2	0.0	1
37	4.370[a]	45	15	1	3	8x10^4	2.29x10^4	0.8	0.65	0.2	0.0	1
38	4.352[a]	40	15	1	3	8x10^4	2.29x10^4	0.8	0.65	0.2	0.0	1
39	4.540[a]	35	15	1	3	8x10^4	2.29x10^4	0.8	0.65	0.2	0.0	1
40	4.582[a]	30	15	1	3	8x10^4	2.29x10^4	0.8	0.65	0.2	0.0	1
41	4.828[a]	25	15	1	3	8x10^4	2.29x10^4	0.8	0.65	0.2	0.0	1
42	5.176[a]	20	15	1	3	8x10^4	2.29x10^4	0.8	0.65	0.2	0.0	1
43	1.164	50	10	1	3	8x10^4	2.29x10^4	0.8	0.65	**0.5**	0.0	1
44	1.124	50	10	1	3	8x10^4	2.29x10^4	0.8	0.65	**0.8**	0.0	1
45	1.342	50	10	4	1.5	8x10^4	2.29x10^4	0.8	0.65	0.2	0.0	1
46	1.338	50	10	4	0.75	8x10^4	2.29x10^4	0.8	0.65	0.2	0.0	1
47	1.367	50	10	10	0.75	8x10^4	2.29x10^4	0.8	0.65	0.2	0.0	1
48	1.326	50	10	2	1.5	8x10^4	2.29x10^4	0.8	0.65	0.2	0.0	1
49	1.359	50	10	7	0.75	8x10^4	2.29x10^4	0.8	0.65	0.2	0.0	1
50	1.395	50	10	15	0.75	8x10^4	2.29x10^4	0.8	0.65	0.2	0.0	1
51	30.29	120	30	1	3	8x10^4	2.29x10^4	0.8	0.65	0.2	0.0	1
52	1.862	50	10	1	3	8x10^4	2.29x10^4	0.8	0.65	0.2	0.0	1
53	46.10	120	35	1	3	8x10^4	2.29x10^4	0.8	0.65	0.2	0.0	**2**
54	18.25	120	25	1	3	8x10^4	2.29x10^4	0.8	0.65	0.2	0.0	1
55	1.331	50	10	1	1.5	**3.2x10^5**	2.29x10^4	0.8	0.65	0.2	0.0	1
56	1.374	50	10	1	3	8x10^4	2.29x10^3	0.8	0.65	0.2	0.0	1
57	2.325	50	10	1	3	8x10^4	2.29x10^4	0.8	0.65	0.2	0.0	**3**
58	2.767	50	10	1	1.5	**3.2x10^5**	2.29x10^4	0.8	0.65	0.2	0.0	**4**
59	66.13	120	40	1	3	8x10^4	2.29x10^4	0.8	0.65	0.2	0.0	1
60	90.27	120	45	1	3	8x10^4	2.29x10^4	0.8	0.65	0.2	0.0	1
61	119.2	120	50	1	3	8x10^4	2.29x10^4	0.8	0.65	0.2	0.0	1

[a] A steady-state discharge rate was never achieved although an estimate may be shown.

Chapter 3

Cohesive Materials and Cohesive Forces

In this chapter, I present an implementation of cohesion into a numerical model aimed at the study of the dynamics of granular materials that comprise the surfaces and, in some cases, the interiors of small solar system bodies. For validation, low-speed impact experiments on glass bead agglomerates are compared against simulations using the same impact conditions with a numerical model of the experimental targets. The impact experiments were performed in Japan at Kobe University, the main results of which have been published by Machii & Nakamura (2011). In Section 3.1, I briefly present the experiments and the outcomes to be considered in this chapter for comparison with simulations. Section 3.2, describes the numerical code PKDGRAV and its adaptation to address granular material physics and cohesion (see Section 2.1 for more of the details). Comparison between experiments and simulations are then presented in Section 3.3. Conclusions and perspectives are provided in Section 3.4. Much of the material for this chapter appeared as Schwartz et al. (2013).

3.1 Kobe University impact experiments

Machii & Nakamura (2011) performed their impact experiments on sintered glass bead agglomerates using a gas gun in Kobe University in Japan. Impact speeds ranged from 40 to 280 m/s and the sintered agglomerates used as targets contained $\sim$ 40% porosity. Two kinds of targets were manufactured to differ in their bulk strength; the difference between the groups comes from the sintering times in the oven (8 hours and 20 hours). The size ratio of the beads to each target was 0.19, with the average bead size measuring $\sim$ 5 mm in diameter. The experiments showed that the energy density required to catastrophically break the agglomerate is much less than that required for previously investigated sintered glass bead targets with the same porosity (e.g., Setoh et al. (2010)). However, the sizes of the beads that comprised those targets and the size ratio of the beads to the targets were both 100 times smaller than the agglomerates used by Machii & Nakamura (2011). The authors suggest that this weaker strength is probably due to the much smaller number of cohesive links (necks) that a stress wave must travel through in this study, which minimizes the energy dissipation at the necks (this theory will be investigated and quantified in a future numerical study). Also, the fact that the particles are larger and less numerous enables them to move more freely and thus to be broken more easily. Catastrophic disruption of an agglomerate was shown to occur when the projectile kinetic energy was a few times the total energy needed to break all of the necks of the agglomerate. The distribution of fragment size and number was shown to be extremely dependent upon the impact point of the target.

3.2 Numerical method to include cohesion

3.2.1 Adding cohesion in `pkdgrav`

In order to account for the potential presence of cohesion between grains within a granular medium such as regolith on the surfaces of solid celestial bodies, I have implemented a cohesive force into PKDGRAV. This added cohesive force acts between bonded particles' centers of mass (COMs) as a restoring force that opposes distention of the bond. Here the particle, and the neighbor to which it is bound, are called particle 1, and particle 2, respectively.

A single bond is defined by an equilibrium separation $z(\epsilon, t)$ (a zero-strain-length) between the two particles' COMs, and a maximum strain $\epsilon_{\max}(\dot{\boldsymbol{\epsilon}})$ beyond which the bond has no effect, where the strain $\epsilon(t) \equiv [\rho/z] - 1$. Previously defined as a measure of density, now $\rho \equiv |\boldsymbol{\rho}|$ is the scalar distance between the COMs (thus, when $\rho = z(\epsilon, t)$, the length of the "spring" at rest, the strain, ϵ, vanishes; recall: $\boldsymbol{\rho} \equiv \mathbf{r}_2 - \mathbf{r}_1$ is the relative position between the particle and neighbor COMs).

While $\epsilon(t) < \epsilon_{\max}(\dot{\boldsymbol{\epsilon}})$, a particle feels a cohesive force dependent upon the current strain $\epsilon(t)$, the current strain-rate $\dot{\boldsymbol{\epsilon}}(t) \equiv \mathbf{u_n}/z(\epsilon, t)$, and the effective area of interaction $A_{\rm eff}$, where $\mathbf{u} \equiv \mathbf{v_2} - \mathbf{v_1}$ is the relative velocity between the particle and the neighbor to which it is bound, $\mathbf{u_n}$ is the normal component of this relative velocity.

The default behavior, which treats $\epsilon_{\max}(\dot{\boldsymbol{\epsilon}})$ is taken as a constant $[\epsilon_{\max}(\dot{\boldsymbol{\epsilon}}) \to \epsilon_{\max}]$, independent of the strain-rate, z as a constant independent of the effect of persistent strain $[z(\epsilon, t) \to z]$, and the force on the particle due to its attached neighbor as a linear combination of a strain (elastic) component and a strain-rate (plastic) component. Also, cohesive bonds are to be broken once ϵ exceeds $\epsilon_{\max}$. In default, $A_{\rm eff} \equiv \pi s_{\rm eff}^2$, and $s_{\rm eff} \equiv (s_1 + s_2)/2$, the mean radius of the particle and its neigh-

bor. If one considers particles as effectively representing a continuum deformable agglomerate, this is an appropriate choice for the effective area of interaction, A_{eff}, especially for spheres of similar size. Although not the only option, this choice can also be justified for the area of interaction in the case of this study, when the spheres are treated as discrete particles and not a continuum (see Section 3.2.2).

In this default configuration, from the time at which the bond is formed, up until the time at which ϵ exceeds $\epsilon_{\max}$, the force on a particle due to its cohesive bond (it may have multiple bonds), assuming implicit dependencies on t of the strain and the strain-rate, is given as

$$\mathbf{F_{1,coh}} = Y\epsilon A_{\text{eff}}\hat{\mathbf{n}} + \gamma z\dot{\boldsymbol{\epsilon}}, \tag{3.1}$$

where $\hat{\mathbf{n}} \equiv \boldsymbol{\rho}/|\boldsymbol{\rho}|$ is a unit vector that gives the direction from the particle's center to the neighbor's center, Y is an elastic Young's modulus, and γ is a viscous damping term with the value for critical damping given as $\gamma_{\text{crit}} \equiv \sqrt{4\mu Y A_{\text{eff}}/z}$, with μ being the reduced mass of the two-particle system. Repulsive forces related to the cohesive bonds (for $\epsilon < 0$) can be switched on or off; it is left off by default (this is not to be confused with the normal component of the SSDEM force, which always active). Newton's Third Law gives the force felt by the neighbor due to the cohesion with the particle as

$$\mathbf{F_{2,coh}} = -Y\epsilon A_{\text{eff}}\hat{\mathbf{n}} - \gamma z\dot{\boldsymbol{\epsilon}}. \tag{3.2}$$

This treatment is equivalent to a Hooke's force law for springs with a speed-dependent damping term. Using the default implementation, as is done in this study, gives four parameters that define a cohesive bond: z, Y, $\epsilon_{\max}$, and γ. Also supported however, are more complicated force dependencies such as van der Waals force laws, a strain- and time-dependent zero-strain-length (creep), and cohesive strain limits that are dependent on strain-rates.

In order to allow for more realistic (non-idealized) behavior of cohesive agglomerates, each cohesive element (particle-particle bond) has its own values for z, Y, and $\epsilon_{\max}$, where the distribution of strength (Y) and maximum strain ($\epsilon_{\max}$) are typically fit by a gaussian distribution around specified mean values ($<Y>$ and $<\epsilon_{\max}>$).

Note also that these cohesive forces are central forces, and thus energy and momentum are conserved (although $\gamma > 0$ saps energy from the system). Forces are only applied along the line that connects the two particles' centers, thus there is no coupling with angular or tangential degrees of freedom.

3.2.2 SSDEM and cohesion

In this methodology, particles can be geometrically separated and yet still feel cohesion. This may be the case when cohesion is to be modeled between deformable particles, or to account for the existence of a physical neck that joins two sintered particles together (even if the atomic diffusion involved in the formation of the neck is not modeled explicitly). In such a case, when the separation between the COMs of two bound particles is both greater than the sum of their radii, i.e., $\rho > s_1 + s_2$, and greater than z (with $0 < \epsilon < \epsilon_{\max}$), since they feel a restoring force along the line that connects their two centers, one must also consider coupling of translational and rotational degrees of freedom. This is also the case between particles that feel mutual attraction through surface-surface interactions by way of Van der Waals forces. However, this study does not involve this type of cohesion, which requires a different prescription. Described in the following is a strategy to couple these degrees of freedom in the former case involving deformable particles.

3.2.3 Building SSDEM Cohesive Agglomerates

Setting $z < 2s_{\text{eff}}$ implies that cohesive equilibrium occurs while particles are penetrating each others' surfaces. If one imagines a setup of two mutually bound particles in isolation with zero-strain-length less than the sum of their radii, in HSDEM this amounts to the two particles pushing up against each other with some compressive force, but without ever penetrating (inter-particle penetration is not allowed in HSDEM). In SSDEM, this results in the particles penetrating each other with SSDEM repulsive forces coming into balance with cohesive forces and any mutual gravitational force that may exist between the particles. In such a case, the particles' translational and rotational degrees of freedom are coupled. Furthermore, it means that particles are subject to the full robust treatment of SSDEM contact forces (Schwartz et al. 2012c) together with cohesion. Including both elastic and plastic components, the net normal force on a particle as a result of its interaction with its neighbor, due to both cohesion and the SSDEM normal force is given as

$$\mathbf{F_1} = Y\epsilon A_{\text{eff}}\hat{\mathbf{n}} + \gamma z\dot{\boldsymbol{\epsilon}} - k_n x\hat{\mathbf{n}} + C_n\mathbf{u_n}, \tag{3.3}$$

where k_n is the SSDEM elastic coefficient given in units of kg/s^2, C_n is the SSDEM plastic coefficient given in kg/s, and x is the amount of interparticle penetration as defined in Schwartz et al. (2012c).

A number of studies have developed methodologies to allow for the representation of non-spherical shapes using ensembles of spherical particles (e.g., Gotteland et al. 2009; Azéma et al. 2012). The approach developed here also allows the build-up of arbitrarily shaped objects consisting of spheres in various states of overlap with each other. The spheres need not be of uniform size or mass, and can have differing strength parameters, which provides the freedom to simulate complex combinations of cohesive agglomerates with explicitly defined internal strength distributions.

In order to create the models for such an object, along with the SSDEM parameters, the COM position, the mass, and the radius must be defined for each particle of which it is comprised. Next, to account for cohesion within the object, `pkdgrav`'s tree code is used to perform, for each particle, a search for other particles with which it is in overlap. For each of these overlaps, a unique Young's modulus Y is assigned based upon specification, and then solve for z such that the cohesive restoring force in Eq. (3.2) just cancels the SSDEM repulsive force when the object is at rest and in a state of internal equilibrium. We define ρ_0 for a pair of overlapping particles to be the separation between their centers when the net force between them is zero for the simulation at equilibrium at the start of the simulation (this is not to be confused with z, the separation between their centers when the *cohesive* force is zero—typically ρ_0 will be greater than z). The overlap value, $x = s_1 + s_2 - \rho_0$, gives:

$$z = \frac{\rho_0 Y A_{\text{eff}}}{k_n(s_1 + s_2 - \rho_0) + Y A_{\text{eff}}}. \tag{3.4}$$

Combining Eqs. (3.3) and (3.4), and defining $\delta \equiv [\rho/\rho_0] - 1$, for an unbroken bond where $z \leq \rho \leq 2s_{\text{eff}}$, the force felt by a particle due to its interaction with its neighbor (ignoring gravity) reduces to:

$$\mathbf{F_1} = \delta \left[2k_n s_{\text{eff}} + Y A_{\text{eff}}\right] \hat{\mathbf{n}} + (\gamma + C_n)\mathbf{u_n}. \tag{3.5}$$

The fixed point at $\rho = \rho_0$ (when $\delta = 0$) can be seen in Eq. (3.5); when $\rho > \rho_0$, the elastic force on the particle pushes it toward its neighbor, and when $\rho < \rho_0$, the elastic force on the particle pushes it away from its neighbor, showing that the fixed point is stable (see Fig. 3.1 for a diagram that describes these lengths and dimensionless variables). Each particle that comprises these simulated cohesive objects exhibits this stable equilibrium with each of its neighbors. By default: $\epsilon_{\max} = \frac{2s_{\text{eff}}}{z} - 1$, breaking the bond between a pair of particles when they physically separate; this sets the tensile strength. The shear strength of the bond is set to be the

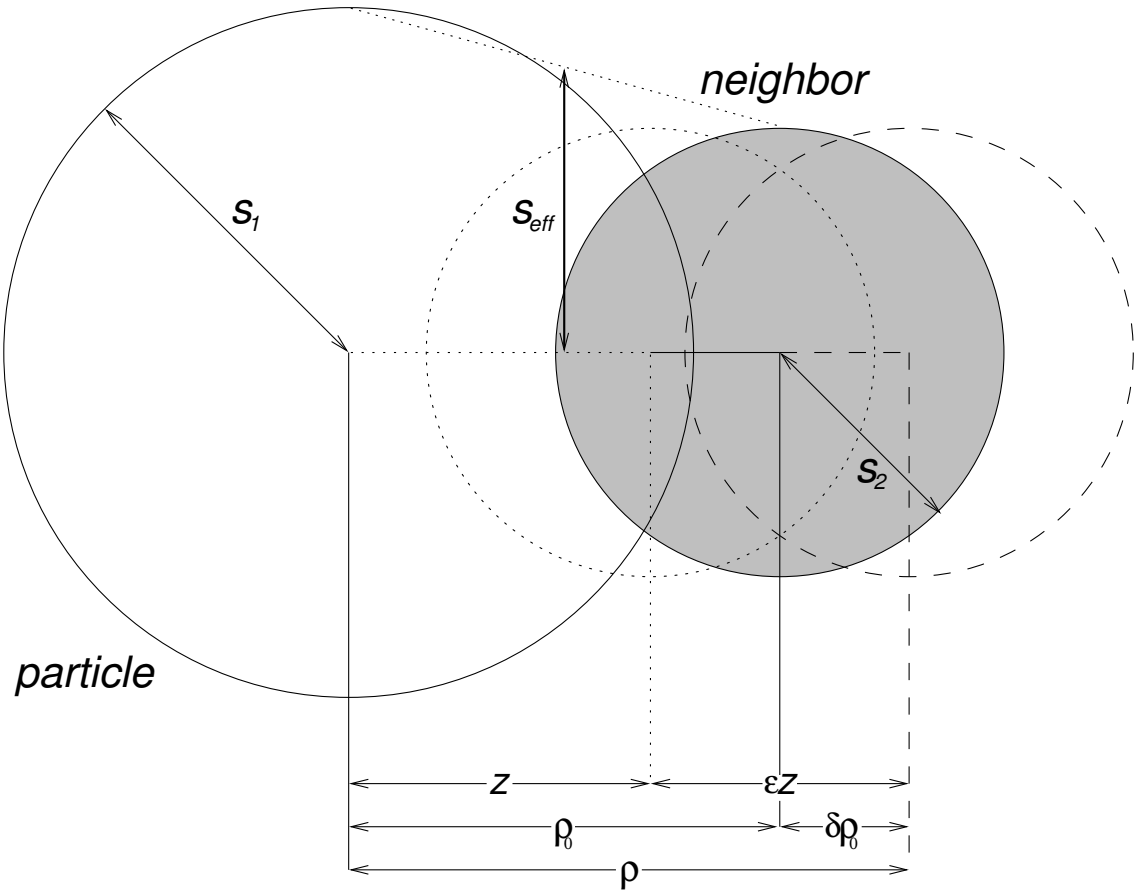

Figure 3.1: A (spherical) particle in overlap with one of its neighbors. Both the particle and its neighbor feel an attractive force due to their cohesive bond and a repulsive SSDEM force (gravity is not considered in this figure). The shaded circle gives the relative position of the neighbor such that δ is zero, and thus these two forces cancel; therefore, the net force acting on the two particles is zero when ρ_0 describes the separation between their COMs, where δ is the fractional deviation of ρ from ρ_0. The dotted circle gives the relative position of the neighbor when the strain, ϵ, is zero, and thus the cohesive "spring" that forms the bond between the particles is at rest, which occurs at a separation of z. Here ρ gives the "current" separation between the particle and its neighbor, the latter inscribed by a dashed circle; thus in this case, they feel a net attractive force since $\rho > \rho_0$, which means that the cohesive force exceeds the SSDEM repulsive force. Here s_p and s_n are the radii of the particle and its neighbor, respectively, and s_{eff} we take to be the effective radius between them. When $\rho = s_1 + s_2 = 2s_{\text{eff}}, \epsilon = \epsilon_{\max}$.

static frictional force limit, such that the bond breaks when the tangential stress exceeds the product of the coefficient of static friction and the normal force (see Schwartz et al. 2012c for an outline of my treatment of static friction in SSDEM).

In this study, the default definition of A_{eff} is used as the mean cross-section of particles in contact. In reality, the contact area between sintered particles is smaller than the mean particle cross-section, especially for weakly sintered particles. However, to avoid unnecessary complexity, A_{eff} remains constant so that one is able to control how the cohesion force depends on the strain, which in this study is taken to be linear. In principle, other methods could be used to set a constant A_{eff}, but as will be seen in Section 3.3.1, this choice allows for consistency with the experimentally measured mean force that is required to break these bonds, which hold the agglomerates together.

When a bond is broken between a particle and its neighbor due to tangential stress, any future contacts between them are governed by standard SSDEM without cohesion. When a bond is broken due to shear stress, one must consider the consequence of losing the cohesive force while particles are still in overlap. Without special treatment, the SSDEM repulsive force would cause the particles to accelerate away from each other, which is not realistic behavior. Once their bond is broken, for the sake of future collisions, the approach is to allow particle pairs with broken bonds to see each other as spheres with contact radii equal to the distance from their respective centers to the contact point at the time of tangential failure of their bond. Under the assumption that collisions between formerly bound particles are likely to occur in similar orientations, this may be a fair approximation to make. For the purposes of this study, where re-colliding particles are not common or important to the outcome, this approximation should suffice.

3.3 Comparison between experiments and simulations

3.3.1 Numerical representation of the target

The first task in this study is to use the above methodology to build a numerical representation of the target that is geometrically and mechanically as close as possible to the one used in experiments. The sizes of the real glass beads are large enough, and their shapes spherical enough, such that each bead can be represented by one spherical particle. The beads have been sintered, and the bonds between them measured. They are numerically modeled with cohesive strengths that correspond to the experimentally measured bonds.

Each 90-bead target was arranged in three layers of 30 beads, with the top and bottom layers arranged in the same, particular pattern. To construct the target, I start with its bottom layer (see Fig. 3.2): I first distribute the 16 particles that comprise the outside perimeter of this layer and then fill the inside with the remaining 14 particles. These 30 particles are placed on a horizontal plane, which is a boundary condition implemented in the numerical code (see Richardson et al. 2011). Indeed, such a boundary condition is necessary to maintain the configuration of those particles, when other ones will be distributed on top of them or inside them. Then, 16 particles are distributed on the outside perimeter of a second layer over the bottom one. Elastic "springs" are then attached to all these 46 particles, and then 14 particles are dropped inside to finish the second layer. Next, another horizontal plane is modeled to slowly move down on top of this second layer, in order to push particles into place. Once done, this plane is removed and a third layer of 30 particles is added on the top of the two bottom layers in a similar way

as previous layers. The motion of those three layers, composed of 90 particles in total, are numerically computed under uniform gravity to make them settle. Then the integration is stopped and particles are made to overlap with their neighbors by decreasing the distance between the centers of the particles by 10%, which means that the values for ρ_0 vary between bonds, but are typically $1.8s_{\text{eff}}$, or just under 4.5 mm.

The last step is to add cohesion to simulate the sintered particles. Each bond is characterized by a Young's modulus and a stress limit (equivalent to a tensile strength). The cohesive force between the glass beads of real targets is not perfectly identical for all bonds. In fact, quite a large variation exists between the strengths of the experimental bonds (see Fig. 4 in Machii & Nakamura 2011). Given that some bonds in the real agglomerate are relatively quite weak and some relatively strong, it is important to represent this in the numerical model as it has a significant effect on how the sintered agglomerate breaks apart. Since there is no obvious way to determine the actual distribution of the bond strengths from the real target, in the modeled target, I arbitrarily distribute the values of the Young's modulus, Y, and stress limit to define the cohesion in the bonds according to truncated Gaussian distributions, with a mean of 4 ± 1 MPa and 1.59 ± 0.06 MPa, respectively. These values are based upon experimental bond strengths between individual pairs of sintered glass beads similar to those used to form the agglomerates (Machii & Nakamura 2011). In this way, the fact that there is variation in the strengths of the bonds in the agglomerate is represented. The stress limit is derived by assuming that the effective area of interaction, A_{eff}, is the entire cross section of a given particle, which is about 19 mm^2. In the experiments, the stress limit is indicated as around $6 - 10$ MPa, considering the cross section of the fused area of contact of the particles, which is typically $2 - 5$ mm^2. By taking the product of the stress limit

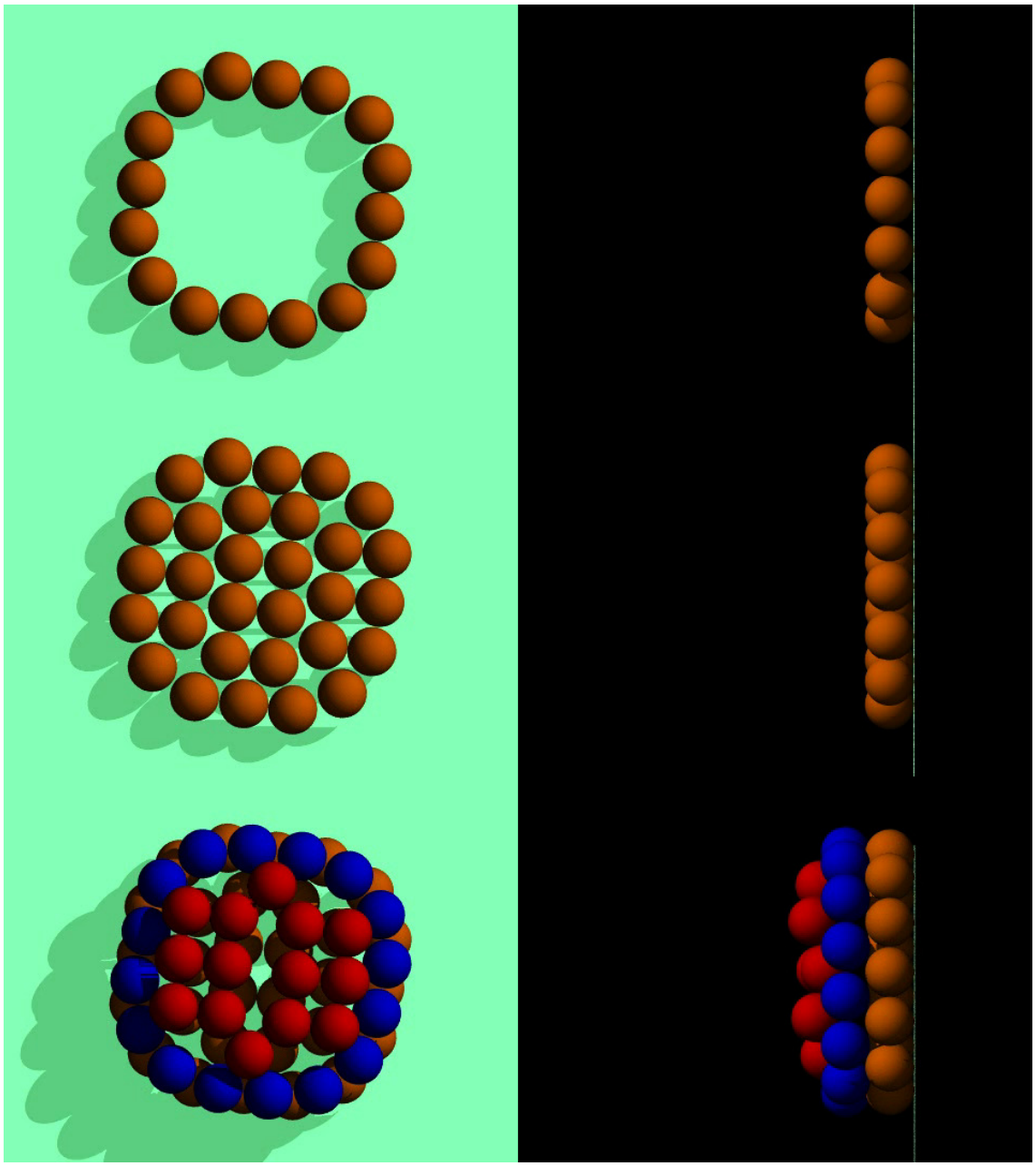

Figure 3.2: Numerical construction of a modeled target. Top: first step in the modeling of the bottom particle layer placed on a horizontal plane. Middle: completed bottom layer. Bottom: modeling of the second layer over the bottom one. The process is repeated in a similar way for the rest of the target (see Fig. 3.3 for an image of the complete target). The left panel shows a top view while the right panel shows a side view. (Particle coloring/shading is used to distinguish the different phases in the fabrication process.)

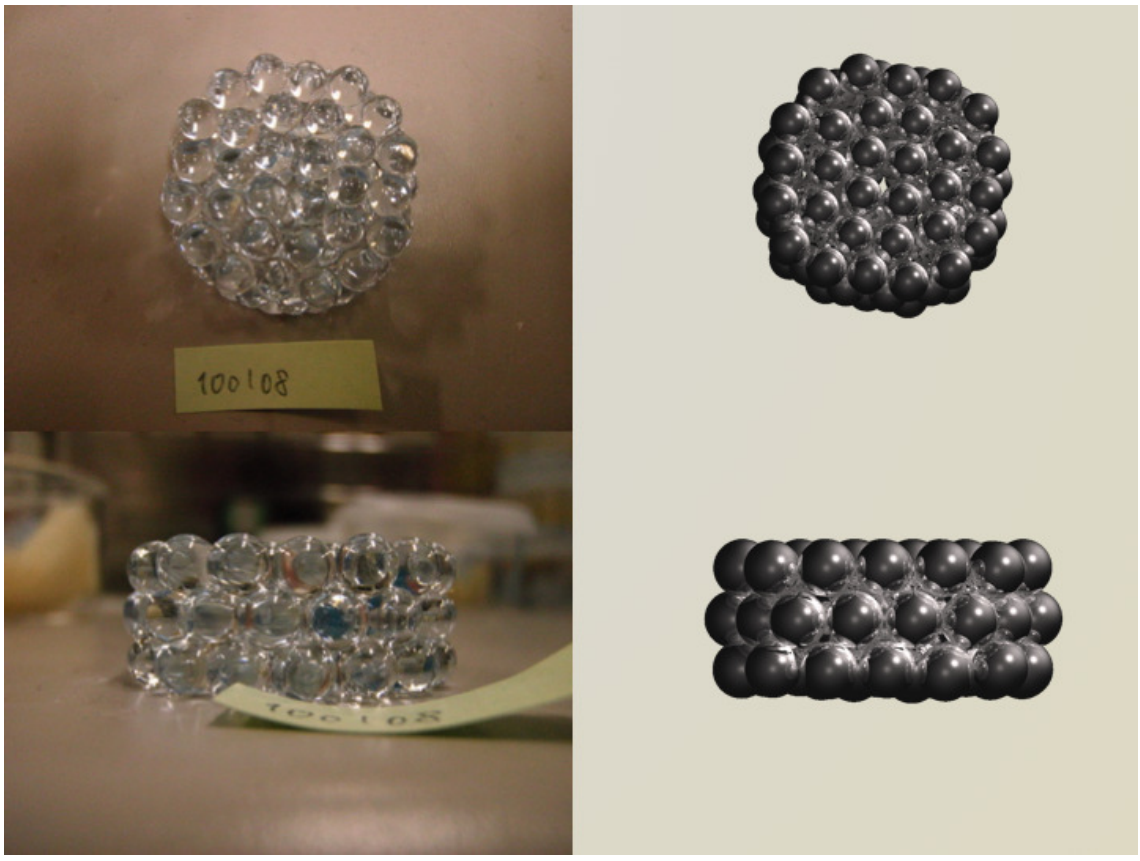

Figure 3.3: Left: experimental target consisting of a sintered glass bead agglomerate; Right: modeled target consisting of soft spheres bound together by cohesive forces. Top and side views are shown.

with the particles' contact area, this means that it requires roughly the same force to break the bonds in the simulations as was required in the experiments, which is about 30 N. As will be seen in Section 3.3.2, this allows for the obtaining of a bulk tensile strength that is similar to those measured experimentally. At the end of the process, the modeled 3-layer target is built with properties similar to the ones used in the laboratory experiments. Figure 3.3 shows a comparison between a real target and a numerical one, using a ray tracer to make a realistic looking image.

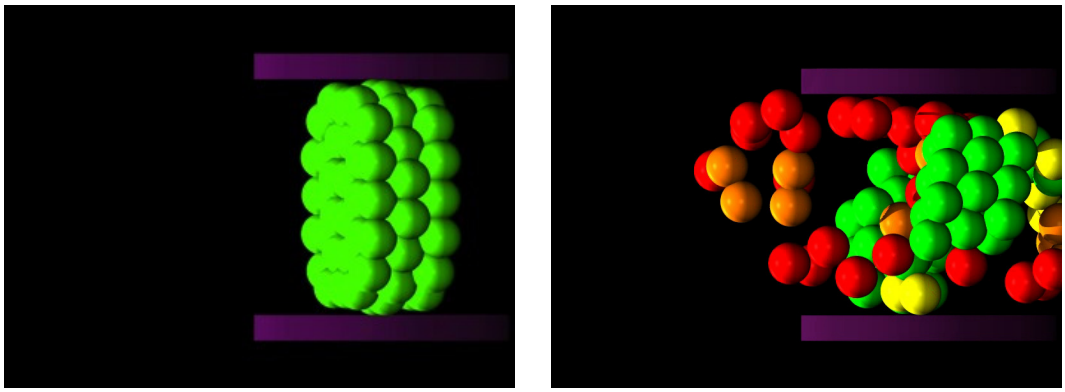

Figure 3.4: Numerical set up and simulation of the Brazilian disk test. Left: the target is placed between two horizontal planes that move vertically towards the center of the target until it breaks. Right: snapshot of the simulation at a time when the target is broken as its tensile strength is reached. The target is broken from its center into two main pieces, and other smaller ones. (Online only: particles in green are bound to three or more other particles, particles in yellow to two other particles, particles in orange to one other particle, and particles in red are unbound.)

3.3.2 Numerical modeling of the tensile strength measurement of the numerical target

Machii & Nakamura (2011) measured the tensile strengths of experimental targets using Brazilian disk tests. This test (first developed by Berenbaum & Brodie 1959, is a common means of indirectly measuring the tensile strength of brittle materials, including rocks and concrete. In order to check that the numerical targets have a similar tensile strength as those used in experiments, numerical simulations of Brazilian disk tests were performed on the numerical targets.

Figure 3.4 shows the numerical set up of the Brazilian disk test. The modeled target is placed between two flat plates, which are modeled as horizontal planes. These plates are set in motion towards each other until the target breaks into pieces. This test was modeled using several strain-rates: 0.1, 0.4, 1, 4 and 10 mm/s. The results are presented in Fig. 3.5 and show that the tensile strength slightly increases

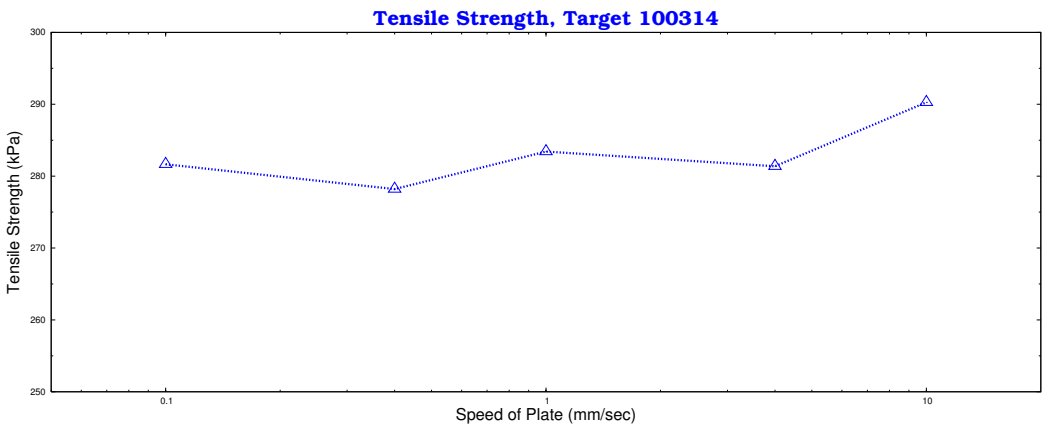

Figure 3.5: Tensile strength (kPa) of the modeled target as a function of the speed of the plates between which it is placed in the simulated Brazilian disk tests.

at higher strain-rates. The tensile strength of the simulated target is comparable to those of the real ones constructed by Machii & Nakamura (2011); they all show significant variance around about 0.5 MPa.

3.3.3 Numerical simulations of impacts

In this section I present the numerical simulations aimed at reproducing the impact experiments of Machii & Nakamura (2011). The experiments led to a wide range of outcomes depending on the initial conditions. Some impacts did not break the target, while others led to the shattering of individual beads. For the modeling, two experiments that led to the fragmentation of the target without any shattering of individual beads were considered so that the full process could be captured in principle with the numerical code.

The two considered experiments were performed using different projectiles and impact speeds. The first considered experiment involves a projectile consisting of an individual 3.07 mm glass bead impacting the target at 78 m/s, which corresponds to a specific impact energy, defined as the kinetic energy of the projectile divided by the target mass, of 8.95 J/kg. The second experiment involves a 2.85 mm individual

glass bead impacting the target at 56 m/s, which corresponds to a specific impact energy of 4.29 J/kg. The projectile hit close to the target's center in each case. However, because the exact location of the impact point could not be measured, and given the sensitivity of the outcome on the exact impact point location, a suite of simulations were performed, varying the impact point position around the target's center. Although able to satisfactorily reproduce both experiments, only the case of the 78 m/s impactor is reported in great detail.

In order to study the case of the 78 m/s impactor, 28 impact points were randomly assigned, all lying within a one-bead-diameter by one-bead-diameter rectangular region (0.24 cm^2), centered at the target's center. Each of the two plots in Fig. 3.6 show the mass histograms of fragments from the experiment along with the mass histogram from a particular simulation. The difference of the two distribution functions from that of the experiment is quantified by an area, which characterizes the extent of the disagreement between the given simulated result and the experimental result. This area is given by:

$$A = \int_{m_f=0}^{m_f=1} \left| \mathcal{F}(m_f) - \mathcal{G}(m_f) \right|, \tag{3.6}$$

where m_f is the mass fraction of the fragment, and $\mathcal{F}(m_f)$ and $\mathcal{G}(m_f)$ are the cumulative mass distribution functions representing the final fragment sizes from the simulation and the experiment, respectively. A lower value of A represents a better match to the experiment. Upon first glance, a Kolmogorov-Smirnov test (K-S test) seems like the appropriate statistic to quantify by how much the datasets from the simulation differ from that of the experiment. However, because the fragment sizes are in integer units of beads, and for the simulations that fit best most fragments are in fact single beads, there is limited discriminatory power. This experiment had 27 fragments of which only 6 were comprised of more than one bead, which is not enough to distinguish well between the distributions using a K-S test. As an

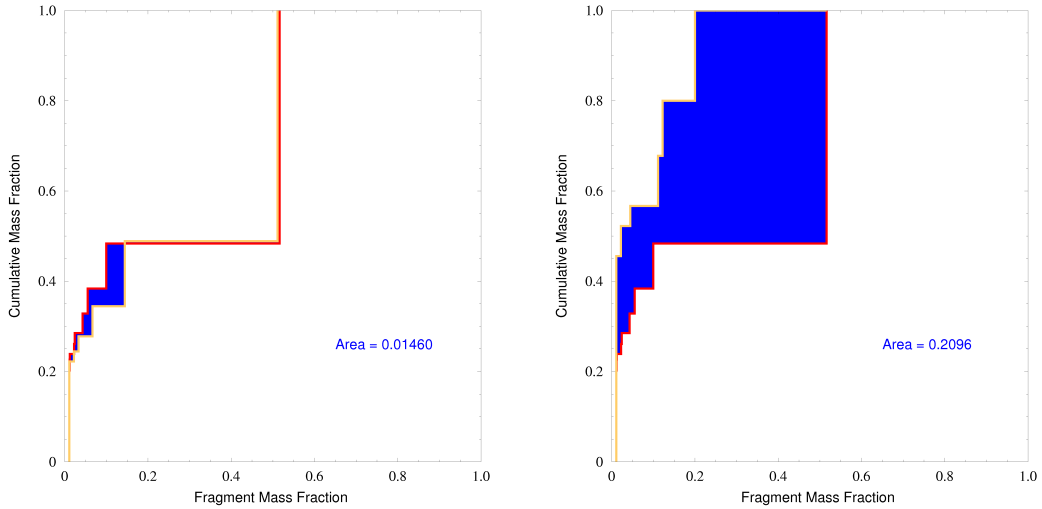

Figure 3.6: Cumulative mass distributions of fragments from both the 3.07 mm-diameter, 78 m/s projectile impact experiment (red line/small dashes) and simulation (yellow line/large circles). Left: Of the 1008 simulations run to represent this experiment, the simulation whose fragment mass distribution curve is closest to the curve corresponding to the experiment (represented on the top row of Table 3.2) is shown. Right: A simulation whose fragment mass distribution curve differs more significantly from that of the experiment.

alternative, I try to match the number of single bead fragments and the sizes of the larger fragments by overlaying the histograms and quantifying the area between them. Using this measure, as well as confirming with visual qualitative comparisons between the actual and simulated impact animations, the relative quality of the fit is assessed.

For each of the 28 impact points, given in Table 3.1 and shown graphically in Fig. 3.7, 36 impacts were simulated, with target SSDEM parameters varied around a region of parameter space where the results from the simulations were close to the experimental results. The "fidelity fit parameter" A from each of the 36 sets of parameters is averaged together, and is also shown in the aforementioned table and figure. The parameters that were varied were the coefficients of static, rolling, and twisting friction, μ_s, μ_r, and μ_t, respectively (see Table 3.2 for the best fit values). Outcomes were found to sometimes be quite different between simulations where

one of these parameters differed only slightly. However, much more important in determining the outcome of a simulated impact was the precise point of impact on the target. Table 3.2 shows the 17 best fits, in order, beginning with the best fit as quantified by its A value. It is worth noting that 12 of these come from a single impact point, highlighting the dependency of outcome on the precise point of impact. The histogram from the best fit derived from the criterion given in Eq. (3.6) is also shown in Fig. 3.6 (left image), overlaid with the experimental histogram.

Table 3.1: Simulation impact conditions for the first considered experiment. In each case, the projectile mass is 0.0382 g, its diameter is 3.07 mm, and the impact speed is 78 m/s. The impact points are randomly chosen to be within one target-bead radius of the target's center in each the horizontal and vertical dimensions, with the offset from the target's center given as X-offset and Y-offset, respectively. The last column of the table gives the derived fidelity parameter, A, which is a measure of the goodness of fit relative to the experiment (Eq. (3.6)), averaged over each of the 36 shots at this location. The table is ordered by increasing $<A>$, with smaller values of $<A>$ implying a better match to the experiment.

X-offset (mm)	Y-offset (mm)	$<A>$	X-offset (mm)	Y-offset (mm)	$<A>$
0.506856	3.54584	0.110412	-5.4794	-2.18385	0.175271
4.04949	-0.611243	0.111942	4.04424	-4.56093	0.201764
-6.05097	-0.0956444	0.113853	7.5203	7.03134	0.214827
0.906545	3.16675	0.119740	-6.40953	-8.23685	0.229588
5.57488	-5.02434	0.123184	-7.37184	-7.76246	0.270061
-5.63123	0.618798	0.124316	-0.721407	-5.98887	0.286138
-6.75735	-2.75084	0.131877	-1.28281	0.0986582	0.714857
-4.47548	2.53149	0.142000	1.51821	1.8634	0.714857
-3.85291	6.84779	0.148301	2.65272	-0.337877	0.714857
4.67133	-3.78316	0.149337	3.58045	-0.630038	0.714857
-5.10094	-3.11317	0.150283	3.6803	-2.13386	0.714857
4.4179	5.21704	0.158512	3.77577	-2.17328	0.714857
4.00789	7.96096	0.167667	-3.85397	0.328069	0.714857
7.24145	-6.76692	0.168172	-0.347942	-4.32904	0.714857

Table 3.2: Best-fit simulation impact conditions for the first considered experiment as given by the fidelity fit parameter A (shown). The SSDEM parameters of static friction, rolling friction, and twisting friction, are represented by μ_s, μ_r, μ_t, respectively. The mass of the largest remnant relative to the target mass is indicated by M_{lr}/M_t. From the first experiment, the value of M_{lr}/M_t was 0.516.

X-offset (mm)	Y-offset (mm)	μ_s	μ_r	μ_t	M_{lr}/M_t	A
-6.75735	-2.75084	0.141	0.1	0.05	0.511	0.01460
-6.75735	-2.75084	0.14	0.1	0.02	0.511	0.01691
-6.75735	-2.75084	0.143	0.1	0.05	0.511	0.01740
-6.75735	-2.75084	0.141	0.15	0.02	0.511	0.01790
-6.75735	-2.75084	0.148	0.2	0.02	0.533	0.02200
-5.4794	-2.18385	0.145	0.1	0.02	0.522	0.02375
-6.75735	-2.75084	0.142	0.1	0.05	0.489	0.02694
-5.4794	-2.18385	0.144	0.1	0.02	0.489	0.02743
-6.75735	-2.75084	0.147	0.2	0.02	0.489	0.02843
4.04949	-0.611243	0.148	0.1	0.02	0.522	0.04031
-4.47548	2.53149	0.145	0.1	0.02	0.522	0.04031
-6.75735	-2.75084	0.143	0.1	0.02	0.544	0.04573
-6.75735	-2.75084	0.145	0.1	0.02	0.533	0.05015
-6.75735	-2.75084	0.146	0.1	0.02	0.544	0.05042
4.47548	2.53149	0.147	0.1	0.02	0.478	0.05119
-6.75735	-2.75084	0.146	0.15	0.02	0.567	0.05346
-6.75735	-2.75084	0.147	0.1	0.02	0.544	0.05437

For one of the impact points, two similar simulations were also performed using different compilers of the code. The rationale for testing different compilers is that such dynamical systems are not purely deterministic, and can often be very sensitive to the different round-off and truncation errors that result from the use of different compilers and computer architectures. Here, results remained nearly the same.

In the simulations of the other experiment, which used the 2.85 mm projectile moving at 56 m/s, using the values of 0.144, 0.2, and 0.2 for μ_s, μ_r, and μ_t, respectively, coupled with a specific impact point, best replicated the impact. Figure 3.8

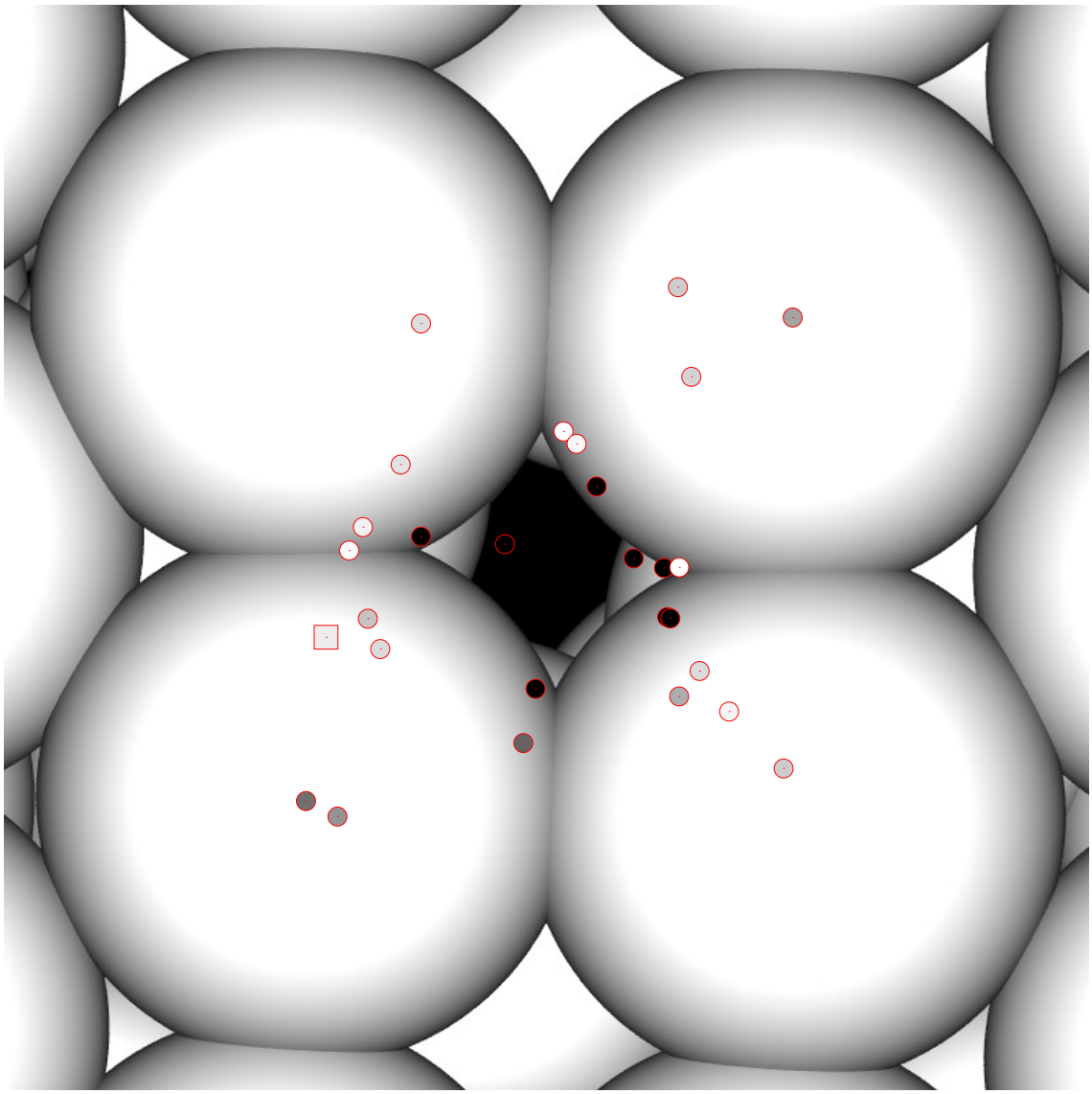

Figure 3.7: Image of the central region of the target, overlaid with the 28 randomly selected impact points used to simulate the 3.07 mm-diameter, 78 m/s projectile impact experiment. Shading shows the quality of the fit, from darkest (worst fit) to lightest (best fit) as measured by the fidelity parameter A as defined in the text, averaged over all 36 shots at the given location. Twelve of the 17 best-fitting simulations, including the top 5 simulations, came from just one of these impact points, indicated with a square (see Table 3.2).

shows the mass histogram of fragments from the simulation imposed on top of the corresponding mass histogram from the experiment.

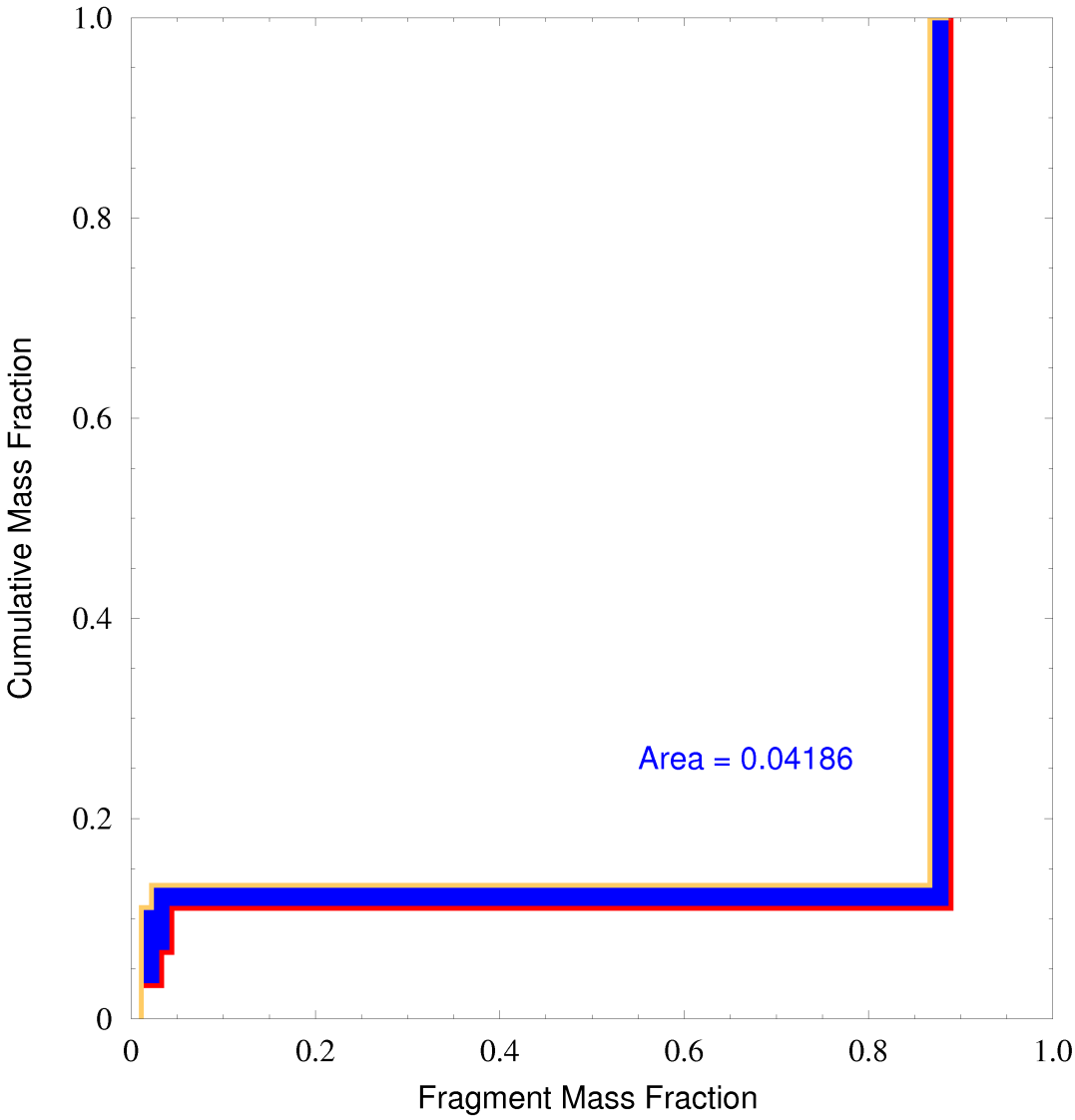

Figure 3.8: Cumulative mass distribution of fragments from the 2.85 mm-diameter, 56 m/s projectile impact experiment (red line/small dashes) and best-fitting simulation (yellow line/large circles).

3.4 Conclusions and perspectives on this work

In this chapter, I investigated the ability of my implementation of cohesion and SSDEM in the numerical N-body code `pkdgrav` to reproduce low-speed impact experiments on targets composed of 90 large glass beads sintered together carried out at the Kobe University in Japan (Machii & Nakamura 2011).

First, I numerically reproduced the targets that were used in the experiments, and checked that they had similar properties, the tensile strength in particular. To do this, I performed a simulated Brazilian disk test, on the numerical targets. This test consists of placing the target between two converging horizontal plates and measuring the stress at which the target breaks. The tensile strength of the numerical target measured in simulation was commensurate with the tensile strengths of similar targets measured in the lab.

Then, I performed suites of simulations to represent two different impact experiments by sweeping the parameter space around reasonable values. I developed a quantitative argument for why some simulations match the experiments better than others and found that the outcome is sensitive to the exact location of the impact point on the target, as was observed in the experiments. For each experiment, I compared qualitatively the outcomes of the simulations by overlaying the histogram of a given simulation to that of the experiment and measuring the area between the two; I found reasonable matches for many simulations. Because of the difficulty involved in measuring the velocity distributions of fragments from the images, the fragment-size distribution is really the best measure of the simulation fidelity to the experiments. I also confirmed, by visually rendering the simulations, the similarity in the fragmentation process and the realistic motion of the ejecta fragments. I compared the simulations to snapshots of the fragmentation process at different instances and assessed that the degree of spreading of the fragments in space was essentially the same in experiment and simulation. By selecting for similarity in the histograms and a careful visual inspection of the post-impact evolution of the fragments, I feel confident that multiple good simulations of both impact experiments were reproduced, and have determined that the outcome is strongly influenced by the precise point of impact.

Thus a satisfying validation test of my implementation of cohesion and SSDEM for these kinds of processes was performed. The understanding of impacts on cohesive targets that do not involve the fragmentation of individual components can be important in the context of planetary formation. This is especially the case in the phase when collisional speeds are low and small particles aggregate. In future studies, I plan to investigate this process in more detail by covering a wider range of parameter space (e.g., cohesion, friction coefficients, etc.), and using targets of various shapes and/or composed of spheres of different sizes and investigating the effect of initial target rotation. I will also apply this numerical method to the process of YORP spin-up on asteroids modeled as cohesive aggregates using as a basis the work performed with `pkdgrav`'s HSDEM collision routine by Walsh et al. (2008, 2012) for purely gravitational aggregates.

Chapter 4

Impacts into Granular Media

4.1 Introduction

The impact process plays a major role in the formation and evolution of planetary systems, including our own Solar System. In particular, the impact cratering process is important because impact craters are the most commonly observed geological features on the surfaces of most solid Solar System bodies. Crater shapes and features are crucial sources of information regarding past and present surface environments, and can provide us indirect information about the internal structures of these bodies as well.

In previous studies, I have demonstrated the ability to simulate the evolution of millions of granular particles in the context of flow from a granular hopper (Chapter 2; Schwartz et al. 2012c), and in low-speed cratering events (e.g., Schwartz et al. 2012a); the latter included an evaluation of ejecta speeds and trajectories, and a preliminary analysis of resulting crater sizes and morphologies at the site of the impact (see Fig. 4.1).

In this study, certain effects of low-speed impacts into granular materials, such as the regolith that covers most of the solid bodies of our Solar System, are considered.

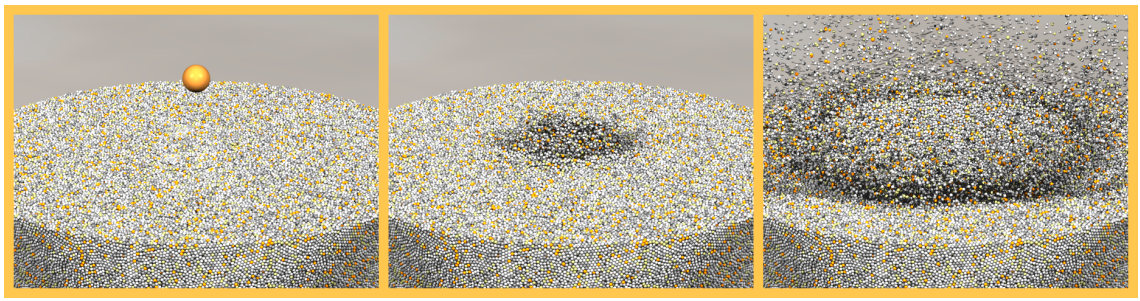

Figure 4.1: Cratering simulation into a target comprised of 1,137,576 particles. A 9 cm-radius projectile impacts perpendicular to the surface at a speed of 100 m/s into a 155 cm-radius half-shell filled with 1 cm-radius grains of collisional restitution coefficient 0.2. From left to right: 5 ms prior to impact; 15 ms and 375 ms after impact.

In principle, if the cratering process involves solid rock and/or if the impact speed is larger than the sound speed of the material, hydrocode simulations (see Section 1.2.3.1) that take into account large plastic deformations and phase changes of particles are the most adapted to model the process (Barr & Citron 2011). However, if the cratering process involves a low-speed impactor into regolith material, then the discreteness of particles as well as the different contact frictional forces between them must be taken into account. Sophisticated constitutive equations may be implemented in hydrocodes to study these types of cases, but numerical codes capable of directly simulating the evolution of particles and the contact forces between them during such a cratering event are probably best suited. I will use the implementation of the Soft-Sphere Discrete Element Method (SSDEM), as developed in Section 2.1 and in Schwartz et al. (2012c), to model the impact cratering process into granular materials to predict the amount of ejected material. Studies of low-speed impact events are suited for understanding the cratering process leading, for instance, to secondary craters. Such craters result from the ejecta of material from a large crater formed by a high-speed impact, which fall back onto the regolith at the surface of the considered body. These types of simulations can be used to investigate the mor-

phologies, shapes, and sizes of such low-speed impacts as a function of the impact conditions and regolith properties, and can therefore help in the interpretation of images of solid-body surfaces sent by space missions. They can also aid in the design of anchoring tools and sampling mechanisms aboard space missions to small bodies. The numerical study presented here is based on the experimental results found by the science team in charge of Hayabusa2's sampling mechanism (Makabe 2008). Simulations are used to determine the effect of differently shaped projectiles on the amount of material ejected. Throughout this chapter, when particle sizes are given, they can be assumed to represent the diameter of the bead, unless explicitly stated as otherwise.

Many laboratory studies analyzing different aspects of the cratering process caused by low-speed (sub-sonic) impacts into loose granular material have been performed. Properties of crater growth and impact ejecta have been correlated to impact conditions, such as the impact speed, target and projectile material, and the gravitational environment. Using primarily small (0.2 mm) glass beads, Uehara et al. (2003) reported that, by varying projectile size, density, and impact speed, the crater diameter scales as the 1/4 power of the impactor energy. They found that the crater depth scales as this energy to the 1/3 power, but that it also depends on the material properties of the impactor (e.g., size and density). Yamamoto et al. (2005) launched polycarbonate projectiles at $\sim$ 250 m s^{-1} into soda-lime glass beads of $\sim$ 0.226 mm at impact angles of 15, 30, 45, 60, 75, and 90 degrees, and found that the number of particles—normalized to crater volume—with speeds over 100 m s^{-1} increases with increasing impact obliquity. The lower the impact angle, the more comparable the ejecta velocities are to those derived from the power-law relation of Housen et al. (1983). Yamamoto et al. (2006) measured the depth-to-rim diameter ratios of transient craters and the final craters, using polycarbonate projectiles and

soda-lime glass bead targets, and found them to be 0.26–0.27 and 0.11–0.14, respectively. Yamamoto et al. (2009), also using polycarbonate projectiles, measured the crater growth that ensued after impacts into 2 types of targets, soda-lime glass beads and dry sand, finding that the size of the transient crater as a function of time follows a power-law relation only at early times, but deviates significantly from a power law relation at later times. Nakamura et al. (2013) performed impact experiments using 6 mm plastic projectiles penetrating glass bead targets of 0.05 mm and 0.42 mm at initial speeds of ~ 70 m s^{-1} in order to determine the drag force on the projectile. They found that the drag force is dominated by a term that depends on the speed squared, but that the data may suggest an additional linearly dependent speed term. Additional experiments performed in parabolic flight (free fall), showed no discernible effects from gravity on the drag. Wada et al. (2006) performed a numerical study of the excavation stage of low-speed cratering and found that the size of the crater cavity, the ejecta speed distribution, and the angle distributions of particles with ejection speeds higher than 1 m s^{-1} are consistent with those obtained in laboratory experiments.

In the current study, certain adaptations to the numerical code had to be made in order to simulate projectiles with shapes other than spheres. To date, the collisional routines in `pkdgrav` have been limited by the fact that inertial particles in the simulation are taken to be spherical. Spherical particles are convenient because intersections are easy to detect: if the sum of the radii of two particles is larger than the distance between their centers-of-mass (COMs), then the two particles are in contact. Further, the "point" of contact is simple to calculate, located a distance $l_1\hat{\mathbf{n}}$ from a particle that is in contact with its neighbor (cf. Eq. (2.9)). This means that orientation is largely irrelevant and that every point on a spherical particle's surface is known given the radius and COM location of the particle. This simplifies the

coding and lessens the number of computations that need to be performed during a given integration timestep, making the simulation run quickly. However, in the real world, perfectly spherical grains are difficult to find, even in a controlled laboratory setting, much less in the surface regolith that appears to cover the vast majority of solid bodies in the Solar System. To this end, tools are developed for `pkdgrav` that help account for the effects of non-spherical objects in both HSDEM and in SSDEM. In HSDEM, and incorporated into SSDEM, these include the rigid aggregate routine, briefly explicated below, and the use of movable, but non-reactionary, boundary walls (Section 2.2 for SSDEM implementation). In SSDEM, this also includes the use of soft-sphere agglomerates (Section 3.2.3), highly tunable friction parameters (Sections 2.1.3–2.1.5), and, recently, "quasi-reactionary" boundary walls, the latter of which are introduced and used in the study below (Section 4.3).

In the HSDEM collisional routine of `pkdgrav` (Richardson et al. 2009a, 2000), developments that go some way to approximate the effects of non-spherical shapes, developments not contained in this work, include the ability to model collections of spherical particles of arbitrary size stuck together to form aggregates comprised of rigidly locked spheres (Richardson 2005; Perrine et al. 2011), and the ability to model non-reactionary (and thus infinitely inertial), non-spherical walls in an HSDEM simulation (Richardson et al. 2011). Also, adjustments to the coefficient of tangential restitution ε_t (Richardson 1994, 1995) can be made to better match the exchange of rotational energies during a collision between particles with shapes that deviate slightly from spherical.

Each of these measures, available for use with HSDEM to account for non-sphericity, can be used in the SSDEM collisional routine: rigid aggregates, non-reactionary walls (Section 2.2), and viscous damping in the tangential direction (analogous to ε_t in HSDEM; see Sections 2.1.3 and 2.1.6 for the SSDEM implemen-

tation). In addition, as discussed in Section 2.2, more complex wall geometries are available in SSDEM, because in HSDEM collisions must be predicted in advance, making complex geometries more difficult, if not impossible to implement. An even more important distinction, however, between the two collisional routines, is the comprehensive set of frictional forces that comprise the SSDEM routine, which can serve as proxy for many very different types of material and can approximate some of the effects of non-sphericity without having to model the shapes explicitly; these frictional forces are covered in detail in Section 2.1.

In addition, another useful tool that I have developed as part of my work to more accurately capture the nature of real materials, which deviate from perfect, smooth spheres, is the ability to overlap adhesive spheres of arbitrary size and number, and with an arbitrary amount of overlap (see Section 3.2.2). In this optional component of the soft-sphere collisional routine, the rigidity of these composite particles can be freely adjusted. The composite particles can bend and flex, and potentially even break, with a distribution of weaknesses that can be controlled by the user. It should be noted that the same limitations to the use of SSDEM in general apply to this tool, which include constraints on stiffness, and on the range in particle size. Limitations on the stiffness of an agglomerate are either the same or are analogous to the limitations on the stiffness of a soft-sphere (as laid out in Sections 2.1.1 and 2.1.7). In the case of two soft-spheres colliding, a larger k_n, the stiffness coefficient along the line of contact, requires shorter timesteps to be taken in order to resolve the motion. Likewise, this holds true for two cohesive spheres in perpetual contact that help comprise an agglomerate object: larger values of k_n and Y, which imply a stiffer object, require shorter timesteps in order to resolve the vibrations and other intra-agglomerate motion. And just as in any of the SSDEM simulations discussed in this work, a large range in the sizes of particles that have the potential to interact

with each other requires a more expensive neighbor search.[1]

In this study, I attempt to model the impact effects on regolith made by non-spherical projectile shapes. To accomplish this, the shapes of the projectile need to be modeled explicitly. The material in this chapter is in preparation as Schwartz et al. (in prep.).

4.2 Laboratory impacts into granular material

Impacts into containers of glass beads using projectiles of different shapes were performed by the science team in charge of Hayabusa2's sampling mechanism (Makabe 2008). The goal of the study was to test the effects of differently shaped projectiles in order to maximize the amount of ejecta to be collected and returned to Earth.

I am now an active member of this science team, and as a preliminary test of the code that I have developed and its usefulness in simulating specific aspects of the sampling mechanism that will be designed and used on the mission, I performed a numerical study attempting to replicate a portion of this experiment. The portion of the experiment that I reproduced involves low-speed impacts, $\sim$ 11 m s^{-1}, of 7 different types of projectiles into cylindrical containers, 100 mm in radius and 150 mm in height, filled with approximately monodisperse glass beads. Two different sizes of glass beads were used for the targets, 5 mm and 0.5 mm. The mass of material that was ejected from the entire container was measured for each of the impact experiments across the range of different projectile shapes. The 7 projectile shapes were [mass, diameter (or diameter of the base for cones)]: a sphere [4.7 g,

[1]When particle sizes in a simulation are all equal, this minimizes the number of neighbors with which a given particle can be in contact. As this range in particle-size increases, this in turn increases the number of neighbors that a particle may find itself in contact with at any given time, and thus requires a more expansive neighbor search to check for contacts.

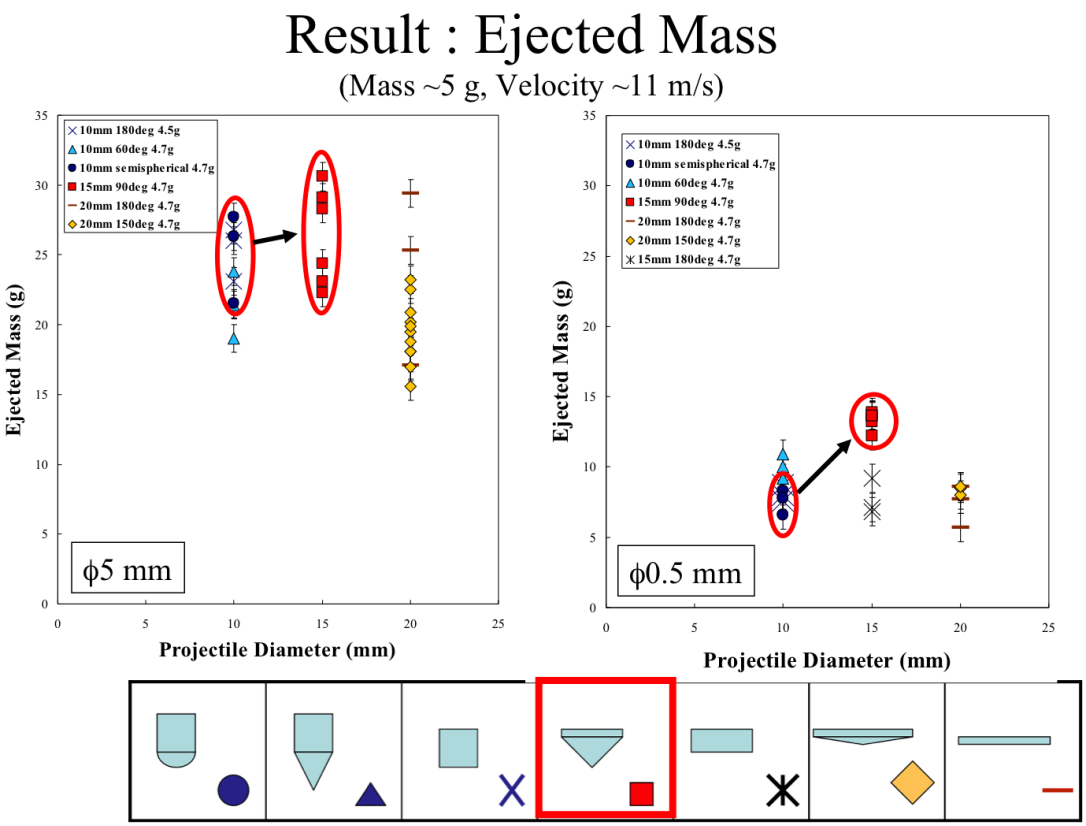

Credit: *Makabe (2008)*

Figure 4.2: Total mass ejected from 2 different experimental targets and 7 impactor shapes.

15 mm], three flat disks [4.5 g, 10 mm; 4.7 g, 15 mm; 4.7 g, 20 mm], and three cones [4.7 g, 10 mm; 4.7 g, 15 mm; 4.7 g, 20 mm]. The experimental results are shown in Fig. 4.2. The team determined that the 90-degree cone produced the greatest amount of ejected material.

4.3 Numerical method

In order to perform a satisfactory replication of the types of experiments described in Section 4.2, we first need support for non-spherical projectile shapes. Thought was given to the idea of making these shapes out of rigid aggregates as described

in Section 4.1, or out of cohesive soft-sphere agglomerates (see Sections 3.2.2 and 4.1). Instead, in order to best replicate the shape of the projectile, I chose to make the simulated projectiles out of wall primitives, which already included each of the shapes that were used in the experiment. Wall primitives can be combined into an assemblage of multiple primitives in order to form a more complex shape. However, although the correct initial velocity of these "projectiles" could be specified, in order to make them slow down after penetrating the target, some modifications had to be made to the routine.

Primitive non-spherical shapes, which can be combined to form complex non-spherical objects (see Section 2.2) were initially implemented into `pkdgrav` with an eye toward being able to replicate confining walls and apparatuses, which could move and oscillate, but did not necessarily need to be reactive. That is, the inertia would far exceed that of the material, and for expediency, infinite inertia was assumed for these boundary walls. Taking advantage of the cylindrical symmetry in each of the impacts described in Section 4.2, I made reactive just the center of mass of a wall-assemblage, i.e., an assemblage of wall-primitives, in one dimension. The implicit assumption is that by allowing momentum transfer from the granular material onto the projectile's COM along the direction of its initial trajectory, that this should account for the majority of the total work that the material does on the projectile in the actual experiment.

In these simulations, grain particles still see the projectile as having infinite mass, but the projectile is slowed down by the reactive force that the grains produce as it penetrates. The reduced mass used for the grain-projectile system during contact is equal to the mass of the grain, as though the projectile's mass were infinite, rather than the proper reduced mass. However, since the projectile's mass is much greater than that of the individual grains in these impact experiments, this is an

acceptable approximation: since the mass of an individual 5 mm glass bead was taken as 0.163 g and the mass of each projectile as 4.7 g (4.5 g, in the case of the flat 10 mm disk), this gives a reduced mass of 0.158 g; for the 3 mm glass bead targets, the mass and reduced mass were 0.0353 g and 0.0351 g, respectively. This slight violation of the law of conservation of energy is not a concern in this scenario since there are significant damping effects (coefficients of restitution of the grains are less than unity) that utterly dominate the energy loss to the system. Figure 4.3 shows a comparison of the penetration depth of the projectile as a function of time from two different impact simulations into targets comprised of 3 mm glass beads: one simulation uses a projectile made from a soft-sphere particle, and the other with a projectile made of a "shell" primitive, both equal to the size and mass of the spherical projectile used in the experiments. It can be seen that the path of the free soft-sphere projectile particle is similar to the path drawn by the shell projectile. The slight differences in the curves can be accounted for by any of these three factors: 1) the assumption that $\mu = m$, as discussed; 2) the fact that torques and translational motion parallel to the surface that are imparted upon the soft-sphere projectile particle are ignored in the case of the shell projectile; 3) differences in computer roundoff as the order of summation may be different ("a + b = b + a" does not necessarily hold for floating-point operations). However, the fact that the latter option might even be a consideration points to the similarity of these two simulations (the final penetration depths of the soft-sphere projectile and shell projectile are 66.22 and 65.31 mm, respectively, a difference of less than 1 mm or about 1 part in 72) and shows that the wall primitive serves as a good proxy for a soft-sphere particle impactor. For different shapes, the second factor above could become more of a concern, as I discuss further in Section 4.6. Any projectile shape that can be created using arbitrary numbers and combinations of

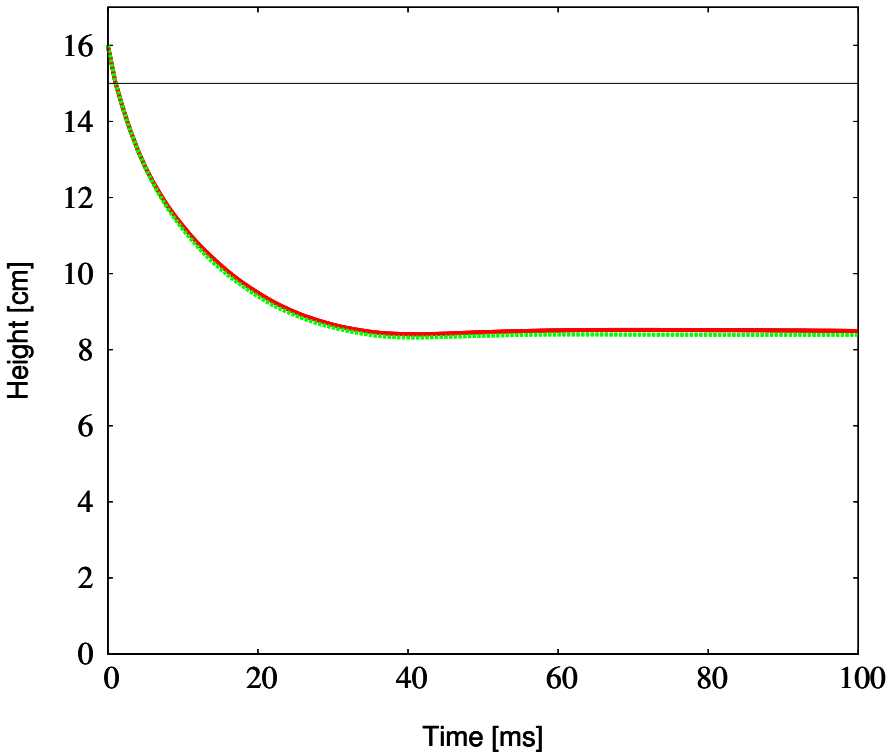

Figure 4.3: Penetration depth of projectile as a function of time using different representations of a spherical intruder for two otherwise identical simulations. The solid (red) line represents the free soft-sphere particle, the dashed (green) line represents the shell of equal size and mass, and the thin solid line at 15 cm shows the initial surface of the target. Results between the two cases are similar, with the final depth of the projectiles differing by less than a single target particle radius, justifying my methodology in situations where the effects from torques on the projectile can be safely ignored. Also evident is a slight rebound effect of the projectiles after hitting their maximum depths (they then exhibit highly damped oscillation around their final, fixed penetration depths).

the six wall primitives described in Section 2.2 can be substituted for the shell. In this study, disks and cones of infinitesimal thickness were also used to simulate projectile shapes.

4.4 Simulating the granular impacts

In order to develop good numerical representations of these impacts, parameters of the target material must first be constrained. There are essentially 5 free parameters in these simulations: μ_s, μ_r, μ_t, ε_n, and C_t. In order to sweep parameter space and analyze the dependencies of these parameters on the amount of material ejected, I performed a large suite of simulations using one experimental configuration (the same shape impactor and target grain size), varying the values of these 5 parameters only. The experimental configuration that I chose to use as the "baseline" configuration was the one involving the 90-degree cone projectile into the target comprised of 5 mm beads. This projectile was chosen because it was highlighted in the experiments for potential use on the mission aboard the sampling mechanism. The grain size of 5 mm was chosen because this matched an actual experiment to which results could be compared. Using the combination of this projectile and this target grain size, 5 impact simulations, each employing sufficiently unique combinations of the parameters μ_s, ε_n, and C_t, were found that match the amount of material ejected in the baseline experiment. The other 2 parameters, μ_r and μ_t, were found to have less influence on the amount of material ejected (see a discussion on the effects of these parameters in Section 4.5, and see Fig. 4.4).

These 5 sets of parameters, listed in Table 4.1, which each provide a good match to the baseline experiment, were then used to simulate impacts using each of the 7 projectiles (Section 4.2) into 2 sets of targets, comprised of monodisperse 5 mm grains and monodisperse 3 mm grains. The experiments used targets comprised of 5 mm particles and 0.5 mm particles. Although it is feasible to calculate an impact on a target comprised of several tens of millions of particles, which would be required for the 0.5 mm case, I chose to use particles of 5 mm and 3 mm in order

to perform a number of simulations in a reasonable amount of time. This gives a total of 70 simulated impacts, in addition to those carried out to perform the aforementioned parameter space sweep. The dependence on density was also analyzed by performing a suite of simulations on 5 mm grains of higher mass. In all, 163 impacts were simulated, all using multi-core parallel processing; each simulation ran for between one day and two weeks, depending on the target size and the preocessor speed. Most of the computation was performed using the Beowulf computing cluster (`yorp`), run by the Center for Theory and Computation at The University of Maryland's Department of Astronomy, while many runs were also performed using this department's public-use machines.

Table 4.1: Listing of the five sets of simulation parameters that were used to compare to experimental results. The parameter sets (PS_1–PS_5) were chosen because each provided a good match to the baseline experiment, which uses the 90-degree conical projectile impacting the target made up of about 45 thousand 5 mm glass beads. Each of these 5 parameter sets were used for targets comprised of the 5 mm beads ($5mmPS_1$–$5mmPS_5$) and targets comprised of the 3 mm beads ($3mmPS_1$–$3mmPS_5$), making 10 simulations for each of the 7 projectiles. Results of the simulations are shown in Figs. 4.5 and 4.6.

Parameter Set	μ_s	ϵ_t^*	ε_n
PS_1	0.000	1.000	0.730
PS_2	0.090	0.650	0.950
PS_3	0.100	1.000	0.800
PS_4	0.180	0.950	0.950
PS_5	0.265	1.000	0.950

*Recall that ϵ_t is defined as it is in Eq. (2.47).

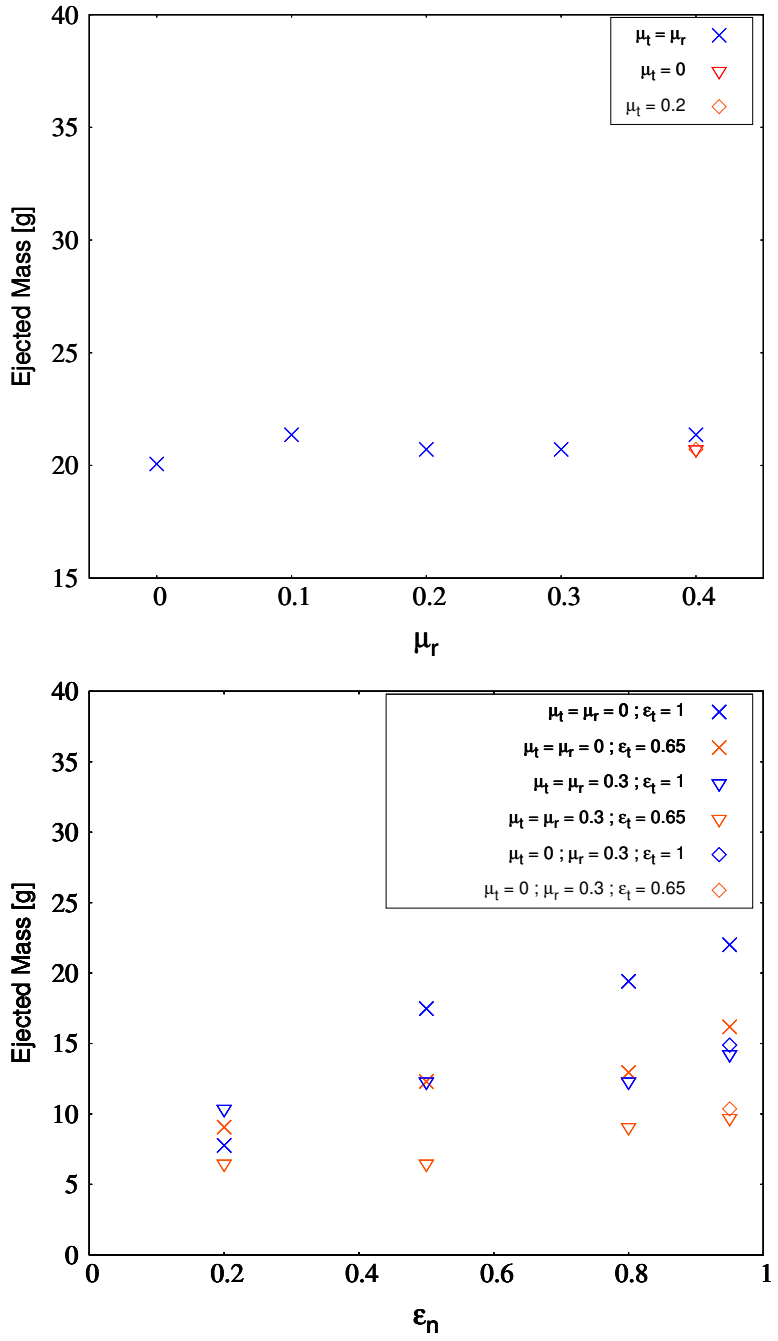

Figure 4.4: Influence of μ_r and μ_t on amount of ejecta. Top: With μ_s fixed at 0.1, μ_r and μ_t have no measurable affect on the amount of mass ejected. Top: With μ_s fixed at 0.3, μ_r, and perhaps to a much less extent, μ_t, lessen the amount of mass ejected. These effects are exacerbated at higher values of ε_n.

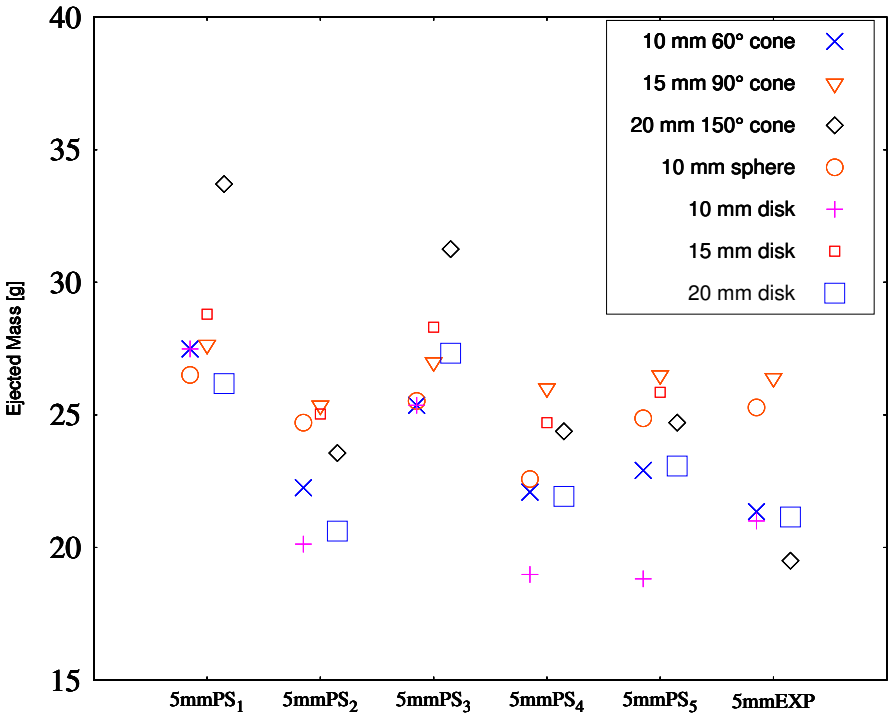

Figure 4.5: Ejected mass from simulations using 5 mm particle targets, the 5 parameter sets, and 7 projectiles. The experiments that use the 5 mm particle targets (5mmEXP) are also shown for comparison. (No experiments were performed using the 15 mm disk projectile into the target of 5 mm particles.)

4.5 Results

The results from the impact simulations were analyzed to discern their relationships to the experimental results, and also to determine how the values of specific parameters influence the amount of mass ejected from the container.

Rolling friction, the macroscopic effect that arises from forces on the microscopic scale that bring rolling particles to rest, controlled in simulation by the parameter μ_r, should not have a great influence on the amount of material that is ejected from the container for the relatively low values of μ_s used in these simulations.[2] It should

[2]Rolling friction will have a large effect in determining the resulting crater shape at later times,

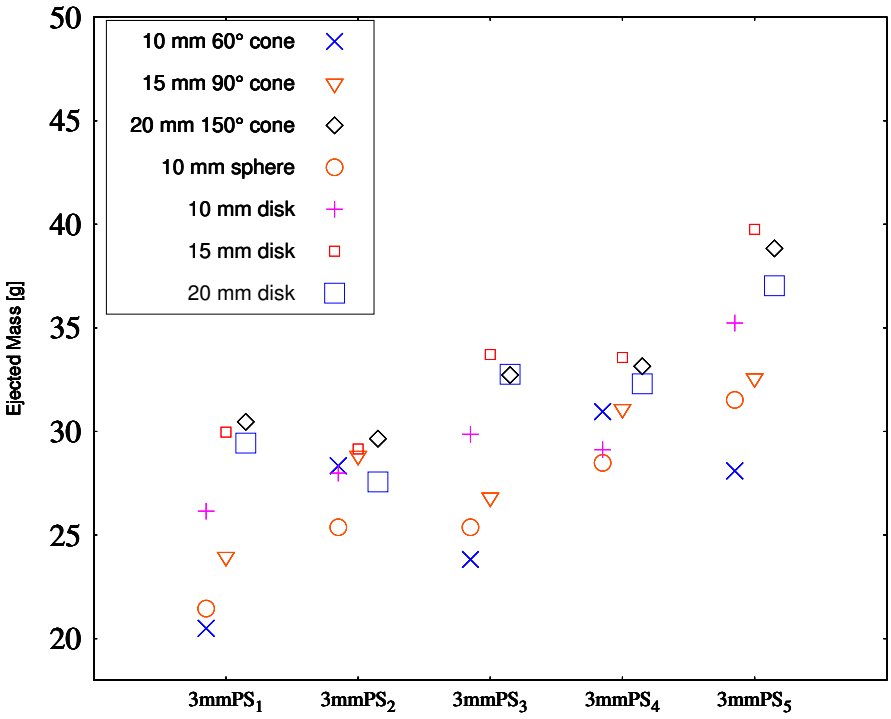

Figure 4.6: Ejected mass from simulations using 3 mm particle targets, the 5 parameter sets, and 7 projectiles.

also be expected that twisting friction, μ_t, would be even less influential. For low values of μ_s, Fig. 4.4 (left side) reveals this to be the case. However, for higher values of μ_s, rolling friction lessens the amount of mass ejected (Fig. 4.4, right side). It is unclear whether μ_t has an influence on the amount of mass ejected in the limited parameter space explored in this study. For the suite of 70 runs that use different projectile shapes, the values of μ_s are low enough such that μ_r and μ_t have little influence on the amounts of mass ejected, and so the parameters μ_r and μ_t are kept at zero.

Using different combinations of 3 parameters, μ_s, ε_n, and C_t, these 5 parameter sets are tuned such that they each eject the same amount of mass for one experimen-

but an analysis of crater shape is not performed in this study.

tal setup: the 90-degree cone impacting into 5 mm beads, as explained in Section 4.4. Therefore, it must be kept in mind that patterns in the results of the 70-run suite (Figs. 4.5–4.6) will be relative to this baseline setup. Impacts from any projectile shape into either of the 2 targets show that an increase in μ_s decreases the amount of mass ejected, an increase in C_t (a decrease in ϵ_t; see Eq. (2.47)) also decreases the amount of mass ejected, but that an increase in ε_n increases the amount of mass ejected.

Results from the use of the 3 mm particles show that the simulations with greater static friction tend to increase mass loss (the parameter sets PS_1–PS_5 are ordered with increasing μ_s). This result means that μ_s, relative to ε_n and C_t, has less of an effect on the total amount of ejected mass for the smaller, 3 mm beads than it does for the larger, 5 mm beads. At the 5 mm grain-size, mass loss does not correlate with static friction across these parameter sets (with the same caveat that parameters are tuned to match the amount of mass ejected using the baseline experiment).

For the 5 mm beads, ε_n seems to be the dominant parameter in determining mass loss: 5mmPS_2, 5mmPS_4, 5mmPS_5 each share the same high value of ε_n, namely 0.95. This means that an increase in ε_n does less to increase the amount of ejecta for the simulations with 5 mm beads than for those with 3 mm beads, save for the baseline experiment and the spherical projectile. The experimental results using the 5 mm beads appear to match better the simulations that use this value of ε_n (see Section 4.6 for continued discussion). For most projectile shapes, larger values of ε_n do less to increase mass ejection of 5 mm beads than they do in the baseline simulations. This is especially the case for the the 20 mm disk, 150-degree cone, and the 10 mm disk projectiles. For each simulation using $\varepsilon_n = 0.95$ and 5 mm beads, the 90-degree cone projectile maximizes the amount of ejected mass, which coincides with the experimental results.

4.6 Conclusions and perspectives on this work

Impact simulations were performed based upon the experiments conducted by the team studying the Hayabusa2 sampling mechanism. The team determined that the projectile shape that corresponds to the 90-degree cone was likely to produce the greatest amount of mass at small target-particle sizes (i.e., the containers filled with 0.5 mm beads). The reason for the differences in the amounts of ejected mass between the two experimental grain sizes in Fig. 4.2 is not immediately obvious. The simulations performed in this study did not use 0.5 mm beads for reasons of computational cost (see Section 4.4). In this study, numerically modeled containers filled with 5 mm beads and containers filled with 3 mm beads were used. A new feature allowing projectiles to take on non-spherical shapes was developed and used, with the primary limitation that it neglected torques on the projectile.

Parameter space was explored based upon the experiments that used the impact of the 90-degree cone projectile into the containers filled with 5 mm glass beads. Ninety-three simulations were performed to replicate this experiment using a wide range of parameters. Five of these simulations were chosen based upon how well they matched the experimental results and with an attempt to include parameter sets that exhibit a wide range in parameter space. These 5 parameter sets were then used to simulate impacts for each of the 7 projectiles into the 2 containers (one filled with 5 mm beads and one filled with 3 mm beads).

The simulated impacts into 5 mm beads matched up well with the experimental results, both in regard to the amount of mass ejected and to the relative ordering of the projectiles that ejected the most mass (see Fig. 4.5). This was especially the case when using beads with a high normal restitution coefficient of 0.95. The spherical projectile in the 5 mm cases shows similar mass loss across the parameter sets,

which means that these parameters affect the results using the spherical projectile in a similar manner as they do using the 90-degree cone. The targets comprised of 3 mm beads did not show the 90-degree cone projectile to eject more mass than the other projectiles tested. It is unclear if simulations of still smaller beads would show the 90-degree cone to eject the most mass, as it did in the experiments on 0.5 mm beads.

Could the neglecting of torques felt by the projectile (Section 4.3) be responsible for the fact that the 90-degree cone did not eject more mass relative to others in the case of the 3 mm beads? Neglecting these torques is clearly warranted for the spherically shaped projectile in this type of impact simulation, however, for shapes that are prone to feel relatively large torques, this assumption is less sound. For example, although the target is cylindrically symmetric on average, small asymmetric forces on, say, a thin flat disk, could cause some modest rotation and lateral motion, influencing the way that energy is delivered to the target grains. This said, it should be noted that this did not seem to be a factor in the simulations that used the 5 mm beads. Additionally, in the experiment, images obtained of a disk projectile penetrating the target show an extremely symmetrical ejecta plume, which may mean that there is very little rotation or lateral motion of the projectile during penetration (Fig. 4.7). Nevertheless, neglecting these degrees of freedom on projectiles in simulation could lead to an overestimation of the amount of material ejected; for these reasons, one should expect this to be more of a factor when considering the wide, flat projectiles, and the 150-degree cone projectile. These projectiles did seem to "over-perform" in simulations using 3 mm beads; that is, they seemed to eject more mass relative to the other projectiles than one might expect based upon the experimental results using other bead-sizes.

The 3 mm bead targets were affected more by the combination of ε_n and C_t than

Figure 4.7: Successive frames showing an experiment that uses a flat projectile impacting into a target comprised of 0.5 mm glass beads, producing a symmetrical ejecta plume.

they were by μ_s, relative to the baseline simulation. The 5 mm bead targets seemed to all be affected by the μ_s parameter in a similar way. It was found that ε_n generally affects the targets comprised of 3 mm beads in a similar way as it affects the baseline simulation. The targets of 5 mm beads using the other projectile shapes, with the exception of the sphere, were more affected by the combination of μ_s and C_t than they were by ε_n.

This implies that ε_n may do more to increase the amount of mass ejected from targets comprised of smaller grains, and that μ_s may do more to suppress the amount of mass ejected from targets comprised of larger grains that are of more comparable size to the impactor. For these larger particles, it would seem that surface friction and adhesion play a strong role, but as particle-sizes become significantly smaller than the impactor, material properties other than energy damping become less important. Although the sample size here is small, these results seem worthy of further investigation.

The next step to take is to simulate granular impacts in micro-gravity, or in various gravitational regimes; such a study is underway. The integration of impacts until later times, in order to analyze the resulting crater morphology and ejecta paths, is also warranted. Numerically, it would be appropriate to add a more comprehensive treatment of non-spherical particle shapes subject to the range of influence as outlined by Euler's equations of motion. This is touched upon in Chapter 5. Also, in low-gravity regimes and when using small particles, van der Waals forces become relevant, and so it would be prudent to include these forces in simulations; this is a

capability of the code.

Chapter 5

Conclusions and Perspectives

5.1 Numerical tools and their applications

Sending spacecraft to take data readings and perform direct high-resolution imaging of small Solar System bodies (SSSBs) is underway. Multiple space agencies across the globe, including NASA, ESA, JAXA, and the China National Space Administration (CNSA), are embracing this idea as new mission priorities. As these agencies continue to take on these endeavors, experience is gained and mission goals become more ambitious. The selection of in-situ missions to SSSBs that collect and return sample surface material are beginning to become the norm, and for under USD $1 billion, which includes the cost of the launch vehicle (David 2012; Kerr 2011). However, when it comes this small body exploration, we are still in the nascent stages.

A necessary component of the research into the exotic surface environments of these bodies is the development of an ability to reliably simulate the ongoing granular processes taking place, which will have implications about the origins and evolution of our planetary system. The same numerical tools developed to answer pressing questions in planetary science can be used to develop and aid in the design of

the sampling mechanisms required. This is a unique opportunity. The fact that the tools developed in the present work take a discrete, soft-sphere approach makes them especially conducive to the modeling of the low-speed granular dynamics inherent to SSSB lander functionality and sampling techniques. The ability to construct in detail both the granular surface environment and the landing/sampling apparatuses, as well as an extremely wide range of laboratory assemblies, makes these important tools.

To this end, I have implemented the soft-sphere discrete-element method (SSDEM) with deformable cohesive bonding into the N-body code PKDGRAV. SSDEM allows for the realistic modeling of contact forces between particles in granular material. Unlike discrete methodologies such as SSDEM, continuum coding is essential for high-speed (supersonic) collisions and is very good at modeling the behavior of fluids. To the extent that impacts or granular processes are fast and fluid-like, continuum approaches can prove to be more advantageous, or even essential, over discrete approaches. There have been many fruitful advances in the use of continuum coding to model granular behavior (see Section 1.2.2.5 for some theoretical background, and Section 1.2.3.1 for a discussion of the numerical implementations). Continuum theory has also contributed much to discrete numerical physics. Discrete numerical approaches (including this one) use the bulk properties derived from continuum mechanics and continuum theory as material parameters that describe the particles (which are internally homogenous, after all). These bulk properties include material stress and strain, and certain friction parameters. Many highly sophisticated modifications have been made to continuum codes to approximate the effects of granular media. It remains the case, however, for its simplicity and accuracy, that the discrete nature of SSDEM is naturally suited for certain regimes, and has great advantages over continuum coding in those that involve slow particle creep or

rotation, and where the discrete, granular nature of the material is important.

In this implementation of SSDEM, to account for surface deformation of particles at contact, colliding particles are allowed to overlap, during which time they are subject to forces that work to oppose deformation, and which depend on the relative spins and velocities of the particles, their material properties, and the history of the contact. Different frictional forces are taken into account, including rolling and twisting friction, which are often neglected in SSDEM implementations. Sophisticated parallelization and tree-code algorithms, part of the PKDGRAV functionality, optimizes the search for particle overlaps and minimizes the computation time required. When an overlap occurs, particles are treated to the various types of contact forces (e.g., static, dynamic, sliding, rolling frictions), and collisions are integrated through their full duration (SSDEM) rather than analytically predicted in advance of the collision (HSDEM). This is particularly important in dense granular regimes and/or when collision durations (stress wave propagation speeds) are non-negligible.

In order to account for the potential presence of cohesion between grains within a granular medium such as regolith on the surfaces of solid celestial bodies, I have implemented a cohesive force into PKDGRAV. The default behavior has a treatment equivalent to a Hooke's force law for springs with a speed-dependent damping term that acts between bonded particles' centers of mass (COMs). Also supported however, are more complicated force dependencies such as van der Waals force laws (Section 1.2.2.4), a strain- and time-dependent zero-strain-bond-length (creep), and cohesive strain limits that are dependent on strain rates. In SSDEM, spheres with a zero-strain-bond-length less than the sum of their two radii results in the particles penetrating each other with SSDEM repulsive forces coming into balance with cohesive forces (and any other forces that may exist between the particles, e.g., gravity). In such a case, particles are subject to the full robust treatment of SSDEM contact

forces (Section 2.1) together with cohesion (Section 3.2). Arbitrarily complex agglomerates can be created from any number of overlapping spheres of various size. In addition, spheres can have differing mass and strength parameters, which provides the freedom to simulate elaborate combinations of deformable cohesive agglomerates with explicitly defined internal strength distributions. This methodology, which allows for grain shapes other than independent, unbound spheres, will be useful to the majority of applications in planetary granular dynamics, since most any could benefit from the inclusion of non-spherical grain-shapes.

Validation tests for the SSDEM numerical coding implementation, for the implementation of deformable cohesive bonds, and for the first-order approximations to non-spherically shaped projectile motion were performed. The effectiveness and accuracy have been demonstrated by reproducing successfully the dynamics of grain flows in granular silo experiments (Chapter 2), and by reproducing the significant results of low-speed impact experiments on cohesive targets (Chapter 3) and into granular beds (Chapter 4).

Successful simulations to capture the important qualities of flow through a granular hopper silo were performed. The flexibility of the code to consider wall boundaries with a wide range of geometries allowed for the design and numerical preparation of the cylindrical hopper; these included funnels that facilitated the computation of the motions of grains as they filled the hopper, in addition to their motions during discharge. This implementation of SSDEM reproduced the well-verified empirical correlations in these flows (e.g., Eq. 2.45), which provides assurance of its efficacy as a granular physics code. The capability to track the instantaneous state of the system throughout, monitoring the system as it evolves, is something that cannot, in general, be done experimentally. In particular, the contact forces were traced, and maps of the force network and its evolution in time were constructed.

The effect that the various SSDEM material parameters have on the flow rate was also explored.

Simulations were performed to replicate experiments that involved disruptive impacts into targets composed of sintered glass bead agglomerates. Precisely measured laboratory experiments at Kobe University in Japan allowed for the testing of the code's handling of cohesion. The targets were reproduced numerically as SSDEM cohesive agglomerates (Section 3.3.1), then checked against those from the laboratory to ensure that they had similar material properties. A simulated Brazilian disk test was performed on the numerical targets to match those performed experimentally (Fig. 3.4); tensile strengths of the numerical targets were found to be commensurate with the tensile strengths of similar experimental targets, as measured in the lab. A quantitative argument was given (in Section 3.3.3) for why some simulations match the experiments better than others. Using this criterion, reasonable matches were found for many simulations by using the fragment-size distribution as a measure of the simulations' fidelity to the experiments. Also, visual renderings of the simulations were compared to films of the experimental fragmentation process, revealing a high degree of similarity in the ways that fragments spread out in space. By selecting for similarity in the histograms, and a careful visual inspection of the post-impact evolution of the fragments, it was confirmed that multiple simulations representative of both impact experiments were indeed produced, and that the outcome is highly influenced by the precise point of impact. This latter finding was also observed in the laboratory experiments. Follow-ups to this study can be used to investigate a wider range of parameter space (e.g., cohesion, friction coefficients, etc.), while using targets of various shapes and investigating the effect of initial target rotation. The understanding of impacts on cohesive targets where fragmentation of individual components is not important is relevant in the context of planetary formation and

in the evolution of SSSBs. In different studies, this methodology can be applied to low-speed collisions between aggregates, as occurred during the early phases of our Solar System's history (Section 5.2.8), or as they occur in Saturn's A and B rings (Section 5.2.6). The numerical approach has been shown appropriate to be applied to low-speed processes of gravitational aggregates in general. Applications include, but are not limited to, those discussed in Sections 5.2.9, 5.2.1, 5.2.7, 2.1.2, and 5.2.10.

Impact simulations were performed based upon the experiments conducted by the team that studies the sampling mechanism of Hayabusa2 (Section 4.2). Using differently shaped projectiles, the team set out to determine the projectile shape that was likely to excavate the most material for use on (162173) 1999 JU3, the target asteroid of the mission. They determined, of the projectiles tested, that the cone-shaped projectile making a 90-degree angle at its apex was likely to eject the greatest amount of mass at small target-particle sizes. In my study, modeled containers, which I filled numerically with 5 mm beads, and containers filled with 3 mm beads, were used. A feature allowing projectiles to take on non-spherical shapes was developed and used, with the primary limitation that it neglected torques on the projectile. The simulated impacts into 5 mm beads matched up well with the experimental results, both in regard to the amounts of mass ejected, and in regard to the relative ordering of the projectiles that ejected the most mass (see Fig. 4.5), especially when using beads with a high normal restitution coefficient of 0.95. The targets comprised of 3 mm beads did not show the 90 degree cone projectile to eject more mass than the other projectile shapes tested. It is unclear if simulations that use smaller beads could reproduce this result, which was found in the laboratory experiment on 0.5 mm beads. It was found that the coefficient of restitution seemed to affect the ejecta amounts of 3 mm bead targets more than those comprised of

5 mm beads, whereas the static friction seemed to affect the 5 mm bead targets more than the 3 mm bead targets. Studies are ongoing to simulate these types of granular impacts in micro-gravity environments. Integrating simulations further in time, in order to analyze crater morphology and ejecta paths, is also being carried out. In general, it would be appropriate to add a more comprehensive treatment of non-spherical particle shapes that can exhibit all relevant degrees of freedom, in addition to the deformable agglomerates described in Section 3.2.2. This is an important next step in the development of the coding methodology, and is one that is currently being pursued.

5.2 Future applications

This work has detailed the development of important tools useful for providing explanations of the different types of geological processes that we are discovering on the surfaces of SSSBs. Besides investigations into their geologies, these tools allow for the direct simulation of the in-situ landers and sampling devices as they touchdown onto the granular surfaces of these bodies. The ability to predict a spacecraft's response to the surface environment aids in the design of the lander/sampling device and of the mission. Work applying these tools to the sampling mechanisms of Hayabusa2 and OSIRIS-REx (Sections 1.1.3.2 and 1.1.3.3, respectively) is ongoing. The functionality of these types of simulations will be important to potential future missions as well, such as MarcoPolo-R (Section 1.1.3.4), the ARU mission (Section 1.1.3.5), and eventual manned missions.

In addition to spacecraft landers and sampling system designs, and to many of the applications that follow directly from the studies included in this work, mentioned in their respective chapters, the numerical tools developed and outlined are at a

stage to be applied to myriad other applications in the realm of planetary science and granular material physics. Mentioned below are some applications, both ones that are ongoing (Sections 5.2.1–5.2.6) and ones suggested for future study (Sections 5.2.7–5.2.10). Several close collaborators are involved.

5.2.1 Rubble pile collisions

(Project lead: Ronald Ballouz, UMD)

The evolution of small solar system bodies is dominated by collisions, starting from the initial build-up of planetesimals (Lissauer 1993) to the subsequent impacts between remnant bodies that exist today (e.g., Michel et al. 2004). Some of the collisions occur at impact speeds that do not exceed the sound speed of the material. Since many small bodies may have low tensile/cohesive strength, the collisions can often be treated as impacts between rubble piles, the outcomes of which are dictated by the dissipation parameters and gravity. Using the SSDEM collisional methodology from Chapter 2, basic head-on (Fig. 5.1) and off-axis collisions involving low-speed rubble piles have been performed, first without frictional or cohesive forces (Richardson et al. 2012b), and then later with the effects of interparticle friction (Michel et al. 2012c).

The SSDEM simulations were able to adequately reproduce simulations based upon older, HSDEM approaches (Leinhardt & Richardson 2005), while offering the benefits of better friction handling and vastly improved scalability (see Section 1.2.3.3). Currently, the effects of SSDEM frictional parameters, both with and without rotation are being explored, solving for Q_D^*, the specific energy required to disperse half the total mass involved in a collision. Work in progress matches the "universal law" of catastrophic disruption curves from Leinhardt & Stewart (2012)

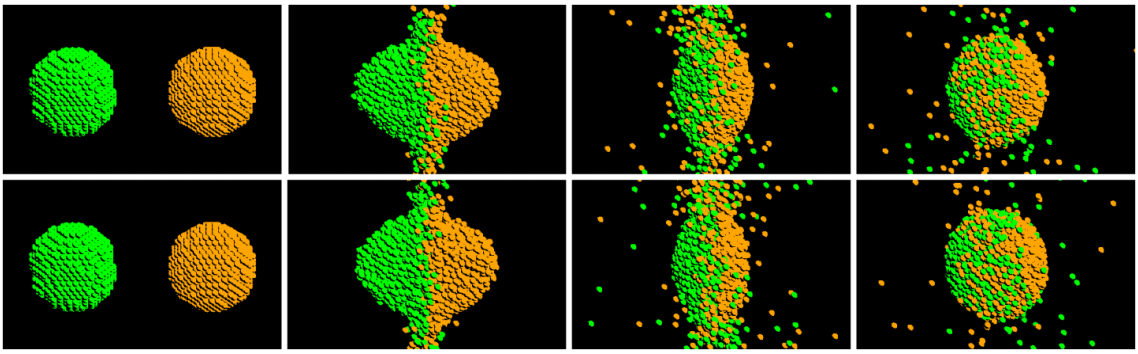

Courtesy: *Ronald Ballouz, UMD*

Figure 5.1: Snapshots from simulations of head-on rubble pile collisions at 2 km s^{-1}. Top: HSDEM; bottom: SSDEM. Rubble piles have mass ratios of 1:1, an initial separation between their centers of 3 km, and are comprised of (randomly packed) spheres of radius ∼1 km and density ∼2 g cm^{-3}.

extremely well. This work will also be expanded to the general case of gravitational aggregates with cohesion.

5.2.2 The Brazil-nut effect

(Project lead: Soko Matsumura, UMD)

The term "Brazil-nut effect" comes from the observation that a can of mixed nuts, when opened, tends to be size-sorted, with the largest nuts (the Brazil nuts) resting on the top. Although extensively studied, the mechanism of the effect is still unresolved. In simulations performed thus far using the collisional SSDEM routine (Section 2.1), convection has played a dominant role (Fig. 5.2). Using a cylinder filled with 1800 spheres, 1 cm across, and a single 3 cm (intruder) sphere placed at the bottom, the container provides forced vertical oscillation (specifics regarding the parameters used are given in the figure caption). This simulation is performed over a range of SSDEM friction parameters and oscillation parameters, some of which show a strong Brazil-nut effect, some of which show a weaker effect, and some of

Courtesy: *Soko Matsumura, UMD*

Figure 5.2: Simulation of the Brazil-nut effect. Snapshots are 2.4 seconds apart and progress from left to right. The diameter of the cylinder, small particles, and red intruder particle are 10 cm, 1 cm, and 3 cm, respectively. 1800 small particles are used in the simulation and are colored according to their initial height. The open cylinder, 25 cm in height, oscillates vertically (z-axis) with an amplitude, $A = 1$ cm, and a frequency $\Omega = 3\sqrt{(g/A)}$ rad/s $= 93.9$ rad/s. The SSDEM parameters for all surfaces are: $\varepsilon_n = \epsilon_t = 0.5$, $\mu_s = 0.7$, and $\mu_r = 0.1$.

which show no effect at all (Matsumura et al., in prep.). When the effect is present, convection tends to carry particles upward along the central vertical axis and downward along the walls. The intruder particle will travel upward but cannot be carried downward.

Research into this effect on asteroids is a complicated matter (Tancredi et al. 2012). Using the tools developed in this work, the Brazil-nut effect will be checked for on a self-gravitating aggregate model. There is speculation that small boulders, e.g., on Itokawa, may be exposed from below by a shaking-induced Brazil-nut effect. Potential sources of shaking are those discussed in Section 1.1.1.6 in regard to resurfacing effects on Itokawa; granular temperature (Section 1.2.2.3) can be provided in multiple fashions, e.g., periodic impacts, varying external gravity fields (tides), etc. Will convection cells develop? Are large boulders required to contain and form convection cells (analogous to the walls of the cylinder)?

5.2.3 Lab Experiment: Avalanches

(Project lead: Derek C. Richardson, UMD)

In collaboration with Braunschweig University in Brunswick, Germany, an effort is underway to build a controlled laboratory experiment specifically to serve as a testbed for calibrating the numerical tools contained in this work (Richardson et al. 2012a). The configuration was specifically chosen to provide a test environment where particle-particle interactions were dominant, minimizing uncertainties about how to handle particle-wall interactions. Figure 5.3 shows an example of a simulation using the same conditions as the experiment: an entire box of particles is slowly tilted while the flow of beads is measured as a function of the angle of the box. Given the simplicity of the configuration and the detailed measurements in the lab, we can explore a wide range of SSDEM numerical parameters for detailed calibration. Preliminary results show that flow initiation requires a steeper angle as the static friction parameter, μ_s, is increased from 0.1(low) to 0.9 (high friction). A value of 0.47 (corresponding to a friction angle of 25 degrees) gives the best match so far to the experiments (Richardson et al., in prep.).

5.2.4 Iapetus' ridge

(Project lead: Kevin Walsh, SwRI)

The ridge along the entirety of Iapetus' equator is up to 15 km tall and hundreds of kilometers wide. One proposed exogenic cause of this feature is the build up of in-falling material from a ring, or disk, of orbiting material (Ip 2006; Levison et al. 2011). However, no detailed models exists to which a comparison can be

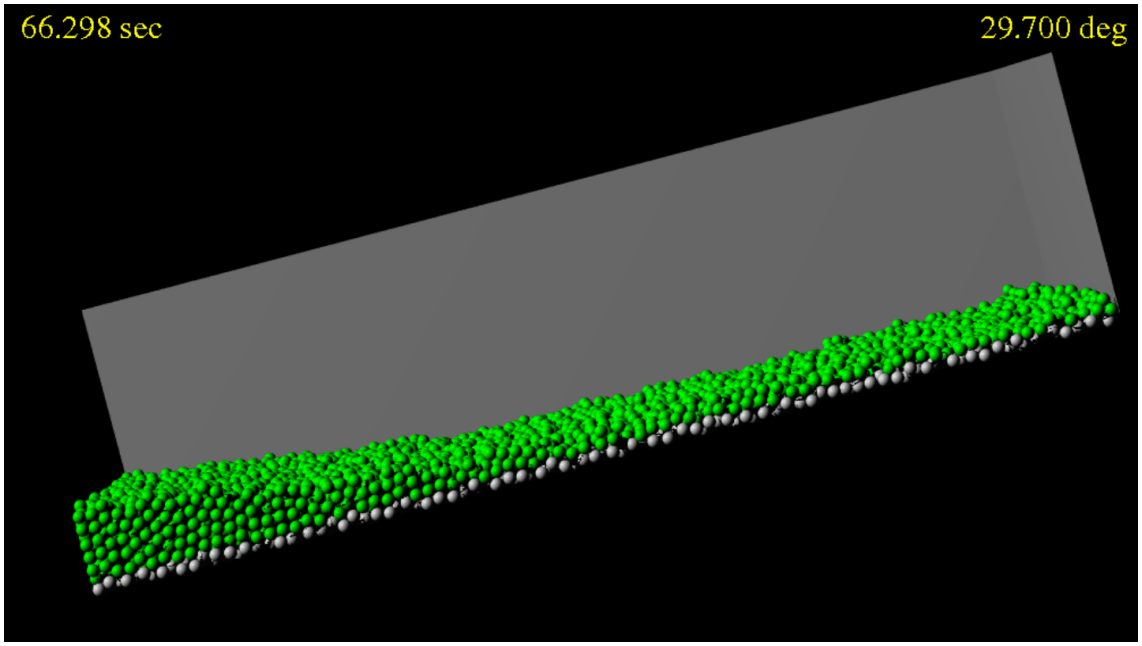

Courtesy: *Derek C. Richardson*

Figure 5.3: Snapshot of a simulation using a 60 x 80 cm tilting bed with loose particles (green) on top of fixed particles (gray). Sustained flow initiates at a tilt angle of approximately 15 degrees for this configuration, which used about 14,000 monodisperse, 5 mm radius particles. SSDEM parameters, $\mu_s = \mu_r = 0.1$ in this simulation (low friction).

made (Walsh et al. 2011). The constraining features of the Iapetan ridge are its general dimensions, morphology, and slopes, along with the possibility of incomplete coverage and some localized cases of parallel ridges or tracks. The magnitude of the tangential velocities of an in-falling debris disk would be a function of the rotation rate of Iapetus at the time its shape was frozen in, estimated to be $\sim$ 16 hr, giving velocities of $\sim$ 300 m s^{-1}, which is subsonic, well within an appropriate regime of an SSDEM simulation. Numerical simulations using `pkdgrav` with SSDEM are being conducted to model ridge growth by way of an in-falling debris disk.

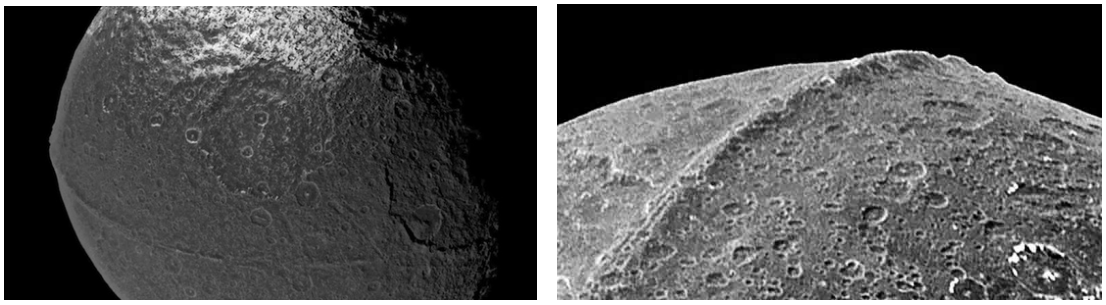

Credit: *NASA / JPL / SSI*

Figure 5.4: The equatorial ridge of Iapetus shown from two perspectives.

5.2.5 Reconfigurations due to tidal encounters

(Project lead: Yang Yu, UMD)

Numerical studies of the effects of tidal forces on rubble-pile SSSBs have been conducted in HSDEM (Richardson et al. 1998; Bottke et al. 1999; Walsh & Richardson 2006). Although HSDEM is capable of producing meaningful results (a comparison study between HSDEM and SSDEM is discussed in Section 1.2.3.3; also see Fig. 5.1), the modeling of SSDEM gravitational aggregates is typically more appropriate. Thus some of the results of these works are being revisited using SSDEM's more precise treatment of contact forces, and using higher resolution ($10^4 \leq N \leq 10^5$ vs. $10^2 \leq N \leq 10^3$ for the previous, HSDEM, studies). Results can be compared with the work of Goldreich & Sari (2009), who propose a model for the structure of a self-gravitating rubble pile; cohesive forces will also be considered.

One source of space weathering for near-Earth objects is proposed to be the result of periodic planetary encounters (Binzel et al. 2010). This hypothesis is being tested numerically by taking a 2-stage approach: first, we perform a flyby of a rigid aggregate at a distance from Earth where global shape change does not occur, but recording all forces at a point on the body's surface (this includes gravitational forces

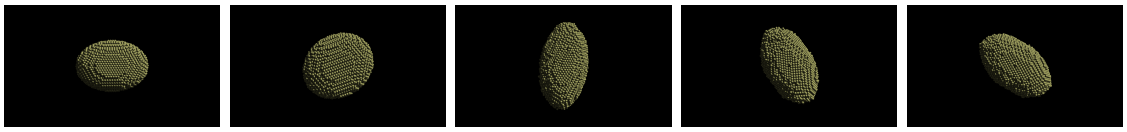

Courtesy: *Yang Yu, UMD*

Figure 5.5: Reshaping of a small Solar System body due a simulated tidal encounter with the Earth. Simulation progresses in time from left to right through closest approach (center frame). The aggregate, made up of about 10,000 monodisperse particles, has a mass of 1.06 x 10^9 kg and initial dimensions of 182 x 130 x 104 (semi-axes in meters), giving an initial bulk density of 0.1 g $cm^{-}3$ (unrealistically low in order to trigger a reshaping). The perigee distance and speed are 4 Earth radii and 10 km s^{-1}. SSDEM parameters used are $\varepsilon_n = 0.8$, $\epsilon_t = 0.9$, $\mu_s = 0.4$, $\mu_s = 0.05$, and $\mu_t = 0.1$. Significant motions of surface particles occur, especially near the extreme ends of the long axis.

from the Earth and from the body, plus the centrifugal force from the rotation of the body). Next, we apply these forces in a new simulation of a sandpile on a local patch of the aggregate centered on the sample point, checking to see if any particle motion is detected (this can be performed for multiple points on the aggregate and be representative of the different surface regions). Preliminary results for the 2029 encounter with (99942) Apophis indicate that particle motion may occur, even at the 6-Earth-radius encounter distance, depending on the exact nature of the grains. A realistic range of SSDEM parameters brackets outcomes from some to no particle motion for the expected encounter scenario (the more fluid-like the SSDEM parameters, the more likely the possibility of particle motion). Any grain motion that we may observe on Apophis during the encounter could be informative of the material properties on the surface.

5.2.6 Saturn's A and B ring systems

(Project lead: Zelong Yu, UMD)

Saturn's A and B rings are an important setting for granular dynamics in the Solar System. There are dense regions where collisions, friction, and cohesion may play important roles in determining the structures observed in the rings, including the detailed images sent back to Earth from the Cassini spacecraft (e.g., see Fig. 1.23). A comprehensive study of the effects of bonding mechanisms in these dense environments requires detailed numerical modeling of the relevant phenomena, which include interparticle self-gravity, planetary tides, and interparticle collisions. Electrostatics and van der Waals forces may also be important for smaller grains (and, for isolated sub-micron grains that carry charge, Saturn's magnetic field could play a dominant role (Jontof-Hutter & Hamilton 2012)). Perrine & Richardson (2012) performed a large suite of simulations using `pkdgrav` with HSDEM collisional particles and a "rigid" cohesion model (Perrine et al. 2011). Both the particles themselves and the bonds were non-deformable. They found a range of simulation parameters that produce the observed size distributions (e.g., French & Nicholson (2000)), which were different between the A and B rings. Overall, the findings were that weak cohesion is consistent with observations (see Fig. 5.6 for an example simulation using "sliding patches" and periodic boundary conditions). Many important questions remain to be answered: e.g., is the amount of cohesion needed in simulation consistent with reasonable levels of van der Waals forces, and what will this say about the material properties of the rings? Were larger "boulders" created through accretion or were they slowly ground down over time?

For reasons detailed in Section 1.2.3.3, SSDEM is much better suited for the

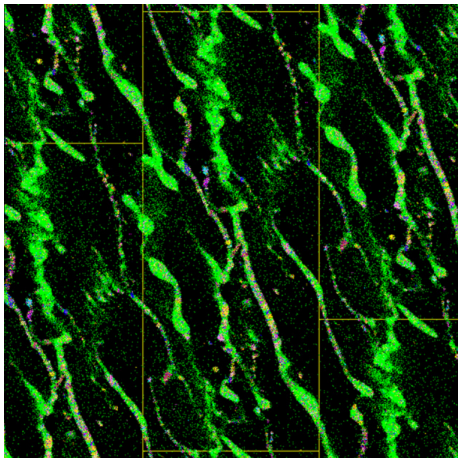

Perrine et al. (2011)

Figure 5.6: Snapshot from a 75,000 monodisperse HSDEM particle simulation using parameters consistent with Saturns outer A ring. The patch (yellow box) is approximately 880 m long (azimuthal) and 350 m wide (radial). A "rigid" (non-deformable) cohesion mechanism was used in this work. Green particles are non-bonded, aggregates are shown in an assortment of colors, and are drawn over non-bonded (green) particles to enhance their visibility.

study of dense granular regimes such as these (e.g., sustained contacts, simultaneous collisions, and robust frictional forces). The core of the B ring can achieve optical depths greatly in excess of unity, strongly indicating that a multi-contact frictional model is needed. The Perrine & Richardson (2012) study used a large number of particles ($N \sim 10^5$), but using SSDEM as is implemented in Chapter 2 will allow for even more ($N > 10^6$), allowing for greater resolution. Using the numerical tools in this work, SSDEM for collisions, and the deformable bonds for cohesion (Chapter 3), these simulations can be revisited, with a range in grain size.

5.2.7 Resettling of grains on Itokawa

Discussed in Sections 1.1.1.6 and 1.1.2.2, ejecta from impacts onto some of the smallest of SSSBs like Itokawa, if not liberated from the asteroid altogether, have the ability to stay aloft for long periods of time relative to their spin-periods. A

numerical simulation of the slow resettling process in micro-gravity may allow small grains to find their way to potential minima while leaving larger rocks and boulders in areas of higher surface potential. Results would be compared to images of Itokawa (Fig. 1.8) and may provide predictions for Bennu and 1999 JU3, the targets of missions OSIRIS-REx (Section 1.1.3.3) and Hayabusa2 (Section 1.1.3.2), respectively.

5.2.8 Build-up of dust grains in the early stellar debris disk

The growth of dust grains into meter-sized boulders in an early stellar system is an unsolved problem in planetary science (Stark & Kuchner 2009), but it is essentially a granular dynamics problem. Accretion by way of low velocity collisions of grains with sufficient cohesion seems to be required. Attractive forces like electrostatics and the van der Waals forces are important in such a regime. Discrete granular dynamics simulations that can control for the strength of these forces and typical shapes, sizes, and impact velocities of grains can be used to put constraints on these parameters. Results can be compared with those taken from cosmochemistry.

5.2.9 Simulations of the YORP effect using SSDEM

For irregularly shaped objects, the impulse provided by sunlight can cause a net torque (the YORP effect) that can change the object's rotation period and the direction of its rotation axis (Section 1.1.2.3). This can eventually lead to global reshaping toward a "top"-shaped obloid that sheds mass at the equator (Fig. 5.7).

The simulations of Walsh et al. (2008, 2012) involved the slow spin-up of hard-sphere granular material (Richardson et al. 2009a, 2000). What is meant by "slow" spin-up is that the rate of angular momentum increase in the simulation should be slow compared to the rate at which that material in the body readjusts to the new

spin-state. This is to say that the movement of the local fixed point of an asteroid's configuration due to spin-up must be slow enough such that the asteroid effectively remains in an equilibrated state.

An additional factor to take into account is the fact that the YORP torque, sensitive to the specific configuration of the topography of the aggregate, may change due to reconfigurations resulting from changes in spin. Cotto-Figueroa et al. (2013) used a triangular facet representation of a model SSSB to self-consistently compute the torques from the YORP effect (Statler 2009) and `pkdgrav` with HSDEM to simulate the subsequent dynamical evolution, taking into account changes in the YORP-torque. They find that continuous changes in the shape of an aggregate can cause a different evolution of the YORP-torque, and therefore the object may not necessarily evolve through the YORP-cycle as would a rigid-body. That is, a weakly cohesive gravitational aggregate prone to reshaping may suffer a random walk of the YORP-torque, slowing the spin-up/down timescale before driving toward an "end-state" (i.e., fast rotation conducive to reshaping/binary formation or slow rotation conducive to tumbling).

Taking into account these results from Cotto-Figueroa et al. (2013), the Walsh et al. (2008, 2012) work on YORP thermal spin-up should be revisited using the SSDEM and cohesive capabilities implemented and outlined in Chapters 2 and 3, and in Schwartz et al. (2012c) and Schwartz et al. (2013). Utilizing the full range of SSDEM frictional parameters and cohesive parameters, we can explore different classes of small gravitational aggregates such as 1999 KW_4 top-like asteroids, asteroids with mildly bifurcated mass distributions (Itokawa-like), asteroids with extreme bifurcated mass distributions (e.g., near-Earth asteroid 2005 CR37; see Benner et al. (2006)), etc. Walsh et al. found that a non-zero angle of repose was needed in order for their model to form and maintain its top-shape, and this was achieved by us-

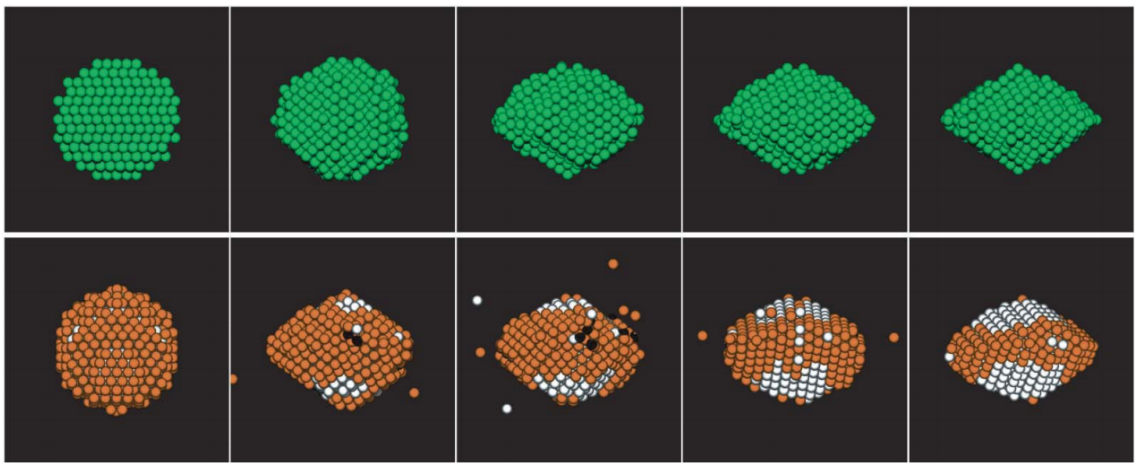

Walsh et al. (2008)

Figure 5.7: Gradual HSDEM spin-up induced shape change and mass loss for a generic rubble-pile asteroid, as seen looking through the equatorial plane. The migration and shedding of original surface particles (orange) and an exposure of interior particles (white) occurs as this model evolves through this simulated YORP-cycle.

ing monodisperse hard spheres in hexagonal-close-pack configuration. In SSDEM, however, material friction parameters are used to tune the angle of repose (e.g., μ_s and μ_r), allowing the investigation into the shapes produced by material of different friction angles. Which classes of gravitational aggregates produce bodies with top-like shapes before shedding material and which instead show fission events? Of the top-shaped gravitational aggregates, which go on to form satellites from accreted ejecta? The investigation would involve aggregates with different size distributions of the constituent grains and rocks, each with their own internal distributions of strength, and include van der Waals cohesive forces.

The inclusion of SSDEM frictional parameters and cohesive forces is expected to delay the onset and alter the qualities of the mass loss and reshaping effects. However, the use of random packing and polydisperse particle distributions will modify the stacking behavior and typically lower the angle of repose if friction and cohesion are neglected.

5.2.10 Cohesive gravitational aggregates: equilibrium shapes and spins

Thermal (YORP) spin-up (Section 1.1.2.3) of cohesionless gravitational aggregates (rubble-piles) has been shown, through recent numerical simulations (Walsh et al. 2008, 2012), to spawn binary asteroid configurations that closely match the observed properties of small binaries, such as near-Earth asteroid 1999 KW4. However, the existence of small asteroids rotating at rates faster than their rotational break-up limits motivates the inclusion of modest cohesion in models of gravitational aggregates (Pravec & Harris 2007).

Discussed in Section 1.2.3.6, gravitational aggregates without cohesion (rubble piles) can maintain non-spherical shapes without bulk spin, unlike a fluid, and can also spin faster than a perfect fluid before shedding mass. Richardson et al. (2005a) investigated the shape and spin limits of self-gravitating rubble piles that consisted of identical HSDEM particles with no sliding friction, and found that this entirely discrete approach is consistent with the theory for the more general continuum (using the MC yield criteria) rubble pile model as analyzed by Holsapple (2004).

Based upon prior investigations using HSDEM (Richardson et al. 2008, 2009b), and complementary to the slow spin-up simulations discussed in Section 5.2.9, a study will be performed that investigates the effects of applying impulsive spins to soft-sphere gravitational aggregates, both with and without weak to modest cohesion; this will give a mapping of equilibrium shape and spin to friction and cohesion parameters over a wide parameter space. Results will be compared to those of Holsapple & Michel (2008), who use the MC and DP yield criteria (Section 1.2.3.6), and to the discrete cohesionless soft-sphere models of (Sánchez & Scheeres 2012).

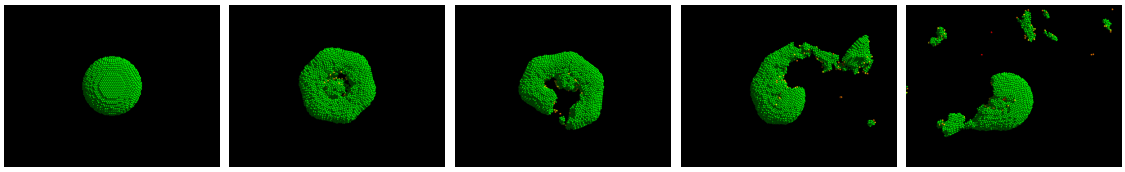

Figure 5.8: Rotational disruption of an impulsively spun gravitational HSDEM aggregate using the cohesion model (Section 3.2.1). Initially oblate, a fissure forms in the center and propagates to the surface preceding the ejection of material. Material parameters: $N = 10000$, bulk density = 2 g cm^{-3}, particle radius = 26.7 m; $\varepsilon_n = 0.5$, $\varepsilon_t = 1.0$; cohesion parameters: $Y = 250$ Pa, $\epsilon_{\max} Y = 125$ Pa.

5.3 Public Availability of the Code

Although the platform of the numerical tools contained in this work, `pkdgrav`, is not released to the public domain, there is an ongoing effort toward that goal by the original authors; the SSDEM implementation will ultimately be part of that code suite. The public release will be accompanied by a web portal for code download, documentation, and bug/feature tracking.

Appendix A

Table of Parameters

Table A.1: Listing of parameters (non-exhaustive)

Symbol	Definition
C_n	SSDEM Normal damping parameter
C_t	SSDEM Tangential damping parameter
$\mathbf{S}$	Tangential vector (points from the point of tangential equilibrium to the current contact point)
Y	Young's modulus of cohesive bond
b	Fraction of tangential strain remaining after static failure (slip)
d	Distance from center-of-mass (COM hereafter) of particle to contact point on wall
h	Timestep
k_n	SSDEM normal spring constant
k_t	SSDEM tangential spring constant
l_1	Particle lever arm: distance from active particle COM to contact point
l_2	Particle lever arm: distance from neighbor COM to contact point
m_1	Mass of active particle
$\hat{\mathbf{n}}$	Unit normal vector that typically points from particle COM to neighbor COM (or to wall)
$\mathbf{r}$	Position with respect to origin
$\mathbf{r_1}$	Position of active particle with respect to origin (subscript "1" denotes active particle
$\mathbf{r_2}$	Position of neighbor with respect to origin (subscript "2" denotes neighbor particle)
s	Radius
$\hat{\mathbf{t}}$	Unit tangential vector (tangential component of total $\mathbf{u}$ at contact point)
$\mathbf{u}$	Total relative velocity, $\mathbf{v_2} - \mathbf{v_1}$
$\mathbf{v}$	Velocity with respect to origin
x	Penetration depth of overlap
z	Equilibrium separation between cohesive particles' COMs (zero-strain-length)
δ	Effective strain of penetrating cohesive SSDEM particles, $[\rho/\rho_0] - 1$
γ	Cohesive damping parameter

Bibliography

Abe, S., Mukai, T., Hirata, N., et al. 2006, Science, 312, 1344

Abercromby, A. F., Chappell, S. P., & Gernhardt, M. L. 2013a, Acta Astronautica, 91, 34

Abercromby, A. F., Gernhardt, M. L., & Jadwick, J. 2013b, Acta Astronautica, 90, 203

Abercromby, A. F. J., Chappell, S. P., Litaker, H. L., & Gernhardt, M. L. 2013, LPI Contributions, 1719, 1671

A'Hearn, M. F., & DIXI Team. 2012, LPI Contributions, 1667, 6334

A'Hearn, M. F., Belton, M. J. S., Delamere, W. A., et al. 2005, Science, 310, 258

Alder, B. J., & Wainwright, T. E. 1959, J. Chem. Phys., 31, 459

Anderson, R. S., & Anderson, S. P. 2010, Geomorphology: the mechanics and chemistry of landscapes (Cambridge University Press)

Andert, T. P., Rosenblatt, P., Pätzold, M., et al. 2010, Geophys. Res. Lett., 37, 9202

Arakawa, M., Saiki, T., Wada, K., et al. 2013, LPI Contributions, 1719, 1904

Asphaug, E. 1997, Meteoritics & Planetary Science, 32, 965

Asphaug, E., & Benz, W. 1994, Nature, 370, 120

Azéma, E., Estrada, N., & Radjaï, F. 2012, Phys. Rev. E, 86, 041301

Barlow, N. 2008, Mars: An introduction to its interior, surface and atmosphere

(Cambridge University Press)

Barnouin, O., & Kahn, E. 2012, NASA Planetary Data System, 176

Barr, A. C., & Citron, R. I. 2011, Icarus, 211, 913

Barucci, M., Michel, P., Böhnhardt, H., et al. 2013, MarcoPolo-R Asteroid Sample Return Mission: Tracing the Origins, http://websites.isae.fr/sites/websites/IMG/pdf/barucci_ippwpapermp-r_juin7.pdf

Belton, M. J. S., Thomas, P., Li, J.-Y., et al. 2013, Icarus, 222, 595

Benner, L. A., Nolan, M. C., Ostro, S. J., et al. 2006, Icarus, 182, 474

Benz, W., & Asphaug, E. 1999, Icarus, 142, 5

Berardi, C. R., Barros, K., Douglas, J. F., & Losert, W. 2010, Phys. Rev. E, 81, 041301

Berenbaum, R., & Brodie, I. 1959, Br. J. Appl. Phys., 10, 281

Berry, K., Sutter, B., May, A., et al. 2013, OSIRIS-REx Touch-And-Go (TAG) Mission Design and Analysis, http://ntrs.nasa.gov/search.jsp?R=20130013409

Bertrand, F., Leclaire, L.-A., & Levecque, G. 2005, Chem. Eng. Sci., 60, 2517

Besse, S., Lamy, P., Jorda, L., Marchi, S., & Barbieri, C. 2012, Icarus, 221, 1119

Beverloo, W. A., Leniger, H. A., & van de Velde, J. 1961, Chem. Eng. Sci., 15, 260

Binzel, R. P., Morbidelli, A., Merouane, S., et al. 2010, Nature, 463, 331

Blair, D. L., Neicu, T., & Kudrolli, A. 2003, Phys. Rev. E, 67, 031303

Bland, M. T., Singer, K. N., & McKinnon, W. B. 2013, LPI Contributions, 1719, 1655

Bottke, Jr., W. 2007, in Bulletin of the American Astronomical Society, Vol. 39, AAS/Division for Planetary Sciences Meeting Abstracts #39, 416

Bottke, W. F., & Chapman, C. R. 2006, in Lunar and Planetary Institute Science Conference Abstracts, Vol. 37, 37th Annual Lunar and Planetary Science Confer-

ence, eds. S. Mackwell & E. Stansbery, 1349

Bottke, W. F., Durda, D. D., Nesvorný, D., et al. 2005, Icarus, 175, 111

Bottke, W. F., & Melosh, H. J. 1996, Nature, 381, 51

Bottke, Jr., W. F., Richardson, D. C., Michel, P., & Love, S. G. 1999, AJ, 117, 1921

Bottke, Jr., W. F., Vokrouhlický, D., Rubincam, D. P., & Nesvorný, D. 2006, Annual Review of Earth and Planetary Sciences, 34, 157

Boyce, J., Wilson, L., Mouginis-Mark, P., Tornabene, L., & Hamilton, C. 2012, in Lunar and Planetary Institute Science Conference Abstracts, Vol. 43, 1017

Brahic, A. 1975, Icarus, 25, 452

—. 1977, Astronomy and Astrophysics, 54, 895

Britt, D., & Consolmagno, G. 2000, Icarus, 146, 213

Brozovic, M., Benner, L., Nolan, M., et al. 2010, in Bulletin of the American Astronomical Society, Vol. 42, 1080

Buczkowski, D. L., Wyrick, D. Y., Iyer, K. A., et al. 2012, Geophysical Research Letters, 39, doi:10.1029/2012GL052959

Bull, W. B. 1977, Progress in Physical Geography, 1, 222

Burchell, M., & Leliwa-Kopystynski, J. 2010, Icarus, 210, 707

Burns, J. A. 1992, Contradictory clues as to the origin of the Martian moons (University of Arizona Press), 1283

Bus, S. J. 1999, PhD thesis, Massachusetts Institute of Technology

Bus, S. J., & Binzel, R. P. 2002a, Icarus, 158, 146

—. 2002b, Icarus, 158, 146

—. 2002c, Icarus, 158, 106

Busch, M. W., Ostro, S. J., Benner, L. A. M., et al. 2007, Icarus, 186, 581

Campbell, C. S. 2006, Powder Technology, 162, 208

Carry, B., Dumas, C., Fulchignoni, M., et al. 2008, A&A, 478, 235

Carry, B., Vernazza, P., Dumas, C., & Fulchignoni, M. 2010, Icarus, 205, 473

Carsenty, U., Wagner, R. J., Boczkowski, D. L., et al. 2013, LPI Contributions, 1719, 1492

Castellanos, A. 2005, Advances in Physics, 54, 263

Chapman, C. R. 1996, Meteoritics and Planetary Science, 31, 699

—. 2010, Nature, 463, 305

Chapman, C. R., Morrison, D., & Zellner, B. 1975, Icarus, 25, 104

Chappell, S. P., Abercromby, A. F. J., Reagan, M. L., & Gernhardt, M. L. 2013, LPI Contributions, 1719, 1724

Chen, K. 2008, Granular Materials Under Vibration and Thermal Cycles (ProQuest)

Cheng, A. F. 2004, Advances in Space Research, 33, 1558

Cheng, A. F., Barnouin-Jha, O., Prockter, L., et al. 2002, Icarus, 155, 51

Chesley, S. R., Ostro, S. J., Vokrouhlický, D., et al. 2003, Science, 302, 1739

Chesley, S. R., Nolan, M., Farnocchia, D., et al. 2012, LPI Contributions, 1667, 6470

Clark, B. E., Bus, S. J., Rivkin, A. S., et al. 2004, Journal of geophysical research, 109, E02001

Clark, B. E., Veverka, J., Helfenstein, P., et al. 1999, Icarus, 140, 53

Cleary, P. W. 1998, Miner. Eng., 11, 1061

Cleary, P. W., & Sawley, M. L. 2002, Appl. Math. Modell., 26, 89

Consolmagno, G., Britt, D., & Macke, R. 2008, Chem. Erde-Geochem., 68, 1

Cotto-Figueroa, D., Statler, T. S., Richardson, D. C., & Tanga, P. 2013, LPI Contributions, 1719, 2945

Cowin, S. 1974, Powder Technology, 9, 61

Crawford, I. 2012, Astronomy & Geophysics, 53, 6

Crosta, G. B., Imposimato, S., & Roddeman, D. 2009, Journal of Geophysical Research: Earth Surface, 114, n/a

Ćuk, M. 2007, The Astrophysical Journal Letters, 659, L57

Ćuk, M., & Nesvornỳ, D. 2010, Icarus, 207, 732

Cundall, P. A., & Strack, O. D. L. 1979, Géotechnique, 29, 47

David, L. 2012, Japan Eyes New Space Mission to Sample an Asteroid, March 2, SPACE.com

De Sanctis, M., Ammannito, E., Capria, M., et al. 2012, Science, 336, 697

Delenne, J.-Y., Soulié, F., El Youssoufi, M. S., & Radjaï, F. 2009, in American Institute of Physics Conference Series, Vol. 1145, American Institute of Physics Conference Series, eds. M. Nakagawa & S. Luding, 893

Denevi, B. W., Blewett, D. T., Capaccioni, F., et al. 2012a, in Lunar and Planetary Institute Science Conference Abstracts, Vol. 43, Lunar and Planetary Institute Science Conference Abstracts, 2308

Denevi, B. W., Blewett, D. T., Buczkowski, D. L., et al. 2012b, Science, 338, 246

Dooling, D. 1998, Mechanics of Granular Materials (MGM): Second round of space experiments on STS-89 will help us understand better the behavior of soils, powders, and other solid particles under very low confining pressures. http://science.nasa.gov/science-news/science-at-nasa/mgm_images/msad01jan98_2a/

Dougherty, M. K., Esposito, L. W., & Krimigis, S. M., ed. 2009, Ring Particle Composition and Size Distribution (Springer, Dordrecht), 459

Elaskar, S. A., Godoy, L. A., Gray, D. D., & Stiles, J. M. 2000, Int. J. Solids Struct., 37, 2185

Fang, J., Margot, J.-L., Brozovic, M., et al. 2011, The Astronomical Journal, 141, 154

Farnocchia, D., Chesley, S. R., Vokrouhlický, D., et al. 2013, Icarus, 224, 1

Fieber-Beyer, S. K., Gaffey, M. J., Abell, P. A., & Reddy, V. 2007, in Lunar and

Planetary Institute Science Conference Abstracts, Vol. 38, Lunar and Planetary Institute Science Conference Abstracts, 1695

Fornasier, S., Belskaya, I., Fulchignoni, M., Barucci, M. A., & Barbieri, C. 2006, A&A, 449, L9

French, R. G., & Nicholson, P. D. 2000, Icarus, 145, 502

Fujiwara, A., Kawaguchi, J., Yeomans, D. K., et al. 2006, Science, 312, 1330

Gaffey, M. J., Bell, J. F., & Cruikshank, D. P. 1989, in Asteroids II, eds. R. P. Binzel, T. Gehrels, & M. S. Matthews, 98

Gehrels, T., Matthews, M., & Schumann, A. 1994, Hazards Due to Comets and Asteroids, Space Science Series (University of Arizona Press)

Geissler, P., Petit, J. M., & Greenberg, R. 1996, in Astronomical Society of the Pacific Conference Series, Vol. 107, Completing the Inventory of the Solar System, eds. T. Rettig & J. M. Hahn, 57–67

Goldreich, P., & Sari, R. 2009, ApJ, 691, 54

Gotteland, P., Villard, P., & Salot, C. 2009, in American Institute of Physics Conference Series, Vol. 1145, American Institute of Physics Conference Series, eds. M. Nakagawa & S. Luding, 361

Goudie, A. S. 2008, Annu. Rev. Earth Planet. Sci., 36, 97

Gradie, J., & Veverka, J. 1980, Nature, 283, 840

Greeley, R., Sullivan, R., Pappalardo, R., et al. 1994, in Lunar and Planetary Institute Science Conference Abstracts, Vol. 25, Lunar and Planetary Institute Science Conference Abstracts, 469

Grensemann, M., & Schwehm, G. 1993, Journal of Geophysical Research: Space Physics (1978–2012), 98, 20907

Grof, Z., Cook, J., Lawrence, C. J., & Štěpánek, F. 2009, Journal of Petroleum Science and Engineering, 66, 24

Haff, P. 1983, Journal of Fluid Mechanics, 134, 401

Hamaker, H. 1937, Physica, 4, 1058

Han, Y., & Cundall, P. A. 2012, International Journal for Numerical and Analytical Methods in Geomechanics

Harms, J. 1969, Geological Society of America Bulletin, 80, 363

Harris, A. W., & Pravec, P. 2006, in IAU Symposium, Vol. 229, Asteroids, Comets, Meteors, eds. L. Daniela, M. Sylvio Ferraz, & F. J. Angel, 439

Hartmann, W. K., Farinella, P., Weidenschilling, S. J., et al. 1997, in Lunar and Planetary Institute Science Conference Abstracts, Vol. 28, Lunar and Planetary Institute Science Conference Abstracts, 517

Hatzes, A., Bridges, F., Lin, D., & Sachtjen, S. 1991, Icarus, 89, 113

Henann, D. L., & Kamrin, K. 2013, Proceedings of the National Academy of Sciences, 110, 6730

Hofmeister, P. G., Blum, J., & Heißelmann, D. 2009, in American Institute of Physics Conference Series, Vol. 1145, American Institute of Physics Conference Series, eds. M. Nakagawa & S. Luding, 71–74

Holsapple, K. A. 1992, in Lunar and Planetary Inst. Technical Report, Vol. 23, Lunar and Planetary Institute Science Conference Abstracts, 547

Holsapple, K. A. 2004, Icarus, 172, 272

—. 2007, Icarus, 187, 500

—. 2009, Planet. Space Sci., 57, 127

Holsapple, K. A., & Michel, P. 2006, Icarus, 183, 331

—. 2008, Icarus, 193, 283

Housen, K. R., & Holsapple, K. A. 2003, Icarus, 163, 102

—. 2011, Icarus, 211, 856

Housen, K. R., Schmidt, R. M., & Holsapple, K. A. 1983, J. Geophys. Res., 88, 2485

Housen, K. R., Wilkening, L. L., Chapman, C. R., & Greenberg, R. 1979, Icarus, 39, 317

Hudson, R. S., & Ostro, S. J. 1995, Science, 270, 84

Ingale, R. A. 2008, Dynamics of vibrated granular matter (ProQuest)

Ip, W.-H. 2006, Geophys. Res. Lett., 33, L16203

Iverson, R. M., & Vallance, J. W. 2001, Geology, 29, 115

Jacobson, R. 2010, The Astronomical Journal, 139, 668

Jacobson, S., & Scheeres, D. 2012, in Lunar and Planetary Institute Science Conference Abstracts, Vol. 43, 2737

Janssen, H. A. 1895, Ver. dt. Ing., 39, 1045

Jaumann, R., Williams, D., Buczkowski, D., et al. 2012, science, 336, 687

Jiang, M., Shen, Z., & Zhu, F. 2013, Granular Matter, 15, 195

Jontof-Hutter, D., & Hamilton, D. P. 2012, Icarus, 220, 487

Jorda, L., Lamy, P. L., Gaskell, R. W., et al. 2012, Icarus, 221, 1089

Jutzi, M., Asphaug, E., Gillet, P., Barrat, J.-A., & Benz, W. 2013, Nature, 494, 207

Jutzi, M., Michel, P., & Benz, W. 2010, A&A, 509, L2

Kaasalainen, M., Torppa, J., & Muinonen, K. 2001, Icarus, 153, 37

Kaasalainen, M., Ďurech, J., Warner, B. D., Krugly, Y. N., & Gaftonyuk, N. M. 2007, Nature, 446, 420

Kacianauskas, R., Maknickas, A., Kaceniauskas, A., Markauskas, D., & Balevicius, R. 2010, Adv. Eng. Software, 41, 52

Keller, H., A'Hearn, M., Angrilli, F., et al. 2009, AGU Spring Meeting Abstracts, A2

Keller, H. U., Barbieri, C., Koschny, D., et al. 2010, Science, 327, 190

Kerr, R. A. 2011, NASA Aims to Grab Asteroid Dirt in 2020, May 25, Science Magazine, ScienceInsider

Klotz, I. 2013, NASA unveils plan to catch asteroid as step to Mars flight, April 10, Reuters

Kosinski, P., & Hoffmann, A. C. 2009, Phys. Rev. E, 79, 061302

Ksanfomality, L. V. 2007, Solar System Research, 41, 174

Lamy, P. L., Kaasalainen, M., Lowry, S., et al. 2008, A&A, 487, 1179

Lauretta, D. S. 2012, SPIE Newsroom

Lebron, I., & Robinson, D. 2003, Vadose Zone Journal, 2, 330

Leinhardt, Z. M., & Richardson, D. C. 2005, ApJ, 625, 427

Leinhardt, Z. M., & Stewart, S. T. 2012, ApJ, 745, 79

Leonard, B. 2011, Human Space Exploration Framework Summary: Report of the Human Exploration Framework Team (HEFT) (DIANE Publishing)

Leone, D. 2013, NASA authorization cycle begins with asteroid retrieval in houses crosshairs, June 17, SpaceNews

Levison, H. F., Walsh, K., Barr, A., & Dones, L. 2011, Icarus, 214, 773

Lewis, J. 2004, Physics and Chemistry of the Solar System, International Geophysics Series (Elsevier Academic Press)

Lissauer, J. J. 1993, ARA&A, 31, 129

Loff, S., & Lind, R. 2013, Orion: America's new spacecraft for human exploration, June 12, http://www.nasa.gov/exploration/systems/mpcv/index.html

London, F. 1936, Proceedings of the Royal Society of London. Series A-Mathematical and Physical Sciences, 153, 576

Lorenz, C., Basilevsky, A., Shingareva, T., et al. 2012, in Lunar and Planetary Institute Science Conference Abstracts, Vol. 43, 1142

Losert, W., Cooper, D., Delour, J., Kudrolli, A., & Gollub, J. 1999, arXiv preprint cond-mat/9901203

Lowry, S. C., Fitzsimmons, A., Pravec, P., et al. 2007, Science, 316, 272

Luzum, B., Capitaine, N., Fienga, A., et al. 2011, Celestial Mechanics and Dynamical Astronomy, 110, 293

Machii, N., & Nakamura, A. M. 2011, Icarus, 211, 885

Madole, R. F., Romig, J. H., Aleinikoff, J. N., VanSistine, D. P., & Yacob, E. Y. 2008, Geomorphology, 99, 99

Makabe, T. 2008, in COSPAR Meeting, Vol. 37, 37th COSPAR Scientific Assembly, 1883

Marchi, S., Barbieri, C., Küppers, M., et al. 2010, Planetary and Space Science, 58, 1116

Marchi, S., McSween, H., OBrien, D., et al. 2012, Science, 336, 690

Marchi, S., Bottke, W. F., O'Brien, D. P., et al. 2013, Planetary and Space Science, in press, doi: 10.1016/j.pss.2013.05.005

McEwen, A., Hansen, C., Delamere, W., et al. 2007, Science, 317, 1706

McKinnon, W. B. 2008, in Bulletin of the American Astronomical Society, Vol. 40, AAS/Division for Planetary Sciences Meeting Abstracts #40, 464

Mehta, A. 2007, Granular Physics (Cambridge, UK: Cambridge University Press)

Michel, P., Ballouz, R., Richardson, D. C., & Schwartz, S. R. 2012a, in AAS/Division for Planetary Sciences Meeting Abstracts, Vol. 44, AAS/Division for Planetary Sciences Meeting Abstracts, #105.05

Michel, P., Benz, W., & Richardson, D. C. 2004, Planet. Space Sci., 52, 1109

Michel, P., O'Brien, D. P., Abe, S., & Hirata, N. 2009, Icarus, 200, 503

Michel, P., & Richardson, D. C. 2013, A&A, 554, L1

Michel, P., Schwartz, S. R., Richardson, D. C., Machii, N., & Nakamura, A. M. 2011, in EPSC-DPS Joint Meeting 2011, 285

Michel, P., Schwartz, S. R., Richardson, D. C., Machii, N., & Nakamura, A. M. 2012b, in Lunar and Planetary Institute Science Conference Abstracts, Vol. 43,

Lunar and Planetary Institute Science Conference Abstracts, 1320

Michel, P., Schwartz, S. R., Richardson, D. C., & Murdoch, N. 2012c, in European Planetary Science Congress 2012, 114

Miner, E. D., Wessen, R. R., & Cuzzi, J. N. 2007, in Planetary Ring Systems, Springer Praxis Books (Praxis), 1–16

Monaghan, J. J. 1988, Computer physics communications, 48, 89

Moore, P. L., & Iverson, N. R. 2002, Geology, 30, 843

Morbidelli, A., Levison, H. F., Tsiganis, K., & Gomes, R. 2005, Nature, 435, 462

Morbidelli, A., & Vokrouhlický, D. 2003, Icarus, 163, 120

Mueller, M. 2007, PhD thesis, Free University of Berlin

Müller, P., & Pöschel, T. 2012, Granular Matter, 14, 115

—. 2013, Phys. Rev. E, 87, 033301

Müller, T., Durech, J., Hasegawa, S., et al. 2010, arXiv preprint arXiv:1011.5029

Murdoch, N., Michel, P., Richardson, D. C., et al. 2012, Icarus, 219, 321

Murdoch, N., Rozitis, B., Nordstrom, K., et al. 2013, Phys. Rev. Lett., 110, 018307

Nakamura, A. M., Setoh, M., Wada, K., Yamashita, Y., & Sangen, K. 2013, Icarus, 223, 222

Nayfeh, S. A., Verdirame, J. M., & Varanasi, K. K. 2002, in SPIE's 9th Annual International Symposium on Smart Structures and Materials, International Society for Optics and Photonics, 158–167

Nedderman, R. M. 2005, Statics and kinematics of granular materials (Cambridge University Press)

Nedderman, R. M., Tüzün, U., Savage, S. B., & Houlsby, G. T. 1982, Chem. Eng. Sci., 37, 1597

Nesvorný, D., & Bottke, W. F. 2004, Icarus, 170, 324

Neugebauer, M., Gloeckler, G., Gosling, J. T., et al. 2007, ApJ, 667, 1262

Nolan, M. C., Magri, C., Ostro, S. J., et al. 2007, in Bulletin of the American Astronomical Society, Vol. 39, AAS/Division for Planetary Sciences Meeting Abstracts #39, 433

O'Brien, D. P., Greenberg, R., & Richardson, J. E. 2006, Icarus, 183, 79

Ogawa, S. 1978, in Proc. of US-Japan Symp. on Continuum Mechanics and Statistical Approaches to the Mechanics of Granular Media, eds. S. C. Cowin & M. Satake (Fukyu-kai: Gakujutsu Bunken), 208

O'Hern, C. S. 2013, The Northeastern Granular Materials Workshop (NEGW). http://gibbs.engr.ccny.cuny.edu/NEGW.php

Okazaki, R., Nagao, K., Miura, Y., et al. 2011, in Lunar and Planetary Institute Science Conference Abstracts, Vol. 42, 1653

Ostro, S. J., Hudson, R. S., Rosema, K. D., et al. 1999, Icarus, 137, 122

Ostro, S. J., Margot, J.-L., Benner, L. A., et al. 2006, Science, 314, 1276

Pätzold, M., Andert, T. P., Asmar, S. W., et al. 2011, Science, 334, 491

Perrine, R. P., & Richardson, D. C. 2012, Icarus, 219, 515

Perrine, R. P., Richardson, D. C., & Scheeres, D. J. 2011, Icarus, 212, 719

Pestana, J. M., & Salvati, L. A. 2006, Journal of geotechnical and geoenvironmental engineering, 132, 1071

Pitjeva, E. V. 2005, Solar System Research, 39, 176

Pitjeva, E. V., & Standish, E. M. 2009, Celestial Mechanics and Dynamical Astronomy, 103, 365

Powers, J. M. 2004, Physics of Fluids, 16, 2975

Prado, M. E. 2013, Obama-NASA Asteroid Retrieval Mission. http://www.permanent.com/keck-obama-nasa-asteroid-retrieval-to-lunar-orbit.html

Pravec, P., & Harris, A. W. 2000, Icarus, 148, 12

Pravec, P., & Harris, A. W. 2006, in Bulletin of the American Astronomical Society, Vol. 38, AAS/Division for Planetary Sciences Meeting Abstracts #38, 614

—. 2007, Icarus, 190, 250

Pravec, P., Harris, A. W., Scheirich, P., et al. 2005, Icarus, 173, 108

Pravec, P., Vokrouhlickỳ, D., Polishook, D., et al. 2010, Nature, 466, 1085

Quinn, T., Perrine, R. P., Richardson, D. C., & Barnes, R. 2010, AJ, 139, 803

Radjaï, F., & Dubois, F. 2011, Discrete-element modeling of granular materials (Berlin: Wiley-ISTE)

Radjaï, F., & Richefeu, V. 2009, Mechanics of Materials, 41, 715

Radjaï, F., Topin, V., Richefeu, V., et al. 2010, in American Institute of Physics Conference Series, Vol. 1227, American Institute of Physics Conference Series, eds. J. Goddard, P. Giovine, & J. T. Jenkins, 240–259

Reagan, M., Janoiko, B., Johnson, J., Steven Chappell, P. D., & Abercromby, A. 2012, NASA's Analog Missions: Driving Exploration Through Innovative Testing (American Institute of Aeronautics and Astronautics)

Reddy, V., Sanchez, J. A., Gaffey, M. J., et al. 2012, Icarus, 221, 1177

Reis, P. M., Ingale, R. A., & Shattuck, M. D. 2006, Phys. Rev. Lett., 96, 258001

Richardson, D. C. 1994, Monthly Notices of the Royal Astronomical Society, 269, 493

—. 1995, Icarus, 115, 320

Richardson, D. C. 2005, in Bulletin of the American Astronomical Society, Vol. 37, AAS/Division for Planetary Sciences Meeting Abstracts #37, 638

Richardson, D. C., Asphaug, E., & Benner, L. 1995, in Bulletin of the American Astronomical Society, Vol. 27, AAS/Division for Planetary Sciences Meeting Abstracts #27, 1114

Richardson, D. C., Blum, J., Weinhart, T., et al. 2012a, in AAS/Division for Plan-

etary Sciences Meeting Abstracts, Vol. 44, AAS/Division for Planetary Sciences Meeting Abstracts, #105.06

Richardson, D. C., Bottke, W. F., & Love, S. G. 1998, Icarus, 134, 47

Richardson, D. C., Elankumaran, P., & Sanderson, R. E. 2005a, Icarus, 173, 349

Richardson, D. C., Leinhardt, Z. M., Melosh, H. J., Bottke, Jr., W. F., & Asphaug, E. 2002, in Asteroids III, eds. W. Bottke, A. Cellino, P. Paolicchi, & R. P. Binzel, 501

Richardson, D. C., Michel, P., Walsh, K. J., & Flynn, K. W. 2009a, Planet. Space Sci., 57, 183

Richardson, D. C., Munyan, S. K., Schwartz, S. R., & Michel, P. 2012b, in Lunar and Planetary Institute Science Conference Abstracts, Vol. 43, Lunar and Planetary Institute Science Conference Abstracts, 2195

Richardson, D. C., Quinn, T., Stadel, J., & Lake, G. 2000, Icarus, 143, 45

Richardson, D. C., Schwartz, S. R., Michel, P., & Walsh, K. J. 2008, in Bulletin of the American Astronomical Society, Vol. 40, AAS/Division for Planetary Sciences Meeting Abstracts #40, 498

Richardson, D. C., Schwartz, S. R., Walsh, K. J., & Michel, P. 2009b, in AAS/Division of Dynamical Astronomy Meeting, Vol. 40, AAS/Division of Dynamical Astronomy Meeting #40, #12.04

Richardson, D. C., & Walsh, K. J. 2006, Annual Review of Earth and Planetary Sciences, 34, 47

Richardson, D. C., Walsh, K. J., Murdoch, N., & Michel, P. 2011, Icarus, 212, 427

Richardson, D. C., Walsh, K. J., Murdoch, N., Michel, P., & Schwartz, S. R. 2010, in Bulletin of the American Astronomical Society, Vol. 42, AAS/Division for Planetary Sciences Meeting Abstracts #42, 1093

Richardson, J. E., Melosh, H. J., & Greenberg, R. 2004, Science, 306, 1526

Richardson, J. E., Melosh, H. J., Greenberg, R. J., & O'Brien, D. P. 2005b, Icarus, 179, 325

Richefeu, V., Radjaï, F., & El Youssoufi, M. S. 2009, in American Institute of Physics Conference Series, Vol. 1145, American Institute of Physics Conference Series, eds. M. Nakagawa & S. Luding, 919–922

Rivkin, A. S., & Volquardsen, E. L. 2010, Icarus, 206, 327

Rose, H. E., & Tanaka, T. 1959, Engineer, 208, 465

Rubincam, D. P. 2000, Icarus, 148, 2

Russell, C. T., Raymond, C. A., Coradini, A., et al. 2012, Science, 336, 684

Saha, P., & Tremaine, S. 1992, JRASC, 86, 291

Saito, J., Miyamoto, H., Nakamura, R., et al. 2006, Science, 312, 1341

Sánchez, D. P., & Scheeres, D. J. 2012, Icarus, 218, 876

Sánchez, P., & Scheeres, D. J. 2011, ApJ, 727, 120

—. 2013, ArXiv e-prints, arXiv:1306.1622

Sayre, C. B., & Clark, A. W. 1938, Agronomy Journal, 30, 30

Scheeres, D., Fahnestock, E. G., Ostro, S. J., et al. 2006, Science, 314, 1280

Scheeres, D. J. 2007, Icarus, 189, 370

Scheeres, D. J., Abe, M., Yoshikawa, M., et al. 2007, Icarus, 188, 425

Scheeres, D. J., Hartzell, C. M., Sánchez, P., & Swift, M. 2010, Icarus, 210, 968

Schmidt, B. E., Thomas, P. C., Bauer, J. M., et al. 2008, in Lunar and Planetary Institute Science Conference Abstracts, Vol. 39, Lunar and Planetary Institute Science Conference Abstracts, 2502

Schröder, S. E., Keller, H. U., Gutierrez, P., et al. 2010, Planet. Space Sci., 58, 1107

Schwartz, S., Richardson, D. C., & Michel, P. 2012a, in AAS/Division for Planetary Sciences Meeting Abstracts, Vol. 44, AAS/Division for Planetary Sciences Meeting Abstracts, #105.07

Schwartz, S. R., Michel, P., & Richardson, D. C. 2013, Icarus, 226, 67

Schwartz, S. R., Michel, P., Richardson, D. C., & Murdoch, N. 2012b, LPI Contributions, 1667, 6473

Schwartz, S. R., Richardson, D. C., & Michel, P. 2012c, Granul. Matter, 14, 363

—. in prep., Icarus

Schwartz, S. R., Richardson, D. C., Michel, P., & Walsh, K. J. 2009, in AAS/Division for Planetary Sciences Meeting Abstracts, Vol. 41, AAS/Division for Planetary Sciences Meeting Abstracts #41, #27.11

Schwartz, S. R., Richardson, D. C., Michel, P., & Walsh, K. W. 2011, in EPSC-DPS Joint Meeting 2011, 1240

Setoh, M., Nakamura, A. M., Michel, P., et al. 2010, Icarus, 205, 702

Sharma, I., Jenkins, J. T., & Burns, J. A. 2009, Icarus, 200, 304

Shaxby, J. H., & Evans, J. C. 1923, Trans. Faraday Soc., 19, 60

Sierks, H., Lamy, P., Barbieri, C., et al. 2011, Science, 334, 487

Sirono, S.-I. 2004, Icarus, 167, 431

Soto, R. 2012, Southern Workshop on Granular Materials 2012 - SWGM12. http://www.dfi.uchile.cl/ granular12/granular12/Home.html

Souraki, Y., Ashrafi, M., Karimaie, H., & Torsaeter, O. 2012, Energy and Environment Research, 2, 140

Spitale, J. N., & Porco, C. C. 2010, AJ, 140, 1747

Springel, V. 2010, ARA&A, 48, 391

Springel, V., & Hernquist, L. 2002, Monthly Notices of the Royal Astronomical Society, 333, 649

Stadel, J. G. 2001, PhD thesis, University of Washington

Stark, C. C., & Kuchner, M. J. 2009, ApJ, 707, 543

Staron, L., Lagrée, P.-Y., & Popinet, S. 2013, arXiv preprint arXiv:1306.6279

Statler, T. S. 2009, Icarus, 202, 502

Statler, T. S., Cotto-Figueroa, D., Riethmiller, D. A., & Sweeney, K. M. 2013, Icarus, 225, 141

Stelzried, C., Efron, L., & Ellis, J. 1986, Nature, 321

Strahler, A. N. 1971, The Earth Sciences (Harper & Row, New York, NY)

Tachibana, S., Sawada, H., Okazaki, R., et al. 2013, LPI Contributions, 1719, 1880

Tancredi, G., Maciel, A., Heredia, L., Richeri, P., & Nesmachnow, S. 2012, MNRAS, 420, 3368

Tancredi, G., Roland, S., & Bruzzone, S. in prep., Icarus

Taylor, P. A., Margot, J.-L., Vokrouhlick?, D., et al. 2007, Science, 316, 274

Tholen, D. J. 1984, PhD thesis, University of Arizona

Thomas, P., Adinolfi, D., Helfenstein, P., Simonelli, D., & Veverka, J. 1996, Icarus, 123, 536

Thomas, P., Veverka, J., Bloom, A., & Duxbury, T. 1979, Journal of Geophysical Research: Solid Earth, 84, 8457

Thomas, P. C., Parker, J. W., McFadden, L. A., et al. 2005, Nature, 437, 224

Thomas, P. C., A'Hearn, M. F., Veverka, J., et al. 2013, Icarus, 222, 550

Toiya, M., Stambaugh, J., & Losert, W. 2004, Phys. Rev. Lett., 93, 088001

Tornabene, L. L., Osinski, G. R., McEwen, A. S., et al. 2012, Icarus

Tremaine, S. 2003, AJ, 125, 894

Tsuji, Y., Tanaka, T., & T., I. 1992, Powder Technol., 71, 239

Uehara, J. S., Ambroso, M. A., Ojha, R. P., & Durian, D. J. 2003, Phys. Rev. Lett., 90, 194301

van der Weele, K., van der Meer, D., Versluis, M., & Lohse, D. 2001, EPL (Europhysics Letters), 53, 328

Van Hecke, M. 2005, Nature, 435, 1041

Varanasi, K. K., & Nayfeh, S. A. 2003, Smart Structures and Materials 2003, 5052, 403

Veverka, J., Belton, M., Klaasen, K., & Chapman, C. 1994, Icarus, 107, 2

Veverka, J., Thomas, P., Harch, A., et al. 1997, Science, 278, 2109

Veverka, J., Thomas, P., Harch, A., et al. 1999, Icarus, 140, 3

Veverka, J., Robinson, M., Thomas, P., et al. 2000, Science, 289, 2088

Veverka, J., Farquhar, B., Robinson, M., et al. 2001, Nature, 413, 390

Vokrouhlický, D., & Čapek, D. 2002, Icarus, 159, 449

von Neumann, J., & Richtmyer, R. D. 1950, Journal of Applied Physics, 21, 232

Wachs, A. 2009, Computers & Fluids, 38, 1608

Wada, K., Senshu, H., & Matsui, T. 2006, Icarus, 180, 528

Walsh, K. J., Levison, H. F., Richardson, D. C., & Schwartz, S. R. 2011, in EPSC-DPS Joint Meeting 2011, 1527

Walsh, K. J., Michel, P., Richardson, D. C., & Schwartz, S. R. 2009, in AAS/Division for Planetary Sciences Meeting Abstracts, Vol. 41, AAS/Division for Planetary Sciences Meeting Abstracts #41, #27.10

Walsh, K. J., & Richardson, D. C. 2006, Icarus, 180, 201

Walsh, K. J., Richardson, D. C., & Michel, P. 2008, Nature, 454, 188

—. 2012, Icarus, 220, 514

Walton, O. R., & Braun, R. L. 1986, Journal of Rheology, 30, 949

Wang, W.-J., & Zhu, Z.-G. 2008, EPL (Europhysics Letters), 82, 24004

Weiss, B. P., Elkins-Tanton, L. T., Antonietta Barucci, M., et al. 2012, Planetary and Space Science, 66, 137

Worth, H. 2001, The End of an Asteroidal Adventure: NEAR Shoemaker Phones Home for the Last Time. http://near.jhuapl.edu/news/flash/01feb28.html

Yamamoto, S., Barnouin-Jha, O. S., Toriumi, T., Sugita, S., & Matsui, T. 2009,

Icarus, 203, 310

Yamamoto, S., Kadono, T., Sugita, S., & Matsui, T. 2005, Icarus, 178, 264

Yamamoto, S., Wada, K., Okabe, N., & Matsui, T. 2006, Icarus, 183, 215

Yano, H., Kubota, T., Miyamoto, H., et al. 2006, Science, 312, 1350

Yeomans, D. K., Barriot, J.-P., Dunham, D. W., et al. 1997, Science, 278, 2106

Yeomans, D. K., Antreasian, P. G., Barriot, J.-P., et al. 2000, Science, 289, 2085

Yingst, R., Mest, S., Garry, W., et al. 2012, in Lunar and Planetary Institute Science Conference Abstracts, Vol. 43, 1359

Yoshikawa, M., Abe, M., Tsuda, Y., Nakazawa, S., & Minamino, H. 2012, in COSPAR Meeting, Vol. 39, 39th COSPAR Scientific Assembly, 2225

Zelenyi, L., Zakharov, A., Polischuk, G., & Martynov, M. 2010, Solar System Research, 44, 15

Zellner, B., & Capen, R. 1974, Icarus, 23, 437

Zhou, Y., Wright, B., Yang, R., Xu, B., & Yu, A. 1999, Physica A, 269, 536

Zhou, Y., Xu, B., Yu, A., & Zulli, P. 2002, Powder technology, 125, 45

Zhu, H. P., & Yu, A. B. 2006, Powder Technol., 161, 122

Zolotov, M. Y. 2009, Icarus, 204, 183

Zuber, M. T., Smith, D. E., Cheng, A. F., et al. 2000, Science, 289, 2097